TECHNISCHE UNIVERSITÄT MÜNCHEN

TUM School of Engineering and Design

Partitioned Coupling Strategies to Simulate Granular Mass Flows Impacting Flexible Protective Structures

Veronika Maria Singer

Vollständiger Abdruck der von der TUM School of Engineering and Design der Technischen Universität München zur Erlangung einer

Doktorin der Ingenieurwissenschaften (Dr. -Ing.)

genehmigten Dissertation.

Vorsitz:

Prof. Dr.-Ing. Roberto Cudmani

Prüfende der Dissertation:

1. Prof. Dr.-Ing. Kai-Uwe Bletzinger
2. Prof. Dr.-Ing. habil. Roland Wüchner
3. Assoc. Prof. Antonia Larese De Tetto, Ph.D.

Die Dissertation wurde am 21.05.2024 bei der Technischen Universität München eingereicht und durch die TUM School of Engineering and Design am 01.10.2024 angenommen.

Schriftenreihe des Lehrstuhls für Statik
TU München

Band 67

Veronika Maria Singer

Partitioned Coupling Strategies to Simulate Granular Mass Flows Impacting Flexible Protective Structures

München 2024

Veröffentlicht durch

Kai-Uwe Bletzinger
Lehrstuhl für Statik
Technische Universität München
Arcisstr. 21
80333 München

Telefon: +49(0)89 289 22422
Telefax: +49(0)89 289 22421
E-Mail: kub@tum.de
Internet: www.cee.ed.tum.de/st/startseite/

ISBN: 978-3-943683-78-3

Kurzfassung

Die Intensität und die Häufigkeit von Naturkatastrophen, wie Lawinen, Muren und Hangrutschungen, haben durch den Klimawandel stark zugenommen. Um die katastrophalen Auswirkungen dieser Ereignisse zu begrenzen, ist es essentiell, geeignete Schutzstrukturen in gefährdeten Gebieten zu errichten. Um diese jedoch entsprechend dimensionieren zu können, sind neben geeigneten Experimenten numerische Simulationsmethoden von entscheidender Bedeutung.

In dieser Arbeit werden partitionierte Kopplungsstrategien entwickelt, um die komplexe Interaktion zwischen gravitationsgetriebenen Massenströmen und flexiblen Schutzstrukturen zu simulieren. Die Aufbringung robuster Randbedingungen in den einzelnen Teilmodellen ist für dieses Kopplungsverfahren essentiell, da die Interaktion durch den Austausch von Randbedingungen am gemeinsamen Interface stattfindet.

Zur Modellierung des granularen Massenflusses wird die Materiel Point Methode (MPM) als Diskretisierungsmethode verwendet, da das fließende Material durch Lagrange-Partikel repräsentiert wird, während die Gleichgewichtsgleichungen am Euler-Hintergrundnetz gelöst werden. Die spezielle Diskretisierung ermöglicht die Abbildung der im granularen Massenfluss auftretenden großen Dehnungen, welche ansonsten bei Lagrange-basierten Berechnungsmethoden zu schlechten Netzqualitäten und rechenintensiven Neuvernetzungsalgorithmen führen würde. Dadurch jedoch, dass das Material lediglich über einzelne Partikel repräsentiert wird, die sich durch das Hintergrundnetz bewegen, müssen Strategien entwickelt werden, um das Interface in MPM während der Berechnung zu definieren. Des Weiteren ist eine schwache Aufbringung der Randbedingungen erforderlich, da sich die Position des Interfaces während der Berechnung durch die Interaktion mit den gekoppelten Teilmodellen verändert.

Aus diesem Grund werden massenlose Randpartikel eingeführt, welche die Position des Interfaces während der Simulation bestimmen und anhand derer die Randbedingungen auf das MPM-Modell aufgebracht werden. Für die partitionierte Kopplung mit der Diskreten Elemente Methode (DEM) wird eine Neumann Interfacebedingung für MPM entwickelt, welche die Kontaktkräfte von DEM als diskrete Punktlasten auf das MPM-Teilmodell aufbringt. Die daraus resultierenden Kinematiken des Interfaces, die durch das anschließende Lösen des MPM-Modells entstehen, werden an das DEM-Modell zurückgegeben, sodass damit aktualisierte Kontaktkräfte bestimmt werden können. Die Kopplung basiert auf dem Gauss-Seidel Kommunikationsschema und es wird eine schwache Kopplungsstrategie angewandt. Die Kombination dieser beiden numerischen Methoden ermöglicht die numerische Simulation von Stützwandsystemen, bestehend aus mehreren gestapelten Blöcken, in Interaktion mit granularen Massenströmen. Insbesondere kann auch der Versagensprozess der Stützwand durch die entwickelte Methode numerisch abgebildet werden, was im Vergleich mit experimentellen Ergebnissen validiert wird.

Darüber hinaus werden in dieser Arbeit auch hochflexible Schutznetze betrachtet und deren Verhalten während eines Füllprozesses mit einem granularen Massenstrom numerisch simuliert. Hierfür wird eine Kopplungsstrategie von MPM und der Finite Elemente Methode (FEM) entwickelt, sodass die komplexen Strukturen mit FEM modelliert werden können, während weiterhin MPM für die flie-

ßenden Massenströme verwendet wird. Voraussetzung für diesen Kopplungsalgorithmus sind Dirichlet Randbedingungen im MPM-Modell, welche schwach aufgebracht werden müssen. Im Rahmen dieser Arbeit werden daher verschiedene Methoden für den impliziten Lösungsalgorithmus von MPM entwickelt und die jeweilige Robustheit in Bezug auf den Kopplungsalgorithmus bewertet.
Neben der Penalty Methode, die insbesondere aufgrund ihrer numerischen Effizienz eingesetzt wird, wird eine Methode entwickelt, die auf Lagrange-Multiplikatoren basiert und für MPM verwendet werden kann. Da die Randbedingungen direkt im Gleichungssystem enthalten sind, ergibt sich hieraus ein Sattelpunktproblem, welches gelöst werden muss. Im Rahmen dieser Arbeit wird eine neue Methodik entwickelt, welche die einfachen elementweisen Interpolationsfunktionen, die klassischerweise in MPM zur Approximation des Verschiebungsfeldes verwendet werden, mit elementweisen konstanten Lagrange Multiplikatoren kombiniert. In Verbindung mit einem mechanisch motivierten Eliminierungsprozess können Randbedingungen robust, effizient und vor allem auch benutzerfreundlich aufgebracht werden, da die umständliche Kalibrierung des Penaltyfaktors entfällt.
Ergänzend wird die Perturbed Lagrange Methode für MPM formuliert, welche sich aus einer Kombination der oben genannten Randbedingungen ergibt und als Interface Randbedingung in die systematische Bewertung mit einbezogen wird.
Basierend auf diesen Entwicklungen wird der partitionierte Kopplungsalgorithmus von FEM und MPM hergeleitet und verschiedene Beispiele mit steigender Komplexität systematisch ausgewertet. Diese Beispiele verifizieren die entwickelte Methodik und demonstrieren gleichzeitig das breite Anwendungsspektrum, das sich durch die Kombination dieser beiden Diskretisierungsmethoden ergibt. Als abschließendes Beispiel wird eine hochflexible Schutzstruktur berechnet, welche mit gravitationsgetriebenem granularem Material gefüllt wird.
Diese Dissertation ermöglicht somit eine allgemeine Interfacebeschreibung für MPM, anhand wessen Neumann und Dirichlet Randbedingungen im impliziten Lösungsalgorithmus von MPM schwach aufgebracht werden können. Diese Entwicklungen vergrößern auch das Anwendungsspektrum von MPM, da Randbedingungen unabhängig vom Hintergrundnetz definiert werden können und für die Dirichletbedingungen auch die Erweiterungen für verschiebliche und geneigte Auflager- sowie Kontaktbedingungen eingeführt werden.
Darauf aufbauend werden partitionierte Kopplungsalgorithmen mit DEM und FEM entwickelt, um komplexe ingenieurtechnische Probleme zu lösen, wobei der Schwerpunkt dieser Arbeit auf der Interaktion von granularem Material mit Schutzstrukturen liegt.

Abstract

The frequency and intensity of natural disasters, including avalanches, mudflows, and landslides, have increased significantly in recent years due to climate change and global warming. In order to mitigate the catastrophic effects of these events, it is essential to construct suitable protective structures in areas at risk. However, the design and dimensioning of protective structures is a complex task that requires advanced numerical simulation techniques in addition to physical experiments.

In this work, partitioned coupling strategies are developed to simulate the complex interaction of gravity-driven mass flows impacting protective structures. Due to the large strains developed in the granular mass flow, the Material Point Method (MPM) is used to discretize the physical problem. Thus, the flowing material is represented by Lagrangian particles, while the governing equations are solved on the computational background grid. However, due to this discretization, the imposition of boundary conditions is a complex task.

In particular, moving boundaries, which are required for partitioned coupling with other numerical methods, are crucial since they cannot be imposed at the nodes of the computational background grid. Moreover, an interface description is required for the coupling strategies. For this purpose, boundary particles are introduced, which provide an adequate description of the boundary position during the computation and are used to weakly enforce boundary conditions on the MPM model. In case of an interface condition they receive and send the necessary data to solve the interface equations.

For the partitioned coupling with the Discrete Element Method (DEM), a Neumann interface condition is developed for the MPM submodel, which allows the imposition of point load conditions along the shared interface, while a wall condition is defined at the DEM submodel, which enforces a Dirichlet constraint. Based on this the partitioned MPM-DEM coupling strategy is derived, which combines the capability of DEM to compute accurate contact forces for rigid bodies with the continuum-based approach of MPM to model large-scale mass flows. This coupling strategy is successfully applied to simulate the failure process of retaining wall systems consisting of multiple stacked massive blocks impacted by granular mass flows.

In addition, highly flexible protective structures being impacted by gravity-driven mass flows are also investigated in this work. For this purpose, a partitioned coupling strategy of the Finite Element Method (FEM) and MPM is derived, which allows to combine the strengths of FEM for accurate and efficient modeling of the complex structures, while MPM is advantageous for simulating the large strain event of flowing masses. For this coupling strategy, a Neumann condition is introduced in the FEM partition, while in MPM the weak imposition of essential boundary conditions along the shared interface is required. Since the robust imposition of these boundary conditions and the calculation of the corresponding reaction forces are crucial for the stability of the coupled problem, a main part of this work focuses on these developments.

The penalty method can be used to weakly impose the essential boundary conditions, providing a computationally efficient method. However, the calibration of the penalty factors is a tedious task, and numerical instabilities are easily in-

troduced with increasing factors, which negatively affects the accuracy of the resulting reaction forces and thus the robustness of the coupled simulation.
As an alternative method to weakly impose essential boundary conditions, the Lagrange multiplier method for implicit MPM is developed. To cope with the challenges in MPM of Lagrangian moving material points through an Eulerian background grid, which causes the active background grid elements to change within each time step, a constant element-wise approximation of the Lagrange multipliers within constrained elements, combined with a methodology to eliminate superfluous constraints is developed. This provides a suitable Lagrange multiplier discretization in combination with the simple element-wise interpolation functions used in MPM to approximate the displacement field. These developments provide a robust, efficient, and user-friendly boundary condition imposition method that avoids the cumbersome calibration of the penalty factor.
In addition, the perturbed Lagrangian method, which is a combination of the aforementioned types of boundary condition imposition methods, is derived for implicit MPM and is included in the systematic assessment of the boundary condition methods as interface conditions in a partitioned coupling scheme.
Based on these developments, the partitioned coupling of MPM with FEM is made possible. Various examples of increasing complexity are systematically evaluated to assess the accuracy of the developed methodology and to demonstrate its wide and flexible application range due to the modular coupling of MPM and FEM. Finally, the coupling strategy is successfully applied to model the impact of a gravity-driven mass flow into a highly flexible protective structure.
In conclusion, this dissertation introduces a general interface description for MPM, which allows to weakly impose Dirichlet or Neumann conditions in implicit MPM. In addition these developments are an enhancement for MPM, allowing the imposition of non-conforming boundary conditions and providing the extension to slip and releasing contact conditions for essential boundary conditions. Based on these advances, partitioned coupling strategies with DEM and FEM are developed to simulate complex engineering problems. In this thesis, these coupling strategies are applied to simulate the collapse of retaining wall systems impacted by granular mass flows using the MPM-DEM coupling strategy. In addition, highly flexible protective structures impacted by gravity-driven mass flows are investigated employing the MPM-FEM coupling strategy.

Acknowledgements

This dissertation was written during my time as a research and teaching associate at the Chair of Structural Analysis at the Technical University of Munich. This time has been a great experience, enriching me both professionally and personally. I would therefore like to take this opportunity to thank all those who have contributed to the successful completion of my dissertation and, in particular, those who have made this journey so memorable.

First of all, I would like to express my gratitude to Prof. Kai-Uwe Bletzinger for giving me the opportunity to work in his research group. I appreciated not only his helpful and inspiring supervision, but also the valuable opportunity to teach with him. Moreover, I would like to thank him for fostering a harmonious and exceptionally good working environment at the chair and for giving me the academic freedom to develop and realize new ideas.

My gratitude extends to Prof. Roland Wüchner for his invaluable guidance throughout my research journey. I would especially like to thank him for initiating my research topic at the beginning of my doctorate and also for all the insightful discussions that have greatly enriched my work.

I would like to sincerely thank Prof. Antonia Larese for her unwavering support during my doctorate. Moreover, I would like to thank her for introducing me to the research community of computational mechanics and particle-based methods as well as for the numerous scientifically valuable and always joyful exchanges we had.

Furthermore, I like to thank all my colleagues who accompanied me over the past years for the insightful discussions, the collaborative work and, above all, for the enjoyable and pleasant time we have spent together. Among them I want to acknowledge Dr.-Ing. Benedikt Philipp who helped me on my way to the chair as well as my teaching assistant colleagues Dr.-Ing. Ann-Kathrin Goldbach, Dr.-Ing. Andreas Winterstein and Dr.-Ing. Martin Fußeder for their excellent and trustworthy cooperation. Additionally Dr.-Ing. Klaus B. Sautter, my longtime roommate, not only for the intense work together as teaching assistants but also for the close collaboration on the numerical simulation of natural hazards. Furthermore, there are Dr.-Ing. Manuel Meßmer, Dr.-Ing. Philipp Bucher, Dr.-Ing. Thomas Oberbichler, Dr.-Ing. Tobias Teschemacher, Dr.-Ing. Máté Péntek, Stefan Grabke and Andi Katili who also greatly enriched my time at the chair, both in terms of technical discussions and personal conversations.

Finally, I would like to express my deepest gratitude to my family, especially my husband Manuel and my children Manolo and Marla. I am very grateful for your constant support and advice, but also for your patience during this challenging but rewarding period of my life.

Veronika Maria Singer
Technical University of Munich
October 2024

Contents

CHAPTER 1

Introduction

1.1 Motivation

In recent decades, the frequency and intensity of natural hazards have increased significantly due to climate change and global warming. Among the wide variety of natural hazards, the current work focuses on gravity-driven natural hazards involving large moving masses. These include landslides, where soil and debris move downhill as well as snow avalanches in mountainous regions. Additionally, rockfall events are included in this category, but are not the primary focus of the current work.

These catastrophic events often cause extensive damage to buildings, roads, and other critical infrastructure systems, resulting in enormous economic costs, with billions of dollars spent each year to rebuild and recover. Furthermore, the social impact of these disasters is profound, with people losing their homes, suffering psychological trauma in the aftermath of such events, and tragically, many losing their lives.

Therefore, in the long term, climate change mitigation measures, such as reducing greenhouse gas emissions and transitioning to renewable energy sources, are essential to reduce the frequency and severity of these disasters. In addition, adaptation measures are indispensable to mitigate the impacts of gravity-driven natural hazards in the short term. In this context, the design and construction of protective structures in areas at high risk of natural disasters is of central importance.

The selection of protective structures depends on the topography of the area in which the structure is to be installed and the expected impact scenario. Depending on these factors, different types of structures may be appropriate.

For instance, in areas where slopes need to be stabilized, particularly along roads or near buildings, retaining walls are often installed. These walls are designed to resist the lateral pressure of soil or rock masses and prevent them from collapsing. They typically consist of stacked massive blocks and are usually constructed of concrete or gabions (wire mesh baskets filled with rock). Figure 1.1a) shows an example of a gabion wall installed along a road, while 1.1b) shows stacked

massive concrete blocks used to stabilize the gravel pile.

a) Gabions in Sonthofen, Germany

b) Stacked concrete blocks in Buchloe, Germany

Figure 1.1: Examples of installed retaining wall systems.

While rigid structures such as retaining walls are primarily installed for slope stabilization, flexible protective structures are required for highly dynamic impact masses due to their enormous energy absorption capacity. Hence, these structures are often installed in rockfall prone areas and are becoming increasingly popular for protecting vulnerable areas from snow avalanches or landslides. Figure 1.2 shows an example of a flexible protective structure installed to protect a nearby village from mudflows.

Figure 1.2: Flexible protective structure installed in Altstätten, Switzerland.

Typically, these structures consist of a net spanned between steel profiles. To enable the structure to undergo significant deformation upon impact, a hinged support is usually incorporated at the base of the profiles. This allows them to rotate around their support point upon impact, activating the stiffness of the cables attached at the top. These cables are spanned uphill and are usually equipped with braking elements to absorb energy through plastic deformation. Also, the cables spanning in the transverse direction are usually equipped with braking elements. Due to this flexible design, the braking distance of the impacting mass flow is increased and consequently the peak impact forces are significantly reduced compared to a rigid structure.
However, the design and dimensioning of protective structures is a complex task that requires advanced numerical simulation techniques in addition to physical experiments.

First, each type of structure has unique characteristics that need to be represented in the numerical model. For instance, in the case of retaining wall systems as shown in Figure 1.1, the mutual contact of the rigid blocks is critical to the design. On the other hand, flexible structures as exemplified in Figure 1.2 require careful modeling of stress distribution, deformation pattern and energy absorption as these factors are interdependent and critical to the design.
Second, various types of natural hazards need to be modeled. This involves the simulation of soil or debris flow in a landslide, the behavior of snow in an avalanche, or the characteristics of rock in case of rockfall impacts.
Finally, the interaction between the protective structure and the natural hazard needs to be modeled to predict the impact and loading scenarios and the subsequent behavior of the structure. The simulation of this interaction provides a deeper understanding of real-world physics and is necessary for the effective and efficient design of protective structures.
Therefore, to accurately simulate these complex problems involving protective structures and natural hazards, it is necessary to divide the modeling process into three key components: the structural modeling, the natural hazard model, and the simulation of the close interaction during the impact.

Among the numerical methods developed to simulate engineering problems, the Finite Element Method (FEM) is the most popular and established numerical method. FEM has earned this distinction due to its versatility, accuracy, and applicability to a wide spectrum of engineering disciplines, making it the primary choice for modeling the complex behavior of flexible protective structures.
Different types of elements can be used to represent various components of the protective structure. For instance, cable elements are used to model the tensioned cables spanned uphill, while truss or beam elements represent the steel profiles. However, the structural modeling of the net spanned between the profiles is more complex, and within the last decades, several approaches have been developed for that (see e.g. [58, 48, 127]). The challenge is to develop computationally efficient methods that still capture the net's main characteristics and the load-carrying behavior for the anticipated impact scenarios.
Recently, [101] introduced a more efficient modeling approach to capture the main characteristics of the complex net structure in the case of rockfall impact. This innovative approach avoids computationally expensive micro-level formulations, but globally resolves the complex structural behavior of the net using surrogate membrane elements. This modeling approach has been extensively investigated to model the impact of rocks on highly flexible protective structures. While these structures were modeled with FEM, the Discrete Element Method (DEM) was used to calculate the rock movement. Bringing together the different physics, a partitioned coupling scheme of DEM and FEM was developed (see e.g. [101, 105, 103]) to model the impact of the rock and the subsequent structural response. The comparison of the numerical results with physical experiments demonstrated a good agreement, confirming the appropriateness of both the simplified structural model and the coupling approach used.
The structural modeling of flexible protective structures within this work builds on the findings and modeling approaches developed in [101] using FEM. However, instead of rockfall events, the anticipated impact scenarios on protective

structures in this work are gravity-driven masses such as landslides or avalanches flowing down a mountainous region. Moreover, various types of protective structures are investigated. While the flexible protective structures, as shown in Figure 1.2, have similarities to rockfall barriers, the retaining wall blocks, exemplified in Figure 1.1 require a completely different modeling approach.

For the latter structure, the mutual contact conditions of the individual blocks and their overall movement are decisive for the proper design of these structures, whereas the strains of the individual blocks are negligible. For this reason, it is common practice to simplify the individual blocks as rigid bodies interacting with each other. Furthermore, understanding the failure process of these structures is critical to a thorough understanding of these structures and therefore needs to be captured by the numerical model. Consequently, DEM serves as an effective and computationally efficient framework for their numerical simulation.

Therefore, for the structural modeling in this thesis, DEM is chosen for the calculation of retaining walls consisting of individual blocks, while Lagrangian FEM is used for the modeling of highly flexible protective structures. Since the failure process of retaining wall blocks is to be incorporated in the numerical models, both types of protective structures are classified as flexible.

However, these numerical methods are limited for modeling gravity-driven natural hazards involving large flowing masses, such as landslides and avalanches. For these large-scale events, the discrete approach has its limitations because of the need to model the individual grains of the large-scale flows and their interactions. A continuum-based technique is therefore more appropriate. However, classical FEM or other Lagrangian mesh-based methods are likely to suffer from mesh entanglement and distortion to model these large strain events, requiring computationally expensive re-meshing schemes to model these masses flowing down a mountainous region.

Therefore, continuum-based particle methods are the natural alternative to simulate these mass flows, including huge topological changes of the material. Among them, the Material Point Method (MPM) is particularly suitable as it combines the advantages of both meshless and mesh-based numerical techniques. As originally proposed by Sulsky et al. [120], the physical domain is discretized by Lagrangian moving particles called material points. Each represents a discrete part of the physical domain and carries the history dependent variables during the computation. In addition to the material points, which represent the continuum body $\mathscr{B}$, an Eulerian computational background grid is introduced in MPM, which is used to solve the governing equations. Thus, MPM inherently has many similarities to the well-established updated Lagrangian FEM.

Another layer of complexity is added to the numerical modeling when gravity-driven masses and protective structures, each of which requires an appropriate numerical method to model its individual characteristics, are in close interaction and therefore interdependent. Figure 1.3 demonstrates this close interaction showing examples of flexible protective structures in their deformed state after restrained mass flows. Therefore, these problems involve several physical phenomena and are referred to as *multi-physics* in the following.

There are either monolithic or partitioned coupling approaches to model the interaction between different physics. While the monolithic approach, which

a) Debris-flow event in Japan b) Mud-flow experiments in Switzerland

Figure 1.3: Examples for restrained mass flows by flexible protective structures. All photographs are property of Geobrugg (https://www.geobrugg.com)

solves all the physics involved simultaneously, usually provides higher accuracy, it is very limited in its application to different multi-physics problems, as new monolithic formulations incorporating the coupling have to be developed for each type of problem. The partitioned approach, on the other hand, is more flexible in this regard, since it solves the physics involved independently, allowing the reuse of solvers and tools that have been thoroughly developed over many years. The involved solvers can be used as black-box solvers, while the interaction between them is shifted to their shared interface. Various techniques have been developed to transfer the interface data while maintaining the accuracy and stability of the partitioned approach. The developments for the partitioned coupling approach are often driven by Fluid-Structure Interaction (FSI) problems, just to mention [138, 130, 136, 135, 108], but are also adapted to various physics. Therefore, in this work, the partitioned approach is adapted to model the interaction of gravity-driven masses impacting different types of protective structures. Thus, this approach preserves the modularity of the involved solvers and simultaneously provides the possibility to couple different numerical methods.

A key component of the partitioned coupling approach is the definition of boundary conditions along the shared interface required for data exchange. For Lagrangian mesh-based methods, such as FEM, the nodal deformations of the mesh always follow the movement of the structure. Therefore, the boundary conditions can be straightforwardly imposed at the nodes of the shared interface (see also Figure 1.4, left). These conditions comply naturally with the Kronecker delta property and will be referred to as *conforming* boundary conditions in the following.

For particle based methods, however, the imposition of boundary conditions along the shared interface is more complex. In DEM, this is solved by introducing a wall condition at the shared interface. This approach, which defines a Dirichlet boundary condition in the DEM partition, was initially developed by [99] to couple DEM with FEM in a partitioned scheme and further used by [101] to model the impact of rocks on highly flexible protective structures. Therefore, the current work builds on these developments by using the wall condition within the DEM solver to impose the boundary conditions required for partitioned coupling with MPM.

However, imposing boundary conditions in MPM is a challenging task as the continuum body $\mathscr{B}$ is discretized by Lagrangian moving particles while the governing equations are solved on the computational background grid. Therefore, in contrast to classical FEM, the boundary conditions can rarely be imposed directly on the nodes of the background grid, which is also illustrated in Figure 1.4, showing the discretization of a continuum body $\mathscr{B}$ using either Lagrangian FEM or MPM.

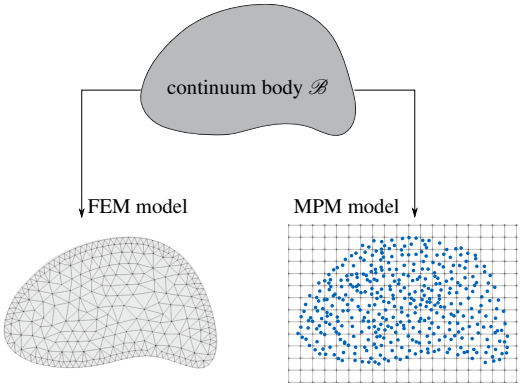

Figure 1.4: Discretization of the continuum body $\mathscr{B}$ by Lagrangian FEM (left) and by MPM (right). The blue dots represent the material points.

Hence, incorporating MPM into a partitioned coupling scheme first requires a methodology to track the shape and topology of the shared interface over time. Second, the boundary conditions need to be weakly imposed, since the boundary definition generally does not coincide with the nodes of the computational background grid. In the following, they will be referred to as *non-conforming* boundary conditions.

For this purpose, boundary particles are introduced along the shared interface, which follow its topology and shape over time. These mass-less particles are used to weakly impose either Neumann or Dirichlet conditions on the MPM model. While the imposition of Neumann conditions is comparatively easy, the weak imposition of Dirichlet conditions is a more challenging task and different methods are developed in this thesis.

The penalty method, which is also known from other immersed methods (e.g., [7] for FEM, e.g., [76] for FCM, e.g., [27, 122] for IBRA), is a numerical approach to impose non-conforming essential boundary conditions. It is particularly attractive since the conditions are imposed numerically without adding additional degrees of freedom (dofs) to the system of equations. As part of a master's thesis supervised by the author [33], this numerical approach was adapted to implicit MPM. The results and verification examples are published in [34].

However, the penalty factor needs to be carefully calibrated to the system being solved. While factors that are too low result in material penetration through the boundary, factors that are too high result in numerical instabilities. This is par-

ticularly problematic when the boundary imposition method is used in a partitioned scheme, and therefore the reaction forces are also important for the stability of the coupled problem.

As an alternative, a method to robustly impose essential boundary conditions in MPM with Lagrange multipliers is developed in this work. The great advantage of this method is that the constraint equations are included in the system of equations, yet requiring the need of additional dofs. However, since a saddle point problem has to be solved, the design of a stable Lagrange multiplier solution is non-trivial. This topic has been studied intensively, especially for FEM and other numerical methods to weakly impose essential boundary conditions [11, 16]. Specifically for the imposition of boundary conditions, Babuška [9] showed that equal order of interpolation of the respective fields demands two different mesh sizes for the displacements and Lagrange multipliers. Following this approach leads to a complicated and computationally expensive construction of the Lagrange multiplier discretization, as proposed for example by Béchet et al. [16] and extended to 3D by Hautefeuille et al. [63] for the extended finite element method.

However, these approaches are not suitable for MPM as the set of active background grid elements can vary at each time step due to the Lagrangian moving particles within the Eulerian background grid. Moreover, the boundary conditions are not necessarily aligned with the body contour, but can be arbitrarily positioned within the background grid, leading to different interactions between the material and the boundary at each time step.

To cope with these challenges, a novel element-wise formulation is introduced to weakly impose non-conforming Dirichlet conditions using Lagrange multipliers. The proposed formulation uses a constant Lagrange multiplier approximation within constrained elements in combination with a methodology to eliminate superfluous constraints. Thus, a suitable Lagrange multiplier discretization is obtained in combination with simple element-wise interpolation functions classically used in MPM to approximate the displacement field. In this way, a robust, efficient, and user-friendly boundary imposition method for immersed methods specified here for implicit MPM is obtained. The developments are published by the author in [117] and are summarized in this thesis.

In addition, the perturbed Lagrangian method is introduced as a combination of the aforementioned two methods. Similar to the Lagrange multiplier approach, the constraint equations are included in the system of equations, assuming a constant Lagrange multiplier approximation. In addition, however, the penalty term is added for stabilization to avoid the elimination procedure of unnecessary constraints. Therefore, this method shows similarities to both the Lagrange multiplier and the penalty approach. Furthermore, it is demonstrated that through static condensation, this approach is consistent with the penalty formulation. Nonetheless, although it results in the penalty formulation, the additional dofs considering the constraint equations reduce to some extent the numerical instabilities introduced by the penalty factor. This effect is demonstrated by the numerical examples in section 3.5, which compare the different methods of imposing boundary conditions. In particular, the performance of these boundary imposition methods is systematically assessed with respect to their application as interface conditions in a partitioned coupling scheme.

The definition of appropriate interface conditions in the numerical methods allows their combination in a partitioned coupling scheme. Thus, depending on the physical problem to be solved, the best suited solvers can be selected for the physics involved, while their interaction is shifted to their shared interface.
However, partitioning introduces additional interface equations which must be solved to compute the overall problem. For this reason, a general framework that provides a systematic exchange of the interface data to solve the interface equilibrium is advantageous. Within this work the *CoSimulation* Application [77], mainly developed by Bucher [31], is used as a general framework to couple the involved solvers and to manage the required data exchange.
Therefore, bringing together all aspects to finally model the challenging physical problem of flowing masses, such as landslides or avalanches, in interaction with different types of protective structures, the MPM-DEM (presented in chapter 5) and the MPM-FEM coupling methodology (presented in chapter 6) are introduced and verified in this thesis. Starting with academic validation examples, their accuracy with physical experiments is also demonstrated.
Due to the modular treatment of the individual solvers within the partitioned coupling scheme, in combination with the developed interface definition in MPM, which allows to impose either Dirichlet or Neumann conditions at the shared interface, the developments can be easily extended to couple MPM with other numerical methods.
The boundary imposition methods for the MPM model as well as the presented coupling methodologies, are all implemented in the open source multi-physics software *KRATOS* [43, 42, 52]. This software is mainly written in C++ and provides a Python interface. The current version is available on [77].

1.2 Contributions of this Work

The current work focuses on the numerical simulation of gravity-driven mass flows, such as avalanches and landslides, in interaction with protective structures. Two specific types of protective structures are investigated, each requiring distinct numerical methods to adequately capture their individual characteristics. An additional numerical method, MPM, is employed to simulate the flowing masses. In order to model the interaction of these masses with these types of protective structures, partitioned coupling schemes are developed, which allow the combination of the numerical methods involved in a modular fashion. A crucial aspect of these schemes is the imposition of boundary conditions along the shared interface within each involved solver. This task becomes particularly challenging in the context of MPM, necessitating the development of methods to weakly impose these boundary conditions.
Therefore, the following contributions and advances have been made in this work:

- Starting with the supervision of a master's thesis [33], the penalty method was developed to weakly enforce boundary conditions in MPM. This involved representing the boundary with boundary particles and enforcing the Dirichlet conditions by penalty augmentation. In collaboration, the

developed methodology to impose non-conforming boundary conditions in implicit MPM by means of penalty augmentation was published in [34].

- To circumvent the numerical errors introduced by the penalty factor, a methodology for weakly imposing the essential boundary conditions in MPM using Lagrange multipliers is developed. This approach introduces a constant Lagrange multiplier approximation within constrained elements in combination with a methodology to eliminate superfluous constraints. Thus, in combination with simple element-wise interpolation functions classically used in MPM to approximate the displacement field, a suitable Lagrange multiplier discretization is obtained. The results are published in [117] by the author and provide a robust, efficient, and user-friendly boundary imposition method for immersed methods specified for implicit MPM.

- As a combination of the aforementioned boundary imposition methods, the perturbed Lagrangian method is formulated for MPM. In this approach, the constraint equations remain part of the system of equations, but are regularized (relaxed) by an additional penalty term. Consequently, the procedure to eliminate superfluous constraints is circumvented, while the characteristics of the penalty approach are introduced.

- The performance of these boundary imposition methods, especially with respect to their use as interface conditions in a partitioned coupling scheme, is systematically assessed.

- In addition to the Dirichlet conditions, a particle point load condition, inspired by the theory introduced by [72], is incorporated. In this work, the point load condition is extended to serve as an interface condition in a partitioned coupling scheme. For this purpose, Lagrangian moving boundary particles are introduced at the shared interface, which receive forces from the coupled counterpart and impose them as point load conditions on the MPM model.

- Based on these developments and in combination with the knowledge of FEM-DEM coupling provided in [105, 103], a partitioned MPM-DEM coupling scheme is developed, which combines the advantages of both numerical methods in a generalized way. The theory as well as verification and validation examples are published in [115] by the author. Another example is given in [114], which demonstrates the applicability of the proposed methodology to model retaining wall blocks and their failure patterns when interacting with gravity-driven mass flows.

- In order to expend the numerical simulation capabilities to highly flexible protective structures affected by gravity-driven mass flows, a partitioned MPM-FEM coupling scheme is developed and presented in chapter 6. Important requirements for this coupling methodology are the prior developments of boundary imposition methods for non-conforming Dirichlet conditions in MPM. Therefore, the performance of the penalty, Lagrange, and perturbed Lagrangian method to weakly impose the conditions on

the MPM sub-solver is also included in the verification of the coupling methodology. Furthermore, various examples of increasing complexity are systematically evaluated, providing the basis for solving complex physical problems. Finally, the application of the MPM-FEM coupling methodology to numerically simulate the impact of gravity-driven mass flows on highly flexible protective structures is demonstrated.

1.3 Outline

The work is subdivided into seven chapters and the respective contents are summarized in the following.

- **Chapter 1**: provides the motivation including a summary of the contents as well as an overview of the contributions of the current work.

- **Chapter 2**: introduces the necessary fundamentals starting with a continuum description of a body, introducing the strong and weak forms of the governing equation, and finally deriving the discretized equations to solve the physical problem numerically.
  In addition, the specifications for Lagrangian FEM are introduced and the element formulations for membrane, truss, and cable elements are derived. This provides the foundations for the numerical examples presented in chapter 6, using the partitioned MPM-FEM coupling scheme.
  Finally, based on the rigid body simplification, the governing equations for DEM are derived. Thus, the DEM calculation procedure is introduced and the calculation of contact forces is discussed. This provides the foundations for the numerical examples presented in chapter 5, using the partitioned MPM-DEM coupling scheme.

- **Chapter 3**: specifies the fundamentals described in chapter 2 for MPM and introduces the basic theory of the method. It includes the inter- and extrapolation procedures used to transfer information between the computational background grid and material points, the particle integration scheme, and the time integration used.
  Additionally, the definition of the interface conditions in MPM are discussed. Due to the Lagrangian moving particles in combination with an Eulerian background grid, the weak imposition of boundary conditions is essential for the partitioned coupling schemes developed in chapter 5 and chapter 6. Thus, the particle representation of the boundary is introduced and non-conforming point load conditions required for the coupling scheme with DEM are presented.

  The main part of this chapter focuses on the development of non-conforming Dirichlet conditions to weakly enforce the constraints in the MPM methodology, which is essential for partitioned coupling with FEM. Therefore, the penalty method, the Lagrange multiplier method, and the perturbed Lagrangian method formulated for implicit MPM are derived. Their performance in terms of their applicability as interface conditions in a partitioned scheme is systematically evaluated.

- **Chapter 4**: introduces the fundamentals and notations for partitioned coupling schemes in general. Starting with the black-box solver notation and the interface transmission conditions, the iteration schemes for solving the interface equations are derived. Finally, interpolation-based mapping techniques are presented, which are required to transfer the interface data of the involved solvers.
- **Chapter 5**: specifies the fundamentals provided in chapter 4 for the partitioned MPM-DEM coupling scheme. It provides a comprehensive description of the coupling scheme, including specifications on the discretization that are essential for the coupling scheme. The chapter concludes with several verification and validation examples, starting with an academic example and proceeding to the numerical simulation of a gravity-driven mass flow impacting retaining wall blocks. The flow process and the subsequent failure pattern of the discrete solids are compared with experimental results from the literature.
- **Chapter 6**: provides a comprehensive description of the partitioned MPM-FEM coupling scheme, which is derived based on the fundamentals introduced in chapter 4. Both the weak and strong coupling schemes are introduced, and the sequence of the solvers to solve the coupled problem is thoroughly discussed and evaluated in the verification examples. Furthermore, the accuracy and robustness of the coupled methodology are evaluated in detail for different discretizations and the different types of boundary imposition methods in the MPM sub-solver. The coupling scheme is applied to various examples of increasing complexity to verify its application in static and dynamic cases, incorporating highly flexible structures. After verification, the coupling methodology is validated against experimental results from the literature. Finally, the chapter concludes with a complex example of gravity-driven mass flow that impacts a highly flexible protective structure.
- **Chapter 7**: gives conclusions and an outlook for future research.

CHAPTER 2

Fundamentals

This section provides the mechanics for a continuum body $\mathscr{B}$ occupying a domain Ω with a regular boundary Γ in a three-dimensional Euclidean space $\mathscr{E}$. Based on the kinematics, strains and stresses for different constitutive laws, the governing equations are derived in strong and weak form. The discretization in space and time integration methods are introduced and specified for FEM. In addition, the rigid body specifications are derived and the fundamentals of DEM are provided.

2.1 Differential Geometry

The position vector of each point within a geometry is defined by $\mathbf{X} = X^j \mathbf{e}_j$ where X^j are the respective coordinates and $\mathbf{e}_j$ are the global Cartesian base vectors with $j = \{1,2,3\}$ in three-dimensional space*.
A more general expression is obtained by a parametric description, where a set of curvilinear coordinates θ^i describes the geometric entity. The number of these parameter lines depends on the dimension of the geometric object. While a curve is described by one parameter, two are required for surfaces, while three are for volumes. Thus, for volumetric geometries, the position vector can be expressed by

$$\mathbf{X}(\theta^1,\theta^2,\theta^3) = X^j(\theta^1,\theta^2,\theta^3)\mathbf{e}_j. \tag{2.1}$$

With this parametric description, a local coordinate system with covariant base vectors $\mathbf{G}_i$ can be defined at each point, which is beneficial for describing local properties of the geometry. These base vectors are tangential to the curvilinear coordinates θ^i and are therefore given by

$$\mathbf{G}_i = \frac{\partial \mathbf{X}}{\partial \theta^i}. \tag{2.2}$$

* Einstein's summation convention is applied.

Therefore, the position vector of a point inside the body $\mathscr{B}$ can be expressed in general by

$$\mathbf{X} = X^j \mathbf{e}_j = \theta^i \mathbf{G}_i = \theta_i \mathbf{G}^i, \tag{2.3}$$

while $\mathbf{G}^i$ are the contravariant base vectors being reciprocal to the covariant base vectors $\mathbf{G}_i$.
The metric coefficients are used to transform the co- and contravariant bases into the respective other coordinate system by

$$\mathbf{G}_i = G_{ij}\mathbf{G}^j \qquad \text{with} \qquad G_{ij} = \mathbf{G}_i \cdot \mathbf{G}_j \tag{2.4}$$

$$\mathbf{G}^i = G^{ij}\mathbf{G}_j \qquad \text{with} \qquad G^{ij} = \mathbf{G}^i \cdot \mathbf{G}^j \tag{2.5}$$

while the contravariant metric coefficients can also be obtained from the covariant coefficients by

$$\left[G^{ij}\right] = \left[G_{ij}\right]^{-1}. \tag{2.6}$$

More details on differential geometry can be found e.g., in [14, 74, 64, 18].

2.2 Kinematics

For the Lagrangian kinematic description, the deformation process of an arbitrary point within the body $\mathscr{B}$ is observed. As visualized in Figure 2.1 the current

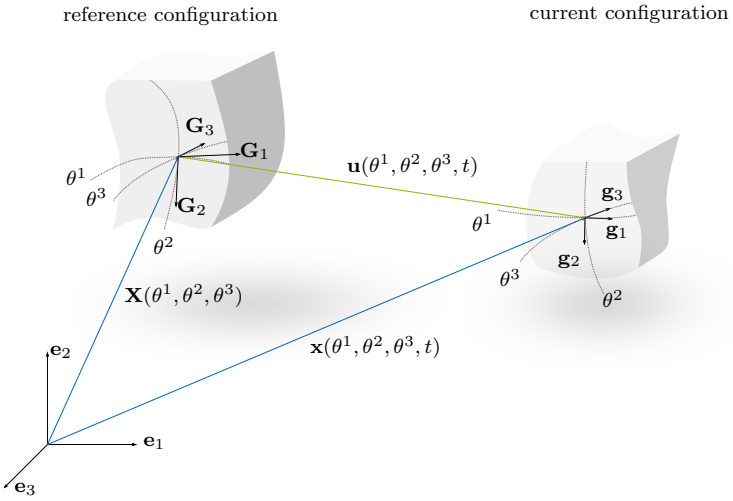

Figure 2.1: Kinematic description of the body $\mathscr{B}$.

deformed configuration $\mathbf{x}$ at time t is compared to the undeformed reference configuration $\mathbf{X}$ at time $t = 0$ which defines the deformation

$$\mathbf{u}\left(\theta^1,\theta^2,\theta^3,t\right) = \mathbf{x}\left(\theta^1,\theta^2,\theta^3,t\right) - \mathbf{X}\left(\theta^1,\theta^2,\theta^3\right). \tag{2.7}$$

The position vector $\mathbf{x}$ in the current configuration is defined by

$$\mathbf{x} = x^j \mathbf{e}_j = \theta^i \mathbf{g}_i = \theta_i \mathbf{g}^i \tag{2.8}$$

and can be described in analogy to the reference configuration by the co- and contravariant base vectors $\mathbf{g}_i$, $\mathbf{g}^i$. Consequently, the metric coefficients g_{ij}, g^{ij} in the current configuration are obtained according to equations 2.4-2.6 using instead the base vectors defined in the current configuration. As commonly applied, uppercase letters are used for all quantities in the reference configuration, while lowercase letters are used for those referring to the current configuration.
The deformation gradient

$$\mathbf{F} = \frac{\partial \mathbf{x}}{\partial \mathbf{X}} = \mathbf{g}_i \otimes \mathbf{G}^i \tag{2.9}$$

links the reference to the deformed configuration and is an important measure to describe strain. Due to the one-to-one mapping between the two configurations, the determinant of $\mathbf{F}$, often called Jacobian, must be non-zero

$$\det[\mathbf{F}] = \frac{\mathrm{d}\Omega}{\mathrm{d}\Omega_0} \neq 0. \tag{2.10}$$

It links the volumes $\mathrm{d}\Omega$ and $\mathrm{d}\Omega_0$ of an infinitesimal element in the respective configurations.
Since the deformation gradient describes the movement of the body, including rigid body motions, it cannot be used directly for the strain measurement. Instead, there exist different strain measures to relate local deformations to certain reference lengths. Among them, the Green-Lagrange strains $\mathbf{E}$ and the Euler-Almansi strains $\mathbf{e}$ are used to describe elastic materials. They are defined as follows

$$\mathbf{E} = \frac{1}{2}\left(\mathbf{F}^T\mathbf{F} - \mathbf{I}\right) = \frac{1}{2}\left(g_{ij} - G_{ij}\right)\mathbf{G}^i \otimes \mathbf{G}^j = E_{ij}\mathbf{G}^i \otimes \mathbf{G}^j \tag{2.11}$$

$$\mathbf{e} = \frac{1}{2}\left(\mathbf{I} - \mathbf{F}^{-T}\mathbf{F}^{-1}\right) = \frac{1}{2}\left(g_{ij} - G_{ij}\right)\mathbf{g}^i \otimes \mathbf{g}^j = e_{ij}\mathbf{g}^i \otimes \mathbf{g}^j \tag{2.12}$$

where $\mathbf{I}$ is the identity tensor. While the Green-Lagrange strains express the distortions with respect to the reference configuration, the Euler-Almansi strains are related to the current configuration. The coefficients $E_{ij} = e_{ij}$ are determined by half the difference between the metrics g_{ij} and G_{ij}.
An important property for element derivation is the transformation rule of the components E_{ij} and e_{ij} to another coordinate system [64]. For example, the transformation to an orthonormal local coordinate system with the bases $\tilde{\mathbf{G}}^k \otimes \tilde{\mathbf{G}}^l$ and $\tilde{\mathbf{g}}^k \otimes \tilde{\mathbf{g}}^l$ respectively can therefore be performed by

$$\tilde{E}_{kl} = E_{ij}(\tilde{\mathbf{G}}_k \cdot \mathbf{G}^i)(\mathbf{G}^j \cdot \tilde{\mathbf{G}}_l) \tag{2.13}$$

$$\tilde{e}_{kl} = e_{ij}(\tilde{\mathbf{g}}_k \cdot \mathbf{g}^i)(\mathbf{g}^j \cdot \tilde{\mathbf{g}}_l) \tag{2.14}$$

which is especially useful for material laws referring to physical quantities.
With the *push-forward* operation

$$\mathbf{e} = \mathbf{F}^{-T}\mathbf{E}\mathbf{F}^{-1} \tag{2.15}$$

the Green-Lagrange strain can be transformed to the current configuration, resulting in the Euler-Almansi strain. The *pull-back* is the inverse operation and is defined by

$$\mathbf{E} = \mathbf{F}^{T}\mathbf{e}\mathbf{F}, \tag{2.16}$$

transforming the quantity based on the current configuration to the reference configuration.
For the description of elastic-plastic materials, which are introduced in section 2.4.2, the Hencky strain measurements are employed which are defined by

$$\mathbf{E}_H = \ln(\mathbf{U}) \quad \text{and} \quad \mathbf{e}_H = \ln(\mathbf{v}) \tag{2.17}$$

in the reference and current configuration, respectively. The *push-forward* and *pull-back* operations can be applied analogously using the equations 2.15 and 2.16 for the Hencky strains.
$\mathbf{U}$ and $\mathbf{v}$ in equation 2.17 are the right (material) and left (spatial) stretch tensor defining the polar decomposition of the deformation gradient

$$\mathbf{F} = \mathbf{R}\mathbf{U} = \mathbf{v}\mathbf{R} \quad \text{with} \quad \mathbf{R}^{T}\mathbf{R} = \mathbf{I}. \tag{2.18}$$

The Hencky strain measure is beneficial for the Mohr-Coulomb constitutive equations used since the principal stretches need to be calculated in the current configuration. They are required to evaluate the yield function (see section 2.4.2), which determines the stress states at which the material response changes from elastic to elastic-plastic.
The principal stretches in the current configuration are the eigenvalues $\boldsymbol{\lambda}$ of the tensor $\mathbf{v}$. They can be computed by a spectral decomposition of the right Cauchy-Green tensor

$$\mathbf{b} = \mathbf{v}^2 = \mathbf{F}\mathbf{F}^{T} = \sum_{a=1}^{3} \lambda_a^2 \hat{\mathbf{n}}_a \otimes \hat{\mathbf{n}}_a \tag{2.19}$$

defining the squares of the principal stretches, while $\hat{\mathbf{n}}_a$ are the normalized eigenvectors in the current configuration. Thus, the principal Hencky strain tensor $\tilde{\mathbf{e}}_H$ is defined by

$$\tilde{\mathbf{e}}_H = \sum_{a=1}^{3} \ln(\lambda_a) \hat{\mathbf{n}}_a \otimes \hat{\mathbf{n}}_a. \tag{2.20}$$

2.3 Stresses

According to Cauchy's stress theorem, the traction vector $\mathbf{p}$ in the current configuration is given by

$$\mathbf{p} = \boldsymbol{\sigma}\mathbf{n} \tag{2.21}$$

where $\mathbf{n}$ is the unit normal vector and $\boldsymbol{\sigma}$ denotes the Cauchy stress tensor

$$\boldsymbol{\sigma} = \sigma^{ij}\mathbf{g}_i \otimes \mathbf{g}_j. \tag{2.22}$$

It is defined in the deformed configuration and is therefore related to the Euler-Almansi strain $\mathbf{e}$ (equation 2.12) and the Hencky strain $\mathbf{e}_H$(equation 2.17). Besides the Cauchy stress tensor, the Kirchhoff stress tensor $\boldsymbol{\tau}$ is often introduced, which is related by

$$\boldsymbol{\tau} = \det[\mathbf{F}]\boldsymbol{\sigma} \tag{2.23}$$

to the Cauchy stress $\boldsymbol{\sigma}$.
It is advantageous for the evaluation of the internal work (see section 2.5) to define contravariant stress components because in combination with the covariant strain the dependence of the bases can thus be eliminated*.
Referring the physical stresses to an undeformed area in the reference configuration leads to the definition of the 1^{st} Piola-Kirchhoff stress tensor

$$\mathbf{P} = \det[\mathbf{F}]\,\boldsymbol{\sigma}\mathbf{F}^{-T} = \det[\mathbf{F}]\,\sigma^{ij}\mathbf{g}_i \otimes \mathbf{G}_j = P^{ij}\mathbf{g}_i \otimes \mathbf{G}_j, \tag{2.24}$$

which is based on the current and reference configuration.
More advantageous, however, is the 2^{nd} Piola-Kirchhoff stress tensor $\mathbf{S}$, which is defined only in the reference configuration and is therefore work conjugate to the Green-Lagrange strain tensor $\mathbf{E}$ (equation 2.11). It is linked to the Cauchy stress $\boldsymbol{\sigma}$ by

$$\mathbf{S} = \det[\mathbf{F}]\,\mathbf{F}^{-1}\boldsymbol{\sigma}\mathbf{F}^{-T} = \det[\mathbf{F}]\,\sigma^{ij}\mathbf{G}_i \otimes \mathbf{G}_j = S^{ij}\mathbf{G}_i \otimes \mathbf{G}_j. \tag{2.25}$$

This equation defines an important relation for calculating the components of the 2^{nd} Piola-Kirchhoff stress tensor by

$$S^{ij} = \det[\mathbf{F}]\,\sigma^{ij}, \tag{2.26}$$

which allows to switch between current and reference configuration.

2.4 Constitutive Equations

The relation between stresses and strains is defined by constitutive equations. These equations describe the response of the material to receive the resulting stresses as a function of the deformation history. Various mathematical models, commonly validated against experimental results, are available in literature to describe different material behaviors. In this thesis, the basic theory for the homogeneous isotropic elastic and elastic-plastic material models that will be used in the later sections is introduced.
First, the basic theory of elastic materials is introduced and then, in section 2.4.2, it is extended to elastic-plastic materials, which are needed to describe the flow behavior of granular materials.

---

* let tensor $\mathbf{A} = A_{ij}\mathbf{G}^i \otimes \mathbf{G}^j$ and tensor $\mathbf{B} = B^{kl}\mathbf{G}_k \otimes \mathbf{G}_l$:
$\mathbf{A} : \mathbf{B} = A_{ij}B^{kl}\left(\mathbf{G}^i \otimes \mathbf{G}^j\right) : \left(\mathbf{G}_k \otimes \mathbf{G}_l\right) = A_{ij}B^{kl}\delta^i_k\delta^j_l = A_{ij}B^{ij}$

2.4.1 Elasticity

A fundamental property of elastic materials is that the stress depends only on the current level of strain, implying that the original shape is recovered upon unloading. Since the stress response of hyperelastic materials is derived from a strain-energy function Ψ that exists for each hyperelastic material, the 2^{nd} Piola-Kirchhoff stress can be obtained by

$$\mathbf{S} = \frac{\partial \Psi(\mathbf{E})}{\partial \mathbf{E}}. \tag{2.27}$$

Since the constitutive equations are invariant with respect to rigid body motions, the strain energy function can be described equivalently by the deformation gradient $\mathbf{F}$, the Green-Lagrange strain tensor $\mathbf{E}$ or the right Cauchy Green tensor $\mathbf{C} = \mathbf{F}^T\mathbf{F}$, yielding

$$\Psi(\mathbf{F}) = \Psi(\mathbf{C}) = \Psi(\mathbf{E}). \tag{2.28}$$

According to equation 2.27, the stress is a function of the strain and therefore depends on the deformations of the body. To solve the governing equations for the continuum body $\mathscr{B}$, which are generally non-linear, an iterative solution technique is applied (see section 2.8.2), which requires the linearized constitutive equation.
The linearization of the constitutive equations yields the elasticity tensor

$$\mathbb{C} = \frac{\partial \mathbf{S}}{\partial \mathbf{E}} = \frac{\partial^2 \Psi}{\partial \mathbf{E} \partial \mathbf{E}}, \tag{2.29}$$

which relates the work conjugate increments of stress and strain by [64]

$$\mathrm{d}\mathbf{S} = \mathbb{C} : \mathrm{d}\mathbf{E}. \tag{2.30}$$

The elasticity tensor $\mathbb{C}$, often called tangent material modulus, is a tensor of 4^{th} order defined in the reference configuration and can be expressed by

$$\mathbb{C} = C^{ijkl}\mathbf{G}_i \otimes \mathbf{G}_j \otimes \mathbf{G}_k \otimes \mathbf{G}_l \tag{2.31}$$

using curvilinear coordinates. In general, it has 3^4 independent coefficients, which can be reduced due to symmetry conditions. Assuming further isotropic material, only Young's modulus E and Poisson's ratio ν are needed as independent parameters to describe the material behavior. In mathematics-based literature these material constants are typically expressed by Lamé operators, which are defined by

$$\lambda = \frac{E\nu}{(1+\nu)(1-2\nu)} \quad \text{and} \quad \mu = \frac{E}{2(1+\nu)}. \tag{2.32}$$

Based on this, the material laws used in this thesis can be formulated.

2.4.1.1 St. Venant-Kirchhoff

For many engineering applications, the St. Venant-Kirchhoff material law can be applied to model the structural behavior. This model is an extension of Hooke's law for large deformations, but with a limitation to small strains. It assumes a linear relation between stress and strain, simplifying equation 2.30 to

$$\mathbf{S} = \mathbb{C} : \mathbf{E} \tag{2.33}$$

and therefore resulting in a constant material tensor. However, especially in the case of compressive strains, the limitation to small strains is crucial, which is described in detail in [137, 104].
The strain-energy function for the St. Venant-Kirchhoff material is defined by [64]

$$\Psi_{\mathrm{SV}} = \frac{1}{2}\lambda\,(\mathrm{tr}\mathbf{E})^2 + \mu \mathrm{tr}\mathbf{E}^2 \tag{2.34}$$

where tr(•) is the trace operator*.
The subsequent derivation of this strain-energy function according to equation 2.29 finally results in the material tensor $\mathbb{C}_{\mathrm{SV}}$. Typically it is formulated in the local Cartesian coordinate system, which allows to express the 4^{th} order tensor in Voigt notation ($\tilde{\bullet}$) following [17]. This results in the constitutive matrix

$$\tilde{\mathbb{C}}_{\mathrm{SV}} = \begin{bmatrix} \lambda+2\mu & \lambda & \lambda & 0 & 0 & 0 \\ & \lambda+2\mu & \lambda & 0 & 0 & 0 \\ & & \lambda+2\mu & 0 & 0 & 0 \\ & & & \mu & 0 & 0 \\ & \text{sym.} & & & \mu & 0 \\ & & & & & \mu \end{bmatrix} \tag{2.35}$$

defining the St. Venant-Kirchhoff material in 3D.
Especially for the implementation of the constitutive equations, the Voigt notation is advantageous because it allows to express the stresses in a matrix-vector product

$$\tilde{\mathbf{S}} = \tilde{\mathbb{C}}_{\mathrm{SV}}\tilde{\mathbf{E}} \tag{2.36}$$

assuming that $\tilde{\mathbf{S}}$ and $\tilde{\mathbf{E}}$ are defined in the local Cartesian coordinate system and are reformulated according to (see e.g. [17])

$$\tilde{\mathbf{E}} = \begin{bmatrix} \tilde{E}_{11} & \tilde{E}_{22} & \tilde{E}_{33} & 2\tilde{E}_{23} & 2\tilde{E}_{13} & 2\tilde{E}_{12} \end{bmatrix}^T \tag{2.37}$$

$$\tilde{\mathbf{S}} = \begin{bmatrix} \tilde{S}^{11} & \tilde{S}^{22} & \tilde{S}^{33} & \tilde{S}^{23} & \tilde{S}^{13} & \tilde{S}^{12} \end{bmatrix}^T. \tag{2.38}$$

For two-dimensional problems, the condensed constitutive matrices can be derived for the plane strain state, assuming

$$\tilde{E}_{33} = \tilde{E}_{23} = \tilde{E}_{13} = 0 \tag{2.39}$$

or plane stress state forcing

$$\tilde{S}^{33} = \tilde{S}^{23} = \tilde{S}^{13} = 0 \tag{2.40}$$

for $\tilde{\mathbf{G}}_3$ being the out-of-plane vector of the local Cartesian coordinate system.

* $\mathrm{tr}\mathbf{A} = A_{ii} = A_{11} + A_{22} + A_{33}$
$\mathrm{tr}\mathbf{A}^2 = A_{ij}A_{ij}$

2.4.1.2 Neo-Hookean

For hyperelastic materials, the Neo-Hookean material model is used, which is derived from the following strain energy function [93]

$$\Psi(\mathbf{C}) = \frac{1}{2}\lambda\left(\ln(\det[\mathbf{F}])\right)^2 - \mu\ln(\det[\mathbf{F}]) + \frac{1}{2}\mu(\mathrm{tr}\mathbf{C} - 3), \tag{2.41}$$

formulated as a function of the right Cauchy Green tensor $\mathbf{C}$, which is related to the Green-Lagrange strain by

$$\mathbf{E} = \frac{1}{2}(\mathbf{C} - \mathbf{I}). \tag{2.42}$$

Therefore, according to equation 2.27, the stress response is derived by

$$\mathbf{S} = \frac{\partial\Psi(\mathbf{C})}{\partial\mathbf{C}}\frac{\partial\mathbf{C}}{\partial\mathbf{E}} = 2\frac{\partial\Psi(\mathbf{C})}{\partial\mathbf{C}} = \lambda\ln(\det[\mathbf{F}])\,\mathbf{C}^{-1} + \mu\left(\mathbf{I} - \mathbf{C}^{-1}\right) \tag{2.43}$$

with the identity

$$\frac{\partial(\det[\mathbf{F}])}{\partial\mathbf{C}} = \frac{\partial(\det[\mathbf{F}])}{\partial\mathbf{F}}\frac{\partial\mathbf{F}}{\partial\mathbf{C}} = \frac{1}{2}\det[\mathbf{F}]\mathbf{C}^{-1}. \tag{2.44}$$

Finally, the elasticity tensor $\mathbb{C}$ in Cartesian coordinates is obtained by

$$\mathbb{C} = 4\frac{\partial^2\Psi(\mathbf{C})}{\partial\mathbf{C}\partial\mathbf{C}} = \lambda\mathbf{C}^{-1}\otimes\mathbf{C}^{-1} + 2\left(\mu - \lambda\ln(\det[\mathbf{F}])\right)\mathbf{I}_{C^{-1}} \tag{2.45}$$

while

$$\mathbf{I}_{C^{-1}} = -\frac{\partial\mathbf{C}^{-1}}{\partial\mathbf{C}} \tag{2.46}$$

is a fourth-order tensor, given in component form by [64]

$$\left(I_{C^{-1}}\right)_{ijkl} = \frac{1}{2}\left(C^{-1}_{ik}C^{-1}_{lj} + C^{-1}_{il}C^{-1}_{kj}\right) \tag{2.47}$$

since $\mathbf{C}$ is a symmetric tensor. A detailed description of this material law can be found e.g., in [17, 20, 137, 67].

2.4.2 Mohr-Coulomb Plastic Law

This section summarizes the main hypothesis on which the elastic-plastic constitutive framework is based. Hyperelastic-plastic materials are assumed, which are based on the multiplicative decomposition of the total deformation gradient $\mathbf{F}$ into an elastic (indicated with superscript e) and a plastic (indicated with superscript p) component of the form

$$\mathbf{F} = \mathbf{F}^e\mathbf{F}^p. \tag{2.48}$$

This decomposition, first introduced by [80], introduces an intermediate configuration $\overline{\Omega}$ as depicted in Figure 2.2, which describes a local stress-free configuration defined by the plastic deformation gradient $\mathbf{F}^p$. However, this configuration

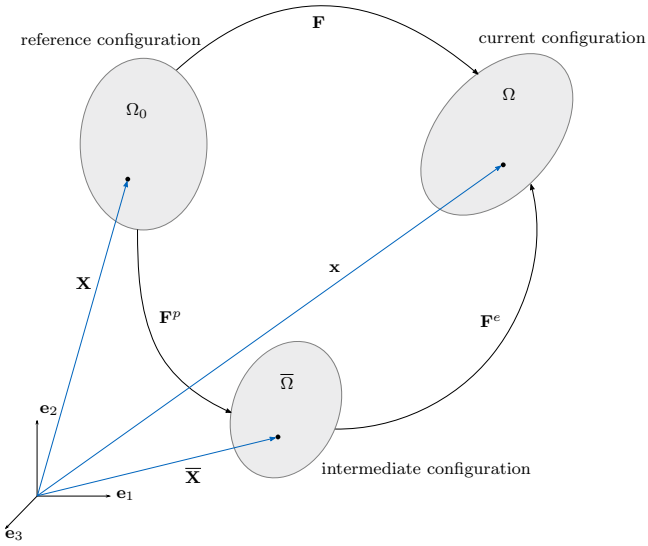

Figure 2.2: Multiplicative decomposition of the deformation gradient and definition of intermediate configuration $\overline{\Omega}$.

is not obtained by a continuous map, but describes a virtual configuration that can be recovered by a purely elastic loading from the fully deformed configuration. Therefore, $\mathbf{F}^e$ is used for pull-backs to describe this intermediate configuration, only used to represent the constitutive response.
Due to the multiplicative decomposition of the deformation gradient, finite strains can be considered within the constitutive model, while the elastic strain is calculated through a hyperelastic potential. In order to determine the state of stress at which the material response changes from elastic to elastic-plastic behavior, a yield criterion needs to be defined.
In this work, the Mohr-Coulomb plastic law, which incorporates pressure dependence into its yield criterion, is employed to characterize the material properties of the granular material. It is based on the concept that yielding occurs when the stress state on a specific plane exceeds the shear strength

$$\tau = c - \sigma \tan(\Phi), \tag{2.49}$$

which is a function of the normal stress σ and the material constants - the cohesion c and the internal friction angle Φ. It is thus based on a phenomenological model that assumes that the macroscopic constitutive behavior arises from the frictional sliding of individual grains at the microscopic level.
In Figure 2.3, the limit line defining the Mohr-Coulomb failure criterion is visualized. Furthermore, a stress state at yield is depicted, assuming that the principal stresses are rearranged as follows

$$\sigma_1 \geq \sigma_2 \geq \sigma_3. \tag{2.50}$$

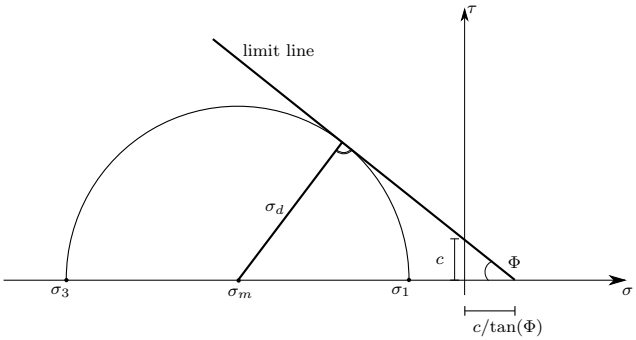

Figure 2.3: Mohr-Coulomb yield behavior.

Consequently, yielding occurs if Mohr's circle, constructed with the principal stresses σ_1 and σ_3 at a current stress state, is tangential to the limit line. The corresponding mean stress σ_m can be calculated by

$$\sigma_m = \frac{1}{2}(\sigma_1 + \sigma_3) \tag{2.51}$$

while the maximum shear stress maxτ, which defines the radius of Mohr's circle, is defined by

$$\sigma_d = \max\tau = \frac{1}{2}|\sigma_1 - \sigma_3|. \tag{2.52}$$

So by using the relationship

$$\sin(\Phi) = \frac{\sigma_d}{c/\tan(\Phi) - \sigma_m} \tag{2.53}$$

the yield criterion can be reformulated to

$$f(\boldsymbol{\sigma}) = |\sigma_1 - \sigma_3| + (\sigma_1 + \sigma_3)\sin(\Phi) - 2c\cos(\Phi) \leq 0 \tag{2.54}$$

describing it in principal stress space. However, the yield surface is a hexagonal pyramid about the $\sigma_1 = \sigma_2 = \sigma_3$ axis in the principal stress space, which introduces difficulties to determine the direction of plastic flow. More details can be found in [67], where different types of stress return and the corresponding constitutive matrices are introduced.
The constitutive matrices are derived following the idea of [111, 110] using the principal stresses to model the elastic response. This allows to extend the small strain return mapping in stress space to the finite deformation regime.
Therefore, to compute the material response of a granular material in the implicit workflow of MPM, which is detailed in chapter 3, first an elastic trial step (indicated by $(\bullet)^{e,\mathrm{tr}}$) is performed calculating the elastic left Cauchy Green tensor $\mathbf{b}^{e,\mathrm{tr}}$ defined in equation 2.19. Performing a spectral decomposition, the principal stretches are determined, which allows to calculate the principal Hencky strain $\tilde{\mathbf{e}}_H^{e,\mathrm{tr}}$ according to equation 2.20.

Based on the strain energy function [111, 110]

$$\Psi(\tilde{\mathbf{e}}_H^{e,\mathrm{tr}}) = \frac{1}{2}\lambda(e_1^{e,\mathrm{tr}} + e_2^{e,\mathrm{tr}} + e_3^{e,\mathrm{tr}})^2 + \mu\Big((e_1^{e,\mathrm{tr}})^2 + (e_2^{e,\mathrm{tr}})^2 + (e_3^{e,\mathrm{tr}})^2\Big), \tag{2.55}$$

which is formulated in terms of the principal Hencky strain tensor $\tilde{\mathbf{e}}_H^{e,\mathrm{tr}}$ with components $e_1^{e,\mathrm{tr}}, e_2^{e,\mathrm{tr}}, e_3^{e,\mathrm{tr}}$, the principal Kirchhoff stresses of the elastic trial step $\tilde{\boldsymbol{\tau}}^{\mathrm{tr}}$ within the Newton iteration can be determined by

$$\tilde{\boldsymbol{\tau}}^{\mathrm{tr}} = \mathbb{C}^e \tilde{\mathbf{e}}_H^{e,\mathrm{tr}}. \tag{2.56}$$

Here $\mathbb{C}^e = \lambda \mathbf{I}\otimes\mathbf{I} + 2\mu I$ is the Hencky elasticity tensor, assuming an isotropic elastic response. λ and μ are the Lamé operators defined by equation 2.32, while the Kirchoff stresses $\boldsymbol{\tau}$ are related to the Cauchy stresses $\boldsymbol{\sigma}$ by equation 2.23. Further details and a comprehensive derivation can be found in [67, 111, 110, 64].
Once the principal trial stresses have been calculated, the Mohr-Coulomb yield criterion defined by equation 2.54 is evaluated in a subsequent step. If the trial stresses satisfy the criterion, no plastic loading occurs. However, if the stresses exceed the criterion, they are adjusted to return to the yield surface. In the case of non-associated plastic flow, the stress return is governed by the plastic potential, which in the case of Mohr-Coulomb plasticity is defined by

$$g(\boldsymbol{\sigma}) = (\sigma_1 - \sigma_3) + (\sigma_1 + \sigma_3)\sin(\psi) \tag{2.57}$$

where ψ is the dilation angle. For isochoric plastic flow, the dilation angle is set to zero to preserve the volume during plastic flow.
This allows to apply the return stress and to calculate the corrected values for the stress and the elastic strain, which is detailed in [67] for the Mohr-Coulomb yield criterion applied for implicit MPM.

2.5 Equilibrium

Considering the Lagrangian moving body $\mathscr{B}$, which occupies the domain Ω with regular boundary Γ, the conservation of linear momentum

$$\mathbf{L} = \int_\Omega \rho \dot{\mathbf{u}} \mathrm{d}\Omega \tag{2.58}$$

needs to be satisfied, while ρ is the spatial mass density and $\dot{\mathbf{u}}$ the velocity. Furthermore, from the conservation of angular momentum the symmetry of the Cauchy stress tensor $\boldsymbol{\sigma} = \boldsymbol{\sigma}^T$ is derived (see [64]).
The material time derivative of the linear momentum leads to the resulting force, which has to be in equilibrium with the body forces (with volume acceleration $\mathbf{b}$) and the external traction $\mathbf{p}$ along the boundary Γ_N resulting in

$$\int_\Omega \rho \ddot{\mathbf{u}} \mathrm{d}\Omega = \int_{\Gamma_N} \mathbf{p} \mathrm{d}\Gamma_N + \int_\Omega \rho \mathbf{b} \mathrm{d}\Omega. \tag{2.59}$$

The left side of this equation postulates the conservation of mass, defined by

$$\rho = \frac{\rho_0}{\det[\mathbf{F}]}, \tag{2.60}$$

while the complete derivation can be found e.g., in [64]. Inserting equation 2.21 and converting the surface integral into a volume integral by the divergence theorem*

$$\int_{\Gamma_N} \boldsymbol{\sigma}\mathbf{n}\mathrm{d}\Gamma_N = \int_{\Omega} \mathrm{div}\boldsymbol{\sigma}\mathrm{d}\Omega \tag{2.61}$$

equation 2.59 transforms to Cauchy's first equation of motion in global form. Since this equation holds for arbitrary volumes, the volume integral can be eliminated, resulting in the local form of Cauchy's first equation

$$\rho\ddot{\mathbf{u}} = \mathrm{div}\boldsymbol{\sigma} + \rho\mathbf{b}, \tag{2.62}$$

which holds for each point $\mathbf{x} \in \Omega$ and for all times t. This second-order differential equation, which is the governing equation for the given problem assuming an isothermal environment, is determined by the Dirichlet and Neumann boundary conditions

$$\mathbf{u} = \overline{\mathbf{u}} \quad \text{on} \quad \mathrm{d}\Gamma_D \tag{2.63}$$

$$\mathbf{p} = \boldsymbol{\sigma}\mathbf{n} = \overline{\mathbf{p}} \quad \text{on} \quad \mathrm{d}\Gamma_N \tag{2.64}$$

where $(\overline{\bullet})$ denotes the prescribed values. Furthermore, the initial conditions at time $t = 0$

$$\mathbf{u}(t=0) = \mathbf{u}_0 \qquad \text{and} \qquad \dot{\mathbf{u}}(t=0) = \dot{\mathbf{u}}_0 \tag{2.65}$$

need to be considered. Together with equations 2.62-2.64 they are describing the initial boundary-value problem.
Since in general no closed-form solution can be found for the given problem, a Galerkin method is applied [142, 53]. Cauchy's first equation of motion (see equation 2.62) is multiplied by a weighting function $\boldsymbol{\eta}$ and integrated over the current volume Ω. By using the variation of the displacements as the weighting function $\boldsymbol{\eta} = \delta\mathbf{u}$ the weak form of the balance equation is obtained

$$\int_{\Omega} (-\mathrm{div}\boldsymbol{\sigma} - \rho\mathbf{b} + \rho\ddot{\mathbf{u}}) \cdot \delta\mathbf{u}\mathrm{d}\Omega = 0, \tag{2.66}$$

which requires that $\delta\mathbf{u}$ vanishes on the boundary Γ_D. The first term of this equation, multiplied by the the variation of the displacements, can be rewritten applying the product rule†

$$-\mathrm{div}\boldsymbol{\sigma} \cdot \delta\mathbf{u} = \boldsymbol{\sigma} : \mathrm{grad}\delta\mathbf{u} - \mathrm{div}(\boldsymbol{\sigma}\delta\mathbf{u}) \tag{2.67}$$

* [64](eq: 1.296): $\int_s \mathbf{A}\mathbf{n}ds = \int_v \mathrm{div}\mathbf{A}\mathrm{d}v$
† [64](eq: 1.290): $\mathrm{div}(\mathbf{A}^T\mathbf{u}) = \mathrm{div}\mathbf{A}\cdot\mathbf{u} + \mathbf{A} : \mathrm{grad}\mathbf{u}$

with $\boldsymbol{\sigma} = \boldsymbol{\sigma}^T$. Additionally, using the divergence theorem* the volume integral can then be transformed into a surface integral by

$$\int_\Omega \mathrm{div}(\boldsymbol{\sigma}\delta\mathbf{u})\mathrm{d}\Omega = \int_{\Gamma_N} \boldsymbol{\sigma}\mathbf{n}\cdot\delta\mathbf{u}\mathrm{d}\Gamma_N = \int_{\Gamma_N} \overline{\mathbf{p}}\cdot\delta\mathbf{u}\mathrm{d}\Gamma_N. \tag{2.68}$$

Considering the consequent variation of the Euler-Almansi strain tensor $\delta\boldsymbol{e} = \mathrm{grad}\delta\mathbf{u}$, the equilibrium can be formulated through the *Principle of Virtual Work* [129] in the spatial description

$$\delta W = \underbrace{-\int_\Omega \boldsymbol{\sigma} : \delta\mathbf{e}\mathrm{d}\Omega}_{\delta W_{\mathrm{int}}} + \underbrace{\int_\Omega \rho\mathbf{b}\cdot\delta\mathbf{u}\mathrm{d}\Omega + \int_{\Gamma_N} \overline{\mathbf{p}}\cdot\delta\mathbf{u}\mathrm{d}\Gamma_N}_{\delta W_{\mathrm{ext}}} - \underbrace{\int_\Omega \rho\ddot{\mathbf{u}}\cdot\delta\mathbf{u}\mathrm{d}\Omega}_{\delta W_{\mathrm{kin}}} = 0 \tag{2.69}$$

which is called the *updated Lagrangian formulation.*
Alternatively, this equation can be expressed in the reference configuration, which is called the *Lagrangian formulation.* By inserting the push-forward relation for the Euler-Almansi strain (see equation 2.15) and transforming the volume integral into the reference configuration (see equation 2.10), the virtual internal work can be transferred into the current configuration by

$$\begin{aligned} -\delta W_{\mathrm{int}} = \int_\Omega \boldsymbol{\sigma} : \delta\mathbf{e}\mathrm{d}\Omega = \int_{\Omega_0} \boldsymbol{\sigma} : (\mathbf{F}^{-T}\delta\mathbf{E}\mathbf{F}^{-1})\det[\mathbf{F}]\,\mathrm{d}\Omega_0 = \\ \int_{\Omega_0} (\det[\mathbf{F}]\,\mathbf{F}^{-1}\boldsymbol{\sigma}\mathbf{F}^{-T}) : \delta\mathbf{E}\mathrm{d}\Omega_0 = \int_{\Omega_0} \mathbf{S} : \delta\mathbf{E}\mathrm{d}\Omega_0 \end{aligned} \tag{2.70}$$

using the formula for the pull-back operation of the 2nd Piola-Kirchhoff stress tensor (see equation 2.25). The remaining volume integrals in equation 2.69 are also transformed by equation 2.10 and due to the conservation of mass (see equation 2.60) the resulting virtual work in the reference configuration reads

$$\delta W = \underbrace{-\int_{\Omega_0} \mathbf{S} : \delta\mathbf{E}\mathrm{d}\Omega_0}_{\delta W_{\mathrm{int}}} + \underbrace{\int_{\Omega_0} \rho_0\mathbf{B}\cdot\delta\mathbf{u}\mathrm{d}\Omega_0 + \int_{\Gamma_{N_0}} \overline{\mathbf{T}}\cdot\delta\mathbf{u}\mathrm{d}\Gamma_{N_0}}_{\delta W_{\mathrm{ext}}} - \underbrace{\int_{\Omega_0} \rho_0\ddot{\mathbf{u}}\cdot\delta\mathbf{u}\mathrm{d}\Omega_0}_{\delta W_{\mathrm{kin}}} = 0, \tag{2.71}$$

where $\mathbf{B}$ is the volume acceleration in the reference configuration and $\overline{\mathbf{T}}$ the respective traction vector acting on the undeformed Neumann boundary Γ_{N_0}.
Generically, equations 2.71 and 2.69 can be written as the variation of the internal, external and kinetic work with respect to $\delta\mathbf{u}$

$$\delta W = \frac{\partial W}{\partial \mathbf{u}}\delta\mathbf{u} = \delta W_{\mathrm{int}} + \delta W_{\mathrm{ext}} - \delta W_{\mathrm{kin}} = 0 \tag{2.72}$$

while the internal work is usually defined negative.
In general, a closed solution for the equilibrium equation 2.72 cannot be found as the number of unknowns would be infinite. Therefore, the problem has to be transformed into a discrete one introducing a discretization in space and time.

* [64](eq: 1.301): $\int_s \mathbf{u}\cdot\mathbf{A}\mathbf{n}\mathrm{d}s = \int_v \mathrm{div}(\mathbf{A}^T\mathbf{u})dv$

2.6 Rigid Body Specifications

Although in theory all materials are deformable and generally deform, when forces are applied it may be convenient to ignore the strains of the materials and consider only the motion of a rigid body. This assumption brings along many simplifications, since the kinematics are usually evaluated at the center of the body, while the integration over the volume can be pre-calculated since it does not change with time.
Performing a pre-integration of equation 2.59 over the volume results in

$$\mathbf{F}_i = m_i \ddot{\mathbf{u}}_i \tag{2.73}$$

where $\mathbf{F}_i$ is obtained by summing all forces, which are acting on the rigid body i. Additionally, the angular momentum needs to be considered. Thus, the material time derivative of the angular momentum results in the equation for the torque $\mathbf{T}$, which is defined by

$$\mathbf{T}_i = \mathbf{I}_i \ddot{\omega}_i + \dot{\omega}_i \times \left(\mathbf{I}_i \dot{\omega}_i\right). \tag{2.74}$$

In this equation, $\mathbf{I}_i$ is the inertia tensor and $\dot{\omega}_i$ and $\ddot{\omega}_i$ the rotational velocity and acceleration, respectively.
The calculation of the inertia tensor highly depends on the choice of the reference frame. Further details can be found e.g., in [70].
A great simplification can be obtained by considering spherical elements with a completely symmetric shape. In this particular case, the torque calculation can be simplified to

$$\mathbf{T}_i = \mathbf{I}_i \ddot{\omega}_i = \frac{2}{5} m_i R_i^2 \ddot{\omega}_i \tag{2.75}$$

where R_i is the radius of the spherical rigid body i. This results in a constant inertia tensor, which simplifies the calculation of discrete spherical particles in DEM as described in section 2.10.

2.7 Spatial Discretization

Spatial discretization is the fundamental concept in numerical analysis and the core of FEM [66, 15, 17, 142] to solve the equilibrium equation 2.72. For this purpose, the continuous spatial domain is subdivided into non-overlapping elements, which are connected at the nodes. This concept reduces the set of unknowns to a finite number and allows to approximate the spatial fields by interpolating the discrete nodal quantities using locally defined basis functions. For example, the displacement field is approximated by

$$\mathbf{u} \approx \mathbf{u}^h = \mathbf{N}\hat{\mathbf{u}}, \tag{2.76}$$

where $\mathbf{N}$ is the shape function matrix and $\hat{\mathbf{u}}$ is the vector containing the discrete displacement values defined by

$$\mathbf{N} = \begin{bmatrix} \mathbf{N}_1 & \mathbf{N}_2 & \dots & \mathbf{N}_{n_n} \end{bmatrix} \qquad \hat{\mathbf{u}} = \begin{bmatrix} \hat{\mathbf{u}}_1 & \hat{\mathbf{u}}_2 & \dots & \hat{\mathbf{u}}_{n_n} \end{bmatrix}^T. \tag{2.77}$$

In this context, n_n represents the total number of nodes considering the total domain. However, when elemental contributions are evaluated, n_n can be reduced to the number of nodes of the element (e.g., in equations 2.104 to 2.106). The same principle is applied to all occurring fields, including the virtual displacement field.
Also the geometry description described by the global curvilinear coordinates θ^i, θ_i (see section 2.2) in the continuum is approximated by discrete nodal positions $\hat{\mathbf{X}}$, $\hat{\mathbf{x}}$ in the reference and current configuration and local basis functions defined by parametric coordinates $\xi_i = \{\xi, \eta, \zeta\}$. Following the isoparametric approach, the same shape functions are utilized to approximate the geometry and the solution field.
Consequently, the discrete base vectors in the reference and current configuration are defined as follows

$$\mathbf{G}_i^h = \frac{\partial \mathbf{X}^h}{\partial \xi_i} = \frac{\partial \mathbf{N}}{\partial \xi_i}\hat{\mathbf{X}} \qquad \mathbf{g}_i^h = \frac{\partial \mathbf{x}^h}{\partial \xi_i} = \frac{\partial \mathbf{N}}{\partial \xi_i}\hat{\mathbf{x}} = \frac{\partial \mathbf{N}}{\partial \xi_i}(\hat{\mathbf{X}} + \hat{\mathbf{u}}). \tag{2.78}$$

Based on this, the discrete forms of the strains according to equations 2.12 and 2.11, respectively can be derived and subsequently lead as well to the definition of the discrete stresses following equation 2.30, which relates the stresses to the strain via the constitutive equations.

Remark 1: Proceeding notation

In order to maintain clarity in the notation, no distinction is made between approximated and exact material tensors in the following. The material tensors utilized in the proceeding derivation are now to be regarded in their discrete form and thus approximated.

Inserting the spatial discretization into equation 2.72 leads to the semi-discrete equilibrium equation

$$\begin{aligned} \delta W^h &= \left(\frac{\partial W_{\text{int}}}{\partial \mathbf{u}^h} + \frac{\partial W_{\text{ext}}}{\partial \mathbf{u}^h} - \frac{\partial W_{\text{kin}}}{\partial \mathbf{u}^h} \right) \delta \mathbf{u}^h \\ &= \delta \hat{\mathbf{u}}^T \left(-\mathbf{F}_{\text{int}}(\hat{\mathbf{u}}) + \mathbf{F}_{\text{ext}} - \mathbf{M}\hat{\ddot{\mathbf{u}}} \right) = \delta \hat{\mathbf{u}}^T \left(-\mathbf{R} \right) = 0, \end{aligned} \tag{2.79}$$

where $\hat{\ddot{\mathbf{u}}}$ are the discrete nodal accelerations and $\mathbf{R}$ is the residual vector. The components of the internal force vector $\mathbf{F}_{\text{int}}$ are obtained from the variation of the internal virtual work with respect to each dof u_r by

$$F_{\text{int},r} = \int_{\Omega_0} \mathbf{S} : \frac{\partial \mathbf{E}}{\partial u_r} \mathrm{d}\Omega_0 = \int_{\Omega} \boldsymbol{\sigma} : \frac{\partial \mathbf{e}}{\partial u_r} \mathrm{d}\Omega, \tag{2.80}$$

while the vector of external forces arises from the external virtual work contribution is defined by

$$\mathbf{F}_{\text{ext}} = \int_{\Omega_0} \rho_0 \mathbf{N}^T \mathbf{B} \mathrm{d}\Omega_0 + \int_{\Gamma_{N_0}} \mathbf{N}^T \overline{\mathbf{T}} \mathrm{d}\Gamma_{N_0} = \int_{\Omega} \rho \mathbf{N}^T \mathbf{b} \mathrm{d}\Omega + \int_{\Gamma_N} \mathbf{N}^T \overline{\mathbf{p}} \mathrm{d}\Gamma_N. \tag{2.81}$$

In this thesis, conservative loads are assumed, which are independent of the deformation $\hat{\mathbf{u}}$.
From the variation of the virtual kinetic work, expressed either in the reference or current configuration, the inertia term is obtained by

$$\mathbf{M}\hat{\ddot{\mathbf{u}}} = \int_{\Omega_0} \rho_0 \mathbf{N}^T \mathbf{N} \mathrm{d}\Omega_0 \hat{\ddot{\mathbf{u}}} = \int_{\Omega} \rho \mathbf{N}^T \mathbf{N} \mathrm{d}\Omega \hat{\ddot{\mathbf{u}}} \tag{2.82}$$

where $\mathbf{M}$ is the mass matrix. Especially for the explicit solution, the mass matrix is often diagonalized, resulting in the lumped mass matrix. Within the scope of this thesis, the lumped mass matrix is computed by summing all entries in each row to the diagonal entry.
Since the virtual nodal displacements $\delta\hat{\mathbf{u}}$ are arbitrary, the residual $\mathbf{R}$ has to vanish for each dof, resulting in an ordinary differential equation each.

Remark 2: Rayleigh damping

To consistently consider the damping forces, the equilibrium equation 2.72 needs to be extended to include the inertial and stiffness proportional terms [66]. Within the scope of this thesis, the well-established Rayleigh damping is considered, which approximates the complex damping influence by an additional term added to the semi-discrete equilibrium equation 2.79

$$\mathbf{R} = \mathbf{M}\hat{\ddot{\mathbf{u}}} + \mathbf{D}\hat{\dot{\mathbf{u}}} + \mathbf{F}_{\mathrm{int}}(\hat{\mathbf{u}}) - \mathbf{F}_{\mathrm{ext}} = \mathbf{0} \tag{2.83}$$

employing the damping matrix $\mathbf{D}$ and the discrete nodal velocities $\hat{\dot{\mathbf{u}}}$. The damping matrix approximates the complex influence of the damping on the stiffness and intertia by a linear combination of the stiffness and mass matrix

$$\mathbf{D} = \alpha_d \mathbf{M} + \beta_d \mathbf{K}. \tag{2.84}$$

The variables α_d, β_d are the damping coefficients which depend on the user-defined damping ratios and the eigenfrequencies [36]. A more detailed introduction to damping can be found in [38, 2].

It should be noted here that the double contraction in the internal force vector can be replaced by a single contraction if the strains and stresses are written in Voigt notation following [17]. Therefore, $\mathbf{F}_{\mathrm{int}}$ can be simplified to

$$F_{\mathrm{int},r} = \int_{\Omega_0} \tilde{\mathbf{S}} \cdot \frac{\partial \tilde{\mathbf{E}}}{\partial u_r} \mathrm{d}\Omega_0 = \int_{\Omega} \tilde{\boldsymbol{\sigma}} \cdot \frac{\partial \tilde{\mathbf{e}}}{\partial u_r} \mathrm{d}\Omega \tag{2.85}$$

while $(\tilde{\bullet})$ indicates the quantities expressed in Voigt notation.
A crucial part, to determine the components of the internal force vector is the calculation of the partial derivative of the strain with respect to the dof u_r. While the variation of the Green-Lagrange strain $\mathbf{E}$, defined by equation 2.11, can be

calculated straight forward, using the discretized base vectors defined by equation 2.78, the variation of the Euler-Almansi strain, defined by equation 2.12, also affects its bases. Therefore, in this case, the variation $\delta\mathbf{E}$ is calculated and then a push-forward operation (see equation 2.15) is performed to obtain

$$\delta\mathbf{e} = \mathbf{F}^{-T}\delta\mathbf{E}\mathbf{F}^{-1} \tag{2.86}$$

which is known as *Lie Time derivative* [64].

2.8 Time Discretization

For the numerical solution of the semi-discrete system of equations (see equations 2.79, 2.83), the continuous time domain needs to be discretized by dividing it into discrete time steps t^n with constant time step size $\Delta t = t^{n+1} - t^n$. Therefore, the time derivatives of the displacement need to be approximated to obtain the velocity $\hat{\dot{\mathbf{u}}}$ and acceleration $\hat{\ddot{\mathbf{u}}}$. For this purpose, time integration methods are used, which approximate the variables of the next time step by integrating their derivatives over the time step length.
Widely-used is the Newmark time integration [90], which approximates the velocity and displacement by

$$\hat{\dot{\mathbf{u}}}^{t+\Delta t} = \hat{\dot{\mathbf{u}}}^{t} + \Delta t\left((1-\gamma)\hat{\ddot{\mathbf{u}}}^{t} + \gamma\hat{\ddot{\mathbf{u}}}^{t+\Delta t}\right) \tag{2.87}$$

$$\hat{\mathbf{u}}^{t+\Delta t} = \hat{\mathbf{u}}^{t} + \hat{\dot{\mathbf{u}}}^{t}\Delta t + \Delta t^2\left((0.5-\beta)\hat{\ddot{\mathbf{u}}}^{t} + \beta\hat{\ddot{\mathbf{u}}}^{t+\Delta t}\right) \tag{2.88}$$

where γ and β are the Newmark constants specified for the applied integration scheme.

2.8.1 Explicit Time Integration

When high frequencies dominate the solution of the physical problem, small time steps are required for the numerical solution. In such cases, the most efficient way to integrate equation 2.79 is provided by an explicit method. In this case, equation 2.79 is solved for the acceleration, which results in

$$\hat{\ddot{\mathbf{u}}} = \mathbf{M}^{-1}\left(\mathbf{F}_{\text{ext}} - \mathbf{F}_{\text{int}}(\hat{\mathbf{u}})\right) \tag{2.89}$$

while the lumped mass matrix is usually used to avoid the time-consuming solution of a system of equations. Among different schemes to progress in time, the central difference scheme [17] is very prominent. Within this scheme, the displacements are updated according to equation 2.88, assuming $\beta = 0$ and $\gamma = 0.5$, while the velocity update is performed in two steps. Before updating the acceleration $\hat{\ddot{\mathbf{u}}}^{t+\Delta t}$ according to equation 2.89, the velocity is updated by

$$\hat{\dot{\mathbf{u}}}^{t+\frac{\Delta t}{2}} = \hat{\dot{\mathbf{u}}}^{t} + \frac{\Delta t}{2}\hat{\ddot{\mathbf{u}}}^{t}. \tag{2.90}$$

Finally, with the updated acceleration, the velocity is updated by equation 2.87, which is equal to

$$\hat{\mathbf{u}}^{t+\Delta t} = \hat{\mathbf{u}}^{t+\frac{\Delta t}{2}} + \frac{\Delta t}{2}\hat{\ddot{\mathbf{u}}}^{t+\Delta t}. \tag{2.91}$$

This scheme is also known as Velocity-Verlet scheme [88] and provides second-order accuracy for both displacements and velocity.

However, explicit methods are not unconditionally stable and the choice of a suitable time step Δt is essential. Further information are provided e.g., in [17, 137].

2.8.2 Implicit Time Integration

In contrast to explicit time integration an unconditional stable solution can be obtained with the implicit time integration, allowing the use of larger time steps Δt. However, it requires an iterative solution procedure and is therefore especially advantageous for problems with lower frequencies.

Since the nodal displacements are the unknown variables, equations 2.87 and 2.88 are reformulated to express the nodal velocity and acceleration from the kinematic values obtained in the previous time step by

$$\hat{\mathbf{u}}^{t+\Delta t} = \frac{\gamma}{\beta\Delta t}\left[\hat{\mathbf{u}}^{t+\Delta t} - \hat{\mathbf{u}}^{t}\right] - \frac{\gamma-\beta}{\beta}\hat{\mathbf{u}}^{t} - \frac{\gamma-2\beta}{2\beta}\Delta t\hat{\ddot{\mathbf{u}}}^{t} \tag{2.92}$$

and

$$\hat{\ddot{\mathbf{u}}}^{t+\Delta t} = \frac{1}{\beta(\Delta t)^2}\left[\hat{\mathbf{u}}^{t+\Delta t} - \hat{\mathbf{u}}^{t}\right] - \frac{1}{\beta\Delta t}\hat{\mathbf{u}}^{t} - \frac{1-2\beta}{2\beta}\hat{\ddot{\mathbf{u}}}^{t}, \tag{2.93}$$

while $\beta = 0.25$ and $\gamma = 0.5$ are assumed corresponding to the implicit Newmark [90] time integration.

A more general approach is the Generalized-α method [37], which introduces additional shift parameters to approximate the solution by midpoint interpolation. This integration scheme is detailed e.g., in [37, 138].

Substituting the equation 2.93 into the semi-discrete equilibrium equation 2.79 yields the discrete residual vector

$$\begin{aligned}\mathbf{R}(\hat{\mathbf{u}}^{t+\Delta t}) = &\frac{1}{\beta(\Delta t)^2}\mathbf{M}\hat{\mathbf{u}}^{t+\Delta t} + \mathbf{F}_{\text{int}}(\hat{\mathbf{u}}^{t+\Delta t}) - \mathbf{F}_{\text{ext}} \\ &-\mathbf{M}\left[\frac{1}{\beta(\Delta t)^2}\hat{\mathbf{u}}^{t} + \frac{1}{\beta\Delta t}\hat{\mathbf{u}}^{t} + \frac{1-2\beta}{2\beta}\hat{\ddot{\mathbf{u}}}^{t}\right] = \mathbf{0}\end{aligned} \tag{2.94}$$

which is a function of the unknown displacement $\hat{\mathbf{u}}^{t+\Delta t}$. The damping term is not explicitly considered here, but can be derived straightforwardly by inserting equations 2.92 and 2.93 into equation 2.83.

Linearization and Iterative Solution

The expression of the residual force vector in equation 2.94 turns out to be nonlinear for the general case, hence necessitating an iterative solution approach like the *Newton-Raphson* algorithm to solve the system at each time step. Subsequently employing the iterative scheme, which corresponds to a Taylor series expansion neglecting higher order terms, leads to the linearized equation system

$$\mathbf{R}(\hat{\mathbf{u}}_{k+1}^{t+\Delta t}) = \mathbf{R}(\hat{\mathbf{u}}_{k}^{t+\Delta t}) + \frac{\partial \mathbf{R}(\hat{\mathbf{u}}_{k}^{t+\Delta t})}{\partial \hat{\mathbf{u}}^{t+\Delta t}} \Delta\hat{\mathbf{u}}_k = \mathbf{R}(\hat{\mathbf{u}}_{k}^{t+\Delta t}) + \mathbf{K}(\hat{\mathbf{u}}_{k}^{t+\Delta t})\Delta\hat{\mathbf{u}}_k = \mathbf{0} \tag{2.95}$$

for each iteration step k, introducing the effective stiffness matrix

$$\mathbf{K} = \frac{1}{\beta(\Delta t)^2}\mathbf{M} + \frac{\partial \mathbf{F}_{\text{int}}(\hat{\mathbf{u}}_{k}^{t+\Delta t})}{\partial \hat{\mathbf{u}}^{t+\Delta t}} \tag{2.96}$$

as the linearization of the residual force vector. The derivative of the internal force vector is also known as the tangential stiffness matrix.
Equation 2.95 is solved for the incremental displacement

$$\Delta\hat{\mathbf{u}}_k = \left(\mathbf{K}(\hat{\mathbf{u}}_{k}^{t+\Delta t})\right)^{-1}\left(-\mathbf{R}(\hat{\mathbf{u}}_{k}^{t+\Delta t})\right), \tag{2.97}$$

which then leads to an update of the displacement, calculated by

$$\hat{\mathbf{u}}_{k+1}^{t+\Delta t} = \hat{\mathbf{u}}_{k}^{t+\Delta t} + \Delta\hat{\mathbf{u}}_k. \tag{2.98}$$

The velocity $\hat{\dot{\mathbf{u}}}^{t+\Delta t}$ and acceleration $\hat{\ddot{\mathbf{u}}}^{t+\Delta t}$ are updated according to equations 2.92 and 2.93 before the obtained solution is re-substituted into equation 2.95, increasing the iteration counter k until the residual equation is fulfilled with a certain accuracy.

Tangent Stiffness Matrix

To obtain the tangent stiffness matrix, the components of the internal force vector defined by equation 2.80 are derived with respect to each dof $\hat{u}_s$, resulting in the entries

$$K_{rs} = \int_{\Omega_0} \frac{\partial \mathbf{S}}{\partial \hat{u}_s} : \frac{\partial \mathbf{E}}{\partial \hat{u}_r} + \mathbf{S} : \frac{\partial^2 \mathbf{E}}{\partial \hat{u}_r \partial \hat{u}_s} \mathrm{d}\Omega_0 = \int_{\Omega_0} \mathbb{C} : \frac{\partial \mathbf{E}}{\partial \hat{u}_s} : \frac{\partial \mathbf{E}}{\partial \hat{u}_r} + \mathbf{S} : \frac{\partial^2 \mathbf{E}}{\partial \hat{u}_r \partial \hat{u}_s} \mathrm{d}\Omega_0 \tag{2.99}$$

where $\mathbb{C}$ is the elasticity tensor defined by equation 2.29. This expression is formulated in the material description, which generally simplifies the element derivation. Alternatively, the same tangent stiffness matrix can be obtained from the formulation in the spatial description yielding

$$K_{rs} = \int_{\Omega} \frac{\partial \boldsymbol{\sigma}}{\partial \hat{u}_s} : \frac{\partial \mathbf{e}}{\partial \hat{u}_r} + \boldsymbol{\sigma} : \frac{\partial^2 \mathbf{e}}{\partial \hat{u}_r \partial \hat{u}_s} \mathrm{d}\Omega = \int_{\Omega} \mathfrak{c} : \frac{\partial \mathbf{e}}{\partial \hat{u}_s} : \frac{\partial \mathbf{e}}{\partial \hat{u}_r} + \boldsymbol{\sigma} : \frac{\partial^2 \mathbf{e}}{\partial \hat{u}_r \partial \hat{u}_s} \mathrm{d}\Omega \tag{2.100}$$

where $\mathfrak{c}$ is the constitutive tensor defined in the current configuration.

The *pull-back* and *push-forward* operations for strains and stresses can be used to transfer quantities between spatial and material description.

Remark 3: Pre-stresses

In addition to stresses resulting from deformation, pre-stresses $\mathbf{S}_0$ can be considered. In this case, $\mathbf{S}_0$ is added to the 2$^{\text{nd}}$ Piola-Kirchhoff stress, and thus the components of the internal force vector are calculated by

$$F_{\text{int},r} = \int_{\Omega_0} (\mathbf{S} + \mathbf{S}_0) : \frac{\partial \mathbf{E}}{\partial \hat{u}_r} \mathrm{d}\Omega_0, \tag{2.101}$$

while the entries of the stiffness matrix are defined by

$$K_{rs} = \int_{\Omega_0} \mathbb{C} : \frac{\partial \mathbf{E}}{\partial \hat{u}_s} : \frac{\partial \mathbf{E}}{\partial \hat{u}_r} + (\mathbf{S} + \mathbf{S}_0) : \frac{\partial^2 \mathbf{E}}{\partial \hat{u}_r \partial \hat{u}_s} \mathrm{d}\Omega_0. \tag{2.102}$$

2.9 Finite Element Method (FEM)

In classical FEM, the spatial discretization, as introduced in section 2.7, is defined such that the continuous body $\mathscr{B}$ is subdivided into non-overlapping finite elements defining the FE-mesh, as illustrated in Figure 1.4(left). Therefore, the continuous body $\mathscr{B}$ is approximated by

$$\mathscr{B} \approx \mathscr{B}^h = \bigcup_{e=1}^{n_e} \Omega^e \tag{2.103}$$

where n_e is the total number of elements.
Therefore, assuming a local approximation of the geometry and the field quantities (see section 2.7), the virtual work of each finite element can be evaluated separately and the local contributions are assembled to obtain the global contribution. Thus, the governing equation defined by equation 2.79 can be rewritten considering the assembly of the elemental contributions. Indicating the elemental contributions with superscript e yields

$$F_{\text{int},r} = \bigcup_{e=1}^{n_e} \int_{\Omega_0^e} \mathbf{S} : \frac{\partial \mathbf{E}}{\partial u_r} \mathrm{d}\Omega_0^e = \bigcup_{e=1}^{n_e} \int_{\Omega^e} \boldsymbol{\sigma} : \frac{\partial \mathbf{e}}{\partial u_r} \mathrm{d}\Omega^e \tag{2.104}$$

and

$$\mathbf{F}_{\text{ext}} = \bigcup_{e=1}^{n_e} \left(\int_{\Omega_0^e} \rho_0 \mathbf{N}^T \mathbf{B} \mathrm{d}\Omega_0^e + \int_{\Gamma_{N_0}^e} \mathbf{N}^T \overline{\mathbf{T}} \mathrm{d}\Gamma_{N_0}^e \right) = \bigcup_{e=1}^{n_e} \left(\int_{\Omega^e} \rho \mathbf{N}^T \mathbf{b} \mathrm{d}\Omega + \int_{\Gamma_N^e} \mathbf{N}^T \overline{\mathbf{p}} \mathrm{d}\Gamma_N^e \right) \tag{2.105}$$

for the internal and external force vector, while the inertia term reads

$$\mathbf{M}\ddot{\hat{\mathbf{u}}} = \bigcup_{e=1}^{n_e} \int_{\Omega_0^e} \rho_0 \mathbf{N}^T \mathbf{N} \mathrm{d}\Omega_0^e \ddot{\hat{\mathbf{u}}} = \bigcup_{e=1}^{n_e} \int_{\Omega^e} \rho \mathbf{N}^T \mathbf{N} \mathrm{d}\Omega^e \ddot{\hat{\mathbf{u}}}. \tag{2.106}$$

To evaluate the integrals in these equations, Gauss integration is typically used, which is detailed e.g., in [66, 17, 137].
To solve the resulting equilibrium equation, an implicit time integration is employed, as described in section 2.8.2, and the non-linear equations are solved iteratively according to equation 2.95.

Due to the Lagrangian description of motion, the FE-mesh deforms as the body deforms. Therefore, for large strains, mesh distortion may occur, requiring computationally expensive re-meshing schemes. To circumvent these issues associated with Lagrangian FEM, alternative discretization methods have been developed. In this work, MPM is employed for this purpose, as it combines Lagrangian moving particles with an Eulerian background grid. Further details are provided chapter 3.
However, for structural modeling, Lagrangian FEM is the primary choice and should be preferred due to its accuracy and efficiency. Therefore, to combine the advantages of these distinct discretization methods, the partitioned coupling strategy of MPM and FEM is developed in section 6.
This coupling strategy requires the imposition of boundary conditions along the shared interface, which is straightforward in classical FEM. Due to the Lagrangian moving FE-mesh, the conditions can be imposed directly at the nodes along the boundary.

Real structures are always volumes and could therefore be described by volumetric finite elements, called solid elements. However, to reduce the dofs and the computational cost, a reduction of the dimensions is typically performed for surface- and curve-like structures. Due to geometric assumptions made for the reduced dimensions, the description of these elements can be reduced to their mid-surface or centerline. In the following, the basic assumptions for geometrically non-linear structural element formulations used in this work are presented.

2.9.1 Membrane Elements

The description of surface-like structures, where the thickness direction is significantly smaller than the other two dimensions, can be reduced to their mid-plane in combination with a vector in the thickness direction. The latter base vector depends on the parametric description of the mid-plane and the assumptions applied to it are the basis for different element formulations.
While element formulations based on the Reissner-Mindlin theory assume a constant thickness t and that the cross-section remains straight, the element formulations based on the Kirchhoff-Love theory also postulate that the cross-section remains perpendicular to the mid-surface. Thus, in the latter theory, the third base vector coincides with the normalized normal vector, defined by

$$\tilde{\mathbf{G}}_3 = \frac{\mathbf{G}_1 \times \mathbf{G}_2}{\|\mathbf{G}_1 \times \mathbf{G}_2\|}, \tag{2.107}$$

which allows the shell to be described by its mid-surface only. Mechanically, the assumption that the cross-section remains normal to the mid-surface means that the transverse shear stress is neglected, and therefore this theory applies to thin

shells. However, due to the kinematic constraint, this shell formulation requires C^1 continuity between the elements. Therefore, the first derivatives of the shape functions, which approximate the continuous fields in the discretized problem, need to be equal at the joint nodes, which can be realized by e.g. higher order shape functions or an isogeometric approach [73].
Membrane elements are a further simplification of the Kirchhoff-Love shell element formulations, assuming that the in-plane stresses of the structure are constant. Therefore, the resistance to bending moments is neglected and the required continuity reduces to C^0. Thus, these elements provide an efficient modeling approach for thin structures mainly carrying the loads by tensile forces.

In this work, membrane elements are used to model the complex structural behavior of the nets stretched along flexible protective structures. This modeling approach follows the efficient and innovative approach of [101, 103, 105]. Therein, rockfall protection structures under extreme loading conditions were intensively studied and the complex structural behavior of the nets stretched along the structures was globally resolved using surrogate membrane elements. Since the flexible protective structures designed for mass flow events, such as mudflows, debris flows or avalanches show similarities to these highly flexible rockfall barriers, the homogenized modeling assumptions are adapted for the flexible barriers studied in this work. Due to the initially plane geometry of the structure, a negligible pre-stress is applied to the elements to avoid a singular stiffness matrix in this configuration.

2.9.2 Truss and Cable Elements

For structural components where one dimension of the structure is significantly larger than the other two, one-dimensional models such as beam, truss, or cable element formulations are used. Hence, these elements are described by a spatial curve, while the assumptions applied to the remaining base vectors are the basis for different element formulations.
Similar to the shell element formulation, the derivation of beam elements differs in that the Timoshenko beam formulation assumes a straight cross-section, while the Bernoulli beam theory additionally postulates that the cross-section remains perpendicular to the centerline.
Truss elements are a further simplification of the latter beam element formulation, assuming a constant stress distribution across the cross-section. Therefore, bending effects are neglected and the continuity between the elements is reduced to C^0. Thus, these assumptions allow for an efficient and simplified model approach, since only translational dofs at the nodes of the truss elements need to be considered. Therefore, the equation 2.104 of the internal force reduces to one dimension, yielding

$$F_{\text{int},r} = \bigcup_{e=1}^{n_e} \int_{\Omega_0^e} (\tilde{S}^{11} + \tilde{S}_0) \frac{\partial \tilde{E}_{11}}{\partial u_r} \mathrm{d}\Omega_0^e \tag{2.108}$$

in the total Lagrangian description, while n_e is the number of truss elements in this case. In addition, a pre-stress $\tilde{S}_0$ can be considered according to equation 2.101.

However, this element formulation can only be used for structural components where bending and shear effects are negligible. For the flexible protective structure considered in section 6.2.8, these model assumptions apply to the steel profiles between which the net is spanned (see Figure 6.41, highlighted in orange). Due to the hinged support of these pillars, the bending effects can be neglected in this particular case.
In addition to trusses, cable elements play an important role in the modeling of flexible protective structures. Unlike truss elements, they can only carry tensile forces. Therefore, an additional check for compressive stresses is added to the element formulation

$$\text{if} \quad \tilde{S}^{11} + \tilde{S}_0 < 0.0: \quad \mathbf{F}^e_{\text{int}} = \mathbf{0}, \tag{2.109}$$

resulting in a zero tangent stiffness matrix in the case of compression.
For the protective structure evaluated in section 6.2.8, this modeling assumption is applied for the cables, which are spanned uphill and are connecting the tip of the steel profiles with the ground (see Figure 6.41, highlighted with dashed gray lines). In the numerical model, each cable is represented by a single geometric non-linear cable element. Also in section 6.2.4 to section 6.2.6 this element formulation is applied to model the flexible structures. Therein however, the structures are discretized by multiple cable elements in order to approximate the deformed geometry of the flexible structures. Due to the initial plane geometry of the respective structures, a pre-stress $\tilde{S}_0$ is additionally considered in order to avoid a singular stiffness matrix.

2.10 Discrete Element Method (DEM)

DEM is a discrete particle method that considers the motion and interaction of individual particles. These particles are approximated as rigid objects and therefore the simplifications introduced in section 2.6 apply to them.
Since its first mention and derivation in [41], DEM has become increasingly popular and is now used in both industrial applications and science. It is often used to model granular materials by representing the individual grains of the material as discrete particles. However, as the number of particles increases, the computational effort increases dramatically, and at some point, continuum-based descriptions such as MPM are required to model larger scale mass flows.
For moderate numbers of particles, however, DEM is a highly efficient computational method. It is particularly useful for simulating the interaction of individual objects that are assumed to be rigid. Therefore, provided the numerical model is calibrated, contact forces can be accurately evaluated.
For this reason, this method has been applied in [103, 102, 105] to model rockfall events. Due to the precise contact force calculation in combination with a partitioned coupling scheme with FEM, the complex interaction of discrete rocks with highly flexible protective structures was successfully modeled.
In this work, DEM is used to model the retaining wall systems composed of several massive blocks stacked on top of each other. These blocks can be simplified as rigid bodies. However, the interaction and contact forces between the blocks

are critical, particularly since the failure patterns of these protective structures are included in the numerical models.
The motion of these rigid bodies is determined by the governing equations 2.73 to 2.74. To facilitate the calculation of torques and in particular the contact algorithms used to detect contacts between particles as well as to determine their interactions with boundaries, spherical particles are considered. This allows a very efficient computation of the model.
However, it is often the shape of the discrete objects that is decisive for their motion and the resulting contact forces in the case of mutual interaction. Therefore, clustering of DEM particles, which was investigated in [75], is applied herein to model arbitrarily shaped particles. The creation of such clusters is discussed extensively in [25, 26] and they provide a free-to-use online tool [24]. However, in contrast to spherical particles where the torque is defined by equation 2.75, the inertia tensor $\mathbf{I}$ is no longer constant for clusters of spheres and a more detailed analysis is required according to [70]. Nonetheless, since spherical particles are glued together to form clusters, this approach still provides efficient contact computation.
In addition to the discrete particles, boundaries must also be included in the numerical model, which is particularly important for partitioned coupling with other discretization methods. Analogous to [99], a wall condition is used to impose the Dirichlet conditions. The geometry of this wall condition can be created similarly to a FE-mesh, consisting of vertices, edges, and faces in 3D requiring the contact detection between spherical particles and geometric entities. This wall condition has been successfully utilized in [99, 101] for partitioned coupling with FEM and is consequently used in this work to couple DEM with MPM in a partitioned strategy, which is detailed in chapter 5.

The DEM in this work uses a penalty-based approach to compute contact forces by considering the overlap of interacting entities. Consequently, the contact partners must first be found before the contact forces are evaluated depending on their overlaps.
For spheres or clusters of spheres, only the sphere-sphere contacts and, near the wall condition, in addition the sphere-line, sphere-vertex, and sphere-surface contacts need to be considered. These are simple operations in which only the shortest distance and the respective sphere radius are compared. This has been investigated in [99, 100], which additionally describes an efficient way to handle various contact partners at the same time, applying the so-called Double Hierarchy Method. A sphere with center $\mathbf{C}_i$ and corresponding radius R_i is in contact with an arbitrary geometric object as soon as the shortest distance d_i from the surface of the object to the center of the sphere $\mathbf{C}_i$ is smaller than the radius, that is $d_i < R_i$. In [100] a detailed description of how to calculate d_i for different geometric entities such as vertices, lines, and surfaces can be found.
After detecting the contact, which is the first step in a DEM calculation procedure, the contact forces are evaluated. For this purpose, a variety of different contact laws can be applied, while a Hertz-Mindlin spring-dashpot (HM+D) [40] model is used in this work. This model is based on a penalty approach and was developed for rigid and perfectly spherical particles. In Figure 2.4 a) the rheological model for interacting spheres is visualized, while in Figure 2.4 b) the model

for a sphere in contact with a geometric entity is displayed.

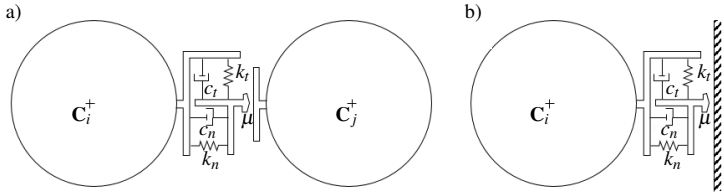

Figure 2.4: Rheological model a) for sphere-sphere contact. b) for sphere-vertex/line/surface contact. Adapted from [99].

Hence, the contact force evaluation based on the HM+D model needs the definition of the following DEM parameters

- k_n, k_t: normal and tangential spring stiffness,
- c_n, c_t: normal and tangential damping coefficients,
- μ: (sliding) friction coefficient, restricted to Coulomb's friction limit [40],

which need to be measured and calibrated for the considered physical problem. Based on these parameters, the contact forces can be evaluated, which is detailed in [40, 106, 123, 107, 100, 99].
All interacting forces are then assembled to derive the forces $\mathbf{F}_i$ and torques $\mathbf{T}_i$ on each particle i. Following [100, 94, 105], they can be calculated by

$$\mathbf{F}_i = \mathbf{F}_{ext,i} + \mathbf{F}_{d,i} + \sum_{j=1}^{n} \mathbf{F}_{ij}, \tag{2.110}$$

$$\mathbf{T}_i = \mathbf{T}_{ext,i} + \mathbf{T}_{d,i} + \sum_{j=1}^{n} \left(\mathbf{r}_c^{ij} \times \mathbf{F}_{ij} \right) \tag{2.111}$$

while the symbols are defined in Table 2.1.
Finally, after the contact force evaluation, the DEM solution process proceeds to the integration of motion to solve the governing equations 2.73-2.74. Different time integration schemes can be applied, ranging from a first-order forward Euler to arbitrarily high-order schemes with an increasing level of complexity. For the simulations in this thesis, a second-order Velocity-Verlet [88] (central difference) scheme is used to integrate the translational degrees of freedom. In contrast to the classical Verlet method [126], the Velocity-Verlet provides second-order accuracy for both displacement and velocity. Furthermore, to provide a robust time integration of the rotations [70] proposes a time integration that works with quaternions [60], which is used in the following examples.

symbol	explanation
n, j	total number n of contact partners j
$\mathbf{F}_{ext,i}, \mathbf{T}_{ext,i}$	external loads and external torques
$\mathbf{F}_{ij}$	interaction contact forces between sphere i and sphere j or between sphere i and a geometric entity of the boundary j resulting in the contact force $\mathbf{F}_{i,\text{Contact}}$
$\mathbf{F}_{d,i}, \mathbf{T}_{d,i}$	external damping loads / boundaries
$\mathbf{r}_c^{ij}$	connection vector between sphere i and the contact point to the neighbor j

Table 2.1: Explanation of the symbols in equations (2.110) and (2.111), adapted from [99, 100]

After the time integration, the particle positions are updated and a new loop of the DEM calculation cycle starts. For a more detailed discussion of DEM please refer to [88, 100, 94, 99, 106, 40, 123, 107, 101].

CHAPTER 3

Material Point Method (MPM)

MPM is an established and powerful numerical method particularly well suited for simulating significant and rapid soil deformations. It originated from the Particle-in-Cell (PIC) method [61, 62], developed for fluid mechanics, and its enhancement the Fluid Implicit Particle (FLIP) [22, 23], before Sulsky et al. [120, 121] extended it to solid mechanics problems incorporating history dependent material laws.

It combines the advantages of both mesh-free and mesh-based methods, as the physical domain is discretized by Lagrangian moving particles carrying the history dependent variables, while the governing equations are solved on the Eulerian background grid. Thus, it can be interpreted as a modified updated Lagrangian finite element technique with moving integration points, called material points, while the background grid is reset at the end of each time step.

Consequently, in contrast to standard FEM or any other Lagrangian mesh-based method, the problem of mesh entanglement and the computational expense of re-meshing during the simulation of large strain problems is circumvented in MPM by systematically resetting the computational background grid.

MPM has been successfully applied to a wide range of challenges during the previous decades, such as hypervelocity impact [87, 141, 132], landslide simulation [4, 91] or avalanches [56, 82, 83], multi-phase geomechanical problems [139, 10, 39], or in computer graphics [119, 59], just to mention a few examples.

In addition, much research has been done to reduce the numerical noise that arises from the transition of material points from one background grid element to another, e.g., the Generalized Interpolation Material Point (GIMP) method [13], the Convected Particle Domain Interpolation (CPDI) [97, 98], the PQMPM [134], or the usage of B-Spline basis functions [54]. Detailed reviews of MPM can be found in [118, 45]. The books published by Zhang et al. [140], Fern et al. [51], and Nguyen et al. [92] provide further examples and a detailed introduction to the theory of MPM.

3.1 Spatial Discretization in MPM

For spatial discretization, a computational background grid is introduced in MPM. It covers the entire computational domain as depicted in Figure 3.1, including empty spaces where the material is expected to move during the computation. It is very similar to a conventional FE-mesh and the governing equations are solved at the nodes of this computational background grid.

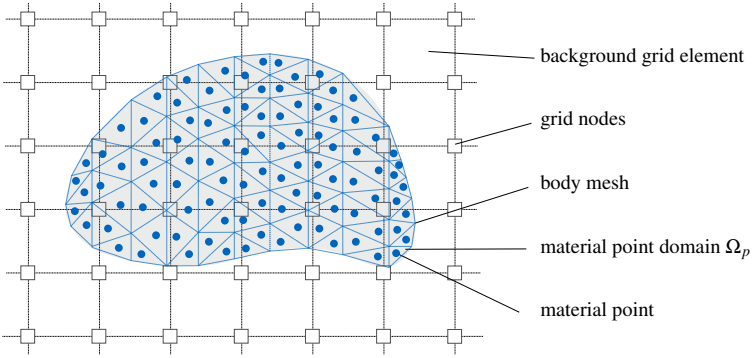

Figure 3.1: Discretization of a continuum body $\mathscr{B}$ into material points, using a body mesh to initialize them and the background grid to discretize the spatial fields.

However, in contrast to Lagrangian FEM where the body $\mathscr{B}$ is approximated by finite elements (see equation 2.103), in MPM Lagrangian moving particles called material points are introduced to represent the body. Each material point represents a finite volume Ω_p of the body

$$\mathscr{B} \approx \mathscr{B}^h = \bigcup_{p=1}^{n_p} \Omega_p, \tag{3.1}$$

while the complete body is represented by n_p material points. Each material point is assigned a mass m_p, which is calculated from the represented finite volume Ω_p of the body and the initial material density ρ_0. The mass remains constant during the simulation time, so the conservation of mass is automatically satisfied, whereas the particle volume Ω_p is updated depending on material compression or expansion. In this work, an additional mesh, the body mesh, which subdivides the body $\mathscr{B}$ into elements, is used to initialize the material points at the beginning of the simulation. Within each element of the body mesh, a predefined number of material points can be initialized while being positioned at the respective Gauss point positions. Thus, the initial positions $\mathbf{X}_p$ of the material points as well as their respective volumes and the resulting mass m_p can be assigned. However, this body mesh is only used to initialize the problem and is not considered in the subsequent calculation.

Furthermore, the classical MPM approach of a Dirac delta density function [120]

$$\rho_p(\mathbf{x}) = m_p \delta(\mathbf{x} - \mathbf{x}_p) \tag{3.2}$$

is applied, which considers the mass to be concentrated at the corresponding material point.

Remark 4: Consequences of Dirac delta density function

Due to the Dirac delta density function (see equation 3.2), which is assumed for the material points representing the body $\mathscr{B}^h$ (see equation 3.1), the volume integral of any spatially varying quantity, in general indicated by $\Phi(\mathbf{x})$, multiplied by the density ρ, is approximated by

$$\int_\Omega \rho \cdot \Phi(\mathbf{x}) \mathrm{d}\Omega \approx \sum_{p=1}^{n_p} m_p \cdot \Phi(\mathbf{x_p}). \tag{3.3}$$

Hence, the volume integrals of the virtual work equation 2.69 are transferred to a summation of particles. The spatial quantities need to be evaluated at the position of the material point $\mathbf{x_p}$, whereas these quantities are approximated by the background grid discretization.

3.2 Solution of the Governing Equations

Due to this discretization of Lagrangian moving material points discretizing the body $\mathscr{B}$ in combination with an Eulerian background grid to approximate the spatial fields, the semi-discrete equilibrium equation 2.79 can be adapted to the MPM discretization. Consequently, the internal force vector yields

$$F_{\mathrm{int},r} = \bigcup_{p=1}^{n_p} \tilde{\boldsymbol{\sigma}}_p \cdot \frac{\partial \tilde{\mathbf{e}}_p}{\partial u_r} \Omega_p, \tag{3.4}$$

assuming that the strains and stresses are written in Voigt notation and therefore the double contraction reduces to a single contraction (see equation 2.85). The external force vector is reformulated as

$$\mathbf{F}_{\mathrm{ext}} = \bigcup_{p=1}^{n_p} m_p \mathbf{N}^T \mathbf{b}_p + \int_{\Gamma_N} \mathbf{N}^T \overline{\mathbf{p}} \mathrm{d}\Gamma_N, \tag{3.5}$$

keeping the traction surface integral unchanged at this point, as the boundary discretization is discussed in section 3.4.1. The shape functions contained in $\mathbf{N}$ are evaluated at the material point position $\mathbf{x}_p$, which is also the case for the inertia term defined by

$$\mathbf{M}\hat{\mathbf{u}} = \bigcup_{p=1}^{n_p} m_p \mathbf{N}^T \mathbf{N} \hat{\mathbf{u}}. \tag{3.6}$$

In these equations, the operator $\bigcup$ is used instead of the $\sum$ symbol to denote the required assembly procedure of the elemental contributions. Furthermore, the updated Lagrangian formulation is used, which is the basis of the subsequent MPM formulation.
Inserting these equations into equation 2.79 finally defines the governing equilibrium equations. As a consequence, one equation is obtained for each dof u_r, since the virtual displacements $\delta\hat{\mathbf{u}}$ at each node are arbitrary and therefore the term in brackets must vanish for each individual $\delta\hat{u}_r$.
Hence, each material point represents an element to which the corresponding nodes of the computational background grid need to be assigned, depending on its current position $\mathbf{x}_p$. Thus, for each material point, a search is required that determines the background grid element containing the material point and thus defines its connectivity.
To solve the system of equations, implicit time integration is used as described in section 2.8.2, and the nonlinear equations are solved iteratively according to equation 2.95, which requires the calculation of the effective stiffness matrix $\mathbf{K}$ according to equation 2.96. Consequently, the solution scheme of these equations is very similar to an updated Lagrangian FEM scheme, differing only in the type of numerical integration. While particle integration is used here, FEM typically uses Gauss integration (see 2.9).
However, due to the dual description of Lagrangian moving material points on the one hand and the computational background grid on the other hand, only the material points carry the information to approximate the spatial fields, whereas no permanent variables are stored at the nodes of the Eulerian background grid. Consequently, in addition to solving the governing equations at each time step, it is necessary to interpolate and extrapolate information between background grid nodes and material points, which consequently results in the MPM update scheme described below.

3.3 MPM Update Scheme

The MPM procedure per time step t can be categorized into the following three phases, which are also visualized in Figure 3.2.

(I) Initialization phase: At the beginning of each time step the connectivity of each material point is defined, i.e. the background grid element containing the respective material point is searched for, so that the required shape function values $\mathbf{N}$ can be evaluated at the current position of the material point $\mathbf{x}_p^t$. The kinematic variables $\dot{\mathbf{u}}_p^t$ and $\ddot{\mathbf{u}}_p^t$ are then mapped via mass projection to the corresponding nodes of the background grid as initial conditions. In order to keep the proceeding notation comprehensible, the values for each background grid node I are provided.

First, the nodal mass m_I^t is calculated by

$$m_I^t = \sum_{p=1}^{n_p} N_I m_p. \tag{3.7}$$

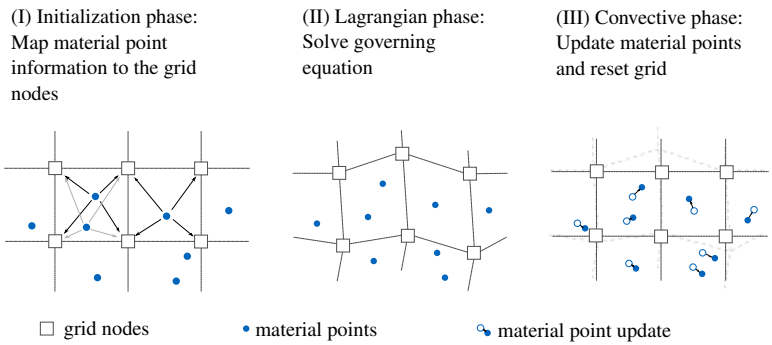

Figure 3.2: MPM update scheme: (I) Initialization phase, (II) Lagrangian phase and (III) Convective phase. Adapted from [115].

Based on this, the nodal velocity $\hat{\mathbf{u}}_I^t$ can be calculated by

$$\hat{\mathbf{u}}_I^t = \frac{\sum_{p=1}^{n_p} m_p \dot{\mathbf{u}}_p^t N_I}{m_I^t}. \tag{3.8}$$

whereas the nodal acceleration $\hat{\mathbf{u}}_I^t$ is obtained from

$$\hat{\mathbf{u}}_I^t = \frac{\sum_{p=1}^{n_p} m_p \ddot{\mathbf{u}}_p^t N_I}{m_I^t}. \tag{3.9}$$

(II) Lagrangian phase: After the extrapolation of the material point information to the nodes of the computational background grid, the governing equations can be solved as described in section 3.2. Further details are also provided e.g.,in [67, 68, 20, 17, 137], since this step is very similar to the classical finite element updated Lagrangian calculation procedure.

As a result, temporally nodal displacements $\hat{\mathbf{u}}^{t+\Delta t}$ are obtained, which cause a deformation of the background grid and the nodal velocity $\hat{\dot{\mathbf{u}}}^{t+\Delta t}$ and acceleration $\hat{\ddot{\mathbf{u}}}^{t+\Delta t}$ are updated accordingly.

At this point, it is important to note that solely those nodes of the computational background grid that are assigned a mass m_I contribute to the final system of equations.

(III) Convective phase: Finally, the solution obtained at the nodes of the computational background grid is interpolated to the material points. Therefore, the position and acceleration of the material points are updated by

$$\mathbf{x}_p^{t+\Delta t} = \mathbf{x}_p^t + \mathbf{N}\hat{\mathbf{u}}^{t+\Delta t} \tag{3.10}$$

and

$$\ddot{\mathbf{u}}_p^{t+\Delta t} = \mathbf{N}\hat{\ddot{\mathbf{u}}}^{t+\Delta t}, \tag{3.11}$$

whereas the material point velocity is updated via the trapezoidal rule by

$$\dot{\mathbf{u}}_p^{t+\Delta t} = \dot{\mathbf{u}}_p^t + \frac{1}{2}\Delta t(\ddot{\mathbf{u}}_p^t + \ddot{\mathbf{u}}_p^{t+\Delta t}). \tag{3.12}$$

Finally, the background grid is reset, an important feature to simulate large strain events without the issues of mesh entanglement and distortion.

Further details of the presented scheme as well as an extension to mixed formulations can be found in [68, 69, 67].

3.4 Boundary Conditions

For the solution of the governing equations, the definition of the boundary conditions according to equations 2.63 to 2.65 is essential. The stress boundary defined by equation 2.64 is included in the external force vector and therefore this kind of boundary condition is often referred to as natural boundary condition. The Dirichlet constraint, however, needs to be prescribed over the discretized boundary Γ_D^h and is therefore often called essential boundary condition.
Since in MPM the governing equations are solved on the computational background grid, boundary conditions can be applied directly in a FEM fashion. However, this is only possible if the boundaries coincide with the background grid discretization, referred to as conforming boundaries.
However, the conforming imposition type is not generally applicable in MPM. Since the material moves independently of the computational background grid, the boundaries are typically not aligned with the grid nodes. Therefore, alternative procedures are required that enforce the boundary conditions in a weak form, which is referred to as non-conforming boundary conditions.
In particular, with regard to the partitioned coupling approaches introduced in chapter 4, the imposition of non-conforming boundary conditions is an essential requirement. In this approach, the interaction of the involved solvers is shifted to their shared interface, along which boundary conditions are imposed within each solver. However, due to the flexible counterpart, the position of the interface and also the contact zone is likely to change during the computation. Therefore, the weak imposition of boundary conditions in MPM is required, since the background grid is reset after each time step and only the material points move according to the body deformation. Moreover, a methodology is required to track the interface during the computation.
For this reason, a major part of this dissertation deals with the weak imposition of boundary conditions in MPM, which is the basis for the partitioned coupling strategies presented in chapter 5 and chapter 6. Some of the proceeding contents were published by the author in [115, 117, 34]. The content is reviewed in the context of this thesis, whereby some parts of the following sections are taken directly from these publications* and are to be interpreted as quotations.

* Whose main author and copyright holder is the author of this dissertation

3.4.1 Particle Representation of the Boundary

Similar to the discretization of the body by material points, the continuous boundary Γ in MPM is subdivided into n_{bp} non-overlapping subdomains, while each subdomain is represented by a boundary particle bp with a corresponding current area Γ_{bp}. This approach is applied to both Neumann and Dirichlet boundaries, yielding

$$\Gamma \approx \Gamma^h = \bigcup_{\text{bp}=1}^{n_{\text{bp}}} \Gamma_{\text{bp}}. \tag{3.13}$$

These boundary particles can be interpreted as mass-less particles carrying the necessary information for the boundary imposition and tracking its spatial position. This method is mature compared to other boundary tracking methods because it does not require the computationally expensive calculation of the intersections of the boundary entities with the elements of the computational grid. Instead, the search algorithms inherent in any MPM scheme can be employed also for the boundary particles, thereby enabling the efficient handling of moving boundaries.
For initialization, these boundary particles are positioned within the respective primitives, e.g., polylines in 2D or meshes in 3D, that define the interface in the geometric model. A user-defined number of boundary particles are placed either evenly distributed or at Gauss point positions of the respective primitive and are assigned the corresponding weights according to the representative area Γ_{bp}. In a two-dimensional case, the individual weight has to be multiplied by the corresponding thickness of the model to obtain the resulting subdomain of each boundary particle.
Due to this boundary particle discretization, the integrals along the boundary segment Γ^h within a background grid element can be approximated by

$$\int_{\Gamma^e} (...)\, d\Gamma^e \approx \sum_{\text{bp}=1}^{n_{\text{bp}}} (...)\, \Gamma_{\text{bp}}\,. \tag{3.14}$$

In this case, the boundary segment inside an intersected background grid element is approximated by summing the respective boundary particle areas located within the respective background grid element. Consequently, a fine discretization of the boundary by mass-less particles leads to a good approximation of the boundary segments.

3.4.2 Non-conforming Point Load Conditions

Following from equation 3.5 and considering the particle discretization of section 3.4.1, the traction surface integral can be rewritten as

$$\int_{\Gamma_N} \mathbf{N}^T \bar{\mathbf{p}}\, d\Gamma_N \approx \bigcup_{\text{bp}=1}^{n_{\text{bp}}} \mathbf{N}^T \bar{\mathbf{p}} \Gamma_{\text{bp}} \tag{3.15}$$

assuming that the boundary Γ_N is represented by n_{bp} boundary particles.

For point load conditions, equation 3.15 can be further simplified to

$$\bigcup_{\mathrm{bp}=1}^{n_{\mathrm{bp}}} \mathbf{N}^T \overline{\mathbf{p}} \Gamma_{\mathrm{bp}} = \bigcup_{\mathrm{bp}=1}^{n_{\mathrm{bp}}} \mathbf{N}^T \mathbf{F}_{\mathrm{M}} \tag{3.16}$$

where $\mathbf{F}_{\mathrm{M}}$ is the respective resulting point load at each boundary particle introduced.
In order to incorporate them into the MPM calculation scheme as described in section 3.3, first a search for each boundary particle is performed during the initialization phase. Based on its spatial position $\mathbf{x}_{\mathrm{bp}}^t$ at time step t, the background grid element containing it can be determined, thus defining the connectivity and the shape functions, which are evaluated at the boundary particle position.
Subsequently, the Lagrangian phase can be executed, solving the governing equations taking into account the boundary particles with their respective shape functions $\mathbf{N}$ and the applied point loads $\mathbf{F}_{\mathrm{M}}$ according to equation 3.16. This equation can be interpreted such, that the point loads are mapped by the nodal shape functions N_I to the corresponding node I of the computational background grid.
Finally, in the convective phase, the position as well as the kinematic variables of the boundary particles are updated, following the concept of material points (see equation 3.10 to equation 3.12). Consequently, the boundary particles move according to the deformation of the body represented by the material points. This is an important feature for tracking the body contour and especially for tracking the spatial position of the shared interface within the MPM domain, which is essential for partitioned coupling with other numerical methods.
However, special consideration is necessary for background grid elements that contain boundary particles but no material points. In order to apply all loads to the body, the point load values are mapped exclusively to those nodes I of the background grid element that are assigned a mass m_I and are therefore connected to the body. This is achieved by modifying all nodal basis functions N_I of the respective background grid element according to

$$\bar{N}_I = \frac{N_I^*}{\sum_I^{n_n} N_I^*} \qquad \text{where:} \quad N_I^* = \begin{cases} 0.0, & \text{if } m_I \leq \epsilon \\ N_I, & \text{otherwise} \end{cases} \tag{3.17}$$

where n_n is the total number of nodes of the respective background grid element, while ϵ is usually considered numeric zero. Due to the weighting procedure, the partition of unity is guaranteed and thus the complete point load value is applied to the material.

3.4.3 Non-conforming Dirichlet Boundary Conditions

In contrast to natural boundary conditions, the weak imposition of essential boundary conditions is a crucial task. It is a typical problem in immersed methods and common approaches in other FEM and immersed FEM methods are the penalty approach ([7] for FEM, e.g., [76] for FCM, e.g., [27, 122] for IBRA, the Nitsche method (e.g., [79] for FCM, e.g., [5] for IGA), Mortar-based methods (e.g., [133] for FEM, e.g., [65] for FCM, [30] for IGA), or the Lagrange multiplier approach ([9] for FEM, e.g., [5, 122] for IGA/IBRA).

In MPM, however, one has to deal with the challenges of Lagrangian moving material points through an Eulerian background grid. Consequently, the set of active nodes, i.e. background grid nodes assigned a mass m_I, may vary at each time step. Moreover, the boundary or interface may be initialized at a position in space that is not necessarily along the contour of the body. Consequently, the boundary imposition method must also address the issue that material points approach the boundary from apart, contact the boundary, and possibly release again.
In the following sections, the penalty approach (section 3.4.3.1), the Lagrange multiplier method (section 3.4.3.2) and the perturbed Lagrangian method (section 3.4.3.3) are derived to weakly impose essential boundary conditions starting from a continuum formulation and specifying it for implicit MPM using boundary particles. Furthermore, their ability to serve as interface condition in a partitioned coupling strategy is thoroughly discussed.

3.4.3.1 Penalty Method

To enforce Dirichlet conditions with the penalty method, the governing equation 2.72 is extended by an additional term

$$\delta W_{\mathrm{P}} = \beta \int_{\Gamma_D} \left(\mathbf{u} - \overline{\mathbf{u}}\right) \cdot \delta \mathbf{u} \mathrm{d}\Gamma_D \tag{3.18}$$

where β is the penalty factor and $\overline{\mathbf{u}}$ is the imposed displacement field. This imposes the Dirichlet constraint given by equation 2.63, which is reformulated as constraint equation

$$g(\mathbf{u}) = \mathbf{u} - \overline{\mathbf{u}} = \mathbf{0}. \tag{3.19}$$

Introducing the space discretization for the displacement fields according to equation 2.76, the term due to the penalty augmentation $\mathbf{R}_{\mathrm{P}}$ is obtained

$$\delta W_{\mathrm{P}}^h = \delta \hat{\mathbf{u}}^T \left(\beta \int_{\Gamma_D} \mathbf{N}^T \mathbf{N} \mathrm{d}\Gamma_D \hat{\mathbf{u}} - \beta \int_{\Gamma_D} \mathbf{N} \mathrm{d}\Gamma_D \overline{\mathbf{u}} \right) = \delta \hat{\mathbf{u}}^T \left(-\mathbf{R}_{\mathrm{P}} \right), \tag{3.20}$$

which is added to the virtual work δW^h defined by equation 2.79.
For the implicit time integration, the additional residual term $\mathbf{R}_{\mathrm{P}}$ needs to be linearized with respect to the nodal displacements, yielding

$$\mathbf{K}_{\mathrm{P}} = \beta \int_{\Gamma_D} \mathbf{N}^T \mathbf{N} \mathrm{d}\Gamma_{\mathrm{D}}. \tag{3.21}$$

which defines the contribution of the penalty augmentation to the stiffness matrix $\mathbf{K}$ defined by equation (2.96). Hence, the resulting equations can be written as

$$\left(\mathbf{K} + \mathbf{K}_{\mathrm{P}}\right) \Delta \hat{\mathbf{u}}_{k+1} = -\left(\mathbf{R} + \mathbf{R}_{\mathrm{P}}\right), \tag{3.22}$$

while $\mathbf{R}$ is defined by equation 2.94 and k is the iterator of the Newton-Raphson iteration.

Since the boundary Γ_D is discretized by n_{bp} boundary particles, the surface integrals in equations 3.20 and 3.21 are evaluated according to equation 3.14, yielding

$$-\mathbf{R}_{\text{P}} = \beta \bigcup_{\text{bp}=1}^{n_{\text{bp}}} \mathbf{N}^T \mathbf{N} \Gamma_{\text{bp}} \hat{\mathbf{u}}_k^{t+\Delta t} - \beta \bigcup_{\text{bp}=1}^{n_{\text{bp}}} \mathbf{N} \Gamma_{\text{bp}} \overline{\mathbf{u}}_M \tag{3.23}$$

$$\mathbf{K}_{\text{P}} = \beta \bigcup_{\text{bp}=1}^{n_{\text{bp}}} \mathbf{N}^T \mathbf{N} \Gamma_{\text{bp}}. \tag{3.24}$$

The shape functions $\mathbf{N}$ are evaluated at the current position of the boundary particles. The respective imposed displacements $\overline{\mathbf{u}}_{\text{bp}}$ at the boundary particles are assembled in the vector $\overline{\mathbf{u}}_M$. This distinction is made because in the partitioned coupling strategy introduced in section 6, $\overline{\mathbf{u}}_M$ represents the imposed displacements at the MPM interface.

Slip Conditions

The boundary particles carry the geometric information such as the current position and the assigned area, as well as the kinematic variables needed for the imposed displacements. Furthermore, at the beginning of each simulation, the unit normal vectors $\hat{\mathbf{n}}_{\text{bp}}$ defined in the outward direction of the imposed boundary are initialized on each boundary particle, which is an important value for inclined slip or contact conditions. To impose these boundary conditions, the normal vectors $\hat{\mathbf{n}}_I$ at the nodes I of the computational background grid are required. Following [34], they are approximated within each time step by

$$\hat{\mathbf{n}}_I = \frac{\sum_{\text{bp}=1}^{n_{\text{bp}}} \hat{\mathbf{n}}_{\text{bp}} \Gamma_{\text{bp}} N_I}{\left\| \sum_{\text{bp}=1}^{n_{\text{bp}}} \hat{\mathbf{n}}_{\text{bp}} \Gamma_{\text{bp}} N_I \right\|}. \tag{3.25}$$

Hence, the nodal normal vectors need to be approximated within each time step, depending on the current position of the boundary particles. Furthermore, since the calculation is performed in the current configuration, the unit normal vectors at the boundary particles need to be updated during the calculation procedure according to the boundary particle movement.
For the imposition of slip conditions, movement in the normal direction to the support is restricted, whereas the body is free to move in tangential directions. Therefore, all globally oriented matrices and vectors are rotated with an orthogonal rotation matrix, which is defined for each background grid node I as

$$\mathbf{Q}_I = \begin{bmatrix} \hat{n}_x & \hat{n}_y & \hat{n}_z \\ \hat{t}_x & \hat{t}_y & \hat{t}_z \\ \hat{q}_x & \hat{q}_y & \hat{q}_z \end{bmatrix}, \tag{3.26}$$

where $\hat{\mathbf{n}}_I$ is the resulting normal unit vector of the background grid node I and $\hat{\mathbf{t}}_I$, and $\hat{\mathbf{q}}_I$ are the normalized tangent vectors. For a global imposition, it is necessary that the rotation is applied locally to those nodes affected by the rotation.

Therefore, the rotation matrix results in a block matrix

$$\hat{\mathbf{Q}} = \begin{bmatrix} \mathbf{I} & \mathbf{0} \\ \mathbf{0} & \mathbf{Q} \end{bmatrix}, \tag{3.27}$$

where $\mathbf{I}$ represents the identity matrix for those nodes, which are not affected by the rotation and $\mathbf{Q}$ includes all nodal rotation matrices. Applying the modified rotation matrix leads to the partially rotated system

$$\left(\hat{\mathbf{Q}}\left[\mathbf{K}+\mathbf{K}_{\mathrm{P}}\right]\hat{\mathbf{Q}}^{T}\right)\left(\hat{\mathbf{Q}}\left[\Delta\hat{\mathbf{u}}_{k+1}\right]\right) = -\left(\hat{\mathbf{Q}}\left[\mathbf{R}+\mathbf{R}_{\mathrm{P}}\right]\right). \tag{3.28}$$

To impose the roller condition, the penalty contribution in tangential directions to the support are set to zero. This can be achieved by setting the respective entries of the rotated penalty stiffness matrix and the corresponding penalty residual vector to zero, which enables the system to move in tangential directions without restriction.

Calculation of Reaction Forces

An essential requirement for partitioned coupling with other numerical methods is the calculation of the reaction forces due to the boundary imposition. Since equation 3.23 defines the additional force vector, which is added to the equilibrium equation due to the boundary imposition, it defines the reaction force $\mathbf{R}_P$ at the nodes of the computational background grid due to the penalty augmentation. Hence, at each node I the reaction force can be calculated by

$$\mathbf{R}_{I,P} = \beta \bigcup_{\mathrm{bp}=1}^{n_{\mathrm{bp}}} N_I \mathbf{N} \Gamma_{\mathrm{bp}} \hat{\mathbf{u}}_k^{t+\Delta t} - \beta \bigcup_{\mathrm{bp}=1}^{n_{\mathrm{bp}}} N_I \Gamma_{\mathrm{bp}} \overline{\mathbf{u}}_{\mathrm{bp}}. \tag{3.29}$$

These nodal reaction forces are interpolated to the boundary particles to obtain the resulting reaction force at each boundary particle by

$$\mathbf{R}_{\mathrm{bp}} = \sum_{I=1}^{n_n} \gamma_{\mathrm{I,bp}} N_I \mathbf{R}_{I,P}, \tag{3.30}$$

where n_n is the total number of nodes of the background grid element containing the boundary particle and $\gamma_{\mathrm{I,bp}}$ is the interpolation weighting factor to maintain the sum of forces. It is defined by the ratio of the boundary particle area Γ_{bp} and the nodal area $\mathbf{A}_I$:

$$\gamma_{\mathrm{I,bp}} = \frac{\Gamma_{\mathrm{bp}}}{\mathbf{A}_I}, \qquad \text{where} \quad \mathbf{A}_I = \sum_{\mathrm{bp}=1}^{n_{\mathrm{bp}}} \mathbf{N}_I \Gamma_{\mathrm{bp}}. \tag{3.31}$$

This applied weighting procedure, a classical MPM approach, provides the resulting reaction forces $\mathbf{R}_{\mathrm{bp}}$ at each boundary particle, which are assembled to the vector $\mathbf{F}_{\mathrm{M}}$. This vector is required in chapter 6 for the partitioned coupling strategy with FEM.

Material and Boundary Interaction

The Dirichlet boundary conditions in the MPM model can be arbitrarily defined within the computational background grid and thus independent of the body contour. Therefore, unlike classical FEM where the conditions are defined along the body contour, in MPM it is not necessarily the case that both boundary particles and material points lie within the same background grid element. Instead, it is possible for the material to move without being influenced by the boundary condition if there is at least one empty background grid element between them, preventing mutual interaction via the nodes of the computational background grid. Thus, for the imposition of weak boundary conditions, different configurations of material points interacting with the boundary particles have to be considered, which are visualized in Figure 3.3. In the configuration visual-

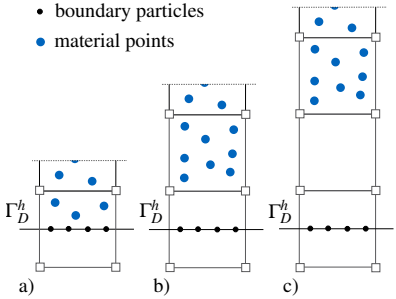

Figure 3.3: Configurations of the boundary and the material. Adapted from [117].

ized in Figure 3.3a), where material points and boundary particles are inside the same background grid element, the imposition of the non-conforming boundary is straightforward as described above. However, configurations b) and c) need to be considered carefully because the boundary particles are located within a background grid element that contains no material points and therefore the stiffness of the respective element is zero. For configuration c) and setups where the material is even further apart, the respective dofs of elements containing material points and those containing the boundary particles are decoupled. Therefore, the material movement is not affected by the respective boundary imposition. Consequently, the corresponding element containing the boundary particles does not need to be considered in the final system of equations.

However, in configurations such as shown in Figure 3.3b), where material points are located in neighboring elements of those being intersected by the boundary, the boundary condition already affects the material movement. Therefore, in this case, the penalty enhancement is only applied to those nodes that are assigned a mass and therefore connected to the body.

Contact Conditions

For contact conditions, the constraint equation 3.19 is reformulated as an inequality condition

$$g_N(\mathbf{u}) = (\mathbf{u} - \overline{\mathbf{u}}) \cdot \mathbf{n} \geq \mathbf{0} \tag{3.32}$$

in the continuum formulation, which considers the normal direction defined by the outward unit normal vector $\mathbf{n}$.
Consequently, in the discrete formulation, the penalty contributions in equation 3.22 of a boundary particle are considered if

$$g_N^h(\hat{\mathbf{u}}_k^{t+\Delta t}) = \left(\mathbf{N}\hat{\mathbf{u}}_k^{t+\Delta t} - \overline{\mathbf{u}}_{\text{bp}}\right)\hat{\mathbf{n}}_{\text{bp}} < \mathbf{0} \tag{3.33}$$

otherwise they are set to zero. Herein, $\hat{\mathbf{n}}_{\text{bp}}$ is the outward unit vector at the boundary particle bp.
For contact conditions, it is also useful to deactivate the boundary particle imposition if no material point is located within the same background grid element. This allows the material to move closer to the boundary. However, this option should be selected with care, as it may lead to material penetration, depending on the discretization of the problem.

3.4.3.2 Lagrange Multiplier Method

As an alternative to the penalty augmentation, the Lagrange multiplier method is developed within this work to weakly enforce the essential boundary conditions in MPM. This approach avoids the cumbersome calibration of the penalty factor, but introduces additional dofs into the system, leading to a modified principle of virtual work equation

$$\delta W(\mathbf{u}, \boldsymbol{\lambda}, \delta\mathbf{u}, \delta\boldsymbol{\lambda}) = \delta W(\mathbf{u}, \delta\mathbf{u}) + \delta W_{LM}(\mathbf{u}, \boldsymbol{\lambda}, \delta\mathbf{u}) + \delta W_{LM}(\mathbf{u}, \boldsymbol{\lambda}, \delta\boldsymbol{\lambda}) = 0 \tag{3.34}$$

where $\boldsymbol{\lambda}$ is the Lagrange multiplier, while the displacement $\mathbf{u}$ is the primal variable. In this equation, $\delta W(\mathbf{u}, \delta\mathbf{u})$ represents the virtual work given by equation 2.72, while the additional terms arising from the Lagrange multiplier imposition are defined by

$$\delta W_{LM}(\mathbf{u}, \boldsymbol{\lambda}, \delta\mathbf{u}) = \int_{\Gamma_D} \boldsymbol{\lambda}^T \delta\mathbf{u} \, \mathrm{d}\Gamma_D \tag{3.35}$$

$$\delta W_{LM}(\mathbf{u}, \boldsymbol{\lambda}, \delta\boldsymbol{\lambda}) = \int_{\Gamma_D} \delta\boldsymbol{\lambda}^T \left(\mathbf{u} - \overline{\mathbf{u}}\right) \mathrm{d}\Gamma_D \, . \tag{3.36}$$

To solve the modified virtual work equation numerically, the continuous fields $\mathbf{u}$ and $\boldsymbol{\lambda}$ need to be approximated by locally defined basis functions and discrete values at the nodes. This discretization, however, has to be chosen carefully to satisfy the inf-sup condition of Ladyzhenskaya, Babuška [8, 9] and Brezzi [28, 29]. At this point, the notation is kept general by using the shape function matrix $\mathbf{N}$ to approximate the displacement field (see equation 2.76) and by introducing the shape function matrix $\mathbf{N}_\lambda$ to approximate the Lagrange multiplier field by

$$\boldsymbol{\lambda} \approx \boldsymbol{\lambda}^h = \mathbf{N}_\lambda \hat{\boldsymbol{\lambda}} \tag{3.37}$$

while $\hat{\boldsymbol{\lambda}}$ are the values at the Lagrange multiplier dofs. Hence, the discretized version of equations 3.35 to 3.36 are obtained by

$$\delta W^h_{LM}(\mathbf{u}^h, \boldsymbol{\lambda}^h, \delta\mathbf{u}^h) = \delta\hat{\mathbf{u}}^T \int_{\Gamma_D} \mathbf{N}^T \mathbf{N}_\lambda \mathrm{d}\Gamma_D \hat{\boldsymbol{\lambda}} \,, \tag{3.38}$$

$$\delta W^h_{LM}(\mathbf{u}^h, \boldsymbol{\lambda}^h, \delta\boldsymbol{\lambda}^h) = \delta\hat{\boldsymbol{\lambda}}^T \left(\int_{\Gamma_D} \mathbf{N}_\lambda^T \mathbf{N} \mathrm{d}\Gamma_D \hat{\mathbf{u}} - \int_{\Gamma_D} \mathbf{N}_\lambda \mathrm{d}\Gamma_D \overline{\mathbf{u}} \right) . \tag{3.39}$$

For the solution of the spatially discretized system, the implicit time integration is utilized and therefore the Newton-Raphson iteration is required to solve the nonlinear equations. This consequently leads to solving the saddle point problem

$$\begin{bmatrix} \mathbf{K}(+\mathbf{K}_{LM}) & \boldsymbol{\Lambda}^T \\ \boldsymbol{\Lambda} & \mathbf{0} \end{bmatrix} \begin{bmatrix} \Delta\hat{\mathbf{u}}_{k+1} \\ \Delta\hat{\boldsymbol{\lambda}}_{k+1} \end{bmatrix} = - \begin{bmatrix} \mathbf{R} + \boldsymbol{\Lambda}^T \hat{\boldsymbol{\lambda}}_k^{t+\Delta t} \\ \boldsymbol{\Lambda}\hat{\mathbf{u}}_k^{t+\Delta t} - \overline{\boldsymbol{\Lambda}}\overline{\mathbf{u}} \end{bmatrix} , \tag{3.40}$$

with

$$\boldsymbol{\Lambda} = \int_{\Gamma_D} \mathbf{N}_\lambda^T \mathbf{N} \mathrm{d}\Gamma_D \qquad \text{and} \qquad \overline{\boldsymbol{\Lambda}} = \int_{\Gamma_D} \mathbf{N}_\lambda \mathrm{d}\Gamma_D \,. \tag{3.41}$$

$\mathbf{K}$ and $\mathbf{R}$ are defined by equations 2.96 and 2.94 respectively, while $\mathbf{K}_{LM}$ is the linearization of equation 3.38 with respect to the displacements. As the constraints are linear in $\mathbf{u}^h$, this term vanishes and is therefore written in parentheses.
The integrals in equation 3.41 are evaluated according to equation 3.14, since the boundary Γ_D is discretized by n_{bp} boundary particles, yielding

$$\boldsymbol{\Lambda} = \bigcup_{\mathrm{bp}=1}^{n_{\mathrm{bp}}} \mathbf{N}_\lambda^T \mathbf{N} \Gamma_{\mathrm{bp}} \qquad \text{and} \qquad \overline{\boldsymbol{\Lambda}} = \bigcup_{\mathrm{bp}=1}^{n_{\mathrm{bp}}} \mathbf{N}_\lambda \Gamma_{\mathrm{bp}}. \tag{3.42}$$

Due to this boundary discretization, the imposed displacements are evaluated at each boundary particle, replacing $\overline{\mathbf{u}}$ by $\overline{\mathbf{u}}_{\mathrm{bp}}$ in equation 3.40. In preparation for the partitioned coupling introduced in chapter 6, these values are assembled to the vector $\overline{\mathbf{u}}_M$.

Suitable Lagrange Multiplier Field

The saddle point problem given by equation 3.40, which results in a minimum of the primal variables and a maximum for the Lagrange multipliers, can only be solved if the inf-sup condition of Ladyzhenskaya, Babuška [8, 9] and Brezzi [28, 29] is satisfied. Hence, also in the discretization of the involved fields the saddle point characteristics must be considered. While in MPM the classical simple element-wise basis functions are chosen for the displacement field, the Lagrange multiplier discretization has to be selected according to this field approximation. As described in detail by the author in [117], a constant element-wise approximation of the Lagrange multipliers is selected, which introduces an additional dof $\boldsymbol{\lambda}$ in spatial direction for the Lagrange multiplier within each background grid element intersected by the boundary. This allows a local definition of the

boundaries at the element level, which is an essential feature for general and robust imposition within MPM. Especially, for the numerical investigation of flow events with large strains as well as a changing interface topology for partitioned coupling approaches, this locality is an essential requirement, since the set of active background grid elements may change in each time step.
However, it is also demonstrated in [117] that the approach of simple element-wise basis functions for the primal variables in combination with the constant approximation of the dual variables does not soundly satisfy the inf-sub condition. Depending on the background grid element type and the topology of the elements intersected by the boundary, this approach may result in a Lagrange multiplier discretization that is locally over-constrained. This consequently leads to spurious oscillations of the resulting Lagrange multipliers.
This effect is also referred to as boundary locking (see e.g., Hughes [66]) with an adverse influence on the convergence behavior of the primal variable. Therefore, the Lagrange multiplier discretization has to be appointed consciously depending on the background grid to ensure that conditions are not imposed twice.
The locking effect can be mechanically explained by the possible deformations of an intersected background grid element. Due to the chosen basis functions for the primal variables, the displacement along the element edges is approximated linearly between the corresponding nodes. However, for the edges intersected by a Dirichlet boundary, this linear interpolation leads to a dependence on the adjacent node deformations to satisfy the constraint within these edges.
Consequently, if a triangular element has common edges with two neighboring constrained elements, the nodal deformations of that element are already determined. Therefore, the constraint imposition within this element is superfluous and needs to be eliminated to avoid spurious oscillations in the Lagrange multiplier solution. In Figure 3.4, such particular elements, whose nodal deforma-

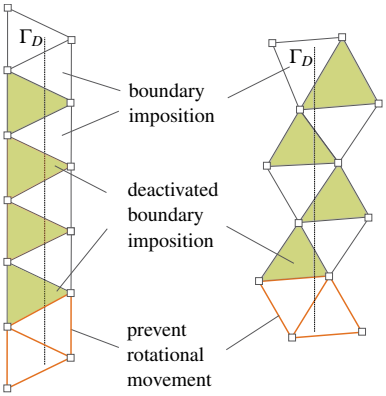

Figure 3.4: The boundary condition should be imposed within the white elements, whereas the Lagrange multiplier dofs should be deactivated in the green highlighted elements. Adapted from [117].

tions and thus the resulting strains are already determined by the neighboring

constrained elements, are highlighted in green. The elimination of these superfluous constraint conditions can be easily achieved by temporarily deactivating the corresponding dofs of the Lagrange multipliers within these elements.
Due to the constant distribution of the Lagrange multiplier within the elements resulting in a single force that constrains the corresponding movement, two adjacent elements intersected by the Dirichlet condition need to be set active once within the boundary geometry definition to prevent the rotational movement of the constrained elements. In Figure 3.4, these elements are graphically highlighted with an orange outline and are defined at the starting point of the line that defines the boundary geometry.
Although there are often several possibilities to select the elements for the boundary imposition, the solution of the primal variable is not affected by this decision as long as the boundary imposition determines all nodal deformations of the intersected elements. However, the resulting values of the Lagrange multipliers may change slightly to satisfy the equilibrium.
For quadrilateral background grid elements, this reasoning holds as well. However, superfluous constraints can only occur if three neighboring elements sharing each an edge with the considered element are also constrained, which rarely happens when imposing boundary conditions.
For 3D space, this theory can be extended accordingly, distinguishing between neighboring elements sharing a surface or an edge. Therefore, three constrained neighboring edge elements are sufficient to describe the nodal deformations of a tetrahedral element, as long as the edges pass through every node of the geometry. All other constraints within the remaining neighboring elements, as well as the constraint within the considered element itself, are superfluous in this case.
For hexahedral elements, where bi-linear functions describe the interpolation of the fields at the element surfaces, while only at the sharing edges a linear interpolation is present, superfluous constraints only occur if one surface has more than two constrained edges.
From a computational point of view, the proposed elimination procedure of eliminating superfluous Lagrange multiplier dofs to obtain a suitable Lagrange multiplier distribution is also attractive. Since the computational background grid does not change its topology, the neighboring elements sharing a common edge or surface need to be found only once for each element being intersected by the boundary. Consequently, within each time step, superfluous constraints are efficiently detected and the corresponding Lagrange multiplier dofs are temporally deactivated.

Slip Boundary Condition

Similar to the penalty augmentation, the boundary particles to impose the Lagrange multiplier condition carry the information about the unit normal vectors $\hat{\mathbf{n}}_{\mathrm{bp}}$ defined in the outward direction of the imposed boundary. Therefore, to consider slip conditions using Lagrange multipliers, the unit normal vector $\hat{\mathbf{n}}_I$ at the node I of the computational background grid is approximated according to equation 3.25. With this information the rotation matrix $\mathbf{Q}$ (see equation 3.26) as well as the block matrix $\hat{\mathbf{Q}}$ (see equation 3.27) to locally rotate the the matrices and vectors can be calculated. Hence, the partially rotated system of equations

is defined by

$$\left(\hat{\mathbf{Q}}\begin{bmatrix}\mathbf{K} & \mathbf{\Lambda}^T\\ \mathbf{\Lambda} & \mathbf{0}\end{bmatrix}\hat{\mathbf{Q}}^T\right)\left(\hat{\mathbf{Q}}\begin{bmatrix}\Delta\hat{\mathbf{u}}_{k+1}\\ \Delta\hat{\boldsymbol{\lambda}}_{k+1}\end{bmatrix}\right) = -\left(\hat{\mathbf{Q}}\begin{bmatrix}\mathbf{R}+\mathbf{\Lambda}^T\hat{\boldsymbol{\lambda}}_k^{t+\Delta t}\\ \mathbf{\Lambda}\hat{\mathbf{u}}_k^{t+\Delta t}-\overline{\mathbf{\Lambda}}\overline{\mathbf{u}}_M\end{bmatrix}\right). \tag{3.43}$$

To impose the roller condition, the Lagrange multipliers in the directions tangential to the support are set to zero. This is achieved by setting the corresponding entries of the rotated stiffness matrix to zero, except for the entry on the main diagonal, which is set to one. Since the entries in the residual vector are also set to zero, the resulting Lagrange multipliers in tangential directions, which can be interpreted as reaction forces, are set to zero. The system is then free to move in tangential directions.

Calculation of Reaction Forces

Another advantage of the Lagrange multiplier method is that the resulting reaction forces that enforce the Dirichlet condition can be calculated directly. From equation 3.40, one can derive the additional force acting on the nodes of the computational background grid due to the boundary imposition

$$\mathbf{R}_{\mathrm{LM}} = \mathbf{\Lambda}^T\hat{\boldsymbol{\lambda}}_k^{t+\Delta t}\,. \tag{3.44}$$

Therefore, the resulting reaction forces $\mathbf{R}_{I,\mathrm{LM}}$ at node I of the computational background grid element in spatial directions are defined by

$$\mathbf{R}_{I,\mathrm{LM}} = \bigcup_{\mathrm{bp}=1}^{n_{\mathrm{bp}}} N_I\Gamma_{\mathrm{bp}}\hat{\boldsymbol{\lambda}}_k^{t+\Delta t}\,, \tag{3.45}$$

assuming a constant Lagrange multiplier distribution within the element. The reaction forces at the boundary particles are obtained by interpolating the discrete nodal reaction forces with the corresponding shape functions

$$\mathbf{R}_{\mathrm{bp}} = \sum_{I=1}^{n_n}\gamma_{\mathrm{I,bp}}N_I\mathbf{R}_{I,LM}\,, \tag{3.46}$$

where $\gamma_{\mathrm{I,bp}}$ is the interpolation weighting factor defined by equation 3.31 to maintain the sum of forces analogous to the penalty approach.

Material and Boundary Interaction

Analogous to the penalty augmentation, different configurations of the material points interacting with the boundary particles need to be considered, as depicted in Figure 3.3. Again, only the configuration depicted in Figure 3.3b) is critical and needs to be consciously considered. Therefore, for those elements that contain only boundary particles but are still connected to the body, an additional stiffness is assigned to the diagonal of the respective elemental stiffness matrix. As a consequence, the material points of neighboring elements are already influenced by the boundary condition, which decelerates the movement of the body to prevent

the material from penetrating the boundary, but still allows the movement towards the boundary itself. From the author's experience, the Young's modulus of the considered material multiplied by the volume of the respective element can be set as artificial stiffness.

Contact Conditions

In the Lagrange multiplier approach, the contact conditions are defined by the Karush-Kuhn-Tucker (KKT) condition, which in the continuum is defined by

$$g_N(\mathbf{u}) \geq 0, \qquad \boldsymbol{\lambda}_N \leq 0, \qquad g_N(\mathbf{u})\boldsymbol{\lambda}_N = 0 \tag{3.47}$$

assuming the outwards pointing unit normal vector $\mathbf{n}$. $g_N(\mathbf{u})$ is defined by equation 3.32, whereas $\boldsymbol{\lambda}_N$ is the normal direction of the Lagrange multiplier $\boldsymbol{\lambda}$, which represents the reaction force.
The equality constraint 3.19 is part of the system of equations (see equation 3.36), which implies after solving the system, that the first and third KKT condition are equal to zero as soon as the material and the boundary are in contact. As a consequence of the contact, reaction forces $\boldsymbol{\lambda}_N$ result.
Consequently, the contact condition can be incorporated into the solution of the discrete problem by evaluating whether

$$\hat{\boldsymbol{\lambda}}_N \leq 0 \tag{3.48}$$

is satisfied. Herein, $\hat{\boldsymbol{\lambda}}_N$ is the discrete Lagrange multiplier within a constrained background grid element. If this condition is satisfied, the condition is applied. Otherwise, the dofs of the corresponding Lagrange multiplier are temporarily deactivated, resulting in zero reaction forces and thus satisfying the KKT condition.

3.4.3.3 Perturbed Lagrangian Method

The advantage of the Lagrange multiplier method is that the imposed conditions are exactly fulfilled by introducing additional dofs into the system of equations, which enforce the Dirichlet conditions. However, the solution of the resulting saddle point problem requires an inf-sub stable discretization of the involved fields. For this purpose, in section 3.4.3.2 a constant Lagrange multiplier approximation within constrained elements in combination with a methodology for eliminating superfluous constraints is introduced, which can be combined with the simple element-wise interpolation functions classically used in MPM to approximate the displacement field.
However, the elimination procedure comes at the cost of additional computational effort. To avoid this problem, the Lagrange multiplier formulation can be stabilized by adding another term to the modified principle of virtual work equation 3.34. As proposed by Simo et al. [112] for the solution of contact problems, a penalty stabilization term defined by

$$\delta W_{\mathrm{PL}} = -\frac{1}{\beta}\int_{\Gamma_D} \boldsymbol{\lambda}^T \delta\boldsymbol{\lambda}\, \mathrm{d}\Gamma_D \tag{3.49}$$

is added to the modified principle of virtual work equation 3.34, resulting in a perturbed Lagrangian formulation. This additional term, depending on β, has the form of a penalty term and serves the purpose of regularizing the saddle point problem. Obviously, only in the limit case, if $\beta \to \infty$, the regularized problem fulfills the imposed conditions exactly, otherwise analogous to the penalty approach, an approximation is obtained.
By discretizing the displacement (see equation 2.76) and the Lagrange multiplier field (see equation 3.37) and rewriting the equations using implicit time integration and the Newton-Raphson iteration, yields

$$\begin{bmatrix} \mathbf{K}(+\mathbf{K}_{LM}) & \mathbf{\Lambda}^T \\ \mathbf{\Lambda} & -\frac{1}{\beta}\mathbf{\Lambda}_\mathrm{P} \end{bmatrix} \begin{bmatrix} \Delta\hat{\mathbf{u}}_{k+1} \\ \Delta\hat{\boldsymbol{\lambda}}_{k+1} \end{bmatrix} = - \begin{bmatrix} \mathbf{R} + \mathbf{\Lambda}^T \hat{\boldsymbol{\lambda}}_k^{t+\Delta t} \\ \mathbf{\Lambda}\hat{\mathbf{u}}_k^{t+\Delta t} - \overline{\mathbf{\Lambda}}\overline{\mathbf{u}} - \frac{1}{\beta}\mathbf{\Lambda}_\mathrm{P}\hat{\boldsymbol{\lambda}}_k^{t+\Delta t} \end{bmatrix} . \tag{3.50}$$

In addition to equation 3.40, the penalty stabilization term is considered, while $\mathbf{\Lambda}_\mathrm{P}$ is defined by

$$\mathbf{\Lambda}_\mathrm{P} = \int_{\Gamma_D} \mathbf{N}_\lambda^T \mathbf{N}_\lambda \, \mathrm{d}\Gamma_D. \tag{3.51}$$

Analogous to the previous approaches, the integrals in equation (3.50) are evaluated according to equation (3.14), since the boundary is discretized by n_bp boundary particles. Furthermore, the constant element-wise approximation of $\boldsymbol{\lambda}$ is utilized for this approach as well, reducing the stabilization term in the matrix to a diagonal matrix.
Applying static condensation to the modified system of equations 3.50 for the displacements $\Delta\hat{\mathbf{u}}_{k+1}$ being the remaining unknowns, this problem results in the penalty approach as presented in section 3.4.3.1.
However, compared to the classical penalty approach, the system conditioning of the perturbed Lagrangian form is less sensitive to the value of the penalty factor β, allowing a larger value to be used for the boundary imposition. This effect is demonstrated in section 3.5.
Except for the additional stabilization term added to the system of equations, the boundary conditions can be imposed analogously to the Lagrange multiplier approach described in section 3.4.3.2. The extension for slip conditions, the calculation of reaction forces and the contact conditions are therefore also valid for the perturbed Lagrangian imposition.

3.4.3.4 Small Cut Instability

In immersed methods, the small cut instabilities are well-known problems and have been addressed by several authors just mentioning [79]. This issue is also crucial in MPM for the weak imposition of boundary conditions. If a boundary cuts an element very closely, the shape function value of the corresponding node may be very small, resulting in ill-conditioned stiffness matrices. Therefore, the most trivial approach to overcome this problem is to modify the shape function values N_I evaluated at the location of the corresponding boundary particle so that the minimum value is larger than a user-defined threshold ε. This leads to

the following equation

$$\bar{N}_I = \frac{N_I^*}{\sum_I^{n_n} N_I^*} \quad \text{where} \quad N_I^* = \begin{cases} \varepsilon, & \text{if } N_I \leq \varepsilon \\ N_I & \text{otherwise} \end{cases} \tag{3.52}$$

where $\bar{N}_I$ is the modified shape function value and n_n the total number of nodes of the considered background grid element. Yet, the partition of unity is ensured by the weighting procedure. Within this work the stabilization tolerance is set to $\varepsilon = 0.01$.

3.5 Verification of Boundary Imposition Types as Interface Condition

The validation of the penalty augmentation in implicit MPM can be found in [34], while the Lagrange multiplier imposition is detailed and validated in [117]. The perturbed Lagrangian method, which theoretically results in the penalty method, approaches the Lagrange multiplier method for large penalty factors and therefore shows similarities to both boundary imposition methods. This will be exemplified and discussed in the following. Furthermore, this section focuses on the comparison of the different boundary imposition methods and discusses their application in partitioned coupling strategies.

3.5.1 Tension Beam

The first example, visualized in Figure 3.5 considers a linear elastic cantilever

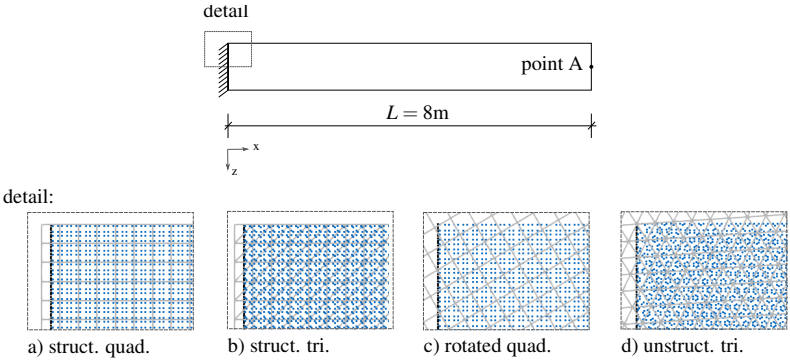

Figure 3.5: System of linear elastic cantilever beam and a detailed view of the non-conforming boundary condition and the particle discretization within four different background grid types (a) - d)). Adapted from [117].

beam under tension loading. The beam has a length of $L = 8$m, a cross-section of $A = 1 \times 1\text{m}^2$ and a density of $\rho = 1000\text{kg/m}^3$. The numerical models are created in

a)	Structured quadrilateral background grid (struct. quad.)
b)	Structured triangular background grid (struct. tri.)
c)	Rotated quadrilateral background grid (rotated quad.)
d)	Unstructured triangular background grid (unstruct. tri.)

Table 3.1: Background grid types for the numerical models.

2D assuming a St. Venant Kirchhoff material with Young's modulus of $E = 90$MPa and a Poisson's ratio of $\nu = 0.0$ for the constitutive equation. To apply a pure tensile load, a horizontal gravitational force of 9.81m/s^2 is considered acting in the global x-direction. As a reference solution, the analytic beam solution of the horizontal displacement at point A at the tip of the cantilever is considered.

The clamped support on the left side of the beam is modeled as a non-conforming boundary, imposing the Dirichlet condition weakly either by penalty augmentation (see section 3.4.3.1), the perturbed Lagrangian method (see section 3.4.3.3), or Lagrange multiplier imposition (see section 3.4.3.2). While for the latter approach the numerical solution is obtained directly, the other models require careful calibration of the penalty factor. If this factor is chosen too small, the material will penetrate through the boundary, while large factors may introduce numerical instabilities into the numerical model. Therefore, the solution obtained is hardly dependent on the chosen penalty factor, which is the main disadvantage of these boundary imposition methods.

The penalty factor β is varied in the range $\beta = 10^{10}$ to $\beta = 10^{30}$ to demonstrate this effect and to quantify the impact of different penalty factors on the resulting displacement solution. Furthermore, the influence of the chosen penalty factor on the reaction forces is investigated, which is particularly important when using the weak boundary imposition method for partitioned coupling schemes.

The study is performed for quadrilateral and triangular background grid elements, distinguishing for each a uniform and non-uniform intersection with the background grid elements. Consequently this results in four different numerical models, which are summarized in Table 3.1 and depicted in Figure 3.5 a) - d). The background grid element size is set to 0.04m each, while further details on the discretization can be found in [117].

In the Diagrams 3.6 a) to d), the relative errors of the horizontal displacement at point A compared to the analytical solution are plotted against the varying penalty factor using the penalty or the perturbed Lagrangian approach for boundary imposition. Additionally, the solution obtained by the Lagrange multiplier imposition is shown in the plots.

As expected, the relative errors of the horizontal displacement at point A decrease with increasing penalty factors until they approach the solution obtained with the Lagrange multiplier method. This behavior can be observed for all types of background grids and for both the penalty augmentation and the perturbed Lagrangian method.

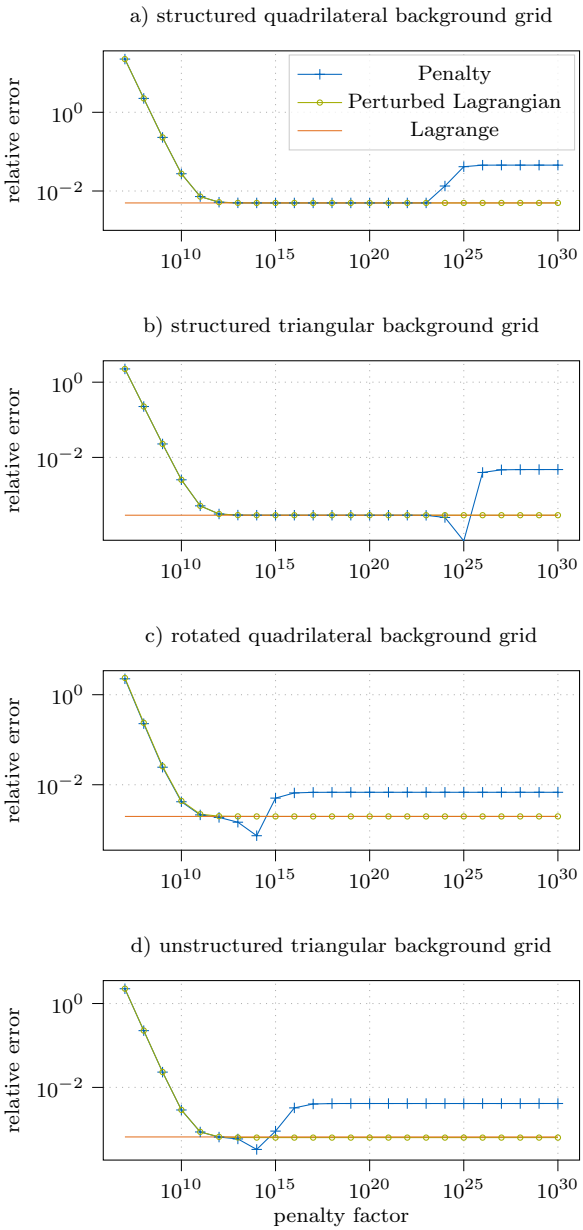

Figure 3.6: Comparison of penalty, perturbed Lagrangian and Lagrange multiplier method. Adapted from [117].

However, a further increase of the penalty factor shows a different pattern for the relative error depending on the background grid element type and the selected boundary imposition method. While the perturbed Lagrangian solution agrees with the Lagrange multiplier solution for all types of background grids, the deformations computed with penalty augmentation converge to a smaller nodal deformation once the penalty factor exceeds a certain value. Thus, the resulting beam deformation converges to the solution that could have been obtained by spatially fixing all nodes of the background grid elements containing boundary particles. Therefore, the system behavior changes from a weaker to a stiffer system compared to the analytical solution by increasing the penalty factor. Nevertheless, certain values closer to the analytical solution can be observed. However, this is a consequence of plotting the absolute values in the Diagrams 3.6.
Moreover, for the structured background grids (see Table 3.1a) and b)), where the boundary uniformly intersects the background grid elements, a wide range of penalty factors can be applied, whereas a non-uniform intersection of the boundaries with the elements significantly reduces the range of well-fitting penalty factors to obtain similar results compared to the Lagrange multiplier method. Thus, the difficulty of choosing an appropriate penalty factor can be demonstrated even for this academic example.
The results obtained with the perturbed Lagrangian method, on the other hand, converge to the solution obtained with the Lagrange multiplier method by increasing the penalty factor. This is because the stability term added to regularize the saddle point problem tends to zero with increasing β.
Nonetheless, even with high penalty factors, the structural deformation can still be approximated quite well with the penalty method, taking into account that the computed system behavior is slightly stiffer than expected. This in turn depends directly on the size of the intersected background grid elements.
However, the penalty method artificially increases the stiffness of the intersected elements to satisfy the Dirichlet constraints. This has a detrimental effect on the conditioning of the matrix and thus on the calculation of reaction forces. As the numerical solution obtained with penalty augmentation begins to transition to a stiffer system behavior, the conditioning of the matrix becomes worse, with a negative impact on the calculation of reaction forces. This effect is demonstrated in Figure 3.7. Herein the resulting reaction forces are plotted for a) a structured quadrilateral and b) a structured triangular background grid considering two different values of the penalty factor. The upper figures show the intermediate particle reaction force $\mathbf{R}_{\mathrm{P}}^{p}$, derived from equation 3.23, which is calculated by

$$-\mathbf{R}_{\mathrm{P}}^{p} = \beta \sum_{I}^{n_n} N_I \mathbf{N} \Gamma_{\mathrm{bp}} \hat{\mathbf{u}}_k^{t+\Delta t} - \beta \sum_{I}^{n_n} N_I \Gamma_{\mathrm{bp}} \overline{\mathbf{u}}_{\mathrm{bp}} \tag{3.53}$$

at each boundary particle. The lower figures show the final reaction forces at the boundary particles after the weighting procedure, which are calculated according to equation 3.30.
It is observed that for both background grid types, the obtained forces are in perfect agreement with the expected theoretical solution by choosing $\beta = 1e20$ for the penalty factor, which in accordance with Diagrams 3.6a) and b), is below the critical values leading to a stiffer system behavior. However, increasing the

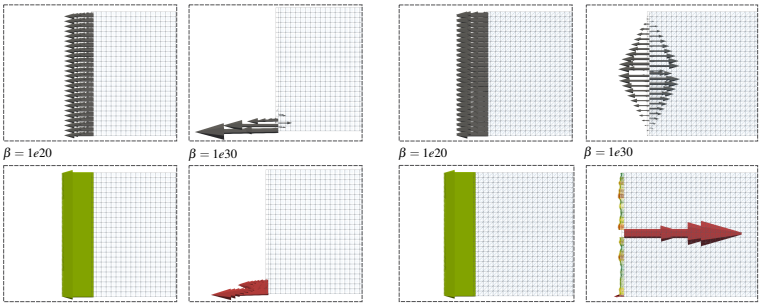

Figure 3.7: Contact forces of penalty method for a) struc. quad. and b) struc. tri. background grid. The reaction forces before the weighting procedure are displayed in the upper figures while the resulting reaction forces after the weighting are displayed in the lower figures.

penalty factor beyond the range of well-fitting penalty factors leads to numerical instabilities and oscillations of the forces, resulting in non-physical values for the forces. This is illustrated in Figure 3.7 for both background grid types considering a penalty factor of $\beta = 1e30$ as an example.

This example emphasizes the need to choose the penalty factor carefully, especially when the penalty method is used to calculate the reaction forces at the boundary in addition to the structural deformations. Selecting an appropriate penalty factor is even more problematic when non-uniform intersections of the boundary with the background grid elements must be taken into account. As shown in the Diagrams 3.6c) and d), the range of admissible penalty factors decreases even further for the rotated quadrilateral and unstructured triangular background grids. Thus, calibration of the system-dependent penalty factor is generally a challenging task, often requiring trial-and-error estimation.

Attractive alternatives to the weak imposition of the Dirichlet condition are the Lagrange multiplier method and the perturbed Lagrangian method. As the penalty factor increases, the latter technique converges to the Lagrange multiplier approach. Hence, assuming a penalty factor that is sufficiently large, the structural deformations and the resulting reaction forces converge to the Lagrange multiplier approach, allowing both options to be used interchangeably.

However, the increase of the penalty factor in the perturbed Lagrangian method transforms the considered problem into a saddle-point problem, which requires an inf-sub stable discretization of the involved fields. The applied approach of a constant element-wise approximation of the Lagrange multiplier field in combination with simple element-wise shape functions for the displacement field leads locally to over-constrained systems, which consequently results in boundary locking. However, for the beam loaded in tension only, this locking does not occur. Therefore, bending is included in the subsequent example to discuss this effect and to evaluate the results for the different types of boundary imposition methods.

3.5.2 Bending Beam

In order to investigate the effect of boundary locking for the different types of boundary imposition methods, the tension beam from the previous example, which is illustrated in Figure 3.5, is loaded in the global z-direction with dead load replacing the tension load and thus causing bending in the beam. The study is performed for the structured quadrilateral and structured triangular background grid depicted in Figure 3.5a) and b) with a mesh size of 0.04m and a uniform cut of the boundary with the background grid elements.

It is known from the Lagrange multiplier method that the imposition of the boundary conditions within all intersected elements can lead to boundary locking, resulting in oscillations of the reaction forces. To avoid this effect, a mechanical based elimination procedure is developed, described in section 3.4.3.2, which temporarily deactivates superfluous constraints and thus eliminates the boundary locking effect. For the types of background grids which are investigated here, the elimination procedure has to be performed for the triangular background grid, while the considered quadrilateral background grid has no superfluous constraints.

The perturbed Lagrangian method eliminates the need for the computationally expensive process of eliminating superfluous constraints due to the stabilization term included to solve the saddle point problem. Therefore, the boundary conditions are imposed on each intersected background grid element the same way as in the penalty method. However, since the perturbed Lagrangian boundary imposition approach converges to the Lagrangian multiplier method as the penalty factor increases, the effect of boundary locking needs to be evaluated.

In Diagrams 3.8 a) and b) the relative error of the vertical displacement of point A at the tip of the cantilever is plotted against the varying penalty factor considering either the penalty, perturbed Lagrangian, or the Lagrange multiplier method for imposing the non-conforming boundary condition. Similar to the previous example, the perturbed Lagrangian and penalty approaches converge to the solution obtained with the Lagrange multiplier method as the penalty factor increases.

Since the structured quadrilateral background grid does not exhibit boundary locking, the perturbed Lagrangian solution converges perfectly to the results obtained with the Lagrange multiplier method. The penalty augmentation, however, leads to a stiffer system behavior if the penalty factor exceeds a certain value. This observation is consistent with the results obtained for the tension beam.

A similar pattern is observed for the structured triangular background grid displayed in Diagram 3.8b), but demonstrating that the range of well-fitting penalty factors for the penalty augmentation is rather small. Furthermore, the results obtained with the perturbed Lagrangian method are slightly stiffer than the Lagrange multiplier solution due to the boundary locking effect.

To support the previous results, the study is repeated with a smaller background grid element size, which increases the boundary locking effects. Thus, the background grid element size is reduced by half to 0.02m and the results obtained with the different types of boundary imposition are plotted in Diagrams 3.9a) and b).

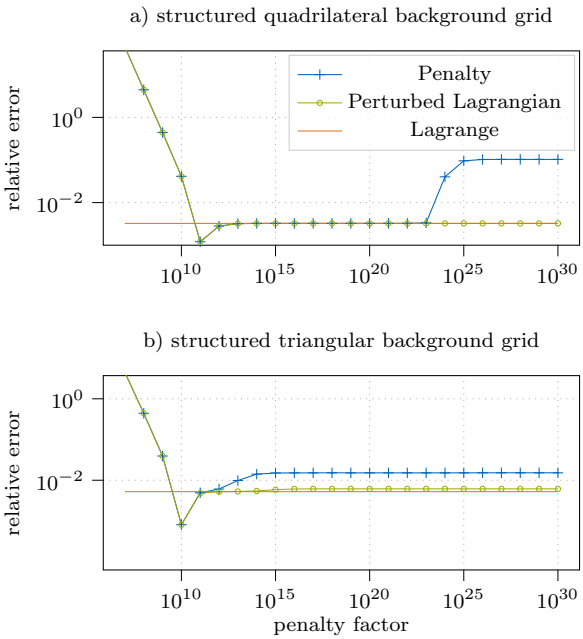

Figure 3.8: Comparison of Penalty, perturbed Lagrangian and Lagrange multiplier method for bending beam with mesh 0.04m.

While the results for the quadrilateral background grid show the same pattern with a smaller relative error compared to the coarser mesh, the effect of the boundary locking in the perturbed Lagrangian method can be distinctly observed for the triangular background grid.
The effect of boundary locking also influences the calculation of the reaction forces, which will be investigated in the following. Particularly in the context of partitioned coupling approaches, the reaction forces at the boundary are of significant importance in addition to the structural deformations. Therefore, the effect of the penalty factor on the resulting forces is discussed in the following, considering the background grid element size of 0.02m and the different types of boundary imposition methods.
To identify the source of error, the resulting reaction force plots include the intermediate particle reaction forces, shown in the upper figures, and the resulting reaction forces at the boundary particles after the weighting procedure, which are shown in the lower figures. For penalty augmentation, the intermediate particle reaction forces are calculated according to equation 3.53, while the final reaction forces are obtained by equation 3.30. In case of perturbed Lagrangian and Lagrange multiplier methods, the intermediate boundary particle reaction forces are the resulting values of the Lagrange multipliers $\hat{\boldsymbol{\lambda}}$. This results in one value

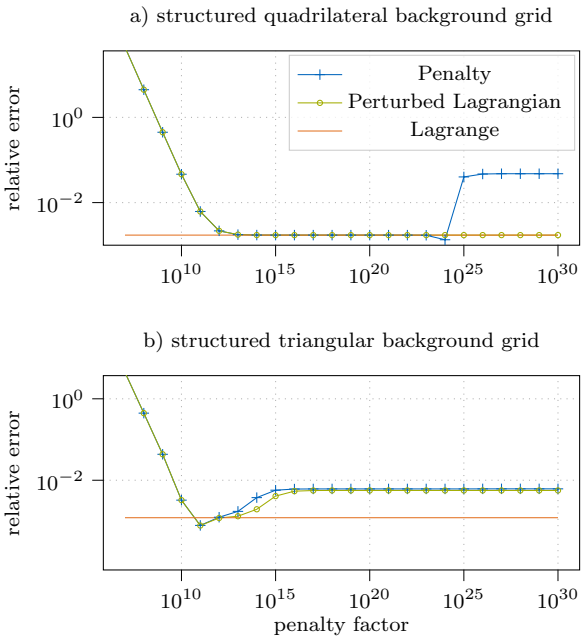

Figure 3.9: Comparison of penalty, perturbed Lagrangian and Lagrange multiplier method for bending beam with mesh 0.02.

per intersected background grid element. However, for visualization purposes only, it is displayed at each boundary particle within the element. The final reaction forces at the boundary particles are calculated by equation 3.46.
In Figure 3.10, the resulting reaction forces exemplified for $\beta = 1e15$ and $\beta = 1e30$ are displayed in a) for the penalty augmentation and in b) for the perturbed Lagrangian method. Analogous to the tension beam, numerical instabilities occur once the penalty factor exceeds the range of well-fitting parameters using the penalty augmentation, whereas the reaction forces obtained with the perturbed Lagrangian imposition method are very similar to those of the Lagrange multiplier imposition method (see Figure3.11a)). They are in very good agreement with the physical expectations, whereas inabilities occur in the penalty augmentation in the case of the large penalty factors.
In the next step, the boundary imposition types are investigated for the structured triangular background grid, which is prone to locking phenomena. Hence, the forces obtained by penalty augmentation for $\beta = \{1e11, 1e15, 1e30\}$ are displayed in Figure 3.12, while the results for the perturbed Lagrangian method are shown in Figure 3.13.
By choosing a penalty factor of $\beta = 1e11$, which is in the range of suitable penalty factors according to Diagram 3.9b), a smooth distribution of the resulting forces

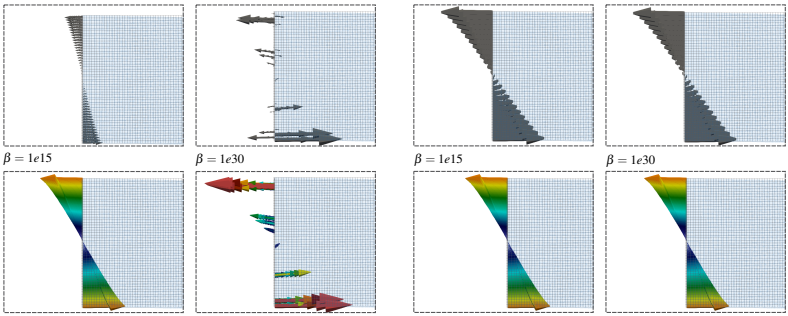

a) Penalty b) Perturbed Lagrangian

Figure 3.10: Contact forces for structured quadrilateral background grid using a) penalty augmentation or b) perturbed Lagrange multiplier method.

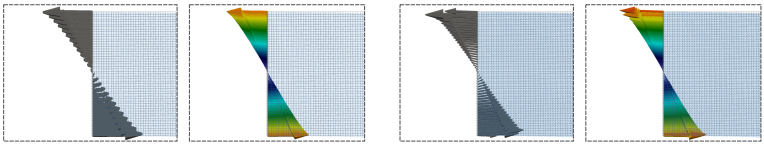

a) structured quadrilateral background grid b) structured triangular background grid

Figure 3.11: Contact forces Lagrange multiplier method for a) struc. quad. and b) struc. tri. background grid.

for both types of boundary imposition is obtained. However, as the penalty factor increases, the intermediate reaction forces shown in the top figures, respectively, start to oscillate due to the local violation of the inf-sub condition. Nonetheless, due to the weighting process to obtain the final boundary particle reaction forces depicted in the lower figures, this effect is largely smoothed out, resulting in a reasonable force distribution for $\beta = 1e22$ for both types of boundary imposition methods.

However, in the case of penalty augmentation (see Figure 3.12), some instabilities can be observed in the lower part of the structure already for $\beta = 1e22$. These instabilities become more severe with increasing penalty factors, as evidenced by the non-physical resulting forces obtained with a penalty factor of $\beta = 1e30$. This issue is not present in the perturbed Lagrangian method, where an oscillation of the intermediate reaction forces is observed, but is smoothed by the weighting procedure even in the case of $\beta = 1e30$.

In contrast to the perturbed Lagrangian method, superfluous constraints are eliminated if the boundary condition is imposed by Lagrange multiplier method. Consequently, the occurrence of spurious oscillations in the Lagrange multiplier solution representing the intermediate reaction forces is successfully prevented, as illustrated in Figure 3.11b) (left). However, as a result of the elimination pro-

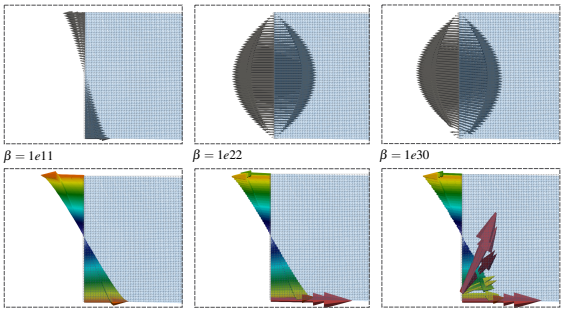

Figure 3.12: Contact forces for structured triangular background grid using penalty method with varying penalty factor.

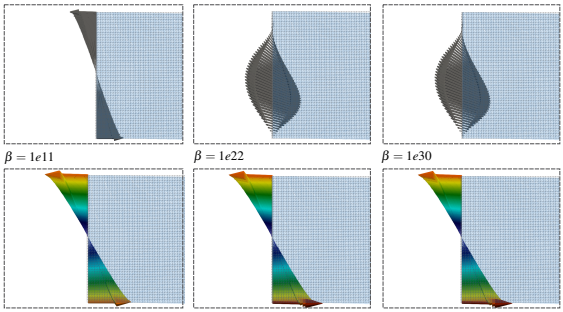

Figure 3.13: Contact forces for structured triangular background grid using perturbed Lagrange multiplier method with varying penalty factor.

cedure, the intermediate reaction forces are present only in certain background grid elements, while no reaction forces are present in the others. This effect is smoothed by to the applied weighting procedure, and the corresponding reaction forces at the boundary particles show the expected physical distribution (see Figure 3.11b) (right)).

In conclusion, it is crucial to carefully consider the choice of penalty factor, especially when using penalty augmentation to weakly impose essential boundary conditions and additionally evaluate reaction forces at the boundary. The perturbed Lagrangian method is more effective in this respect, but at the cost of additional dofs and thus a larger system of equations. However, as the penalty factors increase, this method converges to the Lagrange multiplier method, which can lead to boundary locking and force oscillations depending on the model discretization. Although the applied weighting method used to calculate the reaction forces at the boundary particles largely mitigates the force oscillations, the structural deformations are still underestimated (see Diagram 3.9).

Young's modulus	Poisson's ratio	density
$E = 21.6\text{MPa}$	$\nu = 0.0$	$\rho = 1379 \frac{\text{kg}}{\text{m}^3}$

Table 3.2: Material properties of the elastic body

Consequently, the most accurate technique is the Lagrange multiplier imposition method, incorporating the elimination procedure of superfluous constraints. It allows a user-friendly and robust imposition of weak boundary conditions without the need to calibrate the penalty factor by trial and error. However, in 3D space, the elimination of superfluous constraints can be computationally rather expensive. Thus, the perturbed Lagrangian method serves as an attractive alternative, and the penalty method also has its advantages since it does not require additional dofs for boundary imposition.

3.5.3 Impact Force Evaluation of Elastic Cylinder

While the previous examples evaluated the boundary imposition methods for the specific case where the boundary is defined along the body contour, the following examples examine the consequences of a boundary definition in space that gets in contact with the material during computation.

Therefore, this example considers an elastic cylinder with a radius of $r = 0.5\text{m}$ and a thickness of $t = 0.3\text{m}$, which moves downwards in global z-direction due to an imposed velocity of $\dot{u} = 1\text{m/s}$ until it hits a rigid wall, causing the elastic body to rebound. The setup of the considered system is depicted in Figure 3.14.

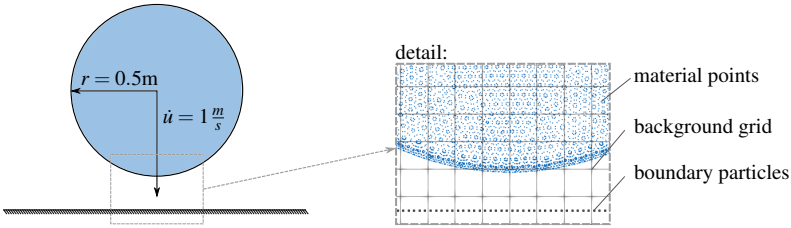

Figure 3.14: System and discretization of the elastic body.

In the Table 3.2 the material properties of the elastic body are summarized and for the 2D models a plane stress behavior is assumed.

The objective of this example is to evaluate the impact forces that occur when the elastic body rebounds at the rigid wall. The wall is modeled as a non-conforming boundary condition that enforces the Dirichlet constraint by penalty augmentation, perturbed Lagrangian method, or the Lagrange multiplier method with varying penalty factor β and changing model discretization. In the following, several studies are conducted to extract individual effects and discuss their implications for the solution.

Influence of Penalty Factor Variation

In the first study, the influence of the penalty factor value is evaluated to calculate the rebound of the elastic body. For the numerical model, a structured quadrilateral background grid with an element size of 0.05m is selected, while for the material point initialization, an unstructured triangular body mesh with a size of 0.02m is chosen, initializing 6 particles each. The non-conforming boundary is positioned in the center of the background grid elements as depicted in the detail of Figure 3.14, and boundary particles are initialized with a distance of 0.01m. These boundary particles impose the Dirichlet condition either by penalty augmentation or by the perturbed Lagrangian method, assuming a value of $\beta = 1e15$ for the penalty factor. Alternatively, the condition is imposed by the Lagrange multiplier method.
The simulation is run for 0.1s with a time step of $\Delta t = 2e-4$s to simulate the impact and the subsequent rebound of the elastic body.
In Figure 3.15, the resulting impact forces during the simulation time are plotted for the different boundary imposition methods. The resulting force at each time step is calculated by summing the reaction forces at the boundary particles. The obtained results demonstrate that the non-conforming boundary imposition methods can be used interchangeably to predict the impact force distribution over time.

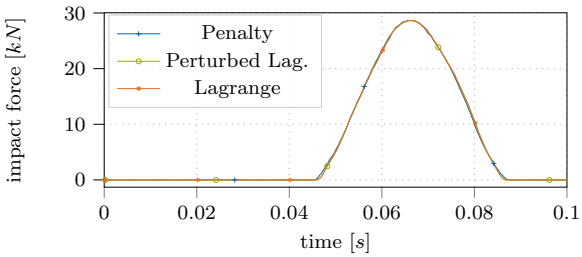

Figure 3.15: Impact forces, obtained with $\beta = 1e15$, for the penalty and perturbed Lagrangian augmentation, in comparison to the imposition of the constraint by Lagrange multiplier method.

Furthermore, the conservation of the energy is measured and the results are plotted in Figure 3.16. For the different methods of boundary condition imposition, the kinetic energy decreases due to the impact while the strain energy increases until it reaches its maximum when the kinetic energy reaches zero. In addition, some energy is stored in the boundary, which is also released after the impact, so that after the rebound, the kinetic energy of the elastic body is fully recovered, while the strain energy disappears.
For this model, an appropriate penalty factor was selected that allows to use the boundary imposition methods interchangeably. However, this factor must be calibrated and is often not known for the numerical model. Frequently, a safe factor is chosen to avoid numerical instabilities in the model caused by large penalty

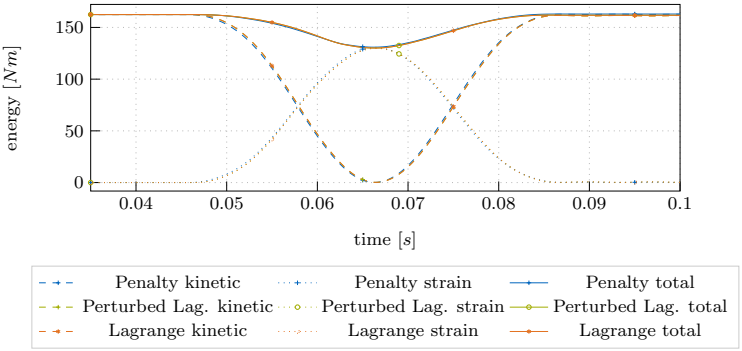

Figure 3.16: Energy plot, obtained with $\beta = 1e15$, for the penalty and perturbed Lagrangian augmentation, in comparison to the imposition of the constraint by Lagrange multiplier method. The total energy is the sum of kinetic and strain energy while the energy stored in the boundary during the impact is not explicitly stated.

factors. However, this also has a negative impact on the numerical results, as the following example illustrates.
Therefore, the calculation of the numerical model is repeated, but assuming a reduced penalty factor of $\beta = 1e10$ for the penalty augmentation and the perturbed Lagrangian method. The resulting force distribution is shown in Figure 3.17 and is compared to the force distribution obtained by Lagrange multiplier imposition, which is independent of any user-defined factor.

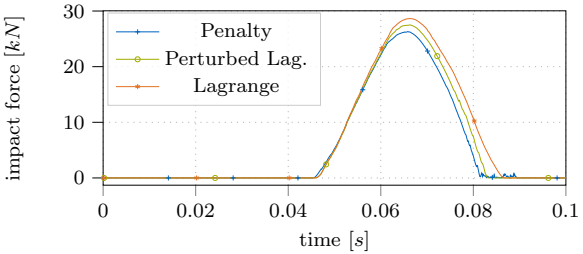

Figure 3.17: Impact forces, obtained with $\beta = 1e10$, for the penalty and perturbed Lagrangian augmentation, in comparison to the imposition of the constraint by Lagrange multiplier method.

It is observed that the influence of the penalty factor on the resulting force peak and its distribution is significant. When the penalty factor is reduced, the peak forces obtained by penalty augmentation are significantly underestimated. The perturbed Lagrangian method performs slightly better, but still underestimates

the peak force compared to the solution obtained by Lagrange multiplier imposition.
Furthermore, when the elastic body is released from the boundary, oscillations of the impact forces are observed when using penalty augmentation with the reduced penalty factor. This is due to the fact that the penalty factor is relatively low, resulting in energy absorption as shown in Figure 3.18. This effect,

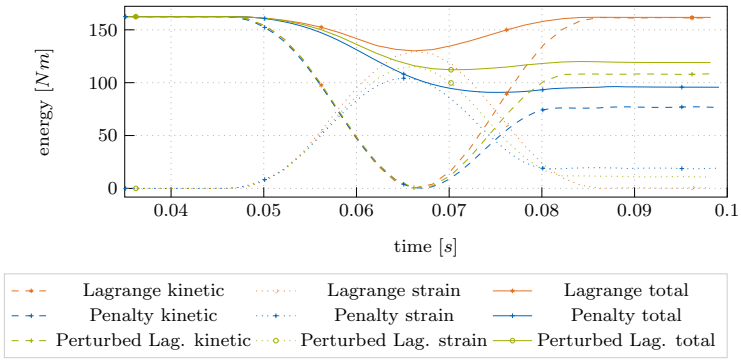

Figure 3.18: Energy plot, obtained with reduced penalty factor of $\beta = 1e10$, for the penalty and perturbed Lagrangian augmentation, in comparison to the imposition of the constraint by Lagrange multiplier method. The total energy is the sum of kinetic and strain energy while the energy stored in the boundary during the impact is not explicitly stated.

which causes the elastic body to have difficulty rebounding from the rigid wall, is more pronounced in the penalty augmentation method than in the perturbed Lagrangian method.
During the impact, the kinetic energy is converted to strain energy and energy stored in the boundary. However, due to the reduced penalty factor, the stored strain energy is much lower compared to the reference solution and this loss of energy is not recovered when the elastic body rebounds.
This again emphasizes the importance of selecting an appropriate penalty factor. Too low a factor leads to energy dissipation and underestimation of the impact force, while higher factors lead to numerical instability (see section 3.5.1 and section 3.5.2). Even though the consequences are not as pronounced in the perturbed Lagrangian method, the factor β still has to be carefully adapted to the numerical model.
The influence of an insufficient penalty factor is also present when comparing the analytical impulse with the results obtained from the numerical simulation. Since the elastic body rebounds at the rigid wall with an imposed velocity of $\dot{u} = 1\text{m/s}$, the analytical impulse is given by

$$p = r^2 \cdot \pi \cdot t \cdot \rho \cdot 2\dot{u} = (0.5\text{m})^2 \cdot \pi \cdot 0.3\text{m} \cdot 1379 \frac{\text{kg}}{\text{m}^3} \cdot 2 \frac{\text{m}}{\text{s}} = 649.84\text{Ns} \tag{3.54}$$

Lagrange	Perturbed Lagrange		Penalty	
	$\beta = 1e10$	$\beta = 1e15$	$\beta = 1e10$	$\beta = 1e15$
$e_r = 0.26\%$	$e_r = 9.4\%$	$e_r = 0.26\%$	$e_r = 15.68\%$	$e_r = 0.02\%$

Table 3.3: Relative error e_r of the impulse p due to the impact of the elastic body.

while the numerical solution is obtained by integrating the impact forces over time. In Table 3.3 the relative error of the impulse is summarized for the different boundary imposition methods and the varying penalty factor. While a very good agreement is obtained for the Lagrange multiplier imposition and the penalty and perturbed Lagrangian method with $\beta = 1e15$, the error increases significantly for the reduced factor $\beta = 1e10$.

Influence of the Time Step Size

In this example, the influence of the selected time step size on the resulting impact forces is examined. For this purpose, the numerical model is recalculated with a time step size of $\Delta t = 1e-3$s and the resulting force distribution over time is plotted in Diagram 3.19. The results confirm that the time step size has minor

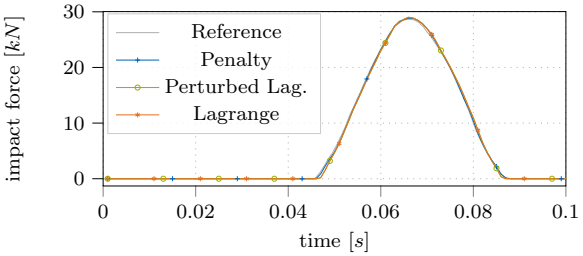

Figure 3.19: Impact forces on non-conforming boundary condition imposed either by penalty with $\beta = 1e15$, Perturbed Lagrangian with $\beta = 1e15$ or Lagrange multiplier method with time step size $\Delta t = 1e-3$ in comparison to the impact force obtained with a time step size of $\Delta t = 2e-4$ which is the reference solution.

impact on the numerical results, provided that the time discretization is small enough to accurately describe the force distribution during the impact. Both the peak force and the force distribution are well predicted even for the larger time step.

Influence of the Background Grid Element Size

Since the contact in MPM is solved via the background grid, the next study investigates the dependence of the impact force on the size of the background grid

elements. For this purpose, several numerical models with structured quadrilateral background grids are created and the impact forces are calculated. For all numerical models, the body mesh used to initialize the material points is chosen to be half the size of the background grid element, using triangular elements and placing 6 particles each. For each model, the rigid wall, modeled as a non-conforming boundary condition using either penalty augmentation with $\beta = 1e15$ or Lagrange multiplier imposition, is positioned in the center of the background grid elements as depicted in Figure 3.14.
Diagram 3.20 shows the peak impact force in relation to the background grid element size. In addition, the corresponding impact duration time, plotted on the right axis, is added to the plots. The plotted results show that for coarse background grids, the peak forces are tremendously underestimated and the impact duration is far too long. Thus, the conservation of linear momentum is still satisfied for coarse discretizations, but the peak forces and impact duration are not well predicted by the numerical model.

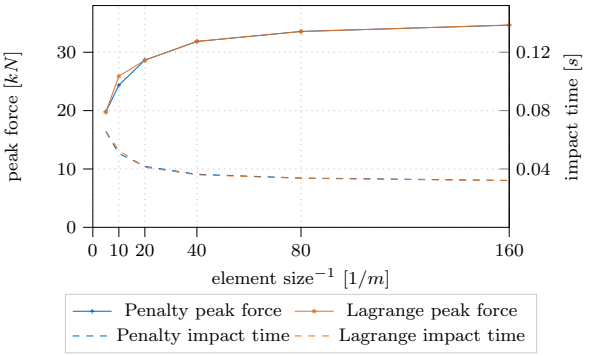

Figure 3.20: Impact force peaks and the impact duration time in dependency with the background grid element size for Lagrange imposition and penalty augmentation with $\beta = 1e15$.

This effect is caused by the fact that the impact duration starts as soon as the material points enter the background grid elements containing the boundary particles. From this moment on, the boundary significantly influences the motion of the material. Therefore, the background grid elements, which weakly impose the boundary conditions, behave like a crumple zone. By refining the background grid, this effect is reduced and the impact forces and the corresponding impact duration converge to a constant value.
Alternatively, the numerical results are also improved if the boundary is not initialized at the centerline of the elements, but is shifted towards the element border to reduce the crumple zone. In Figure 3.21 two alternative discretizations are visualized, while in a) the boundary is initialized at the centerline of the element, in b) the boundary is shifted close to the element border. For both models, a very coarse discretization of the background grid is selected using structured quadrilateral elements of size 0.2m.

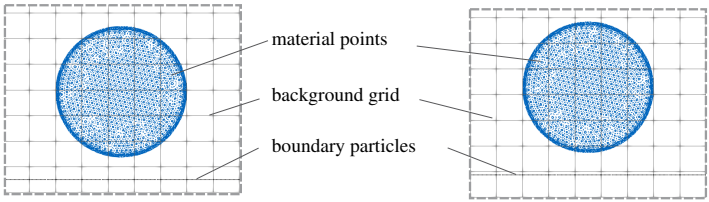

Figure 3.21: Impact force for coarse structured background grid elements initializing the condition either at a) the element center or b) at the element border.

Diagram 3.22a) shows the impact force for the model with the boundary initialized at the centerline of the element. As also demonstrated in the Diagram 3.20, both penalty augmentation with $\beta = 1e15$ and Lagrange multiplier imposition methods result in the same solution, which underestimates the peak forces but predicts a longer impact duration time due to the weak imposition of the boundary conditions.

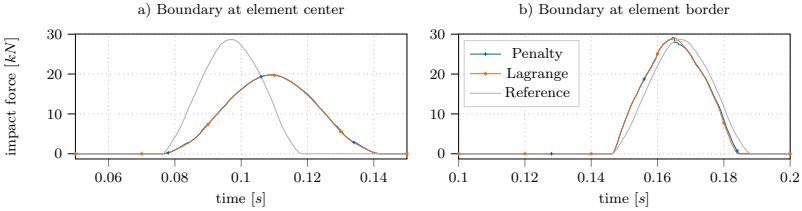

Figure 3.22: Impact force for coarse structured background grid elements initializing the condition either at a) the element center or b) at the element border. The reference solution is the impact force from Diagram 3.22.

Additionally, the reference solution plotted in Diagram 3.15 is added to the Diagram 3.22 to highlight the different force distribution. The reference solution is shifted in time so that the impact starts at the same time. There are two reasons for the timing difference. First, the material is initialized at a different position using the coarse discretization compared to the reference solution, and second, the start of the impact also depends on the background grid discretization. Comparing the start of the impact in Diagram 3.22a) and Diagram 3.22b), a significant difference in the timing is observed even though the material is initialized at the same position. This difference is caused by the background grid discretization and the effect that the impact starts as soon as the material points enter the background grid elements containing boundary particles. Hence, the distance between the initialized material points and the upper element border of the background grid elements containing boundary particles is smaller in con-

figuration a) compared to configuration b), resulting in an earlier start of the impact.
However, concluding from the results depicted in Diagram 3.22b), the force distribution obtained by shifting the boundary initialization close to the element border agrees well with the reference solution. Since the crumple zone is reduced due to the special discretization of the model, the peak force is predicted very well. However, this adjustment only applies to certain examples, while in general the size of the background grid elements must be adjusted. In addition, numerical instabilities may occur when the boundary initialization is shifted towards the element due to the small cut introduced. These numerical instabilities are slightly present close-by the peak force in the solution with penalty augmentation in Diagram 3.22b). Hence, in general, the size of the background grid element must be adapted to the problem at hand in order to calculate reasonable contact forces.

Influence of the Background Grid Element Geometry

For the quadrilateral background grid elements used in the numerical examples so far, there are no oscillations in the solution of the reaction forces. However, if the background grid is discretized with triangular elements, this effect needs to be taken into account, as already demonstrated for the bending beam in section 3.5.2. While an elimination procedure is applied for the Lagrangian multiplier imposition (see section 3.4.3.2) to temporarily deactivate superfluous constraints, the boundary conditions in the penalty and perturbed Lagrangian methods are always set to active. Therefore, increasing the penalty factor will result in partially overconstrained systems, which will adversely affect the resulting impact forces and cause reaction force oscillations.
In Diagram 3.23, the force distribution at the non-conforming boundary during

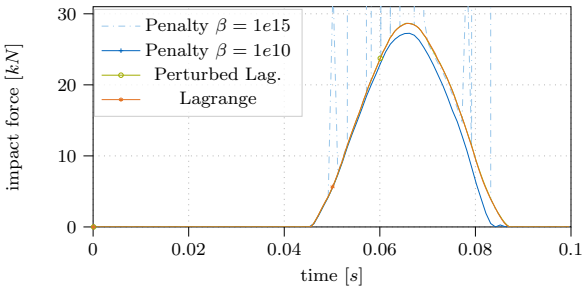

Figure 3.23: Impact force for triangular background grid elements imposing the condition either by penalty with $\beta = 1e15$ and $\beta = 1e10$, perturbed Lagrangian with $\beta = 1e15$ or Lagrange multiplier method.

the impact is plotted over time considering a triangular background grid with an element size of 0.05m. The other model parameters are kept as before.

The results demonstrate that due to the developed elimination procedure for the Lagrange multiplier imposition, the force distribution as well as the peak force are computed equivalently independent of the background grid element type. Furthermore, the perturbed Lagrangian method with $\beta = 1e15$ also calculates the same solution. Due to the introduced stabilization term, the problem can be solved even though superfluous constraints are not eliminated. The penalty augmentation, however, shows difficulties in finding a converged solution when a penalty factor of $\beta = 1e15$ is assumed. This leads to non-physical forces at certain time steps, which are highlighted by dashed lines in Diagram 3.23. By reducing the factor to $\beta = 1e10$, convergence is achieved and a solution is found at each time step. However, due to the relatively low factor, some energy is absorbed and the peak contact force is underestimated. The similar behavior is observed for quadrilateral elements using a reduced penalty factor (see Figure 3.17). Therefore, calibration of the penalty factor is more difficult for triangular than for quadrilateral background grid elements.

Finally, the performance of the different boundary imposition methods in 3D is evaluated considering hexahedral and tetrahedral elements for the background grid as depicted in Figure 3.24.

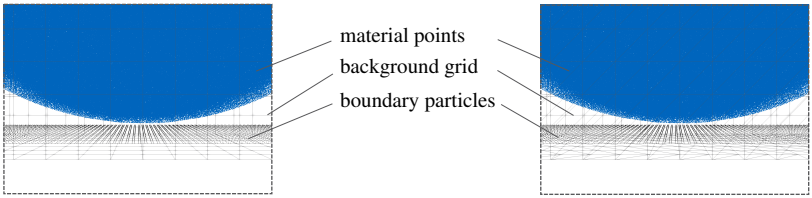

Figure 3.24: Details of the 3D model discretization while a) depicts the hexahedral background grid element and b) the tetrahedral one.

The discretization of the 3D model is selected to be similar to the 2D models, using an element size of 0.05m for both the structured hexahedral and the tetrahedral background grid. The material points are also initialized in a similar manner, creating an unstructured tetrahedral body mesh and placing 6 particles each.
The resulting contact forces for the hexahedral background grid are depicted in Diagram 3.25 considering the three different boundary imposition types. Similar to the triangular background grid in the two-dimensional model, the penalty augmentation with $\beta = 1e15$ introduces convergence difficulties, resulting in non-physical forces at certain time steps. On the other hand, the choice of $\beta = 1e10$ results in a boundary condition that is not stiff enough, leading to energy dissipation and an underestimation of the contact force.
The perturbed Lagrangian method with $\beta = 1e15$ and Lagrange multiplier imposition perform well, computing the same force distribution as obtained for the corresponding 2D models.
Very similar results are obtained for the tetrahedral background grid elements, as depicted in Diagram 3.26.

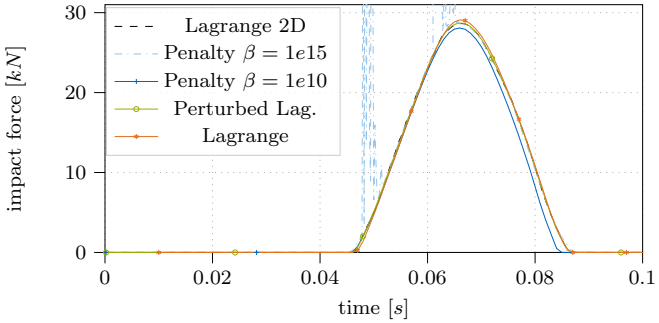

Figure 3.25: Impact force for hexahedral background grid elements for penalty augmentation with $\beta = 1e15$ and $\beta = 1e10$, perturbed Lagrangian with $\beta = 1e15$ and Lagrange multiplier imposition in comparison to the 2D Lagrange solution plotted in Diagram 3.15

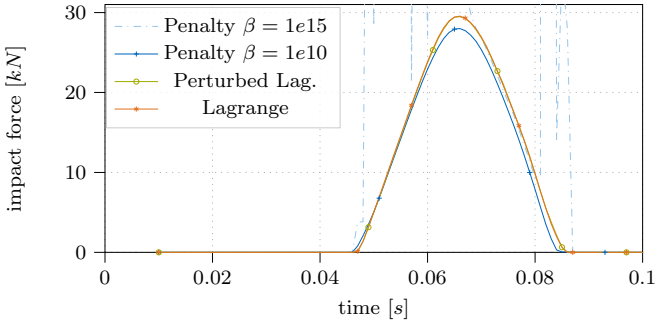

Figure 3.26: Impact force for tetrahedral background grid elements for penalty augmentation with $\beta = 1e15$ and $\beta = 1e10$, perturbed Lagrangian with $\beta = 1e15$ and Lagrange multiplier imposition.

In summary, this example demonstrates again that selecting an appropriate penalty factor can be difficult. Larger values can introduce numerical difficulties, while lower values can lead to energy dissipation and an underestimation of the contact forces. An improvement is obtained with the perturbed Lagrangian method, which robustly calculates the contact forces for a larger range of possible factors β. However, the computational effort increases as additional dofs are added to the global equation system. The Lagrange multiplier approach is the most attractive imposition method in this regard, since it does not require the user to select any problem-dependent parameters. However, it requires a longer computation time. In addition to the additional dofs, the elimination methodology of superfluous constraints must also be accessed at each time step.

Young's modulus	Poisson's ratio	density	friction angle
$E = 21.6\text{MPa}$	$\nu = 0.3$	$\rho = 1379 \frac{\text{kg}}{\text{m}^3}$	$\Phi = 35°$

Table 3.4: Material properties of the granular material.

In addition to the penalty factor, the size of the background grid elements also has a significant impact on the calculated peak forces and the corresponding contact duration time. This dependence results from the contact detection in MPM via the computational background grid.
In contrast to that, the time step size is of secondary importance and only needs to be adjusted to represent the impact force profile.

3.5.4 Impact Force Evaluation of Granular Material

In the final example, the verification of the types of boundary imposition methods is extended to granular materials. To simulate the flow of these elastic-plastic materials is the reason why MPM is selected as discretization method. Therefore, the elastic body of the previous example is replaced by granular material. The geometry and the system setup can be found in Figure 3.14, while the considered material parameters for the granular material law are listed in Table 3.4. The same density and Young's modulus are considered as for the elastic body in the previous example. A Mohr-Coulomb yield criterion is assumed, while the cohesion and the internal dilatancy angle are set to zero.
The calculated impact forces are plotted in Diagram 3.27 considering a struc-

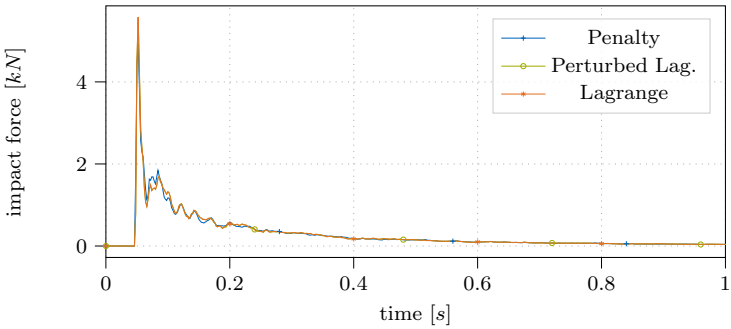

Figure 3.27: Impact forces at the boundary due to the impact of the granular material imposing the boundary condition by penalty with $\beta = 1e15$, perturbed Lagrangian with $\beta = 1e15$ or Lagrange multiplier method.

tured quadrilateral background grid with size 0.05m. The other model parameters are chosen according to the previous example. To capture the short impact peak, a time step of $\Delta t = 1e-5\text{s}$ is selected for the numerical simulation.

Lagrange	Perturbed Lagrange	Penalty
$e_r = 0.63\%$	$e_r = 0.55\%$	$e_r = 0.71\%$

Table 3.5: Relative error e_r of the impulse force p for the granular impact.

The computed force distribution shows a significant impact force when the material points come into contact. After the peak, the force decreases and then fluctuates in smaller waves until it converges to zero over time. Due to the impact on the rigid wall, a shock wave propagates through the material, which can be visualized by plotting the material accelerations during the first impact peak as illustrated in Figure 3.28. This wave causes the impact force to decrease after the

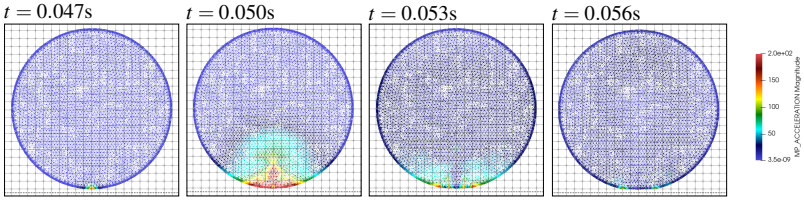

Figure 3.28: Material point acceleration at the first impact showing the shock wave due to the impact.

initial contact and initiates the plastic deformation of the material. Consequently the material moves laterally and the impact force converges to zero, since only an imposed velocity was initially applied.
Therefore, the impulse p is halved compared to the previous example (see equation 3.54) and the relative error for the different boundary imposition types are summarized in Table 3.5 after 4s of simulation time. All are in good agreement with the expected results.

3.6 Conclusions

Due to the Lagrangian moving particles in combination with the Eulerian background grid, the interface description required for partitioned coupling strategies is complex. First, an adequate description of the boundary condition is necessary, which tracks the position of the condition in time. For this purpose, boundary particles are introduced, which impose the boundary conditions in the MPM model and also serve as interface conditions in the partitioned strategy, receiving and sending the necessary data.
In addition, a weak imposition of boundary conditions is required. Many problems solved monolithically with MPM also often require weak boundary conditions. However, in particular for the partitioned coupling strategy, the weak imposition of boundary conditions is essential since the position of the shared interface changes during the computation.
For this purpose, the penalty method, the Lagrange multiplier method and the perturbed Lagrangian method are developed to weakly impose essential bound-

ary conditions. While the penalty method shows its limitations in the selection of appropriate, problem-dependent penalty factors, it outperforms the Lagrange multiplier method as well as the perturbed Lagrangian method in terms of computational efficiency. For the latter methods, additional dofs are required to enforce the conditions, and the developed Lagrange multiplier method additionally involves an elimination procedure for superfluous constraints.
The different types of boundary imposition methods are evaluated in terms of their accuracy as interface condition. Provided that the penalty factor is well calibrated, all methodologies can be applied interchangeably. However, the calibration of the penalty factor is often tedious and, depending on the problem to be solved, only a small range of admissible factors provide an accurate solution of the results. An improvement is obtained with the perturbed Lagrangian method, which robustly calculates the contact forces for a larger range of possible factors β. Analogous to the Lagrange multiplier approach, however, the computational effort increases as additional dofs are added to the global equation system, while still an appropriate penalty factor has to be selected. In this regards, the Lagrange multiplier method provides the most attractive boundary imposition method since it does not require the user to select any problem-dependent parameters.
In addition to the methodology, which weakly enforces the Dirichlet constraints, the size of the background grid elements is crucial for the calculation of the reaction forces, which in turn are required for the partitioned coupling strategies. This dependence results from the contact detection via the computational background grid. On the one hand, it is important to be aware of this dependency when discretizing the problem. On the other hand, contact detection is an inherent part of the MPM computational scheme, providing a computationally efficient method for modeling a wide variety of applications. Moreover, it is an essential requirement for the partitioned coupling strategies detailed in chapter 5 and chapter 6.

CHAPTER 4

Partitioned Coupling

Complex engineering problems often include several physics interacting with each other. However, the numerical simulation of such multi-physics problems is a complex task that requires the coupling of several numerical solution techniques. Among the existing coupling schemes, the partitioned or alternatively called staggered coupling approach is the most generic one, as each involved physics is solved in its preferred environment by using the numerical method that is able to describe the physical behavior best, while the interaction is shifted to the shared interface.

4.1 Black-box Solvers

Assuming two involved partitions, generally denoted by subscripts o and d, their shared interface is defined by

$$\Gamma_{\mathrm{od}} = \Gamma_{\mathrm{o}} \cap \Gamma_{\mathrm{d}}. \tag{4.1}$$

Along this interface, either Dirichlet or Neumann boundary conditions are applied to the individual subsystems. In general, mixed methods that result in Robin type decomposition would also be possible, but are of minor importance and are therefore not considered. Following this approach, each partition is treated as a black-box solver and is solved individually considering the respective boundary conditions at the shared interface.
There exist different ways to combine Dirichlet and Neumann conditions at the interface level, which are presented in [109] for a simple example. Furthermore, it is demonstrated, that the choice of the decomposition is highly problem-dependent. In this work, a Dirichlet-Neumann decomposition is chosen, which is also the classical choice of fluid-structure interaction (FSI) problems [130, 78, 135] and closely follows the real physical problem.
Consequently, introducing a Dirichlet condition at one subsystem, which prescribes the displacements $\mathbf{u}_{\Gamma_{\mathrm{od}}}$ at the shared interface, leads to the black-box system $\mathscr{S}_D$ solving for the traction field

$$\mathbf{p}_{\Gamma_{\mathrm{od}}} = \mathscr{S}_D(\mathbf{u}_{\Gamma_{\mathrm{od}}}). \tag{4.2}$$

Taking the Neumann condition as an input for the solver $\mathscr{S}_N$, the updated displacements $\mathbf{u}_{\Gamma_{\text{od}}}$ at the shared interface are obtained. In general, this can be written as

$$\mathbf{u}_{\Gamma_{\text{od}}} = \mathscr{S}_N(\mathbf{p}_{\Gamma_{\text{od}}}). \tag{4.3}$$

From this partitioning an additional equation system enforcing the interface transmission conditions arises, which has to be solved.

4.2 Interface Transmission Conditions

Enforcing a consistent deformation of the involved sub-solver interfaces without gaps and overlaps the kinematic constraint defined by

$$\mathbf{u}_{\text{o}}(\mathbf{x}) = \mathbf{u}_{\text{d}}(\mathbf{x}) = \mathbf{u}_{\Gamma_{\text{od}}}(\mathbf{x}) \qquad (\mathbf{x} \in \Gamma_{\text{od}}) \tag{4.4}$$

needs to be fulfilled. Herein, $\mathbf{u}_{\text{o}}$ and $\mathbf{u}_{\text{d}}$ are the interface displacement fields of the involved partitions. Additionally, the first and second time derivatives of the displacement, which correspond to the interface velocity and acceleration, need to be equivalent at both interfaces to fulfill the kinematic constraint.
Furthermore, the dynamic interface transmission condition arising from the load balance at the interface needs to be satisfied. It is defined by

$$\mathbf{p}_{\text{o}}(\mathbf{x}) = \mathbf{p}_{\text{d}}(\mathbf{x}) = \mathbf{p}_{\Gamma_{\text{od}}}(\mathbf{x}) \qquad (\mathbf{x} \in \Gamma_{\text{od}}) \tag{4.5}$$

where $\mathbf{p}_{\text{o}}$, $\mathbf{p}_{\text{d}}$ are the traction fields at the respective interface, defined with respect to the corresponding outward normal vectors.
It should be noted that in case of a total Lagrangian formulation, the interface Γ_{od} is defined in the initial reference configuration, requiring a transformation of the traction before applying the dynamic coupling condition.

4.3 Fixed-point Iteration

Classical solution schemes are fixed-point iterations to solve the non-linear interface equations. For example, the Picard iteration with iteration counter k can be formulated as

$$\mathbf{u}_{\Gamma_{\text{od}}}^{k+1} = \mathscr{S}_N \circ \mathscr{S}_D(\mathbf{u}_{\Gamma_{\text{od}}}^{k}) \tag{4.6}$$

which means that the black-box solver $\mathscr{S}_D$ advances first in time with given interface displacements $\mathbf{u}_{\Gamma_{\text{od}}}^{k}$ as input, solving equation 4.2. As a result, the updated traction field $\mathbf{p}_{\Gamma_{\text{od}}}$ is obtained. This result then serves as input for the subsequent solver $\mathscr{S}_N$ (see equation 4.3) solving for the updated interface displacements $\mathbf{u}_{\Gamma_{\text{od}}}^{k+1}$.
Hence, the entire sequence must be solved iteratively until the convergence criteria defined by

$$\|\mathbf{r}^k\| < \epsilon \tag{4.7}$$

is reached. In this equation, ϵ is a user-defined breaking tolerance and $\mathbf{r}^k$ is the residual in the current iteration. For the considered fixed-point iteration defined by equation 4.6, the residual is defined by

$$\mathbf{r}_u^k = \mathscr{S}_N \circ \mathscr{S}_D(\mathbf{u}_{\Gamma_{od}}^k) - \mathbf{u}_{\Gamma_{od}}^k = \mathbf{u}_{\Gamma_{od}}^{k+1} - \mathbf{u}_{\Gamma_{od}}^k \tag{4.8}$$

while the subscript u indicates the residual for the interface displacements.
To accelerate the interface iteration, convergence accelerators can be utilized, which modify the interface displacements $\mathbf{u}_{\Gamma_{od}}^{k+1}$ before feeding them back as input to the black-box solver $\mathscr{S}_D$ in the subsequent iteration. In section 4.3.2 convergence accelerators via relaxation are presented, while in section 4.4 quasi-Newton schemes are introduced which can be applied alternatively to accelerate the iterative solution of the interface equilibrium. For a general notation, the operator ACC is introduced, representing the utilized convergence accelerator. It is frequently the case that these convergence accelerators are also necessary to increase the robustness of the coupled problem.
In Figure 4.1, the resulting flowchart of the coupling scheme based on equation 4.6 is illustrated.

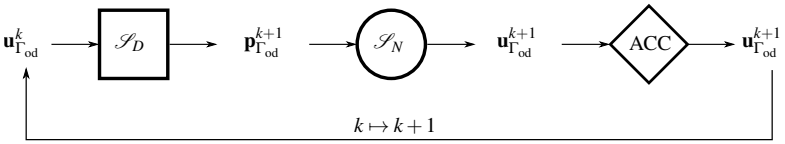

Figure 4.1: Flow chart of Gauss-Seidel strong coupling scheme described by equation 4.6.

Alternatively, formulating the Picard iteration using the traction field as a variable yields

$$\mathbf{p}_{\Gamma_{od}}^{k+1} = \mathscr{S}_D \circ \mathscr{S}_N(\mathbf{p}_{\Gamma_{od}}^k) \tag{4.9}$$

which results in

$$\mathbf{r}_p^k = \mathscr{S}_D \circ \mathscr{S}_N(\mathbf{p}_{\Gamma_{od}}^k) - \mathbf{p}_{\Gamma_{od}}^k = \mathbf{p}_{\Gamma_{od}}^{k+1} - \mathbf{p}_{\Gamma_{od}}^k \tag{4.10}$$

for the residual equation. Herein, the subscript p indicates the residual for the interface traction forces.
Hence, the black-box solver $\mathscr{S}_N$ is solved first, while $\mathscr{S}_D$ is the subsequent solver which solves for the updated traction forces $\mathbf{p}_{\Gamma_{od}}^{k+1}$ as illustrated in Figure 4.2. Also in this coupling sequence, convergence accelerators are often utilized to modify the input for the subsequent iteration loop. However, in contrast to the previous coupling sequence described by equation 4.6, the traction forces $\mathbf{p}_{\Gamma_{od}}^{k+1}$ are modified within this coupling iteration described by equation 4.9.
These introduced fixed-point iterations strictly infer the sequential execution of both solvers, resulting in the Gauss-Seidel communication pattern. Consequently, it can only be applied to Dirichlet-Neumann decomposition, which requires a serial computation of the involved solvers.

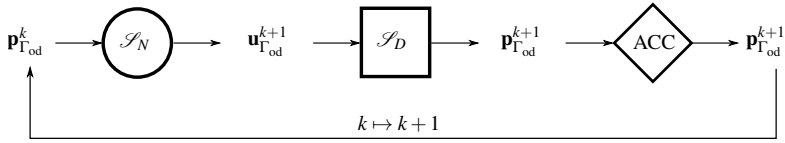

Figure 4.2: Flow chart of Gauss-Seidel strong coupling scheme described by equation 4.9.

An alternative approach is to reformulate the fixed-point equations as a Jacobi system, so that the individual outputs are fed back to each solver iteratively (see e.g. [109, 125]). Besides the advantage that the decomposition type is not restricted to a Dirichlet-Neumann partition, the flexibility to run the involved solvers in parallel may increase the efficiency. However, a better convergence rate is often obtained for the sequential approach, since the subsequent solver already receives the updated variables as input. Therefore, within this work, the Gauss-Seidel communication pattern is considered.

4.3.1 Weak Coupling and Strong Coupling

In general, there are weak and strong coupling algorithms to solve the coupled problem. The former, also known as the explicit or loose coupling approach, performs only one fixed-point iteration, while the latter iterates to fulfill the residual equation defined by equation 4.7. Therefore, it is also known as the implicit approach.
The principles of the weak and strong coupling algorithms are illustrated in Figure 4.3, exemplified for the fixed-point iteration described by equation 4.6.
For many applications, the weak coupling scheme is sufficient and is therefore applied due to its efficiency. However, it is obvious that this approach will lead to instabilities if the input variables differ significantly from the output values, as the interface residual is not converged. Some improvements may be obtained by computing an initial guess for the input variable utilizing the information from previous time steps. This approach is frequently applied for FSI problems, and extrapolation algorithms for this purpose can be found e.g., in [96, 95, 47]. However, the interface transmission conditions are still not fulfilled, which may lead to instabilities in the coupled simulation.
This inaccuracy is not present in the strong coupling approach as the fixed-point problem is solved multiple times within one time step until the interface transmission conditions are fulfilled. Hence, it converges to the same solution as the monolithic approach.
Nevertheless, instabilities can still occur in the strong coupling scheme as the black-box solvers are receiving the interface data as boundary conditions without knowledge of the flexible counterpart. As a result, non-physical interface values may be present within a sub-solver and cause the subsequent solver to overshoot after mapping. This obviously has a negative effect on the convergence behavior and, in the worst case, can lead to instability of the coupled simulation. As

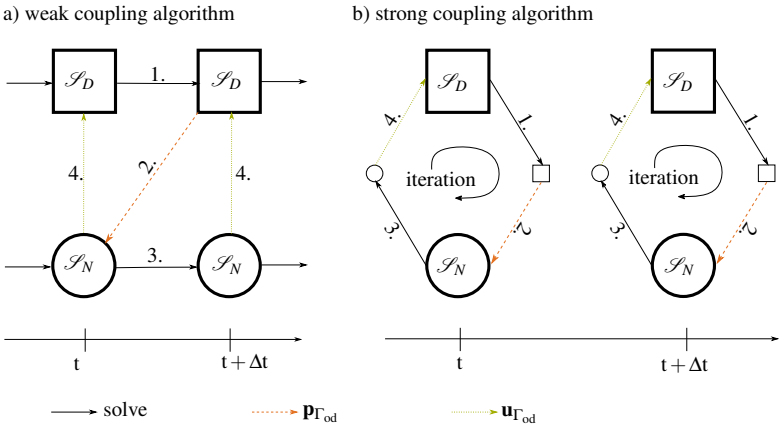

Figure 4.3: Illustration of a) the weak coupling and b) the strong coupling algorithm for the fixed-point iteration defined by equation (4.6).

a remedy, either relaxation as introduced below or a Newton-Raphson iteration (see section 4.4) can be applied to accelerate the interface convergence and increase the robustness.

4.3.2 Convergence Acceleration via Relaxation

The fixed-point iteration can be modified so that the transferred data is applied gradually. This typically allows for faster interface convergence and increased stability of the coupled simulation. Applying this scheme to the interface displacements, the relaxed values at the iteration $k+1$ are obtained by

$$\mathbf{u}_{\Gamma_{od}}^{k+1} = \mathbf{u}_{\Gamma_{od}}^{k} + \alpha^k \mathbf{r}_u^k = \alpha^k \mathbf{u}_{\Gamma_{od}}^{k+1} + (1-\alpha^k)\mathbf{u}_{\Gamma_{od}}^{k} \tag{4.11}$$

where α^k is the relaxation parameter at iteration k. Similarly, the relaxation for the traction forces is obtained by

$$\mathbf{p}_{\Gamma_{od}}^{k+1} = \mathbf{p}_{\Gamma_{od}}^{k} + \alpha^k \mathbf{r}_p^k = \alpha^k \mathbf{p}_{\Gamma_{od}}^{k+1} + (1-\alpha^k)\mathbf{p}_{\Gamma_{od}}^{k}. \tag{4.12}$$

For some exceptional cases, a constant user-defined relaxation factor can be chosen or pre-computed [109]. In general, however, the Aitken method [1] is utilized as it optimizes the scaling factor in each iteration with respect to the current residual $\mathbf{r}^k$ and the previous residual $\mathbf{r}^{k-1}$ by

$$\alpha^k(\mathbf{r}) = -\alpha^{k-1}\frac{\mathbf{r}^{k-1}\cdot(\mathbf{r}^k - \mathbf{r}^{k-1})}{\|\mathbf{r}^k - \mathbf{r}^{k-1}\|^2}. \tag{4.13}$$

Therefore, a user-defined relaxation factor is applied only in the first iteration, otherwise it is dynamically calculated as proposed by [78].

For the relaxation of the displacement by equation 4.11, the residual equation 4.8 is used to compute the relaxation parameter, while for the relaxation of the traction by equation 4.12, the residual equation 4.10 is utilized.
In this thesis, either the Aitken scheme is applied, which is derived from the fixed-point iteration and relaxes the input variables for the subsequent interface iteration loop. Alternatively, convergence accelerators based on the Newton-Raphson iteration are applied. They are introduced in the following section and can alternatively be applied to the coupling scheme to modify the input values for the subsequent iteration loop.

4.4 Newton-Raphson Iteration

As an alternative to the fixed-point iterations, commonly enhanced by a relaxation scheme, a Newton-Raphson iteration can be utilized to accelerate the solution of the strong coupled partitioned system. Formulating the iteration in a Gauss-Seidel way, the equation can be written as

$$\frac{\mathrm{d}\mathbf{r}_u^k}{\mathrm{d}\mathbf{u}_{\Gamma_{\mathrm{od}}}} \Delta\mathbf{u}_{\Gamma_{\mathrm{od}}}^k = -\mathbf{r}_u^k \qquad \text{with} \quad \frac{\mathrm{d}\mathbf{r}_u^k}{\mathrm{d}\mathbf{u}_{\Gamma_{\mathrm{od}}}} = \frac{\mathrm{d}\mathscr{S}_N}{\mathrm{d}\mathbf{p}_{\Gamma_{\mathrm{od}}}} \frac{\mathrm{d}\mathscr{S}_D}{\mathrm{d}\mathbf{u}_{\Gamma_{\mathrm{od}}}} - \mathbf{I} \tag{4.14}$$

while $\mathbf{r}_u^k$ is defined by equation 4.8. Alternatively, it can be formulated by

$$\frac{\mathrm{d}\mathbf{r}_p^k}{\mathrm{d}\mathbf{p}_{\Gamma_{\mathrm{od}}}} \Delta\mathbf{p}_{\Gamma_{\mathrm{od}}}^k = -\mathbf{r}_p^k \qquad \text{with} \quad \frac{\mathrm{d}\mathbf{r}_p^k}{\mathrm{d}\mathbf{p}_{\Gamma_{\mathrm{od}}}} = \frac{\mathrm{d}\mathscr{S}_D}{\mathrm{d}\mathbf{u}_{\Gamma_{\mathrm{od}}}} \frac{\mathrm{d}\mathscr{S}_N}{\mathrm{d}\mathbf{p}_{\Gamma_{\mathrm{od}}}} - \mathbf{I} \tag{4.15}$$

with $\mathbf{r}_p^k$ defined by equation 4.10.
Similar to the fixed-point iteration, the Newton-Raphson iteration may also be formulated in a Jacobi way, which is presented e.g., in [131, 109] however, not considered herein.
The crucial part for this iteration scheme is the determination of the black-box solver derivatives with respect to the interface variables, which are the Jacobian matrices of the subsystems and their inverse. Usually, this information is not available at the interface level.
Instead, most commonly quasi-Newton schemes are applied, which approximate the interface Jacobian or its inverse using the results of multiple iteration loops. Among these, particularly the Interface Quasi-Newton with Interface Jacobian Least-Squares approximation (IQN-ILS) [46] and the Multi-Vector Quasi-Newton (MVQN) method [19] are considered within this work.
Hence, with these approximations, equations 4.14 and 4.15 can be solved for the increments $\Delta\mathbf{p}_{\Gamma_{\mathrm{od}}}^k$ and $\Delta\mathbf{u}_{\Gamma_{\mathrm{od}}}^k$ to update the interface variables

$$\mathbf{u}_{\Gamma_{\mathrm{od}}}^{k+1} = \mathbf{u}_{\Gamma_{\mathrm{od}}}^k + \Delta\mathbf{u}_{\Gamma_{\mathrm{od}}}^k \qquad \text{and} \qquad \mathbf{p}_{\Gamma_{\mathrm{od}}}^{k+1} = \mathbf{p}_{\Gamma_{\mathrm{od}}}^k + \Delta\mathbf{p}_{\Gamma_{\mathrm{od}}}^k, \tag{4.16}$$

respectively.
Therefore, the quasi-Newton schemes also modify the displacements $\mathbf{u}_{\Gamma_{\mathrm{od}}}^{k+1}$ and the traction field $\mathbf{p}_{\Gamma_{\mathrm{od}}}^{k+1}$ obtained by the solvers $\mathscr{S}_{\mathrm{N}}$ and $\mathscr{S}_{\mathrm{D}}$, resulting in updated

input values for the subsequent iteration loop. Hence, they are an alternative way to accelerate the interface convergence and thus belong to the group of convergence accelerators, which are generally abbreviated by the operator ACC in this work.

4.5 Mapping

For the numerical solution of the partitioned problem, the involved subsystems are discretized individually, resulting in discrete displacements $\hat{\mathbf{u}}_\mathrm{o}$, $\hat{\mathbf{u}}_\mathrm{d}$ at the respective interfaces. Therefore, the kinematic constraint defined by equation 4.4 can be rewritten in the discrete form as

$$\hat{\mathbf{u}}_\mathrm{d} = \mathbf{H}_\mathrm{do}\hat{\mathbf{u}}_\mathrm{o} \tag{4.17}$$

introducing the direct mapping matrix $\mathbf{H}_\mathrm{do}$ that arises from the applied mapping technique [44, 131]. This approach assumes that the discrete displacements at the shared interface of the origin (indicated with subscript o) are mapped to the corresponding interface nodes at the destination (indicated with subscript d). Within the scope of this thesis, either

- the *nearest neighbor mapper*,
  As exemplified in Figure 4.4a), the concept of this mapper is very simple. Each node of the destination interface searches for its geometrically closest neighbor on the original interface. Once these relationships are established, the destination nodes are assigned the values of the original nodes. Therefore, the mapping matrix becomes a Boolean matrix with a single one in each row. Due to its efficiency, it is often applied. However, especially for non-matching discretization with varying coarseness at both partitions, oscillations may occur.

- the *nearest element mapper*,
  As illustrated in Figure 4.4b), each node of the destination interface is projected orthogonally to the closest element at the interface of the origin. The origin values are then interpolated using the shape function values and are assigned to the destination nodes. Therefore, this approach is more suitable for non-matching discretization, however, it requires the definition of elements between the interface nodes of the origin, which is not the case for MPM.

- or the *barycentric mapper*
  This approach is very similar to the nearest element mapper, however, it does not require the definition of elements at the interface of the origin. Instead, the two or three closest nodes in 2D and 3D, respectively, are selected, and then the original values are interpolated between them by constructing shape functions between these closest nodes, as illustrated in Figure 4.4c). Therefore, this mapping approach is very useful, especially for sub-solver discretizations where the interface nodes are not connected by elements as in MPM.

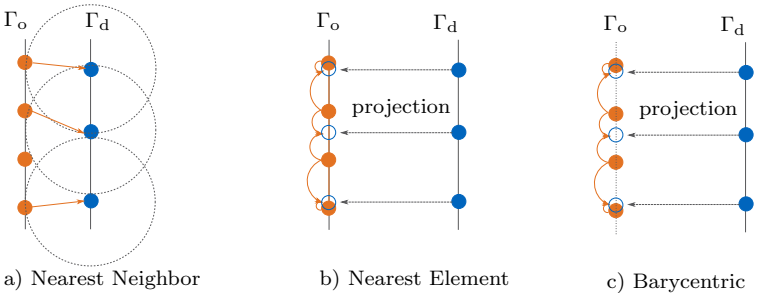

Figure 4.4: Illustration of a) the nearest neighbor, b) the nearest element, and c) the barycentric mapping concept.

are utilized, belonging to the group of interpolation-based mapping algorithms. As a consequence of the discretization, the traction forces $\mathbf{p}_o$ and $\mathbf{p}_d$ within the partitions result in discrete forces $\mathbf{F}_o$ and $\mathbf{F}_d$ at the interface nodes, representing the distributed traction forces at discrete locations.
Similar to the displacement mapping matrix, a separate direct mapping matrix can be constructed to map the forces between the sub-solver discretizations, resulting in a consistent mapping approach.
Alternatively, a conservative mapping matrix can be derived from the continuum interface energy conservation equation defined by

$$\int_{\Gamma_{od}} \mathbf{u}_o(\mathbf{x})\mathbf{p}_o(\mathbf{x})\mathrm{d}\Gamma_{od} = \int_{\Gamma_{od}} \mathbf{u}_d(\mathbf{x})\mathbf{p}_d(\mathbf{x})\mathrm{d}\Gamma_{od}. \tag{4.18}$$

Reformulating this equation in the discrete form

$$\hat{\mathbf{u}}_d^T\mathbf{F}_d = \hat{\mathbf{u}}_o^T\mathbf{F}_o \tag{4.19}$$

and inserting equation 4.17 finally results in

$$\mathbf{F}_o = \mathbf{H}_{do}^T\mathbf{F}_d \tag{4.20}$$

using the transposed displacement mapping matrix to map the forces. This approach is called conservative mapping [49, 44] and has the great benefit that the mapping matrix needs to be constructed only once, while the transpose can be reused to map the forces.

4.6 Conclusions

As presented in this chapter, one of the significant advantages of the partitioned approach lies in treating the involved solvers as black-box solvers, while the interaction is shifted to their shared interface. This allows the reuse of well-established solvers and tools that have been developed over many years to solve various

physical problems. Additionally, it offers flexibility by allowing the coupling of different numerical methods to solve the respective problems. For a more detailed discussion of partitioned coupling approaches see e.g. [31, 125, 50, 131, 55].
Within this work the partitioned approach is applied to couple the particle methods DEM and MPM, which is detailed in chapter 5, and to couple MPM with FEM, which is detailed in chapter 6. These different numerical methods are combined to solve the complex interaction of gravity-driven mass flows with different kinds of protective structures.

CHAPTER 5

MPM-DEM Coupling

To stabilize slopes, particularly along roads or nearby buildings, retaining walls are often installed. These walls commonly consist of stacked massive blocks and are designed to resist the lateral pressure of soil or rock. In the numerical simulation, these blocks can usually be approximated as rigid bodies. However, for more detailed simulations, the failure process needs to be taken into account. Therefore, DEM, which allows to carefully consider the contact conditions among the blocks is the best-suited numerical method to model these blocks and their interaction.

However, to model the mechanical behavior of the flowing masses, a continuum-based approach is more appropriate and computationally efficient. Therefore, MPM is the preferred numerical method to discretize this physical event due to its ability to handle large strains in gravity-driven flows.

To capture the interaction of the gravity-driven mass flows and protective structures consisting of stacked massive blocks, the partitioned coupling scheme, introduced in general in chapter 4, is adapted for MPM and DEM. This allows to exploit the advantages of both methods and to perform complex numerical simulations of flowing masses interacting with discrete blocks. Moreover, due to the partitioning, the best-suited solution strategies can be selected for each subproblem without the necessity to develop individual coupling strategies, which makes it very attractive compared to the monolithic coupling schemes of MPM and DEM, just mentioning [86, 71, 3].

In this chapter, the partitioned coupling scheme of MPM and DEM is introduced and several examples of increasing complexity are presented to verify the approach and to compare the numerical solutions with experimental results from the literature. Main parts of this chapter were published by the author in [115], while the content is discussed below in the context of this thesis. Furthermore, parts of the final example were published by the author in [116]. Some of the following text passages are directly taken from these publications and therefore are to be interpreted as quotations.

5.1 MPM-DEM Coupling Scheme

In the partitioned coupling scheme, the sub-solvers MPM and DEM are treated as black-box solvers, while the interaction is shifted to their shared interface. Adapting the notation introduced in chapter 4, all quantities related to the MPM solver are denoted from hereon with subscript M (instead of o in chapter 4), while for the DEM partition the subscript P (instead of d in chapter 4) is utilized. Hence, the shared interface between the MPM domain Ω_M and the DEM domain Ω_P is defined by

$$\Gamma_\mathrm{MP} = \Gamma_\mathrm{M} \cap \Gamma_\mathrm{P}, \tag{5.1}$$

while within each partition, a boundary is introduced along this interface to ensure the communication among them.
As mentioned before, the main advantage of DEM is the accurate calculation of contact forces. Therefore, it is the natural choice to define a Dirichlet condition within the DEM partition to take advantage of this. Hence, a wall condition, originally proposed by [99] for partitioned coupling with FEM, is introduced within the DEM domain. In the discretized model, the geometry of this wall condition is represented similarly to an FE-mesh, comprising vertices, edges and faces in 3D. This wall condition, which represents the shared interface in the DEM partition, needs to represent the characteristics of the coupled counterpart. Furthermore, the spatial position and its velocity need to be updated according to the kinematics of the coupled counterpart.
Based on this, contact forces can be calculated between the spherical particles themselves as well as between the particles and geometric entities of the wall condition. Within the scope of this work, the HM+D contact model introduced in section 2.10 is applied to calculate these forces, whereas the Double Hierarchy Method [100] is used to efficiently detect the contacts.
Therefore, the DEM back-box solver requires the interface displacement and velocity as input, which are provided by the coupled counterpart. Hence, in the discretized model, the nodal displacement $\hat{\mathbf{u}}_\mathrm{P}$ and nodal velocity $\hat{\dot{\mathbf{u}}}_\mathrm{P}$ of the discretized wall condition Γ_P^h are prescribed values and serve as input for the subsequent solution of the DEM partition. In case of contact between a DEM particle i and the discretized wall condition, a resulting contact force $\mathbf{F}_{i,\mathrm{Contact}}$ is calculated at the DEM particle i. The associated reaction force at the wall condition is interpolated by linear shape functions to the corresponding nodes of the wall condition entity, resulting in discrete forces $\mathbf{F}_\mathrm{P}$ after completing one time step of the DEM calculation. Further details of the DEM solution scheme are provided in section 2.10.
Consequently, the DEM black-box solver with the Dirichlet interface $\mathscr{S}_\mathrm{D} \hat{=} \mathscr{S}_\mathrm{DEM}$ can be expressed as

$$\mathbf{F}_\mathrm{P} = \mathscr{S}_\mathrm{DEM}(\hat{\mathbf{u}}_\mathrm{P}, \hat{\dot{\mathbf{u}}}_\mathrm{P}) \tag{5.2}$$

representing the discrete subproblem.
In the MPM counterpart, a Neumann condition is introduced along the shared interface, which allows to solve the partitioned problem sequentially with a fixed-point iteration as introduced in section 4.3. This boundary Γ_M^h is discretized by boundary particles that can receive external point loads $\mathbf{F}_\mathrm{M}$. These mass-less

particles apply the external point loads to the MPM partition and their kinematics are updated analogously to the material points. Hence, they track the spatial position of the shared interface and carry the displacement and velocity information, $\hat{\mathbf{u}}_\mathrm{M}$ and $\hat{\dot{\mathbf{u}}}_\mathrm{M}$, at the boundary particle location.
Therefore, the expression for the MPM black-box solver with the Neumann interface $\mathscr{S}_\mathrm{N} \hat{=} \mathscr{S}_\mathrm{MPM}$ can be written as

$$\left\langle \hat{\mathbf{u}}_\mathrm{M}, \hat{\dot{\mathbf{u}}}_\mathrm{M} \right\rangle = \mathscr{S}_\mathrm{MPM}(\mathbf{F}_\mathrm{M}) \tag{5.3}$$

in the discrete form.
Consequently, to solve the multi-physics problem with the partitioned approach, the DEM and the MPM model are discretized separately. Within each model, the respective boundary conditions along the shared interface need to be defined. Typically, the spatial position of this interface is initialized along the contour of the MPM body and then follows its motion. In addition, it is advantageous to initialize the boundary particles in the MPM model at the same spatial positions as the nodes of the discretized DEM wall in order to avoid errors due to data mapping at the interface.
The non-linear interface equations, which arise due to the partitioning, are solved by a fixed-point iteration that sequentially executes the solvers, as introduced in section 4.3. Furthermore, a weak coupling scheme, as illustrated in Figure 4.3a), is applied. Due to the explicit time integration used to solve the DEM model and the resulting small time step size for the overall problem, the weak coupling scheme is sufficient for the considered problems and is therefore used for its efficiency.
Hence, the partitioned weak MPM-DEM coupling scheme, which is summarized by Algorithm 1 and illustrated in Figure 5.1, works as follows:

Algorithm 1 Weak MPM-DEM Coupling Scheme

while time < t_end **do**

(1).	DEM Solver: $\mathbf{F}_\mathrm{P} = \mathscr{S}_\mathrm{DEM}(\hat{\mathbf{u}}_\mathrm{P}, \hat{\dot{\mathbf{u}}}_\mathrm{P})$	▷ (equation 5.2)
(2).	Mapper: $\mathbf{F}_\mathrm{M} = \mathbf{H}_\mathrm{PM}^T \mathbf{F}_\mathrm{P}$	▷ (equation 5.4)
(3).	MPM Solver: $\left\langle \hat{\mathbf{u}}_\mathrm{M}, \hat{\dot{\mathbf{u}}}_\mathrm{M} \right\rangle = \mathscr{S}_\mathrm{MPM}(\mathbf{F}_\mathrm{M})$	▷ (equation 5.3)
(4).	Mapper: $\hat{\mathbf{u}}_\mathrm{P} = \mathbf{H}_\mathrm{PS} \hat{\mathbf{u}}_\mathrm{M}$ and $\hat{\dot{\mathbf{u}}}_\mathrm{P} = \mathbf{H}_\mathrm{PM} \hat{\dot{\mathbf{u}}}_\mathrm{M}$	▷ (equation 5.5)

First, the DEM partition is solved with given displacements $\hat{\mathbf{u}}_\mathrm{P}$ and velocities $\hat{\dot{\mathbf{u}}}_\mathrm{P}$ at the nodes of the discretized wall condition, possibly leading to some contact between the DEM particles and the wall condition. The resulting contact forces at Γ_P^h are then transferred to the interface of the MPM partition as external forces $\mathbf{F}_\mathrm{M}$.
For this transfer process, a mapping technique as introduced in 4.5 is needed to map the data between the sub-solvers. For the forces, the conservative mapping approach (see equation 4.20) is utilized resulting in

$$\mathbf{F}_\mathrm{M} = \mathbf{H}_\mathrm{PM}^T \mathbf{F}_\mathrm{P} \tag{5.4}$$

and thus reuse the transpose of the direct mapping matrix $\mathbf{H}_\mathrm{PM}$. This matrix is defined by the mapping process of the nodal displacement and velocity values

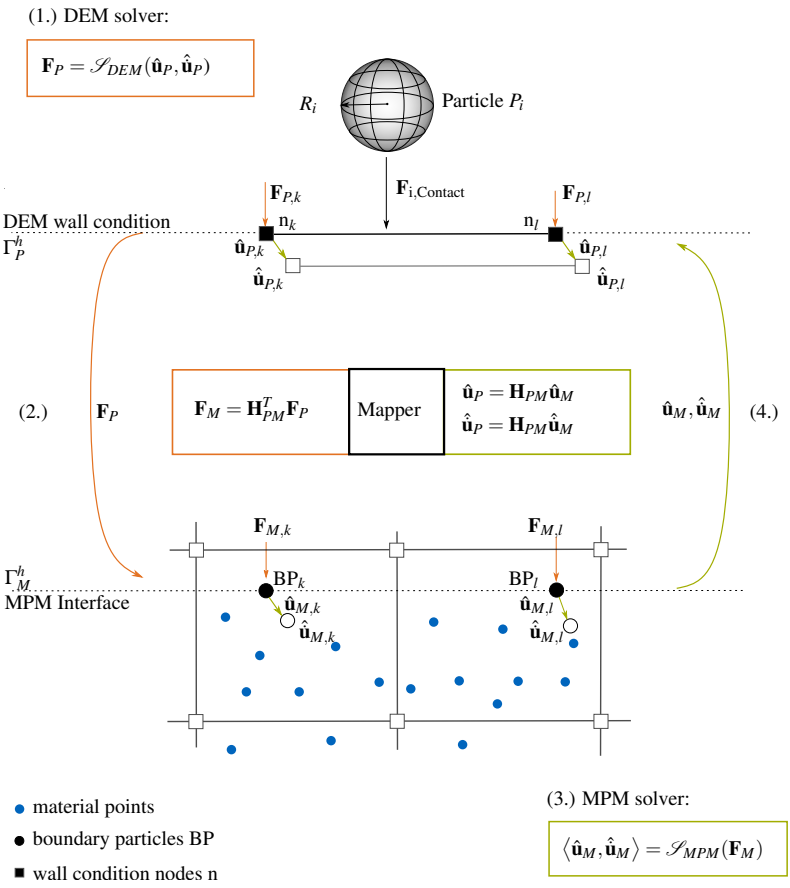

Figure 5.1: Partitioned MPM-DEM coupling scheme: In each time step, DEM is solved first (1). The resulting forces are mapped to MPM as external forces (2). Then MPM is solved leading to a kinematic update of the MPM interface (3), which is mapped back to DEM interface (4). Due to weak coupling, the steps are repeated for the next time steps. Adapted from [115].

from the MPM to the DEM partition by

$$\hat{\mathbf{u}}_\mathrm{P} = \mathbf{H}_\mathrm{PM} \hat{\mathbf{u}}_\mathrm{M}, \qquad \hat{\dot{\mathbf{u}}}_\mathrm{P} = \mathbf{H}_\mathrm{PM} \hat{\dot{\mathbf{u}}}_\mathrm{M} \tag{5.5}$$

according to equation 4.17.
Herein, the nearest neighbor interpolation technique [44] is used for the data transfer between the interfaces, resulting in a copy operation in most of the cases.

This is because the boundary particles are usually located at the same spatial positions as the nodes of the discretized wall condition in DEM to reduce errors arising from the mapping.
Due to the mapping process described by equation 5.4, the boundary particles in the MPM model that discretize the shared interface receive the contact forces from the DEM solver as external point loads $\mathbf{F}_{\mathrm{M}}$. Hence, within the MPM calculation, these boundary particles are treated as non-conforming Neumann conditions, as described in section 3.4.2. Thus, the solution of the MPM partition, taking into account the applied forces, leads to a kinematic update at the nodes of the computational background grid (see section 3.3). Therefore, in the convective phase of the MPM calculation procedure, the boundary particles are updated analogously to the material points, resulting in boundary particle displacements $\hat{\mathbf{u}}_{\mathrm{M}}$ and velocities $\hat{\dot{\mathbf{u}}}_{\mathrm{M}}$.
Finally, this kinematic update is mapped by equation 5.5 to the DEM partition, updating the nodal displacements $\hat{\mathbf{u}}_{\mathrm{P}}$ and velocities $\hat{\dot{\mathbf{u}}}_{\mathrm{P}}$ of the DEM wall condition.
Applying a weak coupling scheme, the DEM solver advances in time and solves the DEM model with the updated wall condition. These steps are repeated within each time step until the end of the simulation t_{end}.

It is important to note that a DEM particle i calculates one resulting contact force $\mathbf{F}_{i,\mathrm{Contact}}$, depending on the shortest distance between the interacting object and the center of the particle. This can lead to difficulties during the coupled simulation, especially when considering solid or granular material in the MPM partition that interacts with obstacles that are relatively large compared to the background grid element size.
As illustrated in Figure 5.2a) the DEM particle i calculates a single contact force $\mathbf{F}_{i,\mathrm{Contact}}$ with the wall condition in each time step. This consequently results in forces $\mathbf{F}_{\mathrm{P}}$ at the corresponding nodes of the discretized wall condition.
Assuming a two-dimensional case and a DEM particle interacting with a line segment as depicted in Figure 5.2a), this results in two forces at the corresponding nodes of this segment. Mapping these forces to the MPM partition results in point loads at the boundary particles. Since a matching discretization of the interface is usually used, this results in two point loads in this case.
Depending on the location of the boundary particles within the background grid and the element size of this grid, only a certain area of the MPM domain is affected by the interface forces in each time step. As a result, this could lead to an insufficient representation of the shared interface. This is especially true for granular materials modeled with MPM that interact with relatively larger DEM particles compared to the background grid element size of the MPM model. Due to the singular forces applied to the MPM model within each time step, the granular material can penetrate into the DEM particle and thus negatively affect the results of the coupled simulation.
To resolve this issue, clustering of DEM particles [75] can be applied. Besides the advantage that arbitrarily shaped obstacles can be modeled efficiently by clustering DEM particles, each DEM particle within the cluster can calculate a contact force. This leads to a more accurate representation of the interface as depicted in Figure 5.2b). Therefore, the clustering method should be applied when the

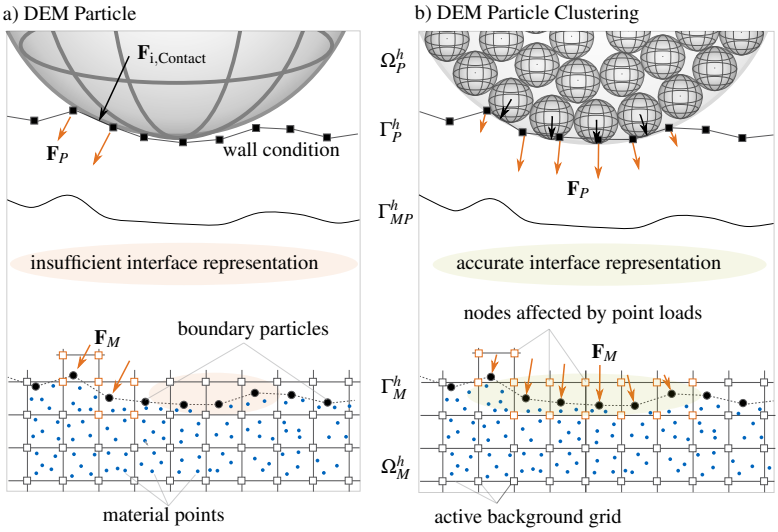

Figure 5.2: Calculation of contact forces in DEM and influence of the MPM partition. a) One DEM particle calculates one resulting contact force, affecting only a limited number of background grid nodes in the MPM partition. b) By clustering the DEM particles, also suited for arbitrarily shaped particles, the contact forces are distributed over the interface, leading to an accurate interface representation. Adapted from [115].

particle shape is to be accurately considered and/or a detailed interface representation is required in the MPM model.
In the following chapter, several examples for the partitioned coupling of MPM and DEM are presented, validating the novel approach and demonstrating the broad application range.

5.2 Verification and Validation

A series of tests is conducted to demonstrate the application of the proposed partitioned MPM-DEM coupling scheme and its accuracy. First of all, the results are compared to an example with an analytical solution from the literature for two- and three-dimensional problems. An extension of the first example to a more challenging impact scenario can be found in [115]*. In addition, the application of the proposed scheme to soil-particle interaction is demonstrated by comparing the numerical solution to experimental data from the literature. The first example considers a granular flow, which after release flows down due to gravity

* published by the author of this dissertation

	Young's modulus	Poisson's ratio	density
beam/particle	215.82GPa	0.289	7960kg/m^3

Table 5.1: Material properties of the hinged beam and the spherical particle.

and then impacts on stacked wooden obstacles. In the second system, the failure of a retaining wall due to soil pressure is modeled and compared to experimental results.

5.2.1 Particle Impact on Simply Supported Beam

For the validation of the proposed algorithm, an academic particle-structure interaction example is chosen, which was first proposed by Timoshenko [124] in 1951, reviewed in detail by Meijaard [89] and performed as a benchmark test for partitioned coupling of FEM and DEM in [99, 101]. It consists of a simply supported beam with a total length of 15.35cm and a square cross-section of $1 \times 1\text{cm}^2$. This elastic beam, modeled with MPM, is impacted at its center by a sphere, which in turn is modeled with a discrete DEM particle. The system setup is visualized in Figure 5.3, while the material parameters taken from [89] are summarized in Table 5.1.

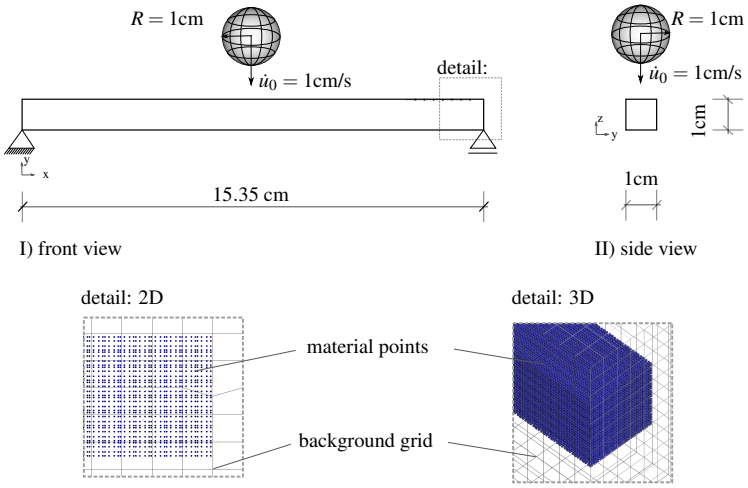

Figure 5.3: Single spanned beam hit at its center by a sphere. Adapted from [115].

The benchmark test is performed for both 2D and 3D models. As visualized in the details in Figure 5.3, a quadrilateral background grid is chosen for the 2D MPM model, while a structured hexahedral mesh is considered in 3D. In [115] a detailed description of the background grid size as well as the material point initialization for both models can be found.

For the contact force calculation in the DEM model the HM+D contact law is assumed with a coefficient of restitution of 1.0, according to [99, 101]. For the interaction of MPM and DEM a zero friction coefficient is assumed and a time step of $\Delta t = 5e{-}8$s is selected for the computation.
During the calculation, the displacement of the sphere and the deformation of the beam center are measured and visualized in Figure 5.4 in comparison to the

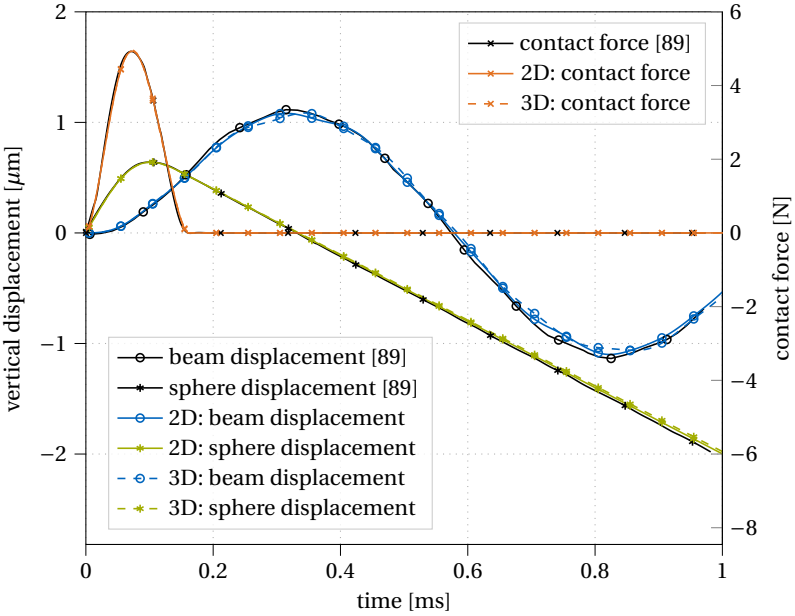

Figure 5.4: Single spanned beam hit laterally at its center by a sphere. Numerical results for 2D and 3D models in comparison to reference solution [89].

reference solution obtained by [89] showing excellent agreement. Due to the chosen geometry, a single impact between the beam and the sphere is observed, resulting in an oscillation of the beam which corresponds to its natural frequency. Furthermore, the resulting contact force is plotted against the reference solution in Figure 5.4, confirming the accuracy of the proposed coupling scheme.

5.2.2 Granular Flow Impacting DEM Obstacles

The second example considers the interaction of significant strain flow events with obstacles. For this purpose, the experiment of granular material impacting wooden blocks, which was initially conducted by [86], is simulated and the ob-

tained results are compared with the available data from the literature at specific time steps.
The initial configuration of the two-dimensional model representing the experiment is depicted in Figure 5.5. It consists of the granular material, which is ini-

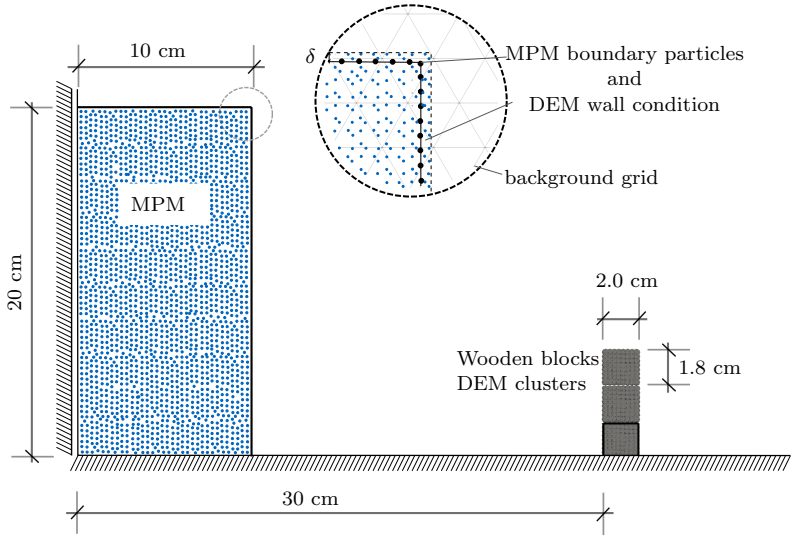

Figure 5.5: Granular material calculated with MPM impacting wooden blocks modeled with DEM cluster. Adapted from [115].

tially confined to a region of $10 \times 20 \times 20\text{cm}^3$ and, after being released, flows down due to gravity. Additionally, three identical wooden blocks are considered, which are placed on top of each other at a distance of 30cm from the granular material. The block on the bottom is glued to the desk to simulate a foundation of a building. Due to gravity, the granular flow impacts these wooden blocks, pushing the upper two wooden particles to the right side, resulting in an angular velocity, whereas the block on the bottom remains fixed.
In the numerical model, the bottom wall of the box containing the material is modeled as a fixed boundary, while a slip condition is assumed for the vertical wall. The granular flow is simulated by MPM using the Mohr-Coulomb plane strain material law with the respective material parameters summarized in Table 5.2, which are taken from [86].
For the discretization of the MPM model, an unstructured triangular background grid with an element size of 0.5cm is chosen. Meanwhile, for the initialization of the material points, a body mesh of structured triangles with half the element size, containing three particles each, is selected. As the granular material undergoes large deformations, boundary particles are placed at a distance of 0.005cm around the initial configuration of the granular material to ensure a suitable discretization of the shared interface throughout the simulation. However, for this

material properties	granular material (MPM)	wooden blocks (DEM)
density	1300 kg/m^3	500 kg/m^3
Young's modulus	50 kPa	50 MPa
Poisson's ratio	0.4	0.5
cohesion	0 Pa	0 Pa
friction angle	22 °	-
dilation angle	0 °	-
restitution coeff.	-	0.05

Table 5.2: Material properties for the granular flow and the wooden blocks

example, these boundary particles are not placed exactly at the outline of the body, but are shifted marginally inside the body to avoid numerical instabilities during the calculation.
Considering gravity-driven granular material, this modification is necessary as the boundary particles receive the resulting contact forces from the DEM partition and apply them to the MPM model as point loads. If these point loads are applied to elements containing only a few single material points - which is a general case at the body outline - this could lead to an non-physical behavior of these elements and therefore to large movements of the material points within these elements. Therefore, to ensure that the forces are applied to the main material flow, the boundary particles are defined within the first row of the material points. In this particular case, the marginal shift δ is one third of the body mesh size, much smaller than the size of the background elements, and therefore almost negligible for the final solution.
The wooden blocks are simulated by DEM. Each block is of size $2 \times 1.8 \times 19.8$ cm^3 and consists of 8×8 spherical particles which are compacted into a cluster to model the squared shape of the blocks. Since the bottom block is glued to the desk, it can be modeled as a fixed boundary in the simulation. Therefore, only the first and second blocks, counted from the top, are represented as DEM cluster particles. The discretization of the boundary wall follows the initialization of the boundary particles in MPM, i.e. that the nodes of the wall condition coincide with the boundary particle positions to avoid errors occurring from data mapping.

For the calculation of the contact forces within the DEM partition, a Hertzian contact law is considered. Friction and adhesion between the wooden clusters themselves are set to $\mu = 0.6$ and $c = 30$Pa, respectively. For the interaction with the rigid boundary, $\mu = 0.3$ and $c = 60$Pa are assumed and a time step of $\Delta t = 5\text{e}{-5}$s is considered for the simulation.
The numerical results obtained with the partitioned MPM-DEM coupling strategy are presented in Figure 5.6 compared to the experimental results published by [86]. The visual comparison with the experimental results at the specific times shows that the numerical model can replicate the experimental results very well.

Similar to the experiment, the granular flow reaches the wooden blocks at $t = 0.25$s. Due to the impact, the DEM clusters start moving and rotating around the fixed block at the bottom. Comparing the results at time $t = 0.30$s, one can observe that the two cluster blocks are still in touch over the full width of the block, which

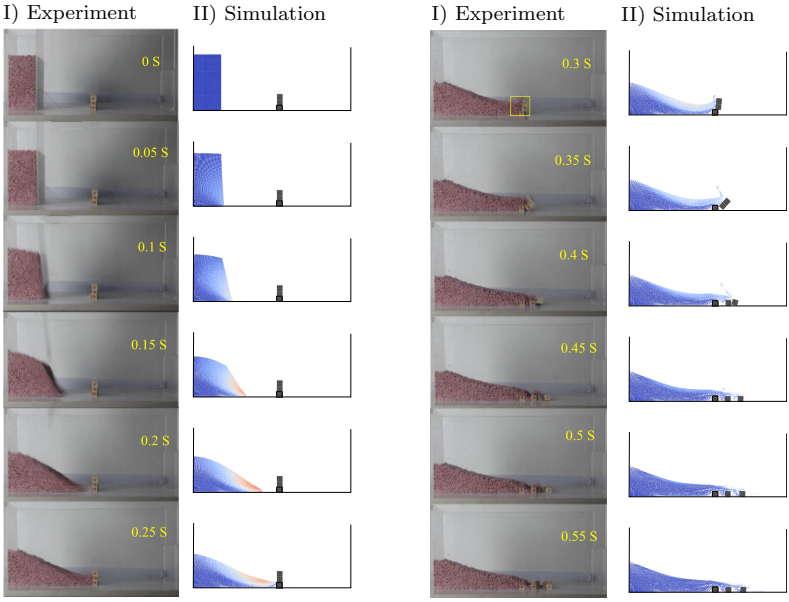

Figure 5.6: Granular material calculated with MPM impacting wooden blocks modelled with DEM cluster. Comparison of the experimental results [86] and the obtained numerical solution. Adapted from [115].

agrees well with the experiment. This is an improvement compared to the numerical results obtained by [71], as the adhesion between the DEM blocks can be considered by the implemented Hertzian contact law within the DEM application.

The second block first touches the ground between $t = 0.36$s and $t = 0.37$s with one edge and subsequently rotates until the complete outer edge is in touch with the ground at $t = 0.40$s, which corresponds to a rotation of 90° in total. Figure 5.7 shows the rotation angle of the second block in comparison to the experiment and the results from the literature [86, 71]. The obtained solution is in good agreement for the entire simulation time.

Block number one, the top block, starts to move and rotate together with the second block and touches the ground for the first time between $t = 0.38$s and $t = 0.39$s with its corner. This impact causes its detachment from the ground and its rotation around its axis, which coincides with the picture of the experiment at $t = 0.40$s and finally comes to rest with a total rotation of 180° at about $t = 0.45$s. Finally, comparing the runout configuration of the simulation with the experiment, the resting distance of the two moving blocks can be measured. In the experiment [86], the distance between the left boundary of the second block and the left boundary of the box was measured to be 34.6cm, whereas in this simu-

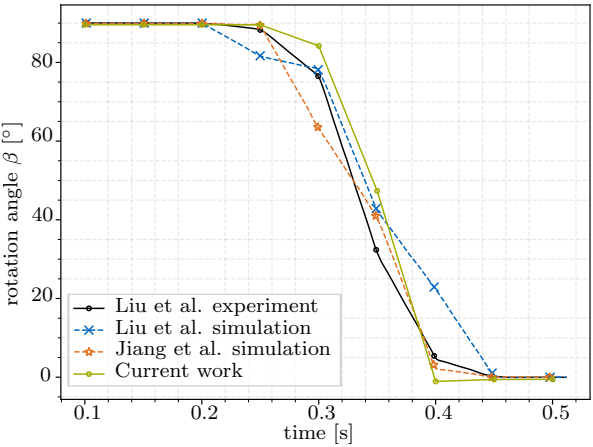

Figure 5.7: Rotation angle of the second block compared to the experiment [86] and the numerical solutions of Liu et al. [86] and Jiang et al. [71]. Adapted from [115].

lation the distance turned out to be 34.5cm. Likewise for the top block, where the distance in the experiment was measured at 40.1cm compared to 39.7cm in the simulation, which is in very good agreement. In order to achieve even higher accuracy of the results, the calculation parameters, especially within the DEM application, have to be calibrated for the respective experiment.

Additionally, to prevent the penetration of material points into the DEM particles at the very end of the simulation, a finer discretization of the interface as well as a smaller size of the background grid elements in MPM could be chosen. Apart from that, the numerical solution agrees very well with the experimental results, proving the applicability of the proposed partitioned MPM-DEM coupling scheme for large strain flow events interacting with discrete obstacles.

5.2.3 Retaining Wall Collapse

In the final case study, the proposed MPM-DEM coupling strategy is applied to simulate large deformation and post-failure behavior of soil and retaining wall blocks. The numerical solution of a two-dimensional simulation is compared to the experimental results conducted by Bui et al. [32]. Within the experiment, Aluminum bars with a length of 5cm were used as the model ground to simulate the two-dimensional conditions.

The segmental retaining wall within this study consists of six identical Aluminum blocks, which are stacked on top of each other with an overlap of 1.2cm, as depicted in Figure 5.8. These rectangular blocks have a width of 3.2cm, a height of 2.5cm and a length of 5.0cm. The material properties of the blocks, as well as those of the model ground taken from [32], are summarized in Table 5.3.

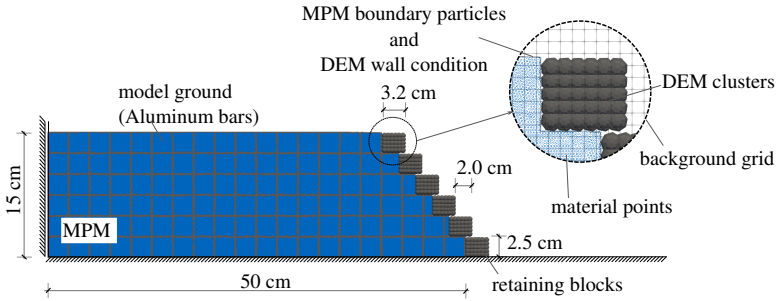

Figure 5.8: Initial system of the retaining wall. The wall blocks are discretized by DEM cluster particles, whereas the model ground is discretized by MPM. Adapted from [116].

material properties	model ground (MPM)	retaining wall blocks (DEM)
specific weight	20.4 kN/m^3	25.5 kN/m^3
Young's modulus	5.84 MPa	69 GPa
Poisson's ratio	0.3	0.3
cohesion	0 Pa	0 Pa
friction angle	21.9 °	-
dilation angle	0 °	-
restitution coeff.	-	0.316

Table 5.3: Material properties for the model ground and the retaining wall blocks

Furthermore, the static friction coefficients between the wall blocks $\mu_{b-b} \approx 0.31$ themselves, the blocks and the bottom wall boundary $\mu_{b-w} \approx 0.40$, and between the blocks and the model ground $\mu_{b-s} \approx 0.38$ were determined experimentally by [32] and are therefore also assumed in the numerical simulation herein.
While the retaining wall blocks are modeled with DEM by clustering 6×5 spherical particles to obtain the rectangular shape, the model ground is simulated by MPM using Mohr-Coulomb plane strain material law. As boundary conditions for the model ground a fixed support is assumed at the bottom, while a slip condition is imposed in the lateral direction. Therefore, the numerical model is comparative to the SPH model created by Bui et al. [32] to numerically investigate the collapse of the retaining wall system.
For the discretization of the MPM model, a structured quadrilateral background grid with an element size of 0.4cm is selected, whereas for the initialization of the material points, an unstructured triangular body mesh with an element size of 0.1cm, containing 3 particles each, is chosen. Similar to the previous example, also in this case the model ground undergoes significant deformation. Therefore, the boundary particles are placed at a distance of 0.01cm at the top and right contour of the Aluminum bar collection. Once again, a marginal shift of the interface inside the body of $\delta = 0.05$cm is assumed. Analogous to the previous example, this shift is very small compared to the background grid element size,

but it increases the numerical stability of the partitioned coupling scheme. The simulation is performed with a time step of $\Delta t = 2e-5$s.
Figure 5.9 shows the comparison of the numerical and experimental results at

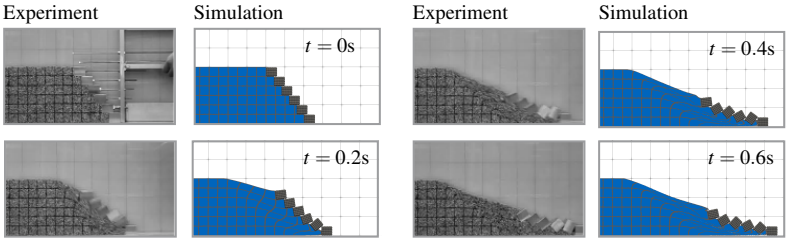

Figure 5.9: Simulation results compared to the experiment conducted by [32]. Adapted from [116].

several times for the failure process of the retaining wall block system. Due to the pressure forces of the backfilled soil, the retaining wall blocks start to move to the right, causing the collapse of the retaining wall system. While the block at the bottom only slides horizontally, triggering the failure of the system, translational and rotational motions are observed for the other blocks, which are in very good agreement with the experimental results. For further improvements, the parameters such as static and dynamic friction coefficients as well as the cohesion between the blocks need to be calibrated for the DEM cluster particles used.
In addition, the comparison of the final runout between the experimental data and the obtained numerical solution are displayed in Figure 5.10. While in the experiment the final runout of the block at the bottom was measured to be about 66.4cm, 66.9cm are obtained in this numerical study. Again, the friction coefficients, which are critical to the failure pattern of the segmental retaining wall system and the final runout, need to be calibrated for the particular experiment.
Summarizing the results, a very good agreement of the results can be observed and the application of the proposed coupling scheme for various scenarios is demonstrated. A major advantage is that the modeling of the blocks by DEM inherently allows the separation of the blocks, while a continuum-based description can still be used to model the backfilled soil. This is a great advantage especially for the numerical investigation of large-scale events.

5.3 Conclusions

The validation examples demonstrate the capability of the partitioned MPM-DEM coupling scheme to simulate the interaction between gravity-driven mass flows and structures composed of multiple massive blocks. The numerical model accurately predicts the flow process of the gravity-driven flows as well as the failure pattern and the subsequent movement of the blocks upon impact.
In contrast to monolithic coupling schemes of MPM and DEM, the partitioned approach provides the possibility to couple the physics involved in a generalized

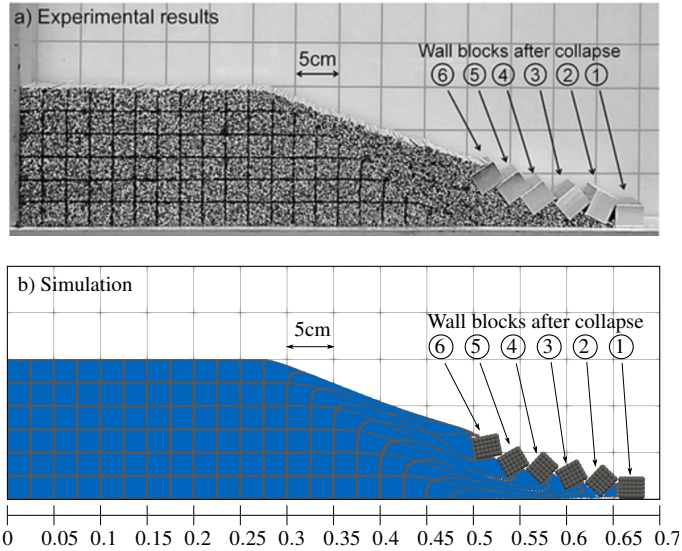

Figure 5.10: Comparison of the final failure pattern between the experiment conducted by [32] and the MPM-DEM coupling scheme.

way. Each physics involved can be solved independently in its preferred reference frame, while the interaction is transferred to the shared interface.
Along the shared interface, boundary conditions are imposed within the respective solvers. For this purpose, a wall condition is defined in the DEM partition that represents the properties of the coupled counterpart. It imposes a Dirichlet constraint on the DEM model, and its spatial position as well as its velocity are updated according to the kinematics of the coupled sub-solver.
Therefore, the DEM back-box solver calculates contact forces with the introduced wall condition, which are subsequently mapped to the MPM partition as external forces. Therefore, a Neumann condition is introduced in the MPM submodel, which is discretized by boundary particles that receive the forces from the coupled counterpart as external point load conditions. Due to the applied forces, the MPM body is deformed and the spatial position as well as the kinematics of the boundary particles are updated within the MPM calculation procedure, analogous to the material points.
This leads to a kinematic update of the shared interface, which in turn is mapped back to the DEM partition, updating the spatial position of the wall condition as well as its velocity. Therefore, the coupled problem is solved by a classical fixed-point iteration using a Gauss-Seidel communication pattern. Since small time steps are required to compute the DEM model anyway, a weak coupling scheme is used in this work, omitting the computationally expensive interface iterations. The shared interface is typically initialized at the spatial positions of the coupled MPM body contour. However, as detailed in examples 5.2.2- 5.2.3, a marginal

shift of the shared interface in the MPM body is recommended to avoid singularities when applying the forces to the MPM model. This shift ensures that the forces are applied to the main material flow, thus increasing the numerical stability of the coupled simulation.
In the DEM solver, spherical particles are used to model the discrete objects, which provides very efficient contact detection. Particle clustering is used to represent arbitrarily shaped particles (see examples 5.2.2- 5.2.3). In addition, this clustering of particles also provides a more accurate interface representation in the coupled scheme.
In conclusion, the partitioned MPM-DEM coupling scheme is a powerful method for simulating large strain flow events interacting with discrete objects. It is successfully applied to simulate the impact of gravity-driven mass flows on structures composed of multiple massive blocks. In addition, this methodology can be used to simulate rocks or other significant obstacles within a mass flow, including possible interactions of these discrete objects.
However, for the numerical simulation of highly flexible structures which are being impacted by mass flows, FEM rather than DEM should be used for the structural modeling. The partitioned coupling scheme for these discretization methods is presented in the following chapter.

CHAPTER 6

MPM-FEM Coupling

For the numerical simulation of gravity-driven mass flows impacting highly flexible protective structures, the advantages of Lagrangian FEM for modeling the complex structure need to be combined with MPM, which allows modeling of large strain events of mass flows.
Besides the monolithic coupling schemes of MPM and FEM, just mentioning [85, 84, 35, 6, 81], a partitioned coupling scheme has been introduced in [132]. In this work, a mortar mapping between non-conforming FEM and MPM meshes was developed and a FETI (Finite Element Tearing and Interconnect) based coupling scheme was applied. However, a critical component of this coupling scheme is the efficient tracking of the interface throughout the simulation. By exploiting the assumption of small interface deformations, it has been successfully applied to calculate two-dimensional solid structures which are partially modeled by MPM and FEM. However, for larger interface deformations, the mortar mapper has to be reconstructed at each time step and material points are likely to penetrate the FEM domain. Moreover, contact problems of the MPM and FEM submodels are not considered and the extension to three dimensions is still pending. Therefore, further enhancements are required to simulate the filling process of highly flexible protective structures with granular mass flows using a partitioned MPM-FEM coupling scheme.
Starting from the continuous multi-physics problem, the individual discretized numerical models are derived. Within each model, the respective boundary conditions at the shared interface need to be defined. Subsequently, the solution schemes introduced in chapter 4 are tailored to the solvers involved and coupling algorithms for weak and strong coupling are formulated accordingly.
The derived coupling algorithms are assessed and evaluated in depth in the examples in section 6.2. First, the convergence rate for the coupled problem is proved and the effect of different coupling sequences is studied. In addition, the coupling of MPM and FEM with different discretizations is discussed in an illustrative way, highlighting in particular the requirements for the interface discretization for robust coupling schemes. Within these studies, the impact of the type of boundary imposition method in the MPM partition, using either penalty augmentation, perturbed Lagrangian or Lagrange multiplier methods to weakly

impose the Dirichlet conditions, is also included.
These intensive investigations form the basis for the subsequent examples of increasing complexity. In these examples, the coupling scheme is also verified in the dynamic regime and with highly flexible structures. Then, the coupling methodology is validated with experimental results from the literature, and finally, the chapter concludes with a complex example of gravity-driven mass flow impacting a highly flexible protective structure.

6.1 MPM-FEM Coupling Scheme

As illustrated in Figure 6.1a), the continuous problem is decomposed into the

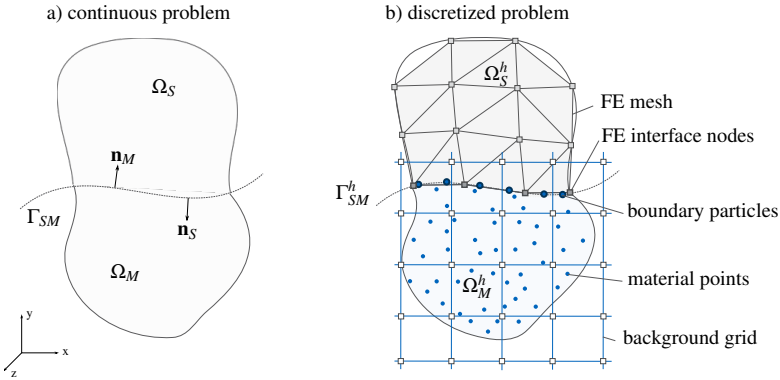

Figure 6.1: a) Continuous non-overlapping domain decomposition and b) discretization of the FEM domain with a mesh and MPM domain with material points, boundary particles and background grid.

FEM domain Ω_S with outwards pointing normal vector $\mathbf{n}_S$ at the interface Γ_S and the MPM domain Ω_M with normal vector $\mathbf{n}_M$ at the interface Γ_M. Therefore, the shared interface of the non-overlapping subsystems is defined by

$$\Gamma_{SM} = \Gamma_S \cap \Gamma_M, \tag{6.1}$$

while within each partition boundary conditions are imposed along this interface to ensure the communication among them. Specifying the notation from chapter 4, all variables belonging to the MPM sub-solver are denoted by the subscript M (instead of d), while those belonging to the structural part are indicated with the subscript S (instead of o) in the following.
Solving the problem in a partitioned manner, each subsystem is discretized individually, as illustrated in Figure 6.1b). The structural domain Ω_S is subdivided into non-overlapping elements that define the FE-mesh, while in MPM material points represent the domain Ω_M. In addition, a computational background grid is introduced for the MPM sub-solver to solve the governing equations, and

boundary particles are defined at the shared interface to weakly enforce the interface conditions.
In this work, Neumann conditions are defined at the interface in the FEM partition. Therefore, the interface nodes of the FEM subsystem receive external forces $\mathbf{F}_S$ as input and after solving the FEM subsystem result in the nodal interface displacements $\hat{\mathbf{u}}_S$, which can be expressed by

$$\hat{\mathbf{u}}_S = \mathscr{S}_{\text{FEM}}(\mathbf{F}_S) \tag{6.2}$$

using the black-box solver notation.
Since a Dirichlet-Neumann partitioning is selected to solve the partitions sequentially, the MPM solver receives as input imposed displacements $\overline{\mathbf{u}}_M$ at the boundary particles and outputs the corresponding reaction forces $\mathbf{F}_M$ after solving the MPM partition. Thus, the weak imposition of Dirichlet conditions in the MPM domain is essentially for this coupling scheme and for this purpose either the penalty augmentation (see section 3.4.3.1), the perturbed Lagrangian method (see section 3.4.3.3) or the Lagrange multiplier method (see section 3.4.3.2) can be used. Adapting the black-box solver notation from chapter 4 consequently yields

$$\mathbf{F}_M = \mathscr{S}_{\text{MPM}}(\overline{\mathbf{u}}_M). \tag{6.3}$$

This coupling scheme is schematically illustrated in Figure 6.2, while the details are provided in subsections 6.1.1 and 6.1.2
The alternative approach, swapping the interface definitions, is discussed by the author in [113]. In this case, the Neumann conditions are imposed on the MPM partition, while Dirichlet constraints are introduced in the FEM partition. Depending on the problem considered, this approach can be used alternatively if both partitions have approximately the same stiffness, or in case the MPM partition is the stiffer domain, this approach may even increase the convergence rate. However, the interface definition for the swapped approach is more advanced when the contact zone and therefore the shared interface changes during the simulation or is not known a priori. While in MPM the boundary particles can be defined in space independently from the material points and are therefore usually aligned with the outline of the FEM domain, the conditions in the FEM domain need to be defined at the nodes of the FE-mesh boundary. Consequently, in case of a varying interface topology during the simulation, the coupling needs to provide further information during the interface iteration about the contacting counterpart to activate only those nodal Dirichlet constraints at the FEM interface, which are in contact with the MPM partition, while releasing the other nodes.
This issue is solved inherently in the presented approach, where the Neumann conditions are defined at the FEM partition. As in the MPM domain, the boundary particles enforcing the Dirichlet constraint are defined at the outline of the FEM body, solely reaction forces result when they interact with the material, as the contact detection is inherently resolved in the MPM model via the computational background grid. Therefore, by mapping those reaction forces to the FEM partition only non-zero external forces result in the contact zone. Therefore, a varying interface topology can be easily handled and consequently this decomposition is preferred and utilized in this work.

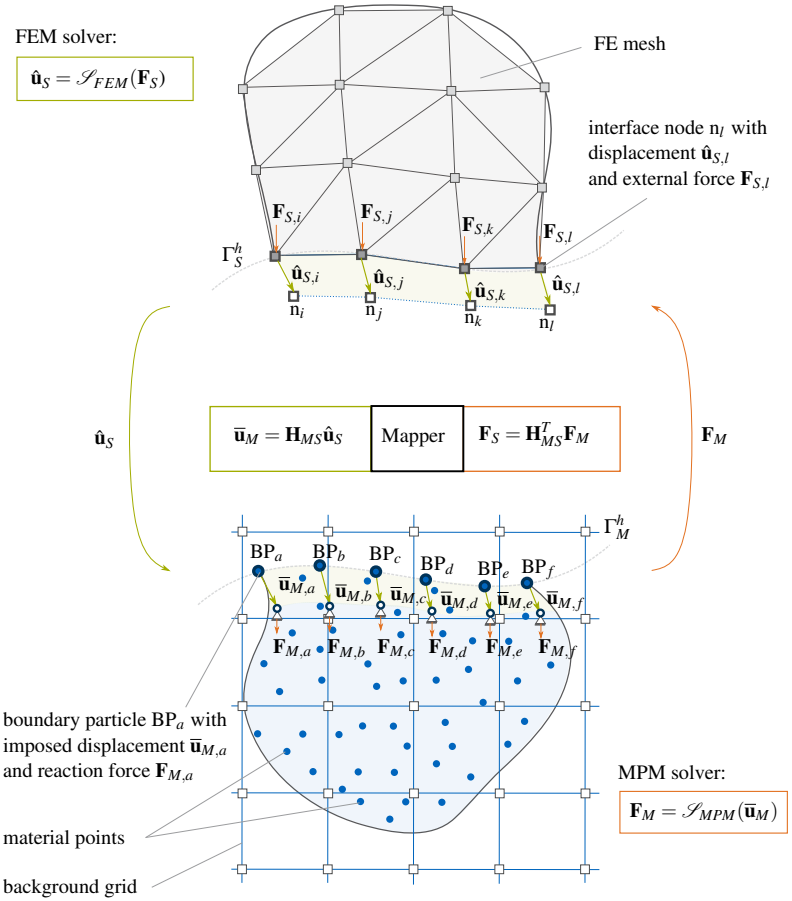

Figure 6.2: Illustration of the MPM-FEM coupling scheme.

To solve the interface equations resulting from the partitioning, a fixed-point iteration (see section 4.3) is used. For the sequential execution of the involved solvers, the solver sequence has to be defined, which results in two alternative coupling algorithms $\mathscr{S}_{\text{FEM}} \circ \mathscr{S}_{\text{MPM}}$ and $\mathscr{S}_{\text{MPM}} \circ \mathscr{S}_{\text{FEM}}$ presented below.

6.1.1 Coupling Sequence: $\mathscr{S}_{\text{FEM}} \circ \mathscr{S}_{\text{MPM}}$

Starting with the solution of the MPM solver, which has the Dirichlet condition, the Picard iteration with iteration counter k is defined by

$$\bar{\mathbf{u}}_{\text{M}}^{k+1} = \mathscr{S}_{\text{FEM}} \circ \mathscr{S}_{\text{MPM}}(\bar{\mathbf{u}}_{\text{M}}^{k}) \tag{6.4}$$

resulting in the interface residual for the displacements (according to equation 4.8)

$$\mathbf{r}_u^k = \mathscr{S}_{\mathrm{FEM}} \circ \mathscr{S}_{\mathrm{MPM}}(\overline{\mathbf{u}}_{\mathrm{M}}^k) - \overline{\mathbf{u}}_{\mathrm{M}}^k = \overline{\mathbf{u}}_{\mathrm{M}}^{k+1} - \overline{\mathbf{u}}_{\mathrm{M}}^k \tag{6.5}$$

formulated at the MPM interface Γ_{M}^h. For a strong coupled algorithm, as depicted in Figure 4.3b), this fixed point iteration has to be repeated until the following equation for the discretized problem is fulfilled

$$\epsilon > \frac{\|\mathbf{r}_u^k\|}{\sqrt{n_{\mathrm{dof}}}} \tag{6.6}$$

where ϵ is a user-defined braking tolerance and n_{dof} is the total number of dofs at the interface Γ_{M}^h [78].
Solving the interface residual equation 6.5 leads to the following coupling sequence, which is summarized by the Algorithm 2.

Algorithm 2 Coupling sequence: $\mathscr{S}_{\mathrm{FEM}} \circ \mathscr{S}_{\mathrm{MPM}}$

while t < t_{end} **do**
  $k = 0$
  while $\epsilon > \|\mathbf{r}_u^k\| / \sqrt{n_{\mathrm{dof}}}$ **do**
    (1). MPM Solver: $\mathbf{F}_{\mathrm{M}}^{k+1} = \mathscr{S}_{\mathrm{MPM}}(\overline{\mathbf{u}}_{\mathrm{M}}^k)$ ▷ (equation 6.3)
    (2). Mapper: $\mathbf{F}_{\mathrm{S}}^{k+1} = \mathbf{H}_{\mathrm{MS}}^T \mathbf{F}_{\mathrm{M}}^{k+1}$ ▷ (equation 6.7)
    (3). FEM Solver: $\hat{\mathbf{u}}_{\mathrm{S}}^{k+1} = \mathscr{S}_{\mathrm{FEM}}(\mathbf{F}_{\mathrm{S}}^{k+1})$ ▷ (equation 6.2)
    (4). Mapper: $\overline{\mathbf{u}}_{\mathrm{M}}^{k+1} = \mathbf{H}_{\mathrm{MS}} \hat{\mathbf{u}}_{\mathrm{S}}^{k+1}$ ▷ (equation 6.8)
    (5). Residual: $\mathbf{r}_u^k = \overline{\mathbf{u}}_{\mathrm{M}}^{k+1} - \overline{\mathbf{u}}_{\mathrm{M}}^k$ ▷ (equation 6.5)
    if $\epsilon < \|\mathbf{r}_u^k\| / \sqrt{n_{\mathrm{dof}}}$ **then**
      (6). Accelerator: $\overline{\mathbf{u}}_{\mathrm{M}}^{k+1} = \mathrm{ACC}(\overline{\mathbf{u}}_{\mathrm{M}}^{k+1})$ ▷ (equation 6.9)
    $k = k + 1$

The MPM subproblem is solved first with prescribed displacements $\overline{\mathbf{u}}_{\mathrm{M}}^k$ at the interface, resulting in updated reaction forces $\mathbf{F}_{\mathrm{M}}^{k+1}$ at the boundary particles.
These forces $\mathbf{F}_{\mathrm{M}}^{k+1}$ are then mapped to the nodes of the FEM interface as external forces $\mathbf{F}_{\mathrm{S}}^{k+1}$ by

$$\mathbf{F}_{\mathrm{S}}^{k+1} = \mathbf{H}_{\mathrm{MS}}^T \mathbf{F}_{\mathrm{M}}^{k+1} \tag{6.7}$$

using a conservative mapping approach (see section 4.5) for the data transfer. For FSI or other multi-physics problems, it may be necessary to reconstruct the mapping matrix within each time step if the topology of the interface nodes changes. Within the proposed mapping algorithm however, the mapping matrix only is required to be calculated once in the initial time step, since the boundary particles are moving according to the nodes of the FE-mesh and therefore their connectivity does not change during the computation. Therefore, the superscript k for the iteration counter is omitted for the mapping matrix.

An important aspect for this coupling sequence to construct the mapping matrix is that MPM is the origin and FEM is the destination and therefore no shape function values are available at the MPM interface. Hence, instead of the nearest element the barycentric mapper has to be used if an interpolation of the nodal values to the destination nodes is desired.
With the external forces obtained at the interface of the FEM solver, the structural domain is solved, resulting in updated interface displacements $\hat{\mathbf{u}}_{\mathrm{S}}^{k+1}$.
These interface displacements are mapped by

$$\overline{\mathbf{u}}_{\mathrm{M}}^{k+1} = \mathbf{H}_{\mathrm{MS}} \hat{\mathbf{u}}_{\mathrm{S}}^{k+1} \tag{6.8}$$

back to the MPM partition as imposed displacements $\overline{\mathbf{u}}_{\mathrm{M}}^{k+1}$ before the residual $\mathbf{r}_u^k$ defined by equation 6.5 is calculated. In case the breaking criteria defined by equation 6.6 is fulfilled, the interface iteration loop stops.
Otherwise, a convergence accelerator can be applied to modify the imposed displacements $\overline{\mathbf{u}}_{\mathrm{M}}^{k+1}$ at the boundary particles by

$$\overline{\mathbf{u}}_{\mathrm{M}}^{k+1} = \mathrm{ACC}(\overline{\mathbf{u}}_{\mathrm{M}}^{k+1}) \tag{6.9}$$

before they are passed to the MPM solver in the next iteration loop. The calculation is repeated until the breaking criteria (equation 6.6) is fulfilled, which ensures that the interface transmission conditions are satisfied.
In contrast to the strong coupling scheme the iteration procedure is neglected in the weak coupling algorithm. Consequently, the calculation procedure reduces to the Algorithm 3, omitting the iteration counter k. Furthermore, the calculation of the residual is skipped and convergence accelerators are superfluous. A predictor step to calculate an initial guess for the subsequent time step is not considered within this work.

Algorithm 3 Weak coupling sequence: $\mathscr{S}_{\mathrm{FEM}} \circ \mathscr{S}_{\mathrm{MPM}}$

while t < t_{end} **do**
(1). MPM Solver: $\mathbf{F}_{\mathrm{M}} = \mathscr{S}_{\mathrm{MPM}}(\overline{\mathbf{u}}_{\mathrm{M}})$ ▷ (equation 6.3)
(2). Mapper: $\mathbf{F}_{\mathrm{S}} = \mathbf{H}_{\mathrm{MS}}^{T} \mathbf{F}_{\mathrm{M}}$ ▷ (equation 6.7)
(3). FEM Solver: $\hat{\mathbf{u}}_{\mathrm{S}} = \mathscr{S}_{\mathrm{FEM}}(\mathbf{F}_{\mathrm{S}})$ ▷ (equation 6.2)
(4). Mapper: $\overline{\mathbf{u}}_{\mathrm{M}} = \mathbf{H}_{\mathrm{MS}} \hat{\mathbf{u}}_{\mathrm{S}}$ ▷ (equation 6.8)

6.1.2 Coupling Sequence: $\mathscr{S}_{\mathrm{MPM}} \circ \mathscr{S}_{\mathrm{FEM}}$

Alternatively, the coupling sequence can start with the execution of the FEM subsolver, updating the displacement first by

$$\hat{\mathbf{u}}_{\mathrm{S}}^{k+1} = \mathscr{S}_{\mathrm{FEM}}(\mathbf{F}_{\mathrm{S}}^{k}) \tag{6.10}$$

before calculating the MPM model

$$\mathbf{F}_{\mathrm{M}}^{k+1} = \mathscr{S}_{\mathrm{MPM}}(\overline{\mathbf{u}}_{\mathrm{M}}^{k+1}) \tag{6.11}$$

which leads to updated reaction forces $\mathbf{F}_{\mathrm{M}}^{k+1}$. Therefore, this coupling sequence results in the interface residual for the forces (according to equation 4.10)

$$\mathbf{r}_p^k = \mathscr{S}_{\mathrm{MPM}} \circ \mathscr{S}_{\mathrm{FEM}}(\mathbf{F}_{\mathrm{S}}^k) - \mathbf{F}_{\mathrm{S}}^k = \mathbf{F}_{\mathrm{S}}^{k+1} - \mathbf{F}_{\mathrm{S}}^k \tag{6.12}$$

at the FEM interface Γ_{S}^h. For a strong coupled algorithm, this iteration has to be performed until the breaking criteria defined by

$$\epsilon > \frac{\|\mathbf{r}_p^k\|}{\sqrt{n_{\mathrm{dof}}}} \tag{6.13}$$

is met while n_{dof} is the total number of dofs at the FEM interface Γ_{S}^h. To accelerate the interface iteration loop, the forces for the subsequent iteration can be modified by

$$\mathbf{F}_{\mathrm{S}}^{k+1} = \mathrm{ACC}(\mathbf{F}_{\mathrm{S}}^{k+1}) \tag{6.14}$$

utilizing a convergence accelerator as presented in section 4.3.2 and section 4.4. The complete calculation for the strong coupling sequence is summarized in Algorithm 4.

Algorithm 4 Coupling sequence: $\mathscr{S}_{\mathrm{MPM}} \circ \mathscr{S}_{\mathrm{FEM}}$

while t < t_{end} **do**
  $k = 0$
  while $\epsilon > \|\mathbf{r}_p^k\| / \sqrt{n_{\mathrm{dof}}}$ **do**
    (1). FEM Solver: $\hat{\mathbf{u}}_{\mathrm{S}}^{k+1} = \mathscr{S}_{\mathrm{FEM}}(\mathbf{F}_{\mathrm{S}}^k)$ ▷ (equation 6.10)
    (2). Mapper: $\overline{\mathbf{u}}_{\mathrm{M}}^{k+1} = \mathbf{H}_{\mathrm{MS}} \hat{\mathbf{u}}_{\mathrm{S}}^{k+1}$ ▷ (equation 6.8)
    (3). MPM Solver: $\mathbf{F}_{\mathrm{M}}^{k+1} = \mathscr{S}_{\mathrm{MPM}}(\overline{\mathbf{u}}_{\mathrm{M}}^{k+1})$ ▷ (equation 6.11)
    (4). Mapper: $\mathbf{F}_{\mathrm{S}}^{k+1} = \mathbf{H}_{\mathrm{MS}}^T \mathbf{F}_{\mathrm{M}}^{k+1}$ ▷ (equation 6.7)
    (5). Residual: $\mathbf{r}_p^k = \mathbf{F}_{\mathrm{S}}^{k+1} - \mathbf{F}_{\mathrm{S}}^k$ ▷ (equation 6.12)
    if $\epsilon < \|\mathbf{r}_p^k\| / \sqrt{n_{\mathrm{dof}}}$ **then**
      (6). Accelerator: $\mathbf{F}_{\mathrm{S}}^{k+1} = \mathrm{ACC}(\mathbf{F}_{\mathrm{S}}^{k+1})$ ▷ (equation 6.14)
    $k = k + 1$

In contrast to the previous coupling sequence, the FEM interface is now the origin partition, since it is executed first. Therefore, the nearest element mapper can be applied as an alternative to the nearest neighbor mapper to construct the mapping matrix $\mathbf{H}_{\mathrm{MS}}$, which is required to directly transfer the displacements by equation 6.8, while for the conservative mapping approach the transposed is used to map the forces by equation 6.7.

Analogous to the previous coupling sequence, the weak coupling algorithm is obtained omitting the iteration counter k, as only one iteration per time step is performed. The resulting scheme is summarized in the Algorithm 5.

Algorithm 5 Weak coupling sequence: $\mathscr{S}_{\text{MPM}} \circ \mathscr{S}_{\text{FEM}}$

while t < t_{end} **do**
(1). FEM Solver: $\hat{\mathbf{u}}_{\text{S}} = \mathscr{S}_{\text{FEM}}(\mathbf{F}_{\text{S}})$ ▷ (equation 6.10)
(2). Mapper: $\bar{\mathbf{u}}_{\text{M}} = \mathbf{H}_{\text{MS}}\hat{\mathbf{u}}_{\text{S}}$ ▷ (equation 6.8)
(3). MPM Solver: $\mathbf{F}_{\text{M}} = \mathscr{S}_{\text{MPM}}(\bar{\mathbf{u}}_{\text{M}})$ ▷ (equation 6.11)
(4). Mapper: $\mathbf{F}_{\text{S}} = \mathbf{H}_{\text{MS}}^{T}\mathbf{F}_{\text{M}}$ ▷ (equation 6.7)

6.2 Verification and Application

In this section, the MPM-FEM coupling scheme is systematically assessed and evaluated to prove its accuracy and demonstrating its ability to simulate the impact of gravity-driven mass flows on highly flexible protective structures. For this purpose, various examples of increasing complexity are examined and presented below, highlighting their respective objectives and the concluding implications for the coupled algorithm.

6.2.1 Static Cantilever

The first example considers a linear elastic cantilever beam under dead load. The beam has a total length of 8m, a cross-section of $A = 1 \times 1\text{m}^2$, and a density of $\rho = 1000\text{kg/m}^3$ and is to be solved in a partitioned manner. Therefore, as depicted in Figure 6.3 the beam is divided into two partitions with a length of 4m

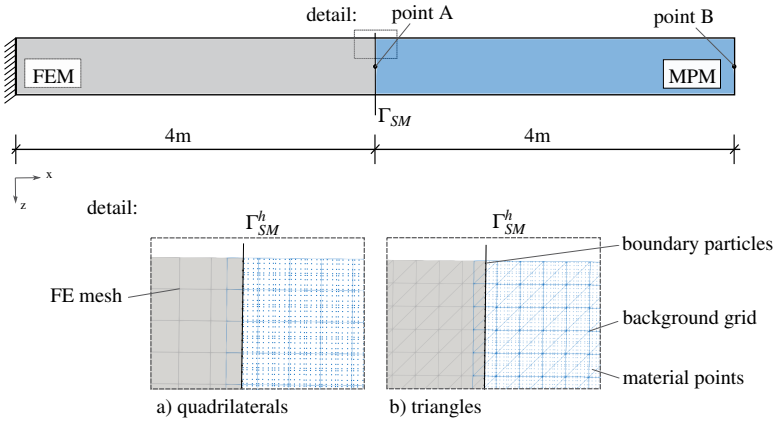

Figure 6.3: System setup of cantilever under dead load solved in partitioned manner.

each and a shared interface Γ_{SM}.
The structural part with the clamped support is modeled with FEM while the right part of the beam is modeled with MPM. As a Neumann condition is defined at the shared interface within the FEM partition for the introduced coupling, the

FEM partition cannot be defined at the loose end of the beam as this would lead to a kinematic system for the FEM subsystem. Instead, a Dirichlet constraint is required at the outer end of the cantilever. Therefore, MPM with a Dirichlet constraint at the shared interface is used to model the right subsystem.
For both models, a St. Venant Kirchhoff plane stress material law with Young's modulus $E = 9\text{GPa}$ and Poisson's ratio $\nu = 0.0$ is assumed.

6.2.1.1 Convergence Rate

To solve the problem, both subsystems are discretized independently defining a mesh in the FEM partition, while material points and a computational background grid are defined for the MPM model, which is depicted in the detail of Figure 6.3. Either quadrilateral or triangular elements are considered for the FE-mesh and the MPM background grid. Additionally, boundary particles are introduced at the shared interface within the MPM model, imposing the Dirichlet constraint. Within this study, this constraint is imposed either by penalty augmentation (see section 3.4.3.1) with $\beta = 1e15$ for quadrilateral and $\beta = 1e13$ for triangular background grid elements, the perturbed Lagrangian condition (see section 3.4.3.3) with constant $\beta = 1e25$ or with Lagrange multipliers (see section 3.4.3.2) to study the effect of the different types of boundary imposition methods in the coupled simulation.
Moreover, the accuracy and efficiency of the coupling sequences described by Algorithm 2 and Algorithm 4 are validated and compared. Therefore, each discretized system is solved twice, while either the MPM sub-solver is executed first following Algorithm 2 or alternatively calculating first the FEM partition according to Algorithm 4 before the MPM subsystem is solved. For both schemes, the Aitken relaxation scheme (see section 6.2.4) is applied, which modifies the particle displacement in the former scheme, whereas the structural loads are adapted in the latter scheme. For the data transfer, the barycentric mapper is utilized in the first coupling sequence, whereas the nearest element mapper is selected in the second algorithm. Therefore, the subsequent solver obtains the interpolated interface displacements from the origin, whereas the forces are mapped using the conservative mapping approach (details are provided in section 4.5).
The effects of these model assumptions are examined in a convergence rate analysis. Therefore, the numerical results for the vertical displacement at the centerline of the beam are compared to the analytical Timoshenko beam solution. The displacement values are evaluated at point A, which is located at the shared interface, and at the tip of the cantilever, which is marked as point B in Figure 6.3.
For the convergence rate, the numerical solutions are calculated for different mesh sizes h, assuming the same element type and size for the FE-mesh and the MPM background grid. For the initialization of the material points within each MPM submodel, a structured quadrilateral body mesh with half the background grid element size is chosen, placing 16 material points each. The initialization of the boundary particles is also guided by the body mesh, defining two boundary particles within each line segment at the interface. Furthermore, these boundary particles are initialized to be on the centerline of the background grid elements, as shown in the detail of Figure 6.3, which exemplifies the model discretization for an element size of 0.05m.

In Figure 6.4, the resulting plots for the convergence rate analysis are collected.

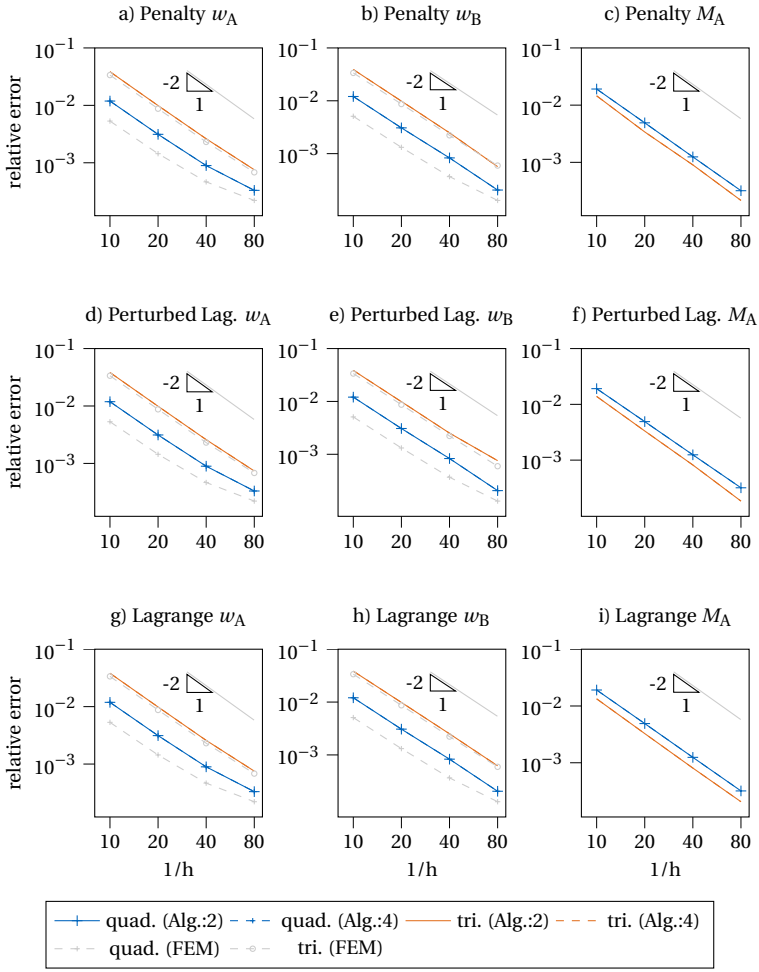

Figure 6.4: Convergence rate of cantilever. Impact of quadrilateral and triangular elements to discretize the coupled problem, the coupling sequence (Alg.: 2 or Alg.: 4) and boundary imposition types (penalty, perturbed Lag., Lagrange) in the MPM sub-solver are investigated.

Hence, within each diagram the relative error of the numerical solution in comparison to the analytical result is plotted against the inverse mesh size $1/h$. The diagrams in the first row show the results obtained by penalty augmentation, while the second and third row provide the solutions when imposing the Dirich-

let constraints with the perturbed Lagrangian method or the Lagrange multipliers, respectively. In order to make the results clearer, the results are presented in separate plots. Thus, the first column of the graphs provide the results for the vertical displacement w_{A} at point A, whereas the results for the vertical displacement w_{B} at point B are collected in the second column.
In the third column of the diagram collection in Figure 6.4, the relative error of the resulting bending moment M_{A} compared to the analytical result is plotted against the inverse mesh size. For the calculation of the numerical bending moment at the shared interface, the external point loads at the FEM interface are multiplied with their respective lever arms to the centerline of the cantilever before being summed.
Consistent with the conclusion of section 3.5, the comparison of the solutions shows that the types of boundary constraints can be used interchangeably. This of course assumes the proper selection of the problem dependent penalty factor β in case of penalty augmentation.
Furthermore, it is demonstrated that both coupling sequences (Algorithm 2 and Algorithm 4) yield the same accuracy for the solution of the strong coupled system, thus allowing their interchangeable use.
Within all plots in Figure 6.4, a quadratic convergence rate is obtained, independent of the type of boundary imposition method utilized in the MPM sub-solver and the coupling sequence chosen. Furthermore, as expected, the discretization of the subproblem with quadrilateral elements provides a higher accuracy for the resulting displacements compared to the discretization with triangular elements. However, in case of the quadrilateral elements, the convergence rate of the displacement at point A decreases slightly with mesh refinement. This effect arises from the imposition of the clamped support on the left side of the beam in combination with the element technology. To demonstrate this, the convergence rate for the monolithic FEM solution is added to the plots in Figure 6.4, which also shows the slight decrease of the convergence rate for the displacement at point A in case of quadrilateral elements.
In case of the discretization with triangular elements, this effect is not present. Furthermore, for triangular elements, the convergence rate for the monolithic and the coupled solution are very similar, whereas in case of quadrilaterals the monolithic approach is more accurate. This discrepancy arises from inaccuracies in the MPM sub-solver due to particle integration, which in case of quadrilaterals requires more material points to improve the numerical integration.
For the resulting bending moment, however, a slightly higher accuracy is obtained for the triangular elements compared to the discretization of the coupled problem with quadrilateral elements. This effect is also related to the MPM subsolver. As detailed in section 3.4.3, the reaction forces at the boundary particles are calculated by interpolating the nodal reaction forces based on an area weighting procedure. Therefore, in case of triangular elements this interpolation results in a more precise distribution of the reaction forces at the boundary particles, which subsequently is the basis to calculate the resulting bending moment.
In Figure 6.5, the forces at the shared interface are presented and the distribution agrees well with the expected solution. Since the number of boundary particles at the MPM interface Γ_{M}^{h} is larger than the number of nodes at the FEM interface Γ_{S^h} the individual reaction forces at the boundary particles in the MPM partition

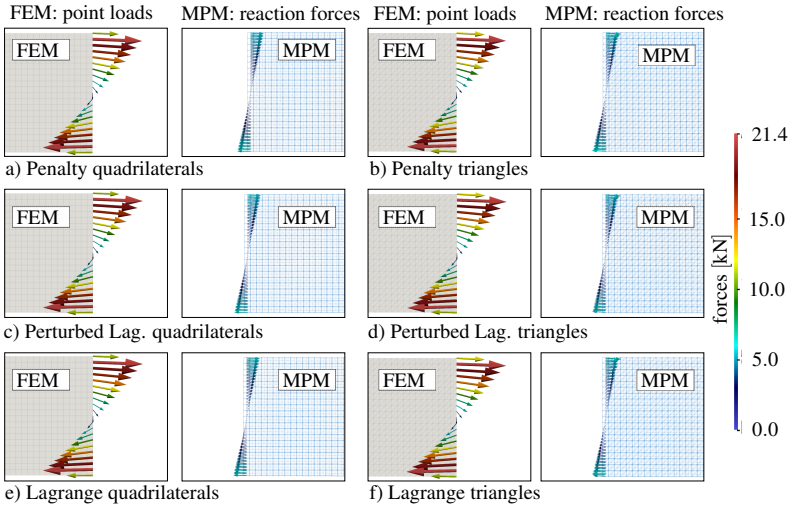

Figure 6.5: Reaction forces at the MPM interface and point loads at the FEM partition illustrated for a mesh size of 0.05m for both quadrilateral and triangular meshes.

are smaller compared to the forces which are imposed as point loads to the FEM counterpart. Hence, the overall balance of forces at the interface is fulfilled. In agreement with the convergence analysis, the resulting forces at the interface are very similar regardless of the type of boundary imposition method used in the MPM sub-solver and the utilized element type to discretize the problem.
In summary, this example shows that quadratic convergence can be achieved in the coupled analysis of MPM and FEM. This is demonstrated for quadrilateral and triangular elements which are used to discretize the individual subsystems. It is also highlighted that penalty, perturbed Lagrangian, and Lagrange multiplier method can be used interchangeably in the partitioned coupling scheme as long as the requirements described in section 3.4.3 are met. Furthermore, this study shows that either coupling sequence, Algorithm 2 and Algorithm 4, can be chosen to achieve the same level of accuracy.

6.2.1.2 Stiffness Ratio

In the preceding example, the two partitions of the cantilever depicted in Figure 6.4 are assumed to be equivalent. In this study however, the Young's modulus of the MPM partition E_{MPM} is varied, while the stiffness of the FEM partition E_{FEM} is kept constant. Due to these modeling assumptions, the interface displacement for the cantilever is kept constant while simultaneously the stiffness ratio of the involved partitions can be varied. Hence, this allows to investigate the impact of the stiffness ratio on the number of interface iterations required to achieve the interface equilibrium.

In analogy to the previous study, the study is performed for quadrilateral and triangular elements used to discretize the problem. Furthermore, the effect of the coupling sequence is studied. Hence, the strong coupled problem is solved either according to Algorithm 2 or Algorithm 4. Within the MPM partition, the weak imposition of the Dirichlet constraints is again varied, analyzing the results for penalty augmentation, perturbed Lagrangian method, and Lagrange multiplier imposition. Again, the results are presented in separate graphs to make the results easier to understand. In case of penalty augmentation, $\beta = 1e15$ is selected, whereas $\beta = 1e25$ is set for the perturbed Lagrangian method.

The individual numerical models for the subproblems are created in accordance with the preceding example, considering a constant mesh size of 0.05m and the results are summarized in Figure 6.6.

The same pattern of results is obtained for all numerical models. As expected, the element type used to discretize the models has a minor influence on the number of coupling iterations. This also applies for the type of boundary imposition method selected in the MPM submodel, assuming an appropriately calibrated penalty factor. Obviously, factors chosen too high will introduce numerical errors into the system, negatively affecting interface convergence or even destabilizing the coupling algorithm.

The results in Figure 6.6 also show that the coupling Algorithm 2 performs slightly better than Algorithm 4, but the difference is not significant.

The stiffness ratio of the involved sub-solvers, however, has a great impact on the required coupling iterations to solve the partitioned problem. While for models with equal stiffness about 20 interface iterations are required, a significant decrease of the required interface iterations is observed when decreasing the stiffness of the MPM partition. However, if the difference in stiffness becomes too large, an increase in the coupling iterations is again observed. This effect is also influenced by the Aitken relaxation scheme, used in its default configuration for this example, as it reaches its upper bound of 2.

In contrast to reducing the stiffness in the MPM partition, increasing E_{MPM} relative to E_{FEM} greatly increases the number of coupling iterations required to solve the partitioned system, and the interface equilibrium limits are quickly reached. This confirms the well-known principle that it is advantageous to impose the Dirichlet constraint on the weaker subsystem when solving a multi-physics problem in a partitioned manner.

6.2.1.3 Interface Discretization

To solve the partitioned problem, data exchange at the shared interface is of paramount importance. Therefore, the discretizations of the involved subsystems have to be adapted to ensure a physical distribution of forces and displacements at the interface. Especially the applied mapping technique in combination with the individual discretizations of the interfaces are crucial in this regards.

Within this work, interpolation-based mappers are utilized which are detailed in section 4.5. In addition, conservative mapping is selected. Consequently, the mapping matrix is constructed for the interface displacements, while its transpose is used for the force transfer.

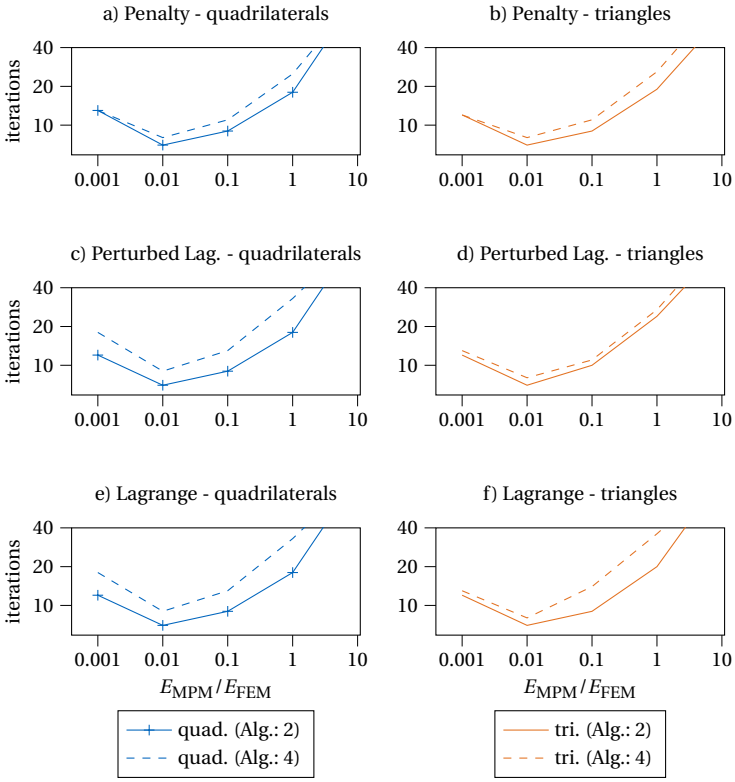

Figure 6.6: Necessary coupling iterations plotted against varying ratio of Young's modulus E_{MPM} and E_{FEM} of MPM and FEM partition, distinguishing the coupling Algorithm 2 and Algorithm 4. The results are displayed for quadrilateral and triangular elements and the boundary imposition types (penalty, perturbed Lag., Lagrange) within the MPM partition.

Therefore, regardless of the chosen coupling sequence (Algorithm 2 or Algorithm 4), a finer interface discretization at the MPM sub-solver is required to subsequently ensure a physical distribution of the forces at the FEM interface after the mapping process.

For the sake of illustration, two models are created with distinctly different discretizations, as illustrated in Figure 6.7. Model I) has a comparatively coarse discretization for the FEM model, while a fine discretization is selected for the MPM model. The interface in the MPM partition is defined by boundary particles, several of which are initialized within each background grid element to properly impose the Dirichlet conditions.

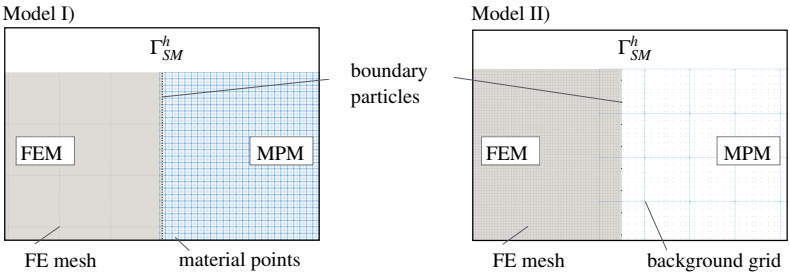

Figure 6.7: Two models to demonstrate the effect of the interface discretization. Model I has a coarse mesh for FEM and fine discretization of MPM model while model II has a fine FE-mesh and coarse MPM discretization.

Therefore, due to this discretization, all nodes at the FEM interface receive a point load as external load by mapping the reaction forces of the boundary particles, which is illustrated in Figure 6.8.

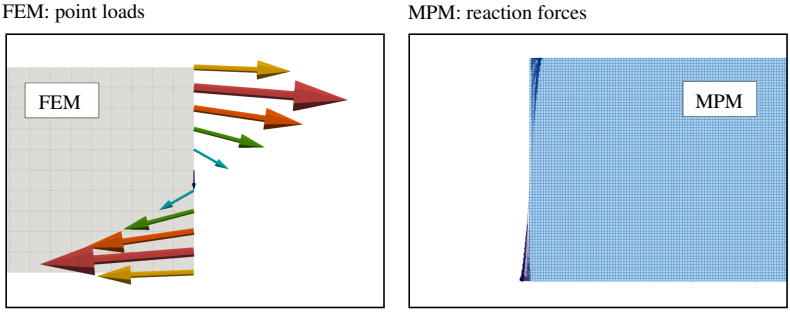

Figure 6.8: Detail of the reaction forces at the MPM interface and the subsequent point loads at the FEM interface for model I. All nodes at the FEM interface are affected by the coupling.

However, this is not the case if the FEM interface discretization is finer compared to the MPM partition, which is illustratively explained by model II) (see Figure 6.7). For this model, a very fine discretization is selected for the FEM partition, while only a few boundary particles are initialized in the MPM model in order to enforce the Dirichlet constraints in the coarsely discretized MPM model. As a consequence, the FEM interface nodes receive only a few singular forces at some interface nodes, while the remaining nodes are not affected by the coupling conditions, as shown in Figure 6.9.
Hence, due to the selected interface discretizations in combination with the mappers, which locally interpolate the interface data, a non-physical distribution of the forces at the FEM interface is obtained, which introduces singularities in the

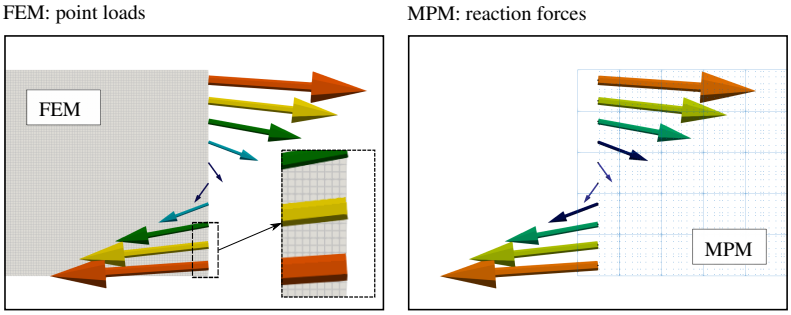

Figure 6.9: Detail of the reaction forces at the MPM interface and the subsequent point loads at the FEM interface for model II. Only few nodes at the FEM interface are affected by the coupling.

FEM model. Furthermore, since the interface data is not properly mapped, resulting in interface nodes that are not affected by the coupling, the solvability of the coupled problem is negatively affected.

Consequently, it is essential for a robust numerical model to select a finer interface discretization of the MPM model in comparison to the FEM counterpart. For the numerical examples in this thesis, this is always the case anyway, since several boundary particles within each background grid element in the MPM model are required for the boundary imposition. Therefore, even if the same element size is selected for the FE-mesh and the MPM background grid, the number of boundary particles will still be larger compared to the number of nodes at the FEM counterpart, ensuring that the interface data is mapped properly.

6.2.2 Dynamic Beam

A dynamic linear elastic 2D plane stress beam subjected to self-weight is considered for the second verification example. Thus, in addition to the previous examples, the partitioned coupling scheme is now applied to a dynamically vibrating system. This verifies the correct data exchange in the coupled simulation for a dynamic system where the spatial position of the interface changes with time.

As in the previous example, the beam has a total length of 8m, a cross-section of $A = 1 \times 1\text{m}^2$ and a density of $\rho = 1000\text{kg/m}^3$ and is divided into two partitions of 4m length each. For both subsystems, a Young's modulus of $E = 90\text{MPa}$ and Poisson's ratio of $\nu = 0.0$ are considered.

The beam is clamped on both sides resulting in a symmetric system, which is illustrated in Figure 6.10.

For the calculation of the coupled system, each subsystem is discretized independently. As for the static beam, an element size of 0.05m is selected to discretize the FEM model and the background grid for the MPM model with quadrilateral elements. To initialize the material points, a quadrilateral body mesh is created with element size of 0.01m, placing 16 material points each. Thus, errors

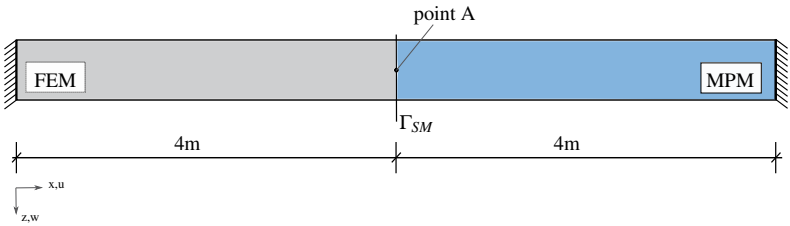

Figure 6.10: System setup of the linear elastic dynamic beam, clamped on both sides modeled with MPM and FEM.

due to cell-crossing and bad integration in the MPM model are negligible due to the fine material point discretization.
At the shared interface, boundary particles are created in the MPM model, initializing 5 particles within each background grid element to ensure a good interface data transfer. These mass-less particles are initialized at the centerline of the background grid elements as depicted in the detail of Figure 6.3. They impose the Dirichlet condition either by penalty augmentation assuming $\beta = 1e14$, the perturbed Lagrangian method with $\beta = 1e25$, or the Lagrange multiplier method. To solve the coupled problem, the FEM solver is executed first and a strongly coupled scheme according to Algorithm 4 is selected. Hence, the nearest element mapper (see section 4.5) can be applied to transfer data between the interfaces. To accelerate the interface convergence the MVQN convergence accelerator according to section 4.4 is selected, which modifies the forces before they are applied to the structure as external forces. The vibration of the beam is in total calculated for 1s with a time step of $\Delta t = 1e-3$s.
During the computation, the vertical displacement w at point A is observed and plotted over time in Diagram 6.11 considering the different types of boundary imposition methods. For comparison, the given problem depicted in Figure 6.10 is also calculated as a monolithic FEM model and the displacement at point A is added to the plot in Figure 6.11.
The results of the monolithic and partitioned system are in perfect agreement, confirming the accuracy and methodology of the partitioned approach also for dynamic problems. Furthermore, since the penalty factor is chosen sufficiently large, all boundary imposition methods can be used interchangeably to obtain the expected solution.

6.2.3 Cylinder Sliding along Rigid Structure

As illustrated in Figure 6.12, a cylinder sliding down an inclined slope of 60° due to gravity is considered to verify the partitioned coupling scheme of MPM and FEM in dynamic scenarios. In addition to the previous dynamic example, the shared interface varies in time as the contact point of the sliding cylinder with the inclined plane changes during the simulation.
The considered cylinder has a radius of $r = 0.5$m, a height of $h = 1$m and a density of $\rho = 7800\text{kg/m}^3$. The material model for the cylinder is assumed to be linear

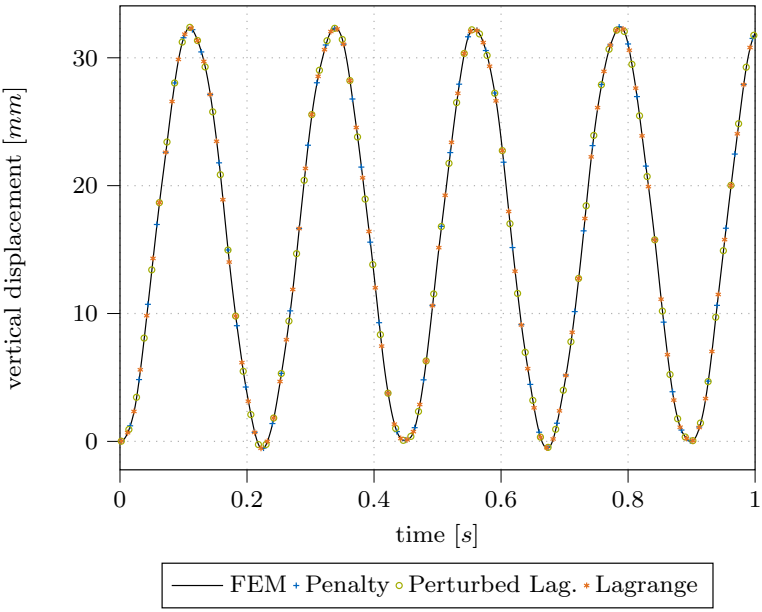

Figure 6.11: The vertical displacement at point A of the dynamic beam subjected to self-weight. Comparison of monolithic FEM solution and partitioned MPM-FEM.

elastic with E = 2*e*9Pa and $\nu = 0.0$ for the Young's modulus and the Poisson's ratio, respectively.

While the sliding cylinder is modeled with MPM, the inclined slope with dimension $6 \times 0.5 \times 1$ m^3, which is fixed at the bottom, is modeled with FEM, assuming a linear elastic material with a significantly higher Young's modulus of E = 2*e*12Pa, while keeping the Poisson's ratio at zero. Therefore, compared to the cylinder, the slope can be considered rigid, allowing for a comparison between the numerical solution of the cylindrical displacement and the analytical one.

This kind of example is used in various literature for verification purposes, just mentioning [12] introducing an contact algorithm in MPM, [34] and [117] to verify the penalty and Lagrange multiplier imposition of non-conforming boundary conditions in MPM, and [81], which are using a hybrid contact method to couple MPM and FEM.

Two different numerical models are created for the MPM partition. The first MPM model uses a structured quadrilateral background grid with size 0.12m combined with an unstructured triangular body mesh with size 0.06m to initialize 3 particles per element. At the interface, boundary particles are introduced with a distance of 0.06m along the upper edge of the slope. The discretization is selected such that the interface and thus the boundary particles are initialized

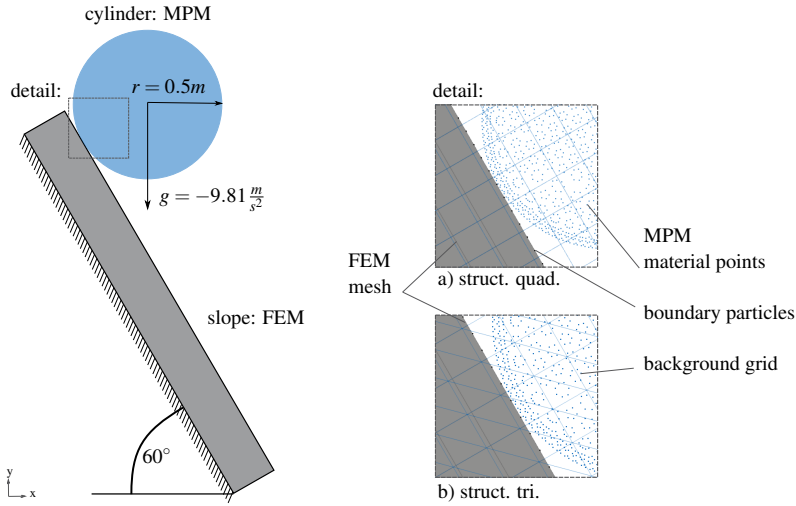

Figure 6.12: System of cylinder sliding down inclined slope.

within the MPM background grid elements as depicted in Figure 6.12 a), which requires a weak imposition of the boundary conditions in the MPM model. For the second MPM model, a structured triangular background grid with size 0.12m is utilized, as depicted in Figure 6.12 b), while maintaining the other model parameters.

FEM is used to discretize the slope selecting a structured quadrilateral mesh with a size of 0.12m for the elements. Thus, two numerical models for the given problem are created by coupling it to the two different MPM models. The latter example, which has a triangular background grid in the MPM model and a quadrilateral mesh in the FEM model, further verifies the coupling scheme also for different element types discretizing the partitions involved.

The cylinder is initialized in direct contact with the slope, which allows a coarse discretization of the numerical models. However, if the material were to approach the interface during simulation time, a finer background grid discretization of the MPM model would be necessary to calculate the resulting contact forces (see also section 3.5.3).

The Dirichlet boundary in the MPM model is imposed either by penalty augmentation with $\beta = 1e15$ or by the Lagrange multiplier method. For the solution of the overall problem, a strong coupled solution scheme is selected executing the individual solvers according to Algorithm 4. Alternatively, a weak coupling scheme according to Algorithm 5 can be applied, since the structural displacements in this example are negligibly small. The calculation is performed for 1s with a time step of $\Delta t = 0.001$s.

In Figure 6.13 the numerical results at times $t = 0$s, $t = 0.5$s and $t = 1$s are displayed illustrating the point loads imposed at the FEM model as well as the resulting displacements at the top of the slope induced by the weight of the sliding

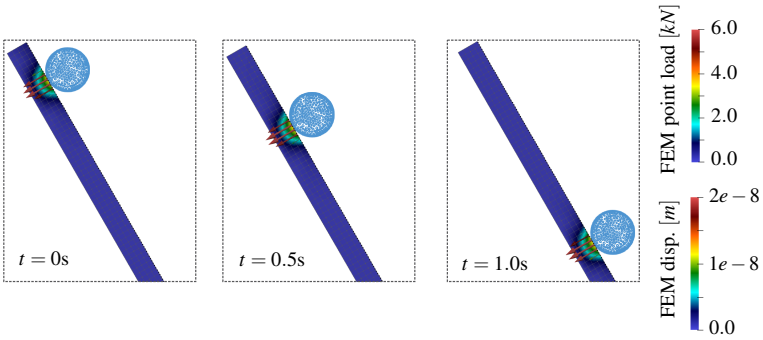

Figure 6.13: Numerical results of the cylinder which slides down the inclined slope visualizing the loads and the resulting displacements at the FEM partition induced by the cylinder modeled with MPM.

cylinder. As expected, the displacements are very small due to the numerical rigidity of the slope, but it still demonstrates the exchange of the interface data in the partitioned scheme.

In Diagrams 6.14 the numerical displacements calculated for the cylinder are plotted against the analytical solution. While Diagram 6.14a) shows the results for the quadrilateral background grid in MPM, Diagram 6.14b) displays the results obtained with the triangular background grid, both in combination with a quadrilateral mesh in the FEM model.

The displacements show a very good agreement, independent of the background grid element type in the MPM model. Furthermore, both the penalty and the Lagrange multiplier imposition of the non-conforming boundary condition within the MPM model predict the solution almost equivalently.

Since the gravitational force in the numerical model is fully applied in the first time step, a harmonic vibration of the elastic cylinder is induced. To numerically damp these structural deformations, Rayleigh damping is applied to the MPM model with the parameters $\alpha_d = 0.0$ and $\beta_d = 0.01$. The results obtained with Rayleigh damping are labeled *damped*, while those without damping are labeled *undamped*. The considered damping has no effect on the resulting displacement of the cylinder, as shown in Diagram 6.14.

However, there is a huge effect of the applied damping on the reaction forces, which are mapped to the FEM partition as external point loads, as illustrated in Diagram 6.15 and Diagram 6.16 for the respective numerical models.

As shown in the plots, significant oscillations of the reaction forces are present for both types of boundary imposition methods in case of quadrilateral as well as triangular background grid elements. This agrees well with the expected numerical solution due to the dynamic calculation of the example combined with the sudden enforcement of the gravity load. As the simulation progresses, the magnitude of the oscillations in the reaction forces decreases and converges to the static load expected from physics.

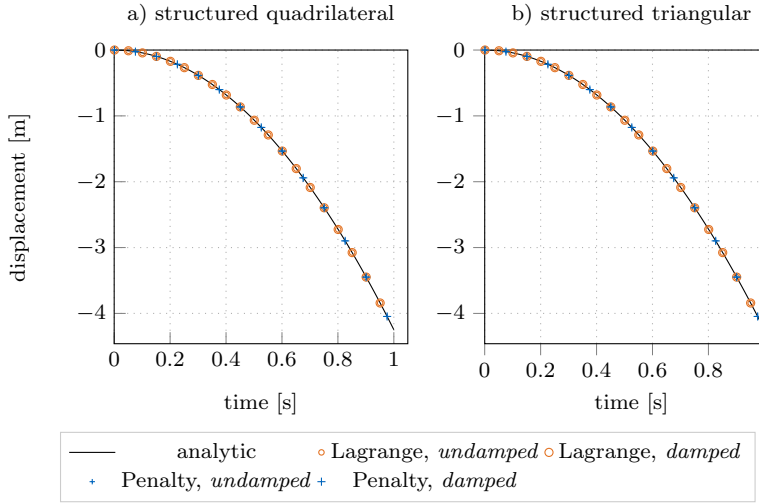

Figure 6.14: Comparison of the cylindrical displacements with analytical solution for both numerical models. Values labeled with *damped* consider Rayleigh damping while it is not considered for the *undamped* cases.

In numerical models with perfect energy conservation, the magnitude of the oscillations is not expected to decrease during the simulation. However, in this particular example, a rather coarse discretization of the MPM model was chosen, which is the main cause of the energy dissipation.
However, the purpose of this particular example is not to prove energy conservation. Rather, it is to prove that the reaction forces calculated at the MPM partition converge to the static load expected from physics by damping the dynamic effects.
The analytic contact force F_C induced by the weight of the cylinder and acting normal to the inclined slope can be calculated by

$$F_C = r^2 \cdot \pi \cdot h \cdot \rho \cdot g \cdot \cos(60^\circ) = 30.05\text{kN} \tag{6.15}$$

and is added to the Diagrams 6.15 and 6.16, respectively. The comparison with the numerical results is therefore as expected, showing the oscillations of the forces around the expected static load and converging towards this value due to damping effects. To accelerate the damping of the dynamic effects Rayleigh damping is applied, which perfectly demonstrates that the contact forces converge to the expected analytical solution.
The numerical solutions obtained with Rayleigh damping are demonstrating that the expected solutions can be obtained with either penalty augmentation or Lagrange multiplier imposition of the interface condition in the MPM partition.

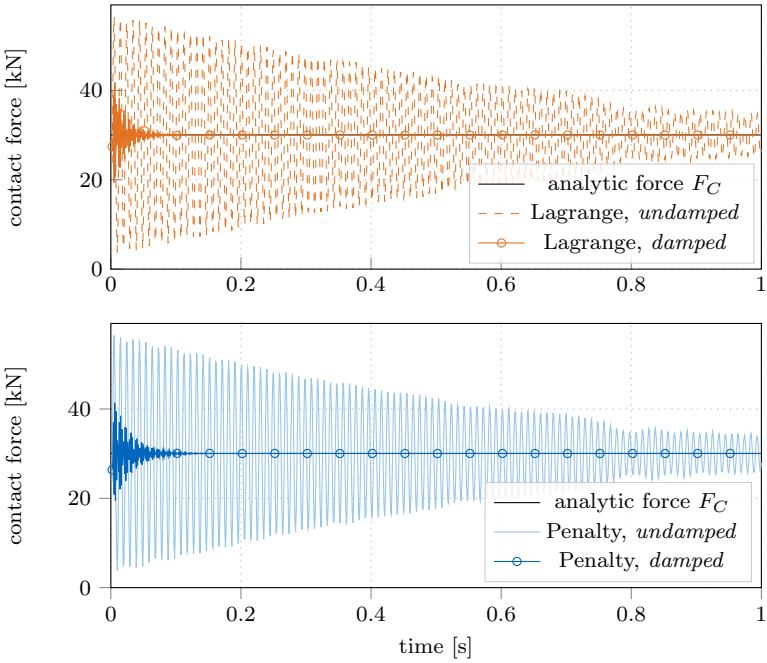

Figure 6.15: Comparison of the contact forces with analytical solution for static loading condition for structured quadrilateral background grid and varying boundary imposition types in the MPM model. Values labeled with *damped* consider Rayleigh damping while it is not considered for the *undamped* cases.

Therefore, in each of the following examples, only one of the types of boundary imposition methods is considered.

This example also showed that quadrilateral and triangular background grid elements can be used interchangeably and coupled respectively to the FEM counterpart. Furthermore, the comparison of the *damped* and *undamped* numerical solution highlights the effect of the applied Rayleigh damping, which does not affect the kinematic values of the sliding cylinder, but effectively damps the oscillations of the contact forces.

6.2.4 Cylinder Sliding along Flexible Structure

This example adds another level of complexity by considering the sliding cylinder on a highly flexible structure. As depicted in Figure 6.17, a horizontal flexible cable spanned between two supports is considered, which is loaded by a cylinder

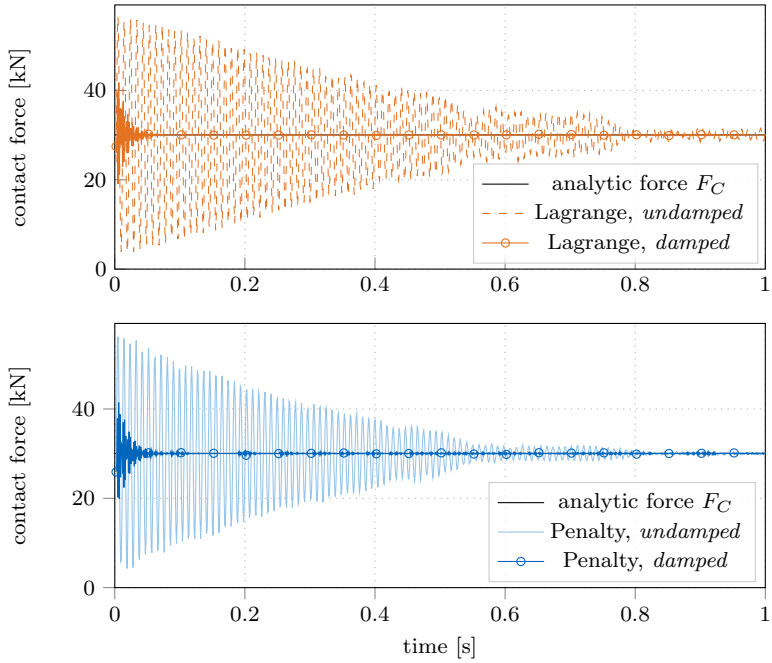

Figure 6.16: Comparison of the contact forces with analytical solution for static loading condition for structured triangular background grid and varying boundary imposition types in the MPM model. Values labeled with *damped* consider Rayleigh damping while it is not considered for the *undamped* cases.

	Young's modulus	Poisson's ratio	density
cylinder	$E = 2.0e7\text{Pa}$	$\nu = 0.0$	$\rho_\text{M} = 7000 \frac{\text{kg}}{\text{m}^3}$
structure	$E = 2.1e10\text{Pa}$	$\nu = 0.0$	$\rho_\text{S} = 7850 \frac{\text{kg}}{\text{m}^3}$

Table 6.1: Material properties of the flexible structure and the sliding cylinder.

on the left. Due to the self weight of the cable and the weight of the cylinder, the cable deforms initiating the cylinder to slide along the flexible structure.
Analogous to the previous example, the considered cylinder has a radius of $r = 0.5\text{m}$ and a height of $h = 1.0\text{m}$. It is modeled with MPM assuming a linear elastic material model.
The cable structure with a total length of $L = 10.0\text{m}$ is modeled with FEM. It has a cross-section of $A = 0.001\text{m}^2$ assuming also a linear elastic material. The material properties of both systems are summarized in Table 6.1.
To solve the given problem with the partitioned MPM-FEM coupling method-

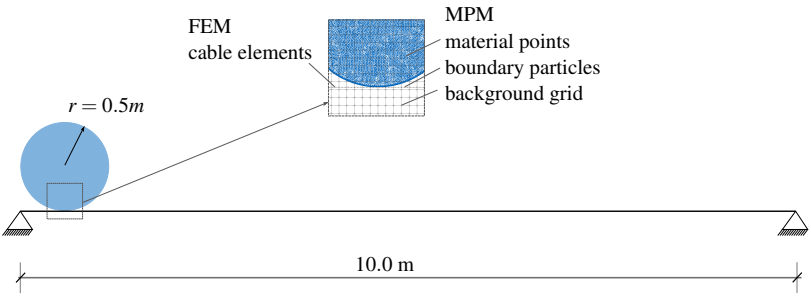

Figure 6.17: Initial system setup of the cylinder modeled with MPM initialized on the left of the horizontal flexible cable which is modeled with FEM.

ology, both models are discretized independently, while the shared interface in both models is initialized at the position of the undeformed cable structure.

A structured quadrilateral background grid with an element size of 0.05m is selected for the MPM calculation, while the material points are initialized by an unstructured triangular body mesh with element size of 0.01m, placing 3 particles within each element. At the shared interface 500 uniformly distributed boundary particles are initialized, introducing a slip Dirichlet condition in the MPM model. The constraint is imposed by Lagrange multiplier method in this example.

In order to accurately model the deformed shape of the cable due to the induced load from the sliding cylinder, the cable is subdivided into 30 equally sized elements. To avoid a singular stiffness matrix at the beginning of the simulation due to the undeformed geometry of the cable elements, a negligible pre-stress of 1N/m^2 is considered.

For the calculation of the complete system a time step of $\Delta t = 1e-4$s is considered and Algorithm 4 is utilized to solve the strongly coupled problem. Furthermore, Rayleigh damping is considered to damp the dynamic effects induced by the sudden initialization of the gravity loading.

A peculiarity of this example is that the geometry and shape of the shared interface changes with time. Consequently, the normal direction, which defines the slip direction of the cylinder, changes direction and must be adjusted according to the cable deformation. Therefore, in addition to the interface displacements and forces which are exchanged at the shared interface, the normals defined at the cable elements in the FEM model need to be transferred to the boundary particles in the MPM partition. Hence, before the MPM model is solved the normals at the boundary particles are updated from the FEM model.

The problem is computed in total for 10s, and the results for certain intermediate steps are displayed in Figure 6.18.

As expected, the cable deforms due to the self-weight of the cylinder and therefore the cylinder starts to slide along it. Due to the applied damping, the cylinder slides toward the right support for about 6s before stopping and sliding back to the middle of the cable, where it finally arrests.

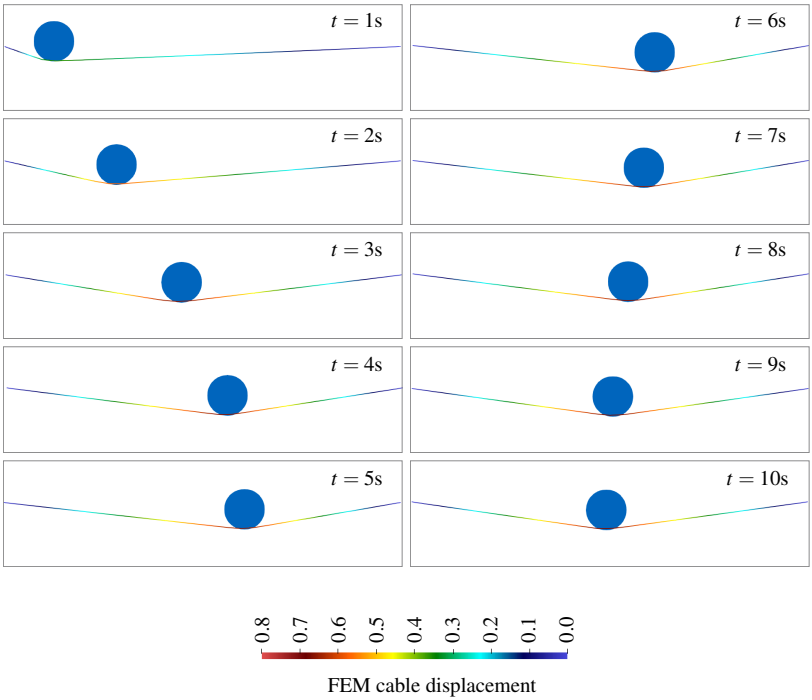

Figure 6.18: Numerical results of sliding cylinder on the flexible structure at specific times.

To verify the results of the numerical simulation, the balance of forces at the cable structure is investigated. First, the sum of the vertical reaction forces at the FEM cable structure is compared in Diagram 6.19 with the theoretical reference solution to ensure that the self-weight of the cylinder modeled with MPM is correctly transferred to the FEM cable elements.
It is observed that after a dynamic force peak caused by the sudden loading of the structure, the reaction forces converge to the expected theoretical solution, which is defined by

$$F_{z,ges} = r^2 \cdot \pi \cdot h \cdot \rho_{\mathrm{M}} \cdot g + A \cdot L \cdot \rho_{\mathrm{S}} \cdot g = 54.70\mathrm{kN}. \tag{6.16}$$

Since the vertical forces are correctly transferred, the horizontal reaction forces are to be analyzed in a second step. For this purpose, a simplified structural model as depicted in Figure 6.20 is used to analytically calculate the horizontal reaction forces of the cable structure.
Hence, the reference solution assumes that the forces induced by the cylinder are concentrated in one vertical force $F_{\mathrm{g,cyl}}$ equal to the total weight of the cylinder.

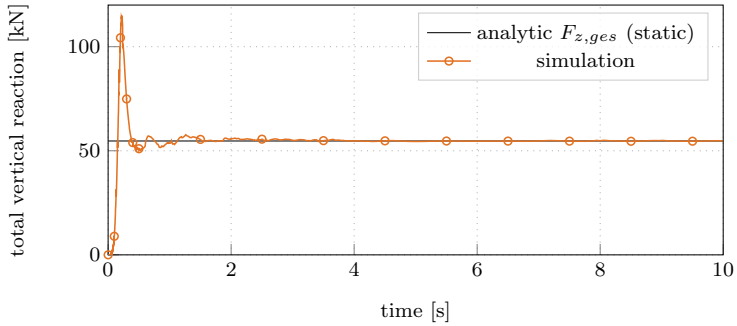

Figure 6.19: Comparison of the vertical reaction forces of the FEM cable with the analytic static solution.

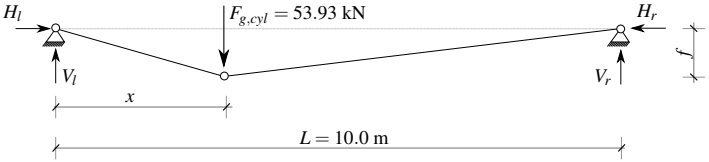

Figure 6.20: Structural model to calculate the analytic reference solution.

The pre-stress and self-weight of the cable are neglected because they are minor in comparison to the force induced by the cylinder.
Therefore, the horizontal force H_l at the left support can be calculated by

$$H_\mathrm{l} = -\frac{1}{f} \cdot \frac{F_\mathrm{g,cyl} \cdot (L - x) \cdot x}{L} \tag{6.17}$$

assuming that f is the vertical deflection at the location x where the vertical force $F_\mathrm{g,cyl}$ acts. The position of the load x and the deflection f are determined from the movement of the center of the cylinder.
The comparison of the left reaction force obtained from the simulation and the theoretical one is plotted in Diagram 6.21.
Since the deflection of the cable is zero at the initialization of the system, the reference solution is not defined in the very first step and then approaches from infinity. In the numerical model, on the other hand, a negligible pre-stress is applied providing a non-singular stiffness matrix at the beginning, and due to the applied loads, the reaction force increases at the beginning of the simulation. After the initiation, a small difference between the two curves is observed until they approach the same solution. The deviation of the curve is due to the fact that the position x and the deflection f are obtained from the motion of the cylinder center. As illustrated in the left Figure 6.22, the inclination of the cable elements on the left side of the cylinder is steep at the beginning of the simulation. Therefore, the loads induced by the cylinder, labeled by $F_\mathrm{g,cyl,sim.}$ in the Figure 6.22,

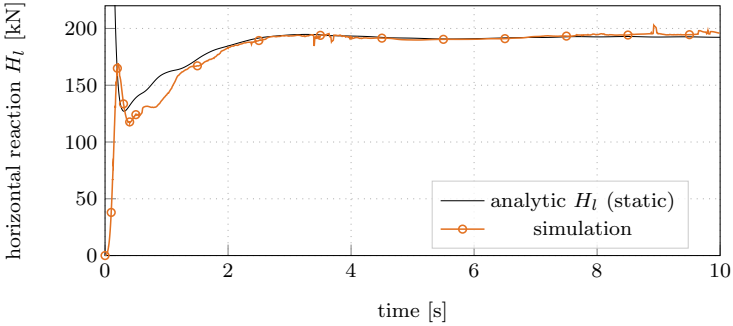

Figure 6.21: Comparison of the horizontal reaction force H_l of the FEM cable at the left support with the analytic static solution.

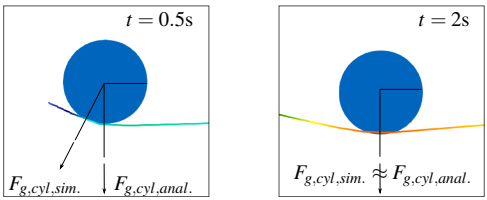

Figure 6.22: Direction of the resulting force dependent on the inclination of the cable.

are acting normal to the inclined elements. For the simplified theoretical solution, however, the force is assumed to act in the vertical direction based on the center of the cylinder. Consequently, the assumed force labeled by $F_{\text{g,cyl,anal.}}$ in Figure 6.22 has a different direction and an increased distance to the support. Therefore, the theoretical approach overestimates the horizontal reaction force at the beginning of the simulation.

After about 2s of simulation time, the inclination of the cable elements is of minor importance, as visualized in the Figure 6.22(right). Therefore, the direction and position of the actual forces $F_{\text{g,cyl,sim.}}$ and the approximated ones $F_{\text{g,cyl,anal.}}$ are nearly identical. Hence, a good agreement of both solutions (see Diagram 6.21) is obtained proving that the interface data is correctly transferred.

Furthermore, this example demonstrates that the proposed approach can efficiently solve complicated loading scenarios on flexible structures. This is particularly interesting when instead of elastic bodies, granular material or fluids cause the deformations of the flexible structure.

6.2.5 Cylinder Impacting Flexible Structure

In section 3.5.3 the impact of an elastic cylinder on a rigid wall is intensively studied. To verify the MPM-FEM coupling methodology, this example is extended by replacing the rigid boundary with a flexible structure.
As illustrated in Figure 6.23, the elastic cylinder with radius $r = 0.5$m and height $h = 0.3$m has a prescribed velocity in the vertical direction. The cylinder is modeled with MPM assuming a linear elastic material. The considered material parameters are equivalent to the example with the rigid boundary (see section 3.5.3) and are therefore summarized in Table 3.2.

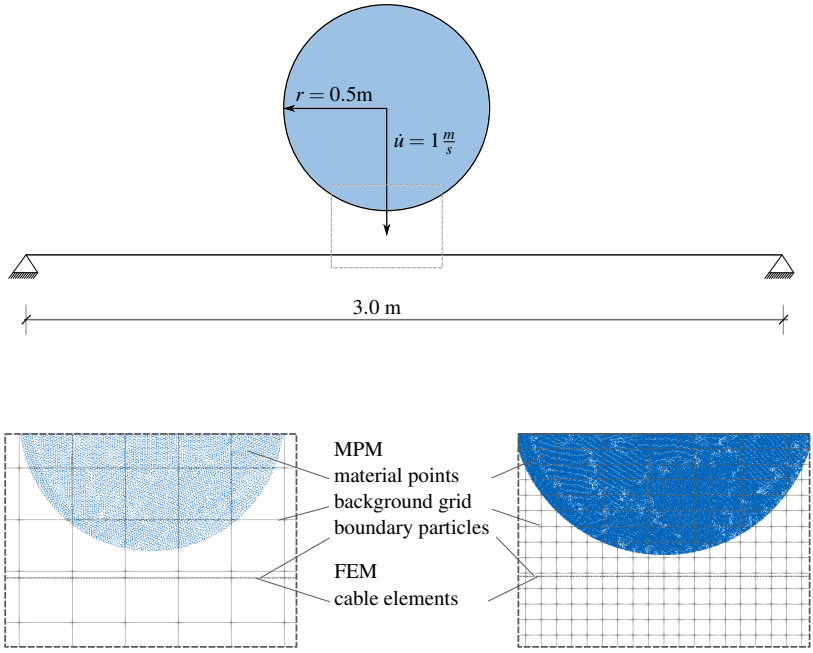

Figure 6.23: System setup of the cylinder modeled with MPM impacting a flexible structure with FEM. The details show two different MPM discretizations which are investigated.

The flexible structure that replaces the rigid boundary is modeled with FEM using cable elements. A length of 3.0m and a cross-section of 0.001m^2 are selected for the structure, while the elastic object impacts at its center. A linear elastic material is selected for the cable elements, while the parameters, which are identical to those of the previous example, are summarized in Table 6.1.
For the calculation of the FEM model, the flexible structure is subdivided into 5 equally sized cable elements. Additionally, a negligible pre-stress of 1.0N/m^2 is considered to stabilize the cable structure in its undeformed configuration.

To model the cylinder, two different discretizations are selected for the MPM model as depicted in the details of Figure 6.23. For the model shown on the left, a coarse discretization of the background grid is selected using a structured quadrilateral background grid with an element size of 0.2m. The discretization is selected analogously to the coarse discretization investigated in section 3.5.3, where the influence of different background grid element sizes are investigated. For the relatively large element size, however, it is important to define the boundary nearby the element border to reduce the artificial crumple zone introduced by the background grid discretization. As demonstrated in Figure 3.21b), even with the coarse discretization a good approximation of the contact force is obtained due to the initialization of the boundary nearby the element border.

The advantage of this special discretization when investigating the interaction with a highly flexible structure is that the boundary particles following the movement of the cable elements remain in the same row of background grid elements. This ensures that as soon as the material points discretizing the cylinder enter the background grid elements containing boundary particles, the contact between the structure and the impacting object is detected until the cylinder rebounds.

This is a major difference to the finer background grid discretization depicted in the right detail of Figure 6.23. For this model, an element size of 0.05m is selected for the structured quadrilateral background grid. Consequently, the boundary particles which are following the movement of the flexible structure are changing their background grid elements due to the impact of the elastic cylinder. Since the contact detected via the computational background grid in MPM is only detected in case material points and boundary particles are within one element, the contact between the structure and the impacting object may get lost during the impact. This is the case when the boundary particles are found in another background grid element while the material points are still in the previous element. Therefore, to investigate the resulting consequences for the calculation of the coupled model, these two different discretization of the MPM model are considered.

The material points discretizing the cylinder are initialized in both models by a triangular body mesh with an element size of 0.01m. While in case of the coarse background grid 1 material point per element is initialized, 6 material points are defined in case of the refined background grid.

Analogous to the example of the cylinder impacting the rigid wall, a time step of $\Delta t = 2e-4$s is selected for the coupled simulation. Structural damping is neglected in this study.

In Diagrams 6.24 and 6.25, the energy of the involved partitions as well as the total energy of the coupled system are plotted for the coarse and the fine background grid discretization, respectively.

The conservation of energy is maintained in both MPM models. The kinetic energy initially stored in the MPM partition is transferred to the FEM submodel during the impact. The maximum energy in the FEM subsystem is stored at the point of maximum deflection when the elastic cylinder stops moving. Subsequently, the energy is transferred back to the MPM partition, causing the cylinder to move upwards again until it separates from the cable. A portion of the energy remains in the structure, causing it to vibrate, while the majority of the energy is transferred back to the MPM system.

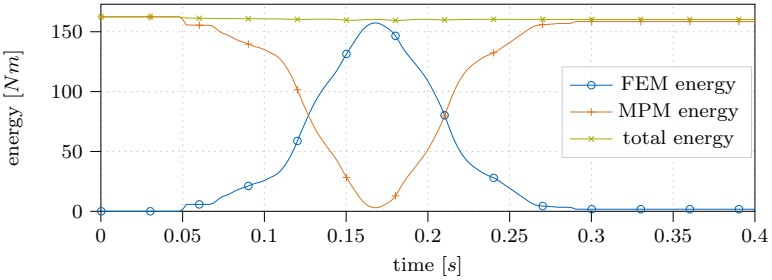

Figure 6.24: Energy plot of coupled MPM-FEM simulation using the coarse MPM background discretization.

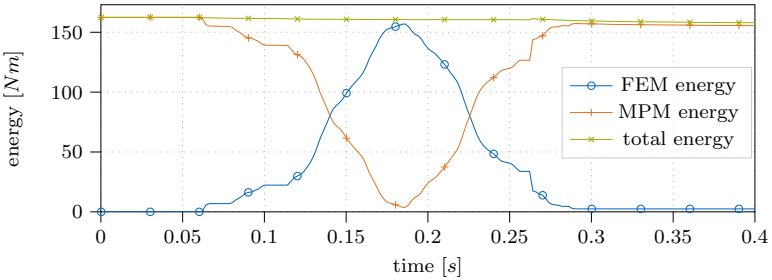

Figure 6.25: Energy plot of coupled MPM-FEM simulation using the fine MPM background discretization.

For both models, it is observed that a portion of energy is transferred at the very first contact between the cylinder and the structure, followed by a short period where almost no energy is transferred. The low energy transfer during this period is due to the low stiffness of the cable elements in their nearly undeformed state, while the initial jump is caused by the sudden contact detection when the material points enter the background grid elements containing the boundary particles.

Thereafter, the model with the coarse background grid discretization shows a continuous energy transfer, whereas the model with the fine discretization exhibits several periods of low energy transfer. These intermediate periods of low energy transfer occur when the boundary particles move to the subsequent background grid element containing no material points and the associated loss of contact.

To illustrate this effect, the MPM model at times $t = 0.09$s and $t = 0.11$s is shown in Figure 6.26. While the material points and boundary particles in the left figure are located within the same background grid elements, they are located in different elements in the right figure causing the loss of contact.

It is important to emphasize that the MPM discretization in this example was

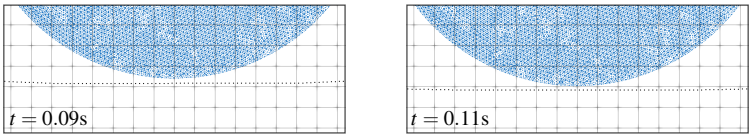

Figure 6.26: In the left figure boundary particles and material points are located in the same background grid elements while in the configuration on the right they are located in different elements.

intentionally selected to study the effects of contact loss during the coupled simulation. Typically, examples are initialized in such a way that not all boundary particles lose contact with the material points at the same time allowing for continuous energy transfer.
In Figure 6.27, the displacements of the cylinder center are plotted for the coarse

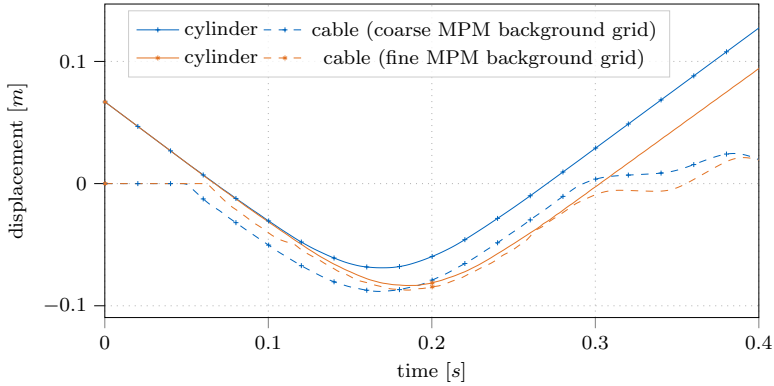

Figure 6.27: Displacement of the cylinder center for the coarse and fine background grid discretization. Additionally the deflection of the FEM cable elements is depicted.

and the fine MPM background grid discretization. It shows less deflection of the cylinder in the case of the coarse background grid discretization compared to the finer background grid.
Again, the main reason for the difference is the contact detection in the MPM solver. Since the contact is detected as soon as the material points enter the background grid elements containing the boundary particles, a gap between the impacting object and the shared interface remains in the calculation. For the coarse discretization, this gap is larger than for the fine discretization, resulting in less deformation of the cylinder in the former case. The gap resulting from the contact detection in the MPM solver is also visible in Figure 6.28, showing the maximum deflection of the cable structure for both the coarse and fine MPM discretizations.

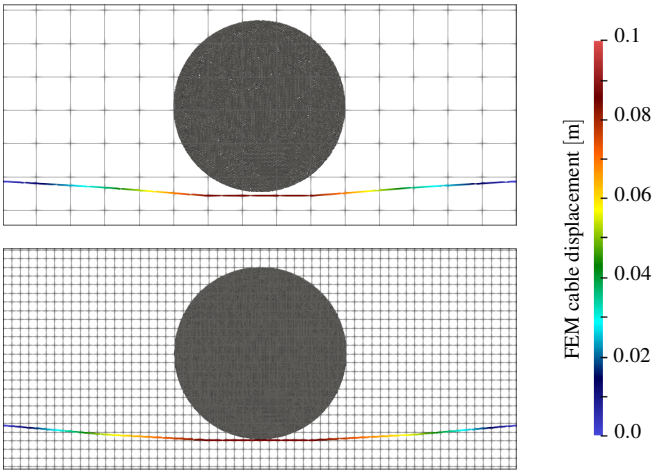

Figure 6.28: Maximal deflection of the flexible structure for the coarse and fine discretization of the MPM model.

However, the deflection of the flexible structure is nearly identical regardless of the considered MPM background grid discretizations. To demonstrate this, the deflection of the cable structure is also added to Diagram 6.27 (dashed line) for both models. Except for a shift in timing due to the first contact detection via the background grid, the structural displacements are almost identical. This is an important finding since the maximum deflection of the flexible structure is an important value for designing the structures for the impact.

Closely related to the structural deformations are the reaction forces at the supports of the structure. In Diagram 6.29, the sum of the vertical reaction forces of the cable structure are plotted for both models.

Analogous to the cable deflection, the resulting reaction forces are shifted in time, but both the coarse and fine MPM background grid discretizations show the same pattern and calculate almost the same peak force, which again is decisive for the design of the structures.

For comparison, the impact force calculated in section 3.5.3 for the cylinder impacting the rigid wall is added to the plot. This illustrates the advantages of flexible structures compared to a rigid ones. Due to the structural deformations, the forces are significantly reduced while the impact duration is extended.

The conclusions of this example are that the energy of the coupled system is well preserved. Furthermore, it is demonstrated that for the design of the flexible structure, the background grid discretization of the MPM model is of minor importance as long as it can model the behavior of the impacting body. Finally, the significant reduction of the impact force peaks due to the flexibility of the structure are evidenced.

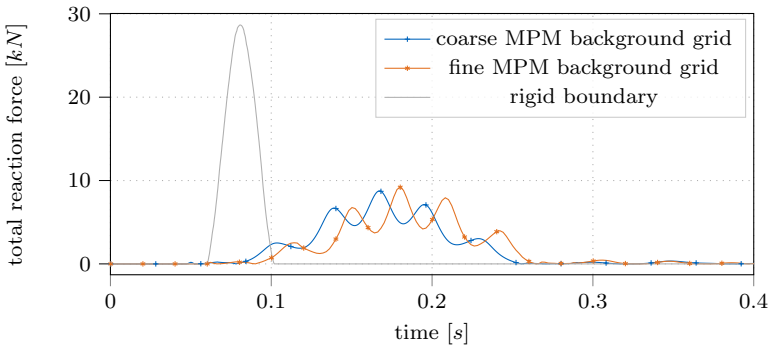

Figure 6.29: Reaction forces at the cable structure due to the impact for the coarse and fine MPM discretization in comparison with the impact forces at a rigid boundary.

6.2.6 Granular Material Impacting Flexible Structure

The previous examples systematically assessed the partitioned MPM-FEM coupling scheme for elastic materials. However, the main advantage of MPM is that materials with large strains can be modeled without mesh entanglement problems. Hence, in this example, the elastic material of the impacting object is replaced by a granular material which includes plastic deformations of the material.
As depicted in Figure 6.30, the granular material, initially confined to a cylindrical shape with radius $r = 0.5$m and height $h = 0.3$m falls down due to gravity and impacts a flexible structure with length 10.0m, while the initial distance between the flexible structure and the cylindrical shape of the impacting object is 0.1m.

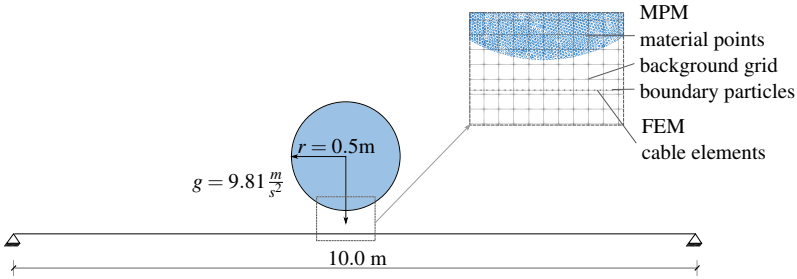

Figure 6.30: System of the cable and the cylinder made of granular material.

As in the previous examples, the impacting body is modeled by MPM, while the flexible structure is analyzed by FEM. The structure is modeled by cable elements with a cross-section of 0.001m^2 and a linear elastic material is assumed. The

selected material parameters, which are identical to the previous examples, are summarized in Table 6.1.
For the impacting object, a Mohr-Coulomb yield criterion is selected to model the elastic-plastic material behavior. The material parameters are selected analogous to the example in section 3.5.4, where the impact of a granular material onto a rigid wall was analyzed. Therefore, the material properties of the granular material are summarized in Table 3.4.
For the numerical simulation, both partitions are discretized individually. The flexible structure is subdivided into 7 equally sized cable elements. As before, a negligible pre-stress of 1.0N/m^2 is applied, while the self-weight of the structure is neglected. Additionally, Rayleigh damping is applied to the structure with the coefficients $\alpha_d = 0.0$ and $\beta_d = 0.1$.
For the calculation of the granular material, a structured quadrilateral background grid with an element size of 0.05m is chosen, while the material points are initialized by a triangular body mesh with an element size of 0.01m, placing 3 material points each. Thus, the discretization is selected analogously to the previous examples (see section 6.2.4).
The shared interface is defined along the flexible structure and in the MPM partition boundary particles are therefore introduced along the geometry of the structure with an initial distance of 0.02m to ensure good mapping properties. These boundary particles follow the structural movement and impose Dirichlet constraints on the MPM submodel using the Lagrange multiplier method. For this example, a fixed condition is assumed which decelerates the side-wards moving granular material after the impact.
Figure 6.31 shows the numerical results of the coupled simulation obtained with a time step of $\Delta t = 1e-4\text{s}$ for specific times.
Furthermore in Diagram 6.32, the structural displacements at the center are plotted during the simulation time. After the maximum deflection at about $t = 0.48\text{s}$, the structural displacements decrease and converge to the static value. For the granular material, a similar progression of the point initially located at the center of the cylinder is observed. Due to the initial gap between the structure and the cylinder, the displacement measure starts at -0.1m. The maximal deflection is also observed at about $t = 0.48\text{s}$. However, the value is larger compared to the structure because the granular material itself deforms due to contact with the structure.
The sum of the vertical reaction forces at the supports of the flexible structure are plotted in Diagram 6.33. After the dynamic impact, the value converges to the expected static solution corresponding to the self-weight of the cylinder

$$F_{\text{g,cyl}} = r^2 \cdot \pi \cdot h \cdot \rho \cdot g = 3.19\text{kN} \tag{6.18}$$

while ignoring the self-weight of the structure itself.
Before the forces converge to the static expected value, a significant impact force consisting of two main peaks is observed. This corresponds well to the results obtained in section 3.5.4 for the impact forces of a granular material onto a rigid wall. Although a different load case is assumed in section 3.5.4, the distribution of the impact force shows some similarities.
For the numerical example with the rigid wall, a significant peak force followed by a sudden decrease of the force is observed before the impact forces fluctuate

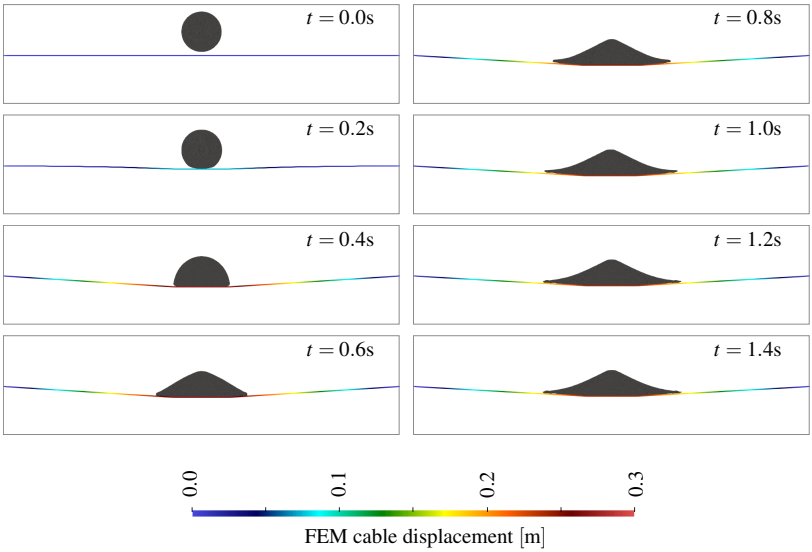

Figure 6.31: System of the cable and the cylinder made of granular material.

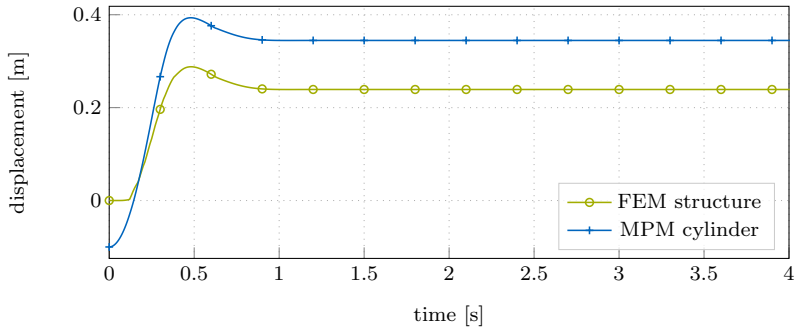

Figure 6.32: Displacement of the cylinder center modeled with MPM and the center of the flexible structure during the simulation.

to zero in smaller waves (see Diagram 3.27). The sudden decrease of the forces is caused by the plastic deformations. This behavior, although not as significant, is also present in this example where the granular material impacts the flexible structure. After the first impact peak, the force decreases due to the plastic deformation of the material before reaching the second main peak and then decreasing to the static value.

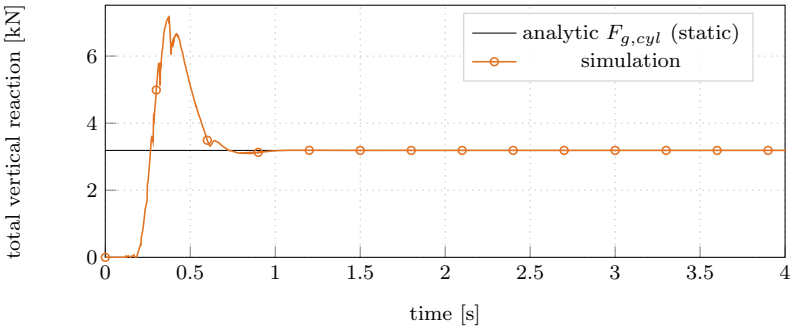

Figure 6.33: Reaction forces at the cable structure due to the impact of the granular material.

6.2.7 CTI Frame

To validate the MPM-FEM coupling methodology, a comprehensive comparison with physical experiments is essential. For this purpose, the impact of a concrete block on a flexible net structure is investigated. The associated experiments were carried out by Geobrugg at their test site in Walenstadt, Switzerland. In these tests, a standardized* concrete block is dropped from a height of 2m onto a DELTAX® G80/2 [57] net spanned into a CTI-frame with rigid boundaries.
Figure 6.34 shows a photograph of the CTI-frame and the concrete block at the test site.
The block dropped into the center of the net has a side length of 0.41m and a total mass of 180kg which includes the attached wire rope strap with a weight of 5kg. The size of the net is $3.9 \times 3.9\text{m}^2$ and it is rigidly attached to the frame by shackles. In Figure 6.35, the schematic system setup is illustrated.
The experiment is designed such that the block rebounds without damaging any of the mesh wires and is conducted in total five times with constant input parameters. Further details of this example and the experimental setup can be found in [101, 103].
To numerically investigate these experiments, the concrete block is modeled with MPM while the flexible net structure is calculated by FEM. Although MPM may not be the most intuitive method to model the impacting concrete block, these experiments offer the significant advantage of well-defined model parameters. This allows to focus on the validation of the coupling methodology, which is the purpose of this example.
Furthermore, the parameters for modeling the complex net structure with FEM can also be taken from the literature without the need for additional calibration. In [103], Sautter et al. numerically investigated these experiments using a partitioned coupling of DEM and FEM. Hence, the model parameters for the FEM model are adopted for this validation example.

* Swiss Agency for Environment, Forests and Landscape (SAEFL)

Figure 6.34: Photograph of the CTI-frame at the testing site in Walenstadt, Switzerland. The photograph is taken from [103].

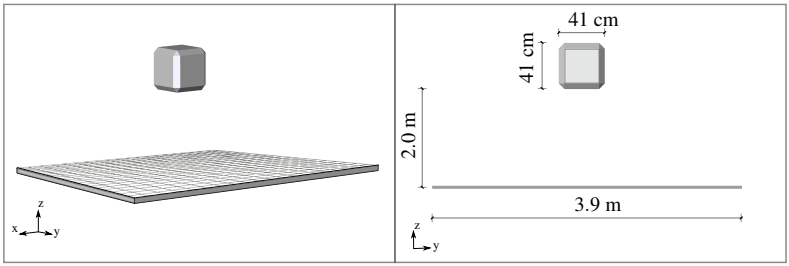

Figure 6.35: Schematic illustration of the experimental setup.

Thus, a simplified structural model is used to capture the load bearing behavior of the net structure for this test setup. Therefore, instead of modeling the wire of the net, the surface is homogenized and membrane elements are used to describe the structural behavior. As these elements have zero out-of-plane stiffness, only in-plane stresses, and no rotational nodal degrees of freedom, a negligible pre-stress of 0.01N/m^2 in the in-plane directions is applied, providing a non-singular stiffness matrix at the beginning of the simulation.
Within the experiments, the initial sag of the net due to gravity varied $+/-5$cm, since the tensioning force of the net was not directly measurable when spanning it into the test frame. Therefore, from the five tests conducted, the data of the experiment with the minimum sag of 0.05m and the one with the maximum sag

Young's modulus	Poisson's ratio	density	thickness
$E = 5e7\text{Pa}$	$\nu = 0.0$	$\rho = 81.25 \frac{\text{kg}}{\text{m}^3}$	$8e-3\text{m}$

Table 6.2: Material properties of the membrane elements to model the net within the CTI-frame.

of 0.10m, labeled exp_1 and exp_2, are extracted and considered for the comparison.
Following [101, 103], the numerical model is designed to fit the measured sag of test exp_1. Therefore, the utilized Young's modulus of the membrane elements is calibrated such that an initial sag of 0.05m is obtained. Furthermore, a linear elastic material model is assumed since no failure of the net is observed. In Table 6.2, the material properties of the structural model, which are taken from [101, 103] are summarized.
For the discretization of the structural model, a structured quadrilateral mesh with an element size of 0.1m is selected.

Also for the impacting object, which herein is calculated with MPM, a linear elastic material law is assumed. The Young's modulus and Poisson's ratio are set to $E = 5e6\text{Pa}$ and $\nu = 0.0$, respectively. The density is adjusted to obtain a total mass of 180kg for the impacting object.
It is important to note that the value of the Young's modulus of the impacting object in the numerical model needs to be adjusted so that the impacting block behaves like a rigid object compared to the deformations of the flexible net structure. Nonetheless, the stiffness of the impacting object should be selected with considerations of the stiffness of the flexible structure. This is because using values that are too large may result in numerical instabilities in the coupled simulation.
For the discretization of the MPM model, a structured hexahedral background grid with an element size of 0.08m is selected, while the material points are initialized by a tetrahedral body mesh with a size of 0.04m, placing 3 particles each. At the shared interface, which coincides with the initial geometry of the FEM membrane structure, the boundary particles in the MPM partition are created. For their initialization, a structured triangular mesh of size 0.01m is selected, initializing 3 boundary particles each. This discretization ensures that the data at the interface can be mapped properly. The interface condition is imposed by penalty augmentation using a penalty factor of $\beta = 1e10$ and modeling a contact condition.
The entire model is solved using the partitioned strong coupling scheme described in Algorithm 2. For the calculation a time step of $\Delta t = 5e-5\text{s}$ is selected and Aitken relaxation (see section 4.3.2) is applied. Furthermore, Rayleigh damping with coefficients of $\alpha_d = 0.0$ and $\beta_d = 0.02$ is used to damp the dynamic response in the numerical model.
During the physical experiments, the displacement and velocity of the impacting object as well as the reaction forces at the edges of the net structure were measured. Further details on the measuring equipment used and the evaluation of the test data can be found in [101, 103].

The measured data are compared to the numerical results of the coupled MPM-FEM model. Although the modeled system setup is more similar to the first experiment, the data from the second experiment are also included in the plots to demonstrate the variability of the measured data even if the overall test setup is kept constant for the experiments.

The displacement of the concrete block over time is plotted in Diagram 6.36 showing the comparison between the experimental data and the numerical re-

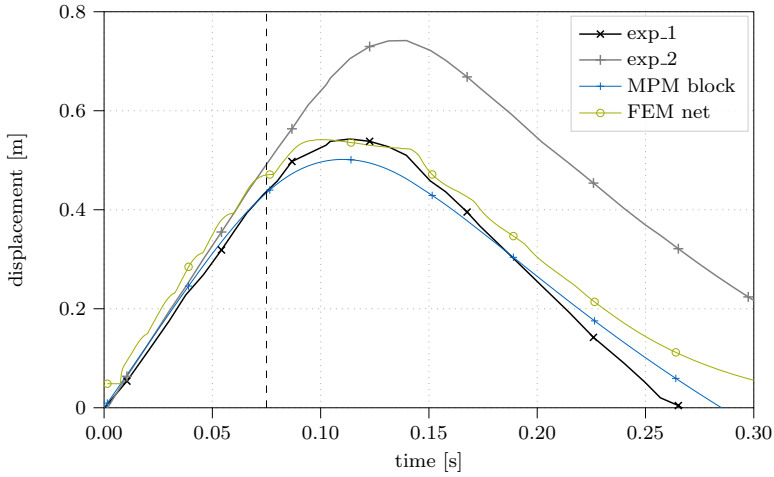

Figure 6.36: Displacement comparison

sults. The plot shows that the displacement of the block modeled with MPM closely follows the measured displacement obtained by exp_1, but slightly underestimates the maximum deflection. The reason for the underestimation arises from the contact detection via the computational background grid in the MPM model.

As detailed in section 3.4, the Dirichlet constraint at the shared interface imposed by boundary particles along the membrane structure affects the material point movement as soon as boundary particles and material points are found within the same background grid element. Consequently, the concrete block represented by material points is constrained before it actually touches the shared interface, resulting in an offset between the boundary particles and material points. This phenomenon is visualized in Figure 6.37 where the discretized model is displayed. Both figures show the offset between the concrete block, represented by material points, and the structural surface, which defines the position of the boundary particles in the MPM model.

In the left figure, both boundary particles and material points are found in the same background grid elements, causing an interaction with the structure although they are not actually in contact. Obviously, a refinement of the computa-

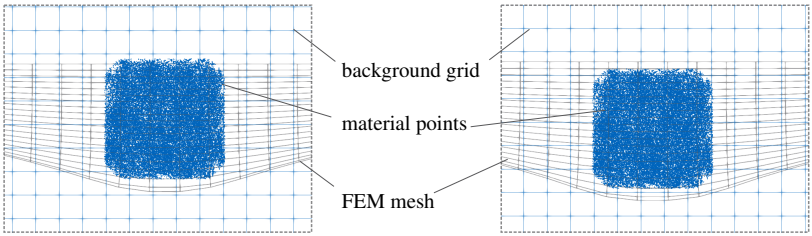

Figure 6.37: Discretization of the coupled model at two different times. The left figure shows the model when material points and boundary particles are within the same background grid element, while in the right figure they are not.

tional background grid will reduce this offset, but simultaneously increases the computational cost.
Hence, in addition to the block displacement, the center deflection of the FEM structure is plotted in Diagram 6.36. It shows that the maximum deflection of the net structure agrees very well with the deformation measured in the experiment. Therefore, although a rather coarse discretization of the background grid with an element size of 0.08m is chosen, the experimental results are still well predicted. This agrees well with the results of the verification example in section 6.2.5.
In addition, Figure 6.38 shows the maximum deflection obtained in the numeri-

a) Maximal deflection, experiment

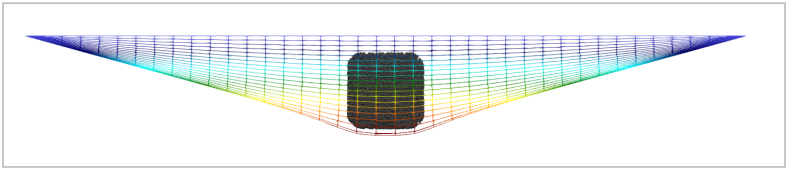

b) Maximal deflection, simulation

Figure 6.38: Comparison of the maximal deflection in the experiment and the numerical solution. Photograph a) is taken from [103]

cal simulation and a corresponding photograph of the physical experiment. Also here, the small offset between the structure and the block in the numerical result

is visible, whereas the deformation of the membrane structure shows an excellent agreement with the actual deformation of the physical net.
However, the comparison of the net displacement and the MPM block displacement plotted in Diagram 6.36 also shows that the offset between them is not constant, but varies slightly during the impact. This is also caused by the background grid discretization within the MPM model.
As depicted in the right of Figure 6.37, in some configurations the boundary particles below the block, which are aligned on the surface structure, may get found in a background grid element not containing material points of the concrete block. Therefore, in this configuration they do not constrain the movement of the block, resulting in an intermediate reduction of the offset. For example, at about $t = 0.075$s, where the dashed line in Diagram 6.36 is drawn, the structural displacements are temporally not affected by the block motion since the boundary particles and material points are decoupled due to the background grid discretization.
The dependence of the numerical results on the computational background grid in the MPM model can also be observed when the reaction forces of the numerical simulation are compared with the experimental results. In Diagram 6.39, the

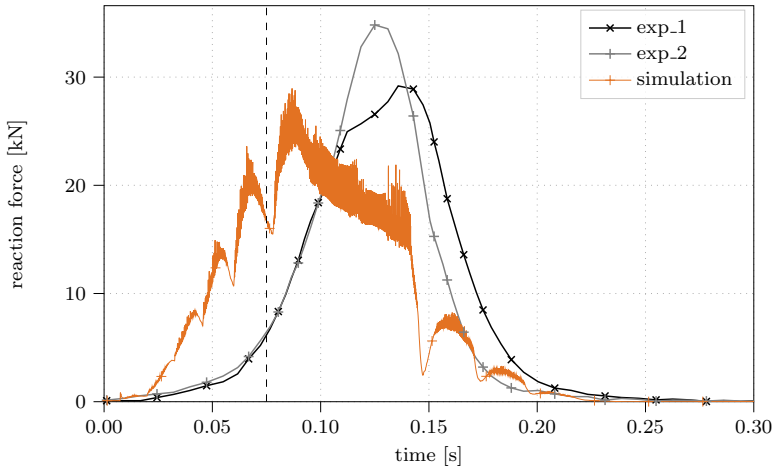

Figure 6.39: Reaction forces comparison

measured forces of the net structure are compared with the force resulting from the numerical simulation. The latter force is obtained by summing the reaction forces along the boundary nodes of the FEM structure.
Again, at about $t = 0.075$s, which is indicated by the dashed line, a significant reduction of the reaction force is observed, which is caused by the loss of contact due to the background grid discretization. This effect can be observed several times during the impact, causing a reduction of the reaction forces and the wave-like curve of the FEM structure center deflection in Diagram 6.36.

	exp_1	exp_2	simulation
total impuls [kNs]	2.29	2.16	2.17

Table 6.3: Total impuls of exp_1 and exp_2 in comparison to the result from the simulation.

Furthermore, there is also a significant difference in the timing of the measured and calculated forces. This is again caused by the background grid discretization of the MPM model and the resulting offset between block and structure. As visualized in Figure 6.36, the center deflection of the FEM structure at the beginning of the impact is larger than the measured deformations of the experiment, causing an earlier increase of the reaction forces. A refinement of the background grid discretization in the MPM model will reduce this effect.

Nonetheless, the peak force, which is the most important value for the design of the structure, is predicted very well by the numerical model not necessarily requiring a further refinement.

In addition to the force distribution, the global behavior of the impact should be analyzed. Therefore, the total impulse which is obtained by integrating the reaction forces over time should be compared to the values from the experiment. In Table 6.3 the results are summarized. While the impulse obtained from the simulation slightly underestimates the impulse from exp_1 by about 5% it is nearly identical to the result from exp_2. Hence, the numerical approach captures the global behavior of the experiments and the obtained value is within the variation of the experiments.

Finally, the measured velocity of the concrete block is compared to the numerical results in Diagram 6.40. Again, a very good agreement of the results is observed,

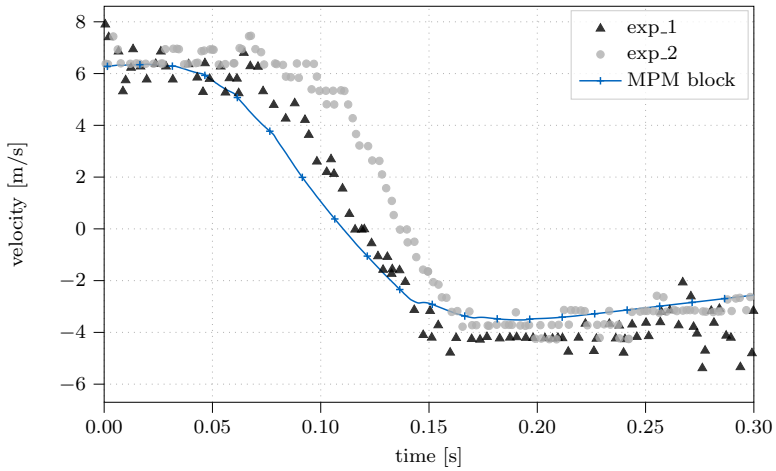

Figure 6.40: Velocity comparison

although the MPM block starts to decelerate slightly earlier than the experimental results. This again results from the contact detection in the MPM model and the resulting offset between the structure and the block. After the maximum deflection, however, the block velocity again agrees very well with the measured values from the experiments.

Summarizing the results of this example, it can be concluded that the background grid discretization in the MPM model is a crucial value when simulating contact. In particular, a coarse background grid discretization results in a time shift and an underestimation of the maximum deflection of the impacting object. Nonetheless, the structural behavior can still be predicted well. Due to the offset between the material points discretizing the impacting object and the boundary particles aligned at the surface of the structure, the structural displacements as well as the peak forces of the structural reactions due to the impact are well predicted. This agrees well with the results of the numerical example in section 6.2.5. In summary, this example shows a good agreement between experimental data and numerical results, thus validating the partitioned MPM-FEM coupling scheme.

6.2.8 Highly Flexible Protective Structure Impacted by Gravity-Driven Mass Flow

The validation and verification examples proved the accuracy of the MPM-FEM coupling methodology. Finally, the developed method is applied to model the impact of gravity-driven granular flow on a highly flexible protective structure. Typically, these structures consist of a net spanned between steel profiles. To enable the structure to undergo significant deformations upon impact, a hinged support is usually incorporated at the base of these profiles. This allows them to rotate around their support point upon impact, activating the stiffness of the cables attached at the top. These cables are spanned uphill and are usually equipped with braking elements to absorb energy through plastic deformation.

To demonstrate that this behavior is captured by the numerical simulation, a 3D model is constructed. This model includes a highly flexible protective structure calculated with FEM, which is subjected to granular mass flow modeled with MPM. As before, the numerical methods are coupled by the developed partitioned coupling scheme.

The design of the protective structure is inspired by the protective barriers deployed at the Veltheim test site in 2010 to experimentally investigate the impact of mudflow on protective structures. However, it is important to note that this example is not intended to be a numerical investigation of these experiments. Rather, it serves as a qualitative demonstration of the methodology developed to analyze the impact of gravity-driven mass flows on highly flexible protective structures.

The protective structure considered has a total length of 15m and a height of 3.5m and is schematically depicted in Figure 6.41.

It is divided into three equally sized fields with two steel profiles at the outer edges and two intermediate ones. They are highlighted in orange in Figure 6.41 and are modeled as truss elements in the FEM model. A linear elastic material is assumed for them, considering the properties of a HEB160 steel profile.

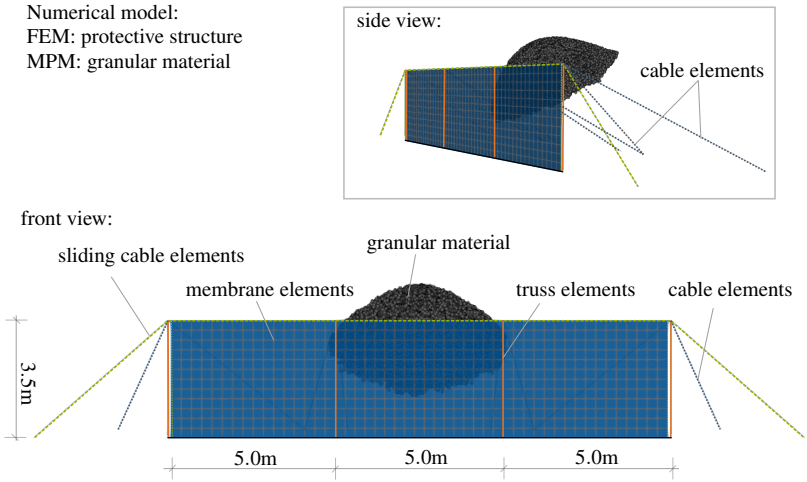

Figure 6.41: System setup of a highly flexible protective structure modeled with FEM and granular material modeled with MPM, which impacts onto the structure.

In between, a flexible net is spanned which is connected to all profiles at the upper and lower point. Furthermore, to prevent lifting of the net due to redirection of the mass flow due to the barrier, the net is fixed to the ground with anchoring nails. In the numerical model a fixed support is therefore considered at the bottom of the net, which is highlighted in black in Figure 6.41. In accordance with the previous example, the net is modeled with surrogate membrane elements in the FEM model. In Figure 6.41, the net modeled with membrane elements is highlighted in blue. The material parameters are approximate and therefore assumed to be the same as in the previous example. Therefore the material properties can be found in Table 6.2.

A cable, to which the net is attached by shackles, is spanned across the width of the structure. It runs along the top of the structure and is then anchored to the ground. In Figure 6.41, this cable is highlighted with dashed green lines. Since the net is attached by shackles to this cable, it can slide along it, allowing larger deformation. To account for this behavior in the numerical model, a sliding cable element according to [21, 127], which was also used by [101] to model the sliding of the net along a cable in rockfall protection nets, is used in the FEM model for this cable. Additionally, this approach is also applied to the cables which are spanned at the outer edges of the net between the top and bottom of the structure. In Figure 6.41 they are also highlighted with dashed green lines.

Finally, the vertical steel profiles with hinged support at the bottom are braced in space with two additional cables each. These cables are spanned uphill and connect the tops of the steel profiles to the ground. Usually, they are not pre-stressed and get activated at the very moment of the impact and the subsequent defor-

mation of the barrier. Furthermore, they are equipped with braking elements. In the numerical model, they are modeled as cable elements and are highlighted with gray dashed lines in Figure 6.41. The top view of the structure, depicted in Figure 6.42, illustrates the geometry of the cables spanned uphill.

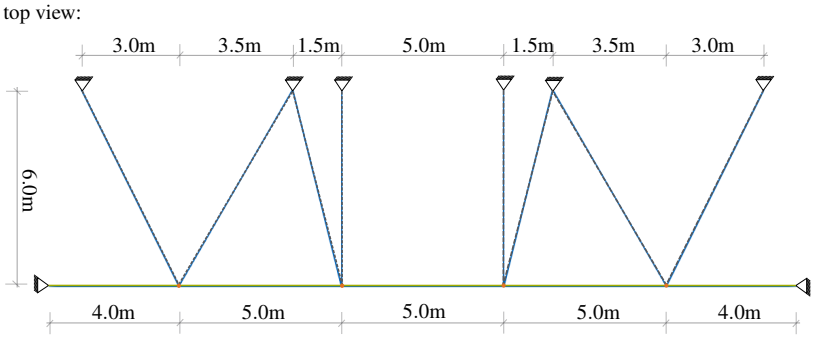

Figure 6.42: Top view of the protective structure.

To simplify the model and to accommodate the flexible nature of the cables spanned uphill, which are additionally equipped by braking elements, a reduced stiffness is applied to these cable elements in the numerical model. Therefore, a Young's modulus of $E = 2.069$MPa is assigned to the cables spanned uphill, whereas $E = 2069$MPa is chosen for the cables in width direction and the steel profiles. The cross-section is assumed to be equivalent for all cable elements, assuming $3.8e-4\text{m}^2$, which corresponds to a diameter of 22mm. The density is set to $\rho = 7850\text{kg/m}^3$ and all cables are modeled without pre-stress.
For the impacting mass flow, dry granular material is considered, which moves down the inclined slope of 30° due to gravity, before impacting the protective structure. In order to approximate the kinematics observed in the experiments, where the mass flow is released 41m upstream of the barrier, a substitute inlet is modeled in this example, focusing on the interaction dynamics.
Therefore, as illustrated in Figure 6.43, the granular material is initially confined into a spherical shape in front of the structure. Due to gravity, the material moves

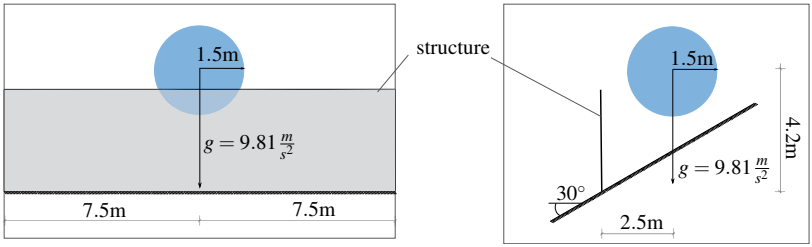

Figure 6.43: Initial geometry of the MPM model.

downward creating an substitute inlet when it hits the inclined slope first and then flows toward the structure. Just before impact, a front velocity of about 8m/s is observed, which is in good agreement with the kinematics of the mass flow observed in the experiments.

For the granular material, a density of $\rho = 2085\text{kg/m}^3$ is selected, which corresponds to the density measured in the experiment for the impacting mass flow. Additionally, a Young's modulus of $E = 6\text{MPa}$, a Poisson's ratio of $\nu = 0.3$, and an internal friction angle of $\Phi = 30°$ are chosen, while Mohr-Coulomb yield criterion is assumed to model the elastic-plastic behavior of the mass flow.

The results of the numerical simulation are visualized for several times in Figure 6.44 and Figure 6.45, visualizing the filling process of the flexible protective structure with the granular mass flow.

Right before the impact, the granular mass flow has a front velocity of approximately 8m/s before contacting the structure at about $t = 0.81\text{s}$. Upon impact, the net, which is modeled by membrane elements, gets deformed locally as visualized in the top snapshot of Figure 6.45.

The comparison of the simulation results at time $t = 0.9\text{s}$ and $t = 1.1\text{s}$ (see Figure 6.44) shows a significant reduction in the velocity of the granular material. This consequently has a great influence on the impact forces which are acting onto the structure. These are plotted in Figure 6.46, showing the peak forces due to the front flow deceleration of the granular mass flow within this time period.

The subsequent reduction of the impact force is accompanied by the redirection of the granular mass, which is in good agreement with the observations made in the experiments and also reported in [128]. This upstream movement of the material is also visible by comparing the images at $t = 1.1\text{s}$ and $t = 1.3\text{s}$ in Figure 6.45. If the net were not fixed to the ground, it would lift and allow some material to pass underneath.

Within this time period, the stiffness of the cables which are spanned uphill are also activated. Due to the deformation of the membrane caused by the impact of the granular material, the steel profiles of the protective structure, which are modeled by truss elements, start to rotate around their support points and their tops move in the direction of the flow. In Figure 6.47, the nodal displacements at the top of the four steel profiles are plotted over time. It shows that the inner steel profiles are the first to be affected by the impact and deform more than the outer profiles, which is well in line with the physical expectation. Furthermore, a very similar deflection of the two outer and two inner steel profiles is observed, which agrees well with the expected symmetry of the system.

The maximum deflection of the inner trusses is reached at about $t = 1.35\text{s}$, triggering the deformation in the outer sections of the flexible structure. The images in Figure 6.44 also show the progression of the structural deformation from a localized disturbance initially to a more widespread effect and finally affecting the hole protective structure. Hence, the deflection of the outer trusses increases, activating the stiffness of the cables attached to their tops, until the peak is reached at about $t = 1.60\text{s}$.

Upon this point, the front flow of the granular mass is stopped, causing the deceleration of the subsequent mass flow without causing further significant deformations of the structure (see Figure 6.45). Also the curve of the impact force in

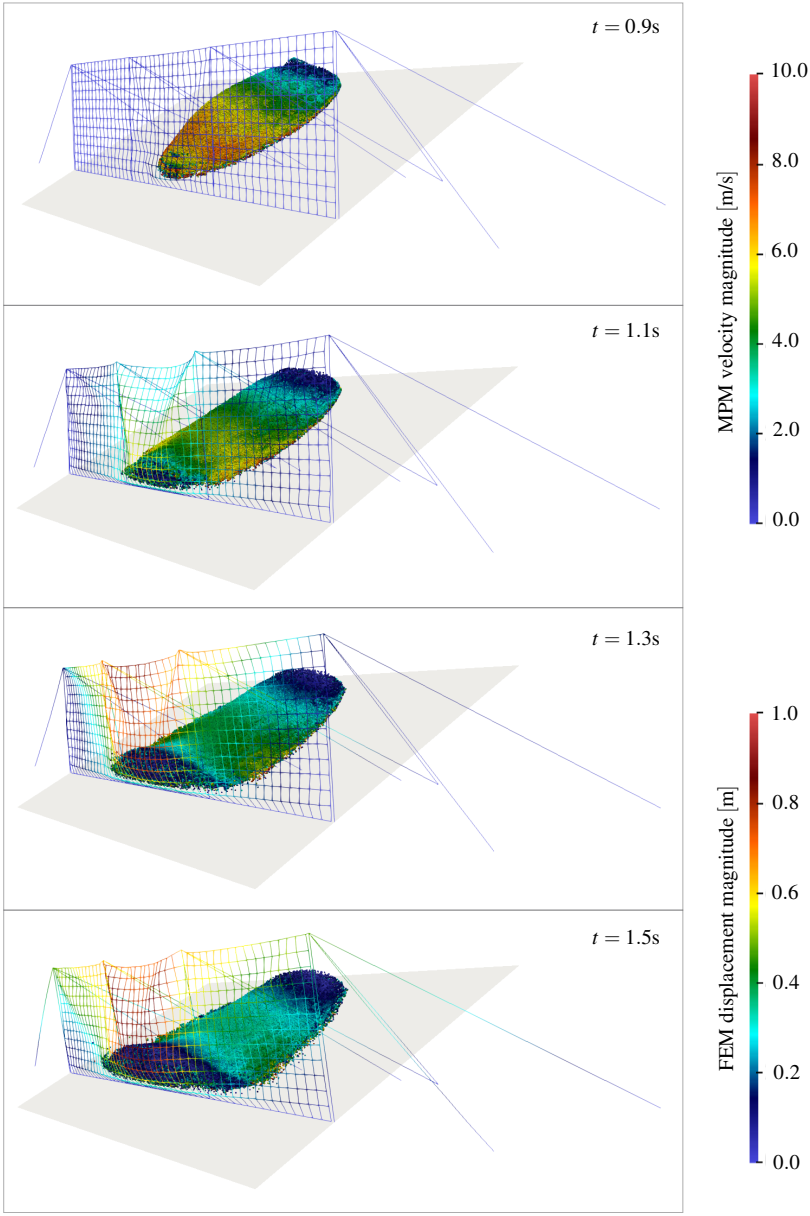

Figure 6.44: Granular material modeled with MPM impacting highly flexible impervious protective structure modeled with FEM. Numerical results for times $t = 0.9$s, $t = 1.1$s, $t = 1.3$s and $t = 1.5$s.

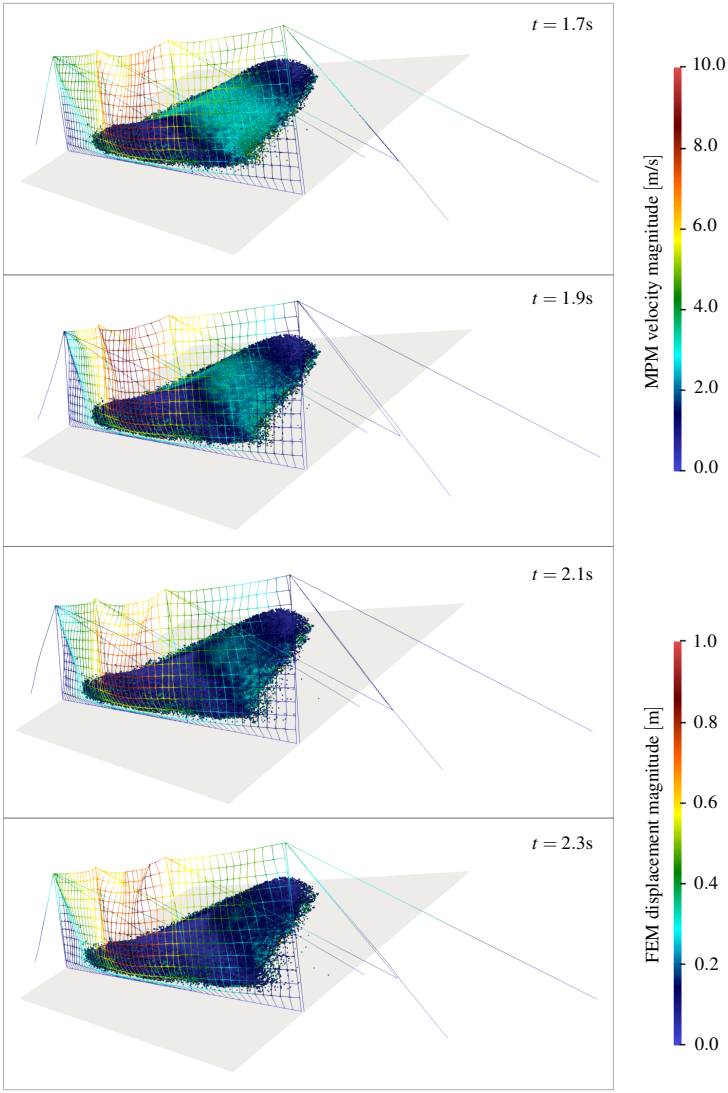

Figure 6.45: Granular material modeled with MPM impacting highly flexible impervious protective structure modeled with FEM. Numerical results for times $t = 1.7$s, $t = 1.9$s, $t = 2.1$s and $t = 2.3$s.

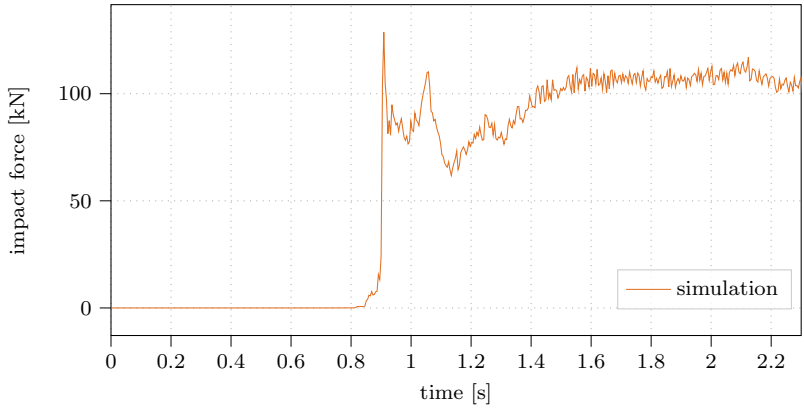

Figure 6.46: Impact force caused by the granular material.

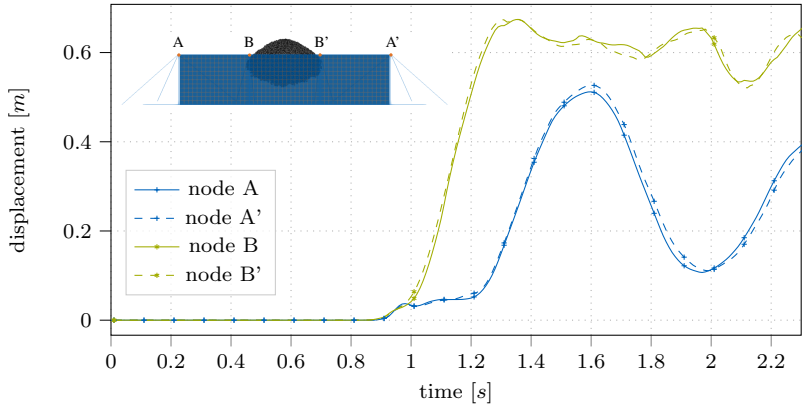

Figure 6.47: Tip deflection of the steel profiles due to the impact of the granular material.

Figure 6.46 shows that upon this time the force converges to the static pressure caused by the granular mass.

The impact force curve depicted in Figure 6.46 highlights the remarkable advantage of flexible protective structures. Due to their flexibility, the structures undergo significant deformation upon impact, which increases the braking distance and thus reduces the impact force. For the example considered the peak force for which the structure needs to be designed is reduced to a value only slightly larger than the static pressure load. Hence, allows the design of both economical and effective protective structures.

However, the design of these structures is a complex task, as they consist of multiple components that must be carefully adapted and harmonized in order to achieve a good load distribution upon impact. For this purpose, numerical simulations supported by physical experiments are inevitable. Additionally, future work is required to enhance the numerical model. For example, in the numerical model of the impacting material, the flow process down the mountains should be considered incorporating terrain data. Furthermore, the constitutive equations need to be adjusted to account for the physical behavior of the material, including the influence of water saturation.

For the structural model, the membrane elements which are utilized to model the ring-net of the protective structures requires further validation and calibration to define an appropriate surrogate. Furthermore, the reduced stiffness of the net in areas that are compressed needs to be incorporated into the numerical model, e.g. using a wrinkling model for the membrane elements. Moreover, the drainage effect of the impacted material and the subsequent flow of the water through the net structure needs to be included in the numerical model.

6.3 Conclusions

The final example demonstrates the effectiveness of the developed partitioned MPM-FEM coupling scheme in simulating the impact of gravity-driven mass flows on highly flexible protective structures. Thus, it enables more efficient design of such structures by allowing detailed investigation of the mass flow behavior during impact through numerical simulations which need to be accompanied by experiments. With these insights, flexible structures can be designed more effectively to ensure even load distribution and proper activation of components such as braking elements integrated into the cable structures.

However, to effectively perform these complicated numerical investigations, the insights gained from the preceding examples are crucial, and the main findings are summarized in the following.

In order to solve the multi-physics problem in a partitioned scheme, the shared interface needs to be defined. It is positioned along the structure and covers at least the areas that are expected to be in contact with the material, modeled with MPM during simulation time. While in the FEM partition point load conditions are initialized at the nodes of the FE-mesh along this interface, boundary particles are created in the MPM partition. The number of boundary particles needs to be larger or at least equal to the number of interface nodes at the FEM counterpart to ensure a proper mapping of the interface data (see section 6.2.1.3). These boundary particles are weakly imposing the Dirichlet condition in the MPM partition. For this purpose the penalty augmentation, the perturbed Lagrangian method and Lagrange multipliers are developed in section 3.4.3 and can be applied interchangeably (see section 6.2.1- 6.2.3). However, for the first two methods, the calibration of the penalty factor is often a crucial task, often requiring pre-knowledge of the numerical solution to set a proper factor. Therefore as an attractive alternative the Lagrange multiplier method is mainly utilized in the examples herein.

All of these types of boundary imposition require a sufficient number of boundary particles to impose the Dirichlet constraints (see [34, 117]) in the MPM submodel. This aligns well with the need for an appropriate interface discretization to ensure accurate data mapping. Another important aspect of the coupling scheme is the inherent handling of the contact detection within the MPM partition via the computational background grid. Hence, when boundary particles aligned at the shared interface are found within the same background grid elements that also contain material points, the Dirichlet conditions are actively imposed and constrain the movement of the material points. Solving the resulting system of equations of the MPM model consequently results in reaction forces at the boundary particles, which are transferred to the FEM partition as external loads due to the mapping process. Conversely, if boundary particles are not interacting with material points zero reaction forces are obtained. Hence, in this case the material discretized by material points is not in contact with the FEM structure and consequently no external loads are applied to the structure. Therefore, the contact detection is inherently included in the MPM submodel, making this approach computationally very efficient and easy to implement.
However, when selecting the element size of the computational background grid, the influence of the contact detection should also be taken into account. The consequences of the discretization, in particular of the computational background grid, on the solution of the coupled problem are discussed in detail in the examples provided in section 6.2.5 - section 6.2.7.
Considering these aspects, the developed MPM-FEM coupling scheme provides a powerful numerical methodology to simulate a wide range of complex engineering problems. It allows to combine the accuracy of FEM to efficiently calculate complex engineering structures with the ability of MPM to model large strain events, such as mass flows in mountainous terrain, using a continuum-based approach. The coupling methodology of these two methods allows to simulate the loading scenarios of mass flows which are impacting highly flexible protective structures. Thus, these numerical simulations provide opportunities to effectively design economical and efficient protective structures in areas at high risk from gravity-driven natural hazards.

CHAPTER 7

Summary and Conclusions

For the numerical simulation of complex engineering phenomena, as the interaction of mass flows impacting protective structures, the coupling of distinct discretization methods is required to simulate these complex physical phenomena. Within the scope of this work, partitioned coupling strategies are developed which allow to solve multi-physics problems by coupling black-box solvers. This approach allows to couple solvers and tools that have been developed over many decades without the need to derive monolithic coupling methodologies. Instead, the interaction of the involved partitions is shifted to their shared interface, thus boundary conditions are imposed in each model along this interface.

The partitioning introduces additional interface equations, which are solved in this work by fixed-point iterations (see chapter 4). These are formulated in a sequential scheme, so that the updated solution of one solver serves as input for the subsequent solver. Hence, the solution strategy uses a Gauss-Seidel communication pattern, while both weak and strong coupling schemes are used to solve the given problems. While strong coupling schemes provide a higher accuracy since the interface transmission conditions are fulfilled up to a certain accuracy, the weak coupling schemes are an attractive alternative due to their computational efficiency. However, the robust imposition of boundary conditions in the involved solvers is required for the coupling strategies.

In this dissertation, gravity-driven granular mass flows acting on flexible protective structures are modeled. Due to the large strains developed in the granular mass flows, MPM is used to discretize the physical problem (see chapter 3). Hence, the flowing material is represented by Lagrangian moving particles, while the governing equations are solved on the Eulerian background grid. This allows granular mass flow to be modeled while avoiding the mesh entanglement problem that limits any Lagrangian mesh-based discretization method. Another advantage of MPM is that its solution scheme includes the solution of a classical updated Lagrangian FEM step. However, it is enhanced by extra- and interpolation strategies to transfer data from material points to the corresponding nodes and vice versa.

However, since the material points move through the Eulerian background grid the imposition of boundary conditions is a complex task. In particular, moving

boundary conditions, which change their position during computation, are crucial since they cannot be imposed at the nodes of the computational background grid in a FEM-like manner. Therefore, boundary particles are introduced, which provide an adequate description of the boundary condition during the computation (see section 3.4.1). They are used to weakly impose both Neumann and Dirichlet boundary conditions in the MPM model, and in case of an interface condition, they receive and send the necessary interface data.

For the partitioned coupling with DEM, a Neumann condition is developed for the MPM submodel, which allows the imposition of point load conditions along moving interfaces (see section 3.4.2). In the DEM counterpart, a wall condition is introduced along the shared interface, which enforces a Dirichlet constraint in the DEM solver. This provides the basis to derive the partitioned coupling of DEM and MPM presented in chapter 5. Due to this coupling, the strength of DEM to compute accurate contact forces, provided the parameters of the numerical model are well calibrated, is combined with the continuum-based approach of MPM to efficiently simulate large scale mass flows. This coupling strategy is successfully applied to simulate the failure process of retaining wall blocks impacted by granular mass flows, and the numerical results are in good agreement with the corresponding physical experiments.

In addition to the numerical simulation of retaining wall systems, the impact of gravity-driven mass flows in highly flexible protective structures is also investigated in this work. For this purpose, the partitioned coupling strategy of FEM and MPM is derived in chapter 6, which allows to combine the strengths of FEM for accurate and efficient modeling of structures, while MPM is advantageous for simulating the large strain event of flowing masses. Along the shared interface, a Neumann condition is introduced in the FEM partition, while in MPM the weak imposition of essential boundary conditions is required.

For this purpose, the penalty method (see section 3.4.3.1) can be used to weakly impose the essential boundary conditions, providing a computationally efficient method. However, the calibration of the penalty factors is a tedious task and numerical instabilities are easily introduced with increasing factors (see section 3.5), which negatively affects the accuracy of the resulting reaction forces and thus the robustness of the coupled simulation. For future improvement, an adaptive calculation of the penalty factor would be beneficial. This could enhance the applicability of the penalty method as a weak boundary imposition method in implicit MPM and thus also in a partitioned coupling strategy.

As an alternative method to weakly impose essential boundary conditions, the Lagrange multiplier method for implicit MPM is developed in this work (see section 3.4.3.2). Consequently, the constraint equations are incorporated into the system of equations of the MPM model. However, this simultaneously introduces difficulties in solving the resulting saddle point problem. Therefore, a constant element-wise approximation of the Lagrange multipliers within constrained elements, combined with a methodology to eliminate superfluous constraints is developed. This provides a suitable Lagrange multiplier discretization in combination with the simple element-wise interpolation functions used in MPM to approximate the displacement field. Furthermore, this boundary imposition method copes with the challenges in MPM of Lagrangian moving material points through an Eulerian background grid, which causes the active background

grid elements to change within each time step.
The developed methodology for weakly imposing essential boundary conditions using Lagrange multipliers provides a robust, efficient and user-friendly boundary condition imposition method that avoids the cumbersome calibration of the penalty factor. Therefore, it can be applied to various application cases (see [117]*) and has proven to be robust also in the partitioned coupling strategy with FEM (see section 6.2).
As a combination of the aforementioned types of boundary imposition methods, the perturbed Lagrangian method is formulated in section 3.4.3.3. In this approach, the constraint equations remain part of the system of equations, but are regularized by an additional penalty term. This avoids the procedure of eliminating superfluous constraints, while introducing the characteristics of the penalty method.
In section 3.5, the performance of the different types of boundary imposition methods is systematically assessed with respect to their applicability as interface condition in a partitioned scheme. Moreover, in section 6.2, the evaluation of the different types of boundary imposition methods is extended to the partitioned coupling strategy with FEM. Provided that the penalty factor is successfully calibrated for the problem to be solved, all types of boundary imposition methods can be used interchangeably as boundary condition and thus as interface condition in a partitioned coupling scheme. However, the Lagrange multiplier method is often preferred because it allows the problem to be solved without requiring prior knowledge of the interface conditions to define the penalty factor.
Various examples of increasing complexity are systematically evaluated in section 6.2 to assess the accuracy of the partitioned MPM-FEM coupling strategy. Finally, the coupling strategy is successfully applied to model the impact of a gravity-driven mass flow simulated by MPM into a highly flexible protective structure calculated by FEM.
Thus, this dissertation provides the foundation for combining the advantages of different discretization methods to solve advanced engineering problems. For future work, some further developments are needed to improve the numerical models of large-scale mass flows acting on protective structures. However, due to the partitioned approach, these developments can be made in the individual sub-solvers without affecting the coupled counterpart.
To enhance the MPM submodel, it is proposed to incorporate the terrain data into the numerical model. This allows the prediction of the flow direction and flow process of mass movement hazards, which is of significant importance for the positioning of protective structures and their dimensions. In combination with calibrated constitutive equations incorporating the influence of water saturation, the developed methodologies can be extended to simulate full-scale experiments for further validation before being extended to large-scale scenarios, which requires additional effort for computational efficiency.
Additional important steps include the improvement of the structural modeling of the highly flexible protective structure. It is of paramount importance to develop and calibrate surrogate membrane elements, which represent the physical behavior of the ring-net. It is essential that these element formulations incorpo-

* published by the author of this dissertation

rate the reduced stiffness in the case of compression, as well as the penetration of some material, including the drainage of water through the net structure. An alternative approach would be to utilize and develop unique element formulations that represent the individual behavior of the rings in the net. This approach may facilitate the modeling of local damage in ring net structures. However, this approach significantly increases the computational cost due to the micro-level element formulations, which include the contact conditions of the individual rings.

Bibliography

[1] A. C. Aitken. XXV.—On Bernoulli's Numerical Solution of Algebraic Equations. In *Proceedings of the Royal Society of Edinburgh*, 1927. DOI: https://doi.org/10.1017/S0370164600022070.

[2] A. Alipour and F. Zareian. Study Rayleigh Damping In Structures: Uncertainties And Treatments [sic]. In *The 14th World Conference on Earthquake Engineering, Beijing, China*, 2008.

[3] F. Alonso-Marroquín and Y. Wang. An efficient algorithm for granular dynamics simulations with complex-shaped objects. *Granular Matter*, 11:317–329, 5, 2009. ISSN: 14345021. DOI: 10.1007/s10035-009-0139-1.

[4] S. Andersen and L. Andersen. Modelling of landslides with the material-point method. *Computational Geosciences*, 14(1):137–147, 2010. ISSN: 1420-0597. DOI: 10.1007/s10596-009-9137-y.

[5] A. Apostolatos, R. Schmidt, R. Wüchner, and K.-U. Bletzinger. A nitsche-type formulation and comparison of the most common domain decomposition methods in isogeometric analysis. *International Journal for Numerical Methods in Engineering*, 97(7):473–504, February 2014. DOI: 10.1002/nme.4568.

[6] E. Aulisa and G. Capodaglio. Monolithic coupling of the implicit material point method with the finite element method. *Computers Structures*, 219:1–15, 2019. ISSN: 0045-7949. DOI: https://doi.org/10.1016/j.compstruc.2019.04.006. URL: https://www.sciencedirect.com/science/article/pii/S0045794919301336.

[7] I. Babuska. The finite element method with penalty. *Mathematics of Computation*, 27:221–228, 1973.

[8] I. Babuška. Error-bounds for finite element method. *Numerische Mathematik*, 16(4):322–333, 1971. ISSN: 0945-3245. DOI: 10.1007/BF02165003. URL: https://doi.org/10.1007/BF02165003.

[9] I. Babuška. The finite element method with lagrangian multipliers. *Numerische Mathematik*, 20:179–192, 1973. URL: http://eudml.org/doc/132183.

[10] S. S. Bandara. *Material point method to simulate large deformation problems in fluid-saturated granular medium*. PhD thesis, University of Cambridge Cambridge, UK, 2013. DOI: 10.17863/CAM.31294.

[11] H. Barbosa and T. Hughes. The finite element method with lagrange multipliers on the boundary: circumventing the babuška-brezzi condition. *Computer Methods in Applied Mechanics and Engineering*, 85(1):109–128, 1991. ISSN: 0045-7825. DOI: https://doi.org/10.1016/0045-7825(91)90125-P. URL: https://www.sciencedirect.com/science/article/pii/004578259190125P.

[12] S. G. Bardenhagen, J. U. Brackbill, and D. Sulsky. The material-point method for granular materials. *Computer Methods in Applied Mechanics and Engineering*, 187(3-4):529–541, 2000.

[13] S. G. Bardenhagen and E. M. Kober. The generalized interpolation material point method. *Computer Modeling in Engineering and Sciences*, 5(6):477–496, 2004.

[14] Y. Başar and W.B. Krätzig. *Mechanik der Flächentragwerke.Theorie, Berechnungsmethoden, Anwendungsbeispiele*. Braunschweig: Vieweg, 1985. ISBN: 3-528-08685-8.

[15] K.J. Bathe. *Finite Element Procedures*. Prentice Hall, 2006. ISBN: 9780979004902.

[16] E. Béchet, N. Moës, and B. I. Wohlmuth. A stable lagrange multiplier space for stiff interface conditions within the extended finite element method. *International Journal for Numerical Methods in Engineering*, 78, 2009.

[17] T. Belytschko, W. K. Liu, B. Moran, and K. Elkhodary. *Nonlinear Finite Elements for Continua and Structures*. John Wiley & Sons, Inc., 2nd edition, 2014. ISBN: 978-1-118-63270-3.

[18] M. Bischoff, K.-U. Bletzinger, W. A. Wall, and E. Ramm. *Models and finite elements for thin-walled structures*. In *Encyclopedia of Computational Mechanics*. John Wiley Sons, Ltd, 2004. Chapter 3. ISBN: 9780470091357. DOI: https://doi.org/10.1002/0470091355.ecm026. eprint: https://onlinelibrary.wiley.com/doi/pdf/10.1002/0470091355.ecm026. URL: https://onlinelibrary.wiley.com/doi/abs/10.1002/0470091355.ecm026.

[19] A.E.J. Bogaers, S. Kok, B.D. Reddy, and T. Franz. Quasi-newton methods for implicit black-box fsi coupling. *Computer Methods in Applied Mechanics and Engineering*, 279:113–132, 2014. ISSN: 0045-7825. DOI: https://doi.org/10.1016/j.cma.2014.06.033. URL: https://www.sciencedirect.com/science/article/pii/S0045782514002199.

[20] J. Bonet and R. D. Wood. *Nonlinear continuum mechanics for finite element analysis*. Cambridge university press, Cambridge, 1997. DOI: 10.1017/CBO9780511755446.

[21] R. Boulaud and C. Douth. A Sliding Cable Model for Rockfall Barrier Simulations Using Dynamic Relaxation. In *IASS Annual Symposium*, 2017. ISSN 2518-6582 (Online).

[22] J. U. Brackbill, D. B. Kothe, and H. M. Ruppel. Flip: a low-dissipation, particle-in-cell method for fluid flow. *Computer Physics Communications*, 48:25–38, 1988. URL: https://api.semanticscholar.org/CorpusID:18473182.

[23] J. U. Brackbill and H. M. Ruppel. Flip: a method for adaptively zoned, particle-in-cell calculations of fluid flows in two dimensions. *Journal of Computational Physics*, 65(2):314–343, 1986. ISSN: 0021-9991. DOI: https://doi.org/10.1016/0021-9991(86)90211-1. URL: https://www.sciencedirect.com/science/article/pii/0021999186902111.

[24] G. Bradshaw. Sphere-Tree Construction Toolkit. http://isg.cs.tcd.ie/spheretree/, 2021.

[25] G. Bradshaw and C. O'Sullivan. Adaptive Medial-Axis Approximation for Sphere-Tree Construction. *ACM Transactions on Graphics*, 2004. DOI: https://doi.org/10.1145/966131.966132.

[26] G. Bradshaw and C. O'Sullivan. Sphere-Tree Construction using Dynamic Medial Axis Approximation. In *Proceedings of the 2002 ACM SIGGRAPH/Eurographics symposium on Computer animation*, 2002. DOI: https://doi.org/10.1145/545261.545267.

[27] M. Breitenberger, A. Apostolatos, B. Philipp, R. Wüchner, and K.-U. Bletzinger. Analysis in computer aided design: nonlinear isogeometric b-rep analysis of shell structures. *Computer Methods in Applied Mechanics and Engineering*, 284:401–457, 2015. ISSN: 0045-7825. DOI: http://dx.doi.org/10.1016/j.cma.2014.09.033. Isogeometric Analysis Special Issue.

[28] F. Brezzi. On the existence, uniqueness and approximation of saddle-point problems arising from lagrangian multipliers. *R.A.I.R.O. Analyse Numérique*, 8(R2):129–151, 1974. DOI: 10.1051/m2an/197408R201291.

[29] F. Brezzi and M. Fortin. *Mixed and Hybrid Finite Element Methods*. Springer New York, NY, 1991. DOI: 10.1007/978-1-4612-3172-1.

[30] E. Brivadis, A. Buffa, B. Wohlmuth, and L. Wunderlich. Isogeometric mortar methods. *Computer Methods in Applied Mechanics and Engineering*, 284:292–319, 2015. ISSN: 0045-7825. DOI: 10.1016/j.cma.2014.09.012.

[31] P. Bucher. Cosimulation and mapping for large scale problems. en, München, 2024.

[32] H. H. Bui, J. K. Kodikara, A. Bouazza, A. Haque, and P. G. Ranjith. A novel computational approach for large deformation and post-failure analyses of segmental retaining wall systems. *International Journal for Numerical and Analytical Methods in Geomechanics*, 38:1321–1340, 2014.

[33] B. Chandra. *Soil-Structure Interaction Simulation Using a Coupled Implicit Material Point - Finite Element Method*. Master's thesis, Technical University of Munich, 2019. (Unpublished).

[34] B. Chandra, V. Singer, T. Teschemacher, R. Wüchner, and A. Larese. Nonconforming dirichlet boundary conditions in implicit material point method by means of penalty augmentation. en. *Acta Geotechnica*, 2021. DOI: 10.1007/s11440-020-01123-3.

[35] Z.P. Chen, X.M. Qiu, X. Zhang, and Y.P. Lian. Improved coupling of finite element method with material point method based on a particle-to-surface contact algorithm. *Computer Methods in Applied Mechanics and Engineering*, 293:1–19, 2015. ISSN: 0045-7825. DOI: https://doi.org/10.1016/j.cma.2015.04.005. URL: https://www.sciencedirect.com/science/article/pii/S0045782515001498.

[36] I. Chowdhury and S. Dasgupta. Computation of rayleigh damping coefficients for large systems. *Int. J. Space Struct.*, 43:6855–6868, January 2003.

[37] J. Chung and G. M. Hulbert. A Time Integration Algorithm for Structural Dynamics With Improved Numerical Dissipation: The Generalized-α Method. *Journal of Applied Mechanics*, 1993. DOI: https://doi.org/10.1115/1.2900803.

[38] R. W. Clough and J. Penzien. *Dynamics of structures*. McGraw-Hill, New York and Düsseldorf, 1975. ISBN: 9780070113923.

[39] A. Yerro Colom, E. Alonso Pérez de Agreda, and N. M. Pinyol Puigmartı. The material point method for unsaturated soils. *Géotechnique*, 65(3):201–217, 2015. DOI: 10.1680/geot.14.P.163.

[40] S. Cummins, C. Thornton, and P. Cleary. Contact Force Models in Inelastic Collisions. In *Ninth International Conference on CFD in the Minerals and Process Industries*, 2012. ISBN: 978-1-922173-01-0.

[41] P. A. Cundall and O.D.L. Strack. A Discrete Numerical Model for Granular Assemblies. *Geotechnique*, 1979. DOI: https://doi.org/10.1680/geot.1979.29.1.47.

[42] P. Dadvand, R. Rossi, M. Gil, X. Martorell, J. Cotela, E. Juanpere, S. Idelsohn, and E. Oñate. Migration of a Generic Multi-Physics Framework to HPC Environments. *Computers & Fluids*:301–309, 2013. DOI: https://doi.org/10.1016/j.compfluid.2012.02.004.

[43] P. Dadvand, R. Rossi, and E. Oñate. An Object-oriented Environment for Developing Finite Element Codes for Multi-disciplinary Applications. *Archives of Computational Methods in Engineering*:253–297, 2010. DOI: https://doi.org/10.1007/s11831-010-9045-2.

[44] A. de Boer, A.H. van Zuijlen, and H. Bijl. Comparison of conservative and consistent approaches for the coupling of non-matching meshes. *Computer Methods in Applied Mechanics and Engineering*, 197(49):4284–4297, 2008. ISSN: 0045-7825. DOI: https://doi.org/10.1016/j.cma.2008.05.001.

[45] A. de Vaucorbeil, V. P. Nguyen, S. Sinaie, and J. Y. Wu. Chapter two - material point method after 25 years: theory, implementation, and applications. In Stéphane P.A. Bordas and Daniel S. Balint, editors. Volume 53, Advances in Applied Mechanics, pages 185–398. Elsevier, 2020. DOI: https://doi.org/10.1016/bs.aams.2019.11.001. URL: https://www.sciencedirect.com/science/article/pii/S0065215619300146.

[46] J. Degroote, K.-J. Bathe, and J. Vierendeels. Performance of a new partitioned procedure versus a monolithic procedure in fluid–structure interaction. *Computers Structures*, 87(11):793–801, 2009. ISSN: 0045-7949. DOI: https://doi.org/10.1016/j.compstruc.2008.11.013. URL: https://www.sciencedirect.com/science/article/pii/S0045794908002605. Fifth MIT Conference on Computational Fluid and Solid Mechanics.

[47] W. G. Dettmer and D. Perić. A new staggered scheme for fluid–structure interaction. *International Journal for Numerical Methods in Engineering*, 93(1):1–22, 2013. DOI: https://doi.org/10.1002/nme.4370.

[48] J.P. Escallón, A. von Boetticher, C. Wendeler, E. Chatzi, and P. Bartelt. Mechanics of Chain-Link Wire Nets With Loose Connections. *Engineering Structures*, 2015. DOI: https://doi.org/10.1016/j.engstruct.2015.07.005.

[49] C. Farhat, M. Lesoinne, and P. Le Tallec. Load and motion transfer algorithms for fluid/structure interaction problems with non-matching discrete interfaces: momentum and energy conservation, optimal discretization and application to aeroelasticity. *Computer Methods in Applied Mechanics and Engineering*, 157(1):95–114, 1998. ISSN: 0045-7825. DOI: https://doi.org/10.1016/S0045-7825(97)00216-8. URL: https://www.sciencedirect.com/science/article/pii/S0045782597002168.

[50] C. A. Felippa, K.-C. Park, and C. Farhat. Partitioned Analysis of Coupled Mechanical Systems. *Computer Methods in Applied Mechanics and Engineering*, 2001. DOI: https://doi.org/10.1016/S0045-7825(00)00391-1.

[51] J. Fern, A. Rohe, K. Soga, and E. Alonso. *The Material Point Method for Geotechnical Engineering. A Practical Guide*. CRC Press, 1st edition, 2019. ISBN: 978-0-367-73194-6.

[52] V. Mataix Ferrándiz, P. Bucher, R. Rossi, J. Cotela, J.M. Carbonell, R. Zorrilla, and R. Tosi. KratosMultiphysics (Version 8.0). *Zenodo*, 2020. DOI: https://doi.org/10.5281/zenodo.3234644.

[53] B. A. Finlayson. *The Method of Weighted Residuals and Variational Principles*. Society for Industrial and Applied Mathematics, Philadelphia, PA, 2013. DOI: https://doi.org/10.1137/1.9781611973242.

[54] Y. Gan, Z. Sun, Z. Chen, X. Zhang, and Y. Liu. Enhancement of the material point method using b-spline basis functions. *International Journal for Numerical Methods in Engineering*, 113:411–431, 3, January 2018. ISSN: 10970207. DOI: 10.1002/nme.5620.

[55] B. Gatzhammer. *Efficient and Flexible Partitioned Simulation of Fluid-Structure Interactions*. Dissertation, Technische Universität München, München, 2014.

[56] J. Gaume, A. van Herwijnen, T. Gast, J. Teran, and C. Jiang. Investigating the release and flow of snow avalanches at the slope-scale using a unified model based on the material point method. *Cold Regions Science and Technology*, 168:102847, 2019. ISSN: 0165-232X. DOI: https://doi.org/10.1016/j.coldregions.2019.102847. URL: https://www.sciencedirect.com/science/article/pii/S0165232X19302149.

[57] Geobrugg. DELTAX®. https://www.geobrugg.com/de/DELTAX-7806,7859.html, 2021.

[58] H. G. Grassl. *Experimentelle und numerische Modellierung des dynamischen Trag- und Verformungsverhaltens von hochflexiblen Schutzsystemen gegen Steinschlag. (German)*. PhD thesis, Swiss Federal Institute of Technology in Zurich, 2002. DOI: https://doi.org/10.3929/ethz-a-004446317.

[59] Q. Guo, X. Han, C. Fu, T. Gast, R. Tamstorf, and J. Teran. A material point method for thin shells with frictional contact. *ACM Trans. Graph.*, 37(4), July 2018. ISSN: 0730-0301. DOI: 10.1145/3197517.3201346.

[60] W. R. Hamilton. On Quaternions, or on a New System of Imaginaries in Algebra. *The London Edinburgh and Dublin Philosophical Magazine*, 1844. Edited by D. R. Wilkins in 2000. https://www.emis.de/classics/Hamilton/OnQuat.pdf.

[61] F. H. Harlow. Hydrodynamic problems involving large fluid distortions. *J. ACM*, 4(2):137–142, April 1957. ISSN: 0004-5411.

[62] F. H. Harlow. The particle-in-cell computing method for fluid dynamics. *Methods in Computational Physics*, 3:319–343, 1964.

[63] M. Hautefeuille, C. Annavarapu, and J. E. Dolbow. Robust imposition of dirichlet boundary conditions on embedded surfaces. *International Journal for Numerical Methods in Engineering*, 90(1):40–64, 2012. DOI: https://doi.org/10.1002/nme.3306.

[64] G. A. Holzapfel. *Nonlinear Solid Mechanics - A Continuum Approach for Engineering*. John Wiley & Sons Ltd, 2000. ISBN: 978-0-471-82319-3.

[65] T. Horger, S. Kollmannsberger, F. Frischmann, E. Rank, and B. Wohlmuth. A new mortar formulation for modeling elastomer bedded structures with modal-analysis in 3d. *Advanced Modeling and Simulation in Engineering Sciences*, 1(1), 2014. DOI: 10.1186/s40323-014-0018-0.

[66] T.J.R. Hughes. *The Finite Element Method: Linear Static and Dynamic Finite Element Analysis*. Prentice-Hail, Englewood Cliffs, N J, 1987.

[67] I. Iaconeta. Discrete-continuum hybrid modelling of flowing and static regimes:169, 2019. URL: https://www.tesisenred.net/handle/10803/668088#.

[68] I. Iaconeta, A. Larese, R. Rossi, and Zhiming Guo. Comparison of a material point method and a galerkin meshfree method for the simulation of cohesive-frictional materials. *Materials*, 10, 10, September 2017. ISSN: 19961944. DOI: 10.3390/ma10101150.

[69] I. Iaconeta, A. Larese, R. Rossi, and E. Oñate. A stabilized mixed implicit material point method for non-linear incompressible solid mechanics. *Computational Mechanics*:1–18, 2018. DOI: https://doi.org/10.1007/s00466-018-1647-9.

[70] J. Irazábal, F. Salazar, M. Santasusana, and E. Oñate. Effect of the Integration Scheme on the Rotation of Non-Spherical Particles With the Discrete Element Method. *Computational Particle Mechanics*, 2019. DOI: https://doi.org/10.1007/s40571-019-00232-5.

[71] Y. Jiang, M. Li, C. Jiang, and F. Alonso-Marroquin. A hybrid material-point spheropolygon-element method for solid and granular material interaction. *International Journal for Numerical Methods in Engineering*, 121:3021–3047, 14, July 2020. ISSN: 10970207. DOI: 10.1002/nme.6345.

[72] I. K. J. al-Kafaji. *Formulation of a dynamic material point method (MPM) for geomechanical problems*. PhD thesis, University of Stuttgart, 2013.

[73] J. Kiendl. *Isogeometric Analysis and Shape Optimal Design of Shell Structures*. PhD thesis, Technical University of Munich, 2011. ISBN: 978-3-8440-0104-4.

[74] E. Klingbeil. *Tensorrechnung für Ingenieure*. BI-Hochschultaschenbücher. Bibliographisches Institut, 1966. ISBN: 9783411001972.

[75] M. Kodam, R. Bharadwaj, J. Curtis, B. Hancock, and C. Wassgren. Force Model Considerations For Glued-Sphere Discrete Element Method Simulations. *Chemical Engineering Science*, 2009. DOI: https://doi.org/10.1016/j.ces.2009.04.025.

[76] S. Kollmannsberger, A. Özcan, J. Baiges, M. Ruess, E. Rank, and A. Reali. Parameter-free, weak imposition of dirichlet boundary conditions and coupling of trimmed and non-conforming patches. *International Journal for Numerical Methods in Engineering*, 101(9):670–699, 2015. DOI: 10.1002/nme.4817.

[77] Kratos multiphysics. https://github.com/KratosMultiphysics/Kratos.

[78] U. Küttler and W. A. Wall. Fixed-point fluid–structure interaction solvers with dynamic relaxation. *Computational Mechanics*, 43(1):61–72, 2008. ISSN: 0178-7675. DOI: 10.1007/s00466-008-0255-5.

[79] K. Larsson, S. Kollmannsberger, E. Rank, and M. G. Larson. The finite cell method with least squares stabilized nitsche boundary conditions. *Computer Methods in Applied Mechanics and Engineering*, 393:114792, 2022.

[80] E. H. Lee. Elastic-Plastic Deformation at Finite Strains. *Journal of Applied Mechanics*, 36(1):1–6, March 1969. ISSN: 0021-8936. DOI: 10.1115/1.3564580. URL: https://doi.org/10.1115/1.3564580.

[81] Z. Lei, B. Wu, S. Wu, Y. Nie, S. Cheng, and C. Zhang. A material point-finite element (mpm-fem) model for simulating three-dimensional soil-structure interactions with the hybrid contact method. *Computers and Geotechnics*, 152:105009, 2022. ISSN: 0266-352X. DOI: https://doi.org/10.1016/j.compgeo.2022.105009. URL: https://www.sciencedirect.com/science/article/pii/S0266352X22003469.

[82] X. Li, B. Sovilla, C. Jiang, and J. Gaume. The Mechanical Origin of Snow Avalanche Dynamics and Flow Regime Transition. *The Cryosphere*, 2020. DOI: https://doi.org/10.5194/tc-14-3381-2020.

[83] X. Li, B. Sovilla, C. Jiang, and J. Gaume. Three-Dimensional and Real-Scale Modeling of Flow Regimes in Dense Snow Avalanches. *Landslides*, 2021. DOI: https://doi.org/10.1007/s10346-021-01692-8.

[84] Y.P. Lian, X. Zhang, and Y. Liu. Coupling of finite element method with material point method by local multi-mesh contact method. *Computer Methods in Applied Mechanics and Engineering*, 200(47):3482–3494, 2011. ISSN: 0045-7825. DOI: https://doi.org/10.1016/j.cma.2011.07.014. URL: https://www.sciencedirect.com/science/article/pii/S0045782511002556.

[85] Y.P. Lian, X. Zhang, X. Zhou, and Z.T. Ma. A femp method and its application in modeling dynamic response of reinforced concrete subjected to impact loading. *Computer Methods in Applied Mechanics and Engineering*, 200(17):1659–1670, 2011. ISSN: 0045-7825. DOI: https://doi.org/10.1016/j.cma.2011.01.019. URL: https://www.sciencedirect.com/science/article/pii/S004578251100034X.

[86] C. Liu, Q. Sun, and G. G. D. Zhou. Coupling of material point method and discrete element method for granular flows impacting simulations. *International Journal for Numerical Methods in Engineering*, 115:172–188, 2, July 2018. ISSN: 10970207. DOI: 10.1002/nme.5800.

[87] S. Ma, X. Zhang, and X. M. Qiu. Comparison study of MPM and SPH in modeling hypervelocity impact problems. *International Journal of Impact Engineering*, 36(2):272–282, 2009. DOI: https://doi.org/10.1016/j.ijimpeng.2008.07.001.

[88] H.-G. Matuttis and J. Chen. *Understanding the Discrete Element Method: Simulation of Non-Spherical Particles for Granular and Multi-Body Systems*. John Wiley & Sons, Inc., 2014. ISBN: 978-1-118-56720-3.

[89] J. Meijaard. Lateral impacts on flexible beams in multibody dynamics simulations. In *IUTAM Symposium on Multiscale Problems in Multibody System Contacts*, pages 173–182, Dordrecht. Springer Netherlands, 2007.

[90] N. M. Newmark. A method of computation for structural dynamics. *Journal of the Engineering Mechanics Division*, 85(3):67–94, 1959. DOI: 10.1061/JMCEA3.0000098.

[91] T. S. Nguyen, K.-H. Yang, Y.-K. Wu, F. Teng, W.-A. Chao, and W.-L. Lee. Post-failure process and kinematic behavior of two landslides: case study and material point analyses. *Computers and Geotechnics*, 148:104797, 2022. ISSN: 0266-352X. DOI: https://doi.org/10.1016/j.compgeo.2022.104797. URL: https://www.sciencedirect.com/science/article/pii/S0266352X22001549.

[92] V. P. Nguyen, A. de Vaucorbeil, and S. Bordas. *The Material Point Method*. Springer International Publishing, Cham, 2023. ISBN: 978-3-031-24069-0. DOI: 10.1007/978-3-031-24070-6.

[93] R. W. Ogden. Non-Linear Elastic Deformations, 1997.

[94] E. Oñate, F. Zárate, M. A. Celigueta, J. M. González, J. Miquel, J. M. Carbonell, F. Arrufat, S. Latorre, and M. Santasusana. *Advances in the DEM and Coupled DEM and FEM Techniques in Non Linear Solid Mechanics*. In *Advances in Computational Plasticity: A Book in Honour of D. Roger J. Owen*. Springer International Publishing, Cham, 2018, pages 309–335. ISBN: 978-3-319-60885-3.

[95] S. Piperno. Explicit/implicit fluid/structure staggered procedures with a structural predictor and fluid subcycling for 2d inviscid aeroelastic simulations. *International Journal for Numerical Methods in Fluids*, 25(10):1207–1226, 1997. DOI: https://doi.org/10.1002/(SICI)1097-0363(19971130)25:10<1207::AID-FLD616>3.0.CO;2-R.

[96] S. Piperno, C. Farhat, and B. Larrouturou. Partitioned procedures for the transient solution of coupled aroelastic problems part i: model problem, theory and two-dimensional application. *Computer Methods in Applied Mechanics and Engineering*, 124(1):79–112, 1995. ISSN: 0045-7825. DOI: https://doi.org/10.1016/0045-7825(95)92707-9.

[97] A. Sadeghirad, R. M. Brannon, and J. Burghardt. A convected particle domain interpolation technique to extend applicability of the material point method for problems involving massive deformations. *International Journal for Numerical Methods in Engineering*, 86(12):1435–1456, 2011. DOI: https://doi.org/10.1002/nme.3110.

[98] A. Sadeghirad, R. M. Brannon, and J. E. Guilkey. Second-order convected particle domain interpolation (CPDI2) with enrichment for weak discontinuities at material interfaces. *International Journal for Numerical Methods in Engineering*, 95(11):928–952, 2013. DOI: https://doi.org/10.1002/nme.4526.

[99] M. Santasusana. *Numerical Techniques for Non-Linear Analysis of Structures Combining Discrete Element and Finite Element Methods*. PhD thesis, Centre for Numerical Methods in Engineering, Barcelona, Spain, 2016. https://www.cimne.com/cvdata/cntr2/dtos/pgs/Research/Theses/Miquel-Santasusana.pdf.

[100] M. Santasusana, J. Irazábal, E. Oñate, and J. M. Carbonell. The Double Hierarchy Method. a Parallel 3D Contact Method for the Interaction of Spherical Particles With Rigid FE Boundaries Using the DEM. *Computational Particle Mechanics*, 2016. DOI: https://doi.org/10.1007/s40571-016-0109-4.

[101] K. B. Sautter. Modeling and simulation of flexible protective structures by coupling particle and finite element methods. en, München, 2022.

[102] K. B. Sautter, H. Hofmann, C. Wendeler, P. Wilson, P. Bucher, K.-U. Bletzinger, and R. Wüchner. Advanced Modeling and Simulation of Rockfall Attenuator Barriers Via Partitioned DEM-FEM Coupling. *Frontiers in Built Environment - Computational Methods in Structural Engineering*, 2021. DOI: https://doi.org/10.3389/fbuil.2021.659382.

[103] K. B. Sautter, H. Hofmann, C. Wendeler, R. Wüchner, and K.-U. Bletzinger. Influence of DE-Cluster Refinement on Numerical Analysis of Rockfall Experiments. *Computational Particle Mechanics*, 2021. DOI: https://doi.org/10.1007/s40571-020-00382-x.

[104] K. B. Sautter, M. Meßmer, T. Teschemacher, and K.-U. Bletzinger. Limitations of the St. Venant–Kirchhoff Material Model in Large Strain Regimes. *International Journal of Non-Linear Mechanics*, 2022. DOI: https://doi.org/10.1016/j.ijnonlinmec.2022.104207.

[105] K. B. Sautter, T. Teschemacher, M.Á. Celigueta, P. Bucher, K.-U. Bletzinger, and R. Wüchner. Partitioned Strong Coupling of Discrete Elements with Large Deformation Structural Finite Elements to Model Impact on Highly Flexible Tension Structures. *Advances in Civil Engineering - Advancements in the Analysis and Design of Protective Structures against Extreme Loadings 2020*, 2020. DOI: https://doi.org/10.1155/2020/5135194.

[106] T. Schwager and T. Pöschel. Coefficient of Restitution and Linear-Dashpot Model Revisited. *Granular Matter*, 2007. DOI: https://doi.org/10.1007/s10035-007-0065-z.

[107] J. Shäfer, S. Dippel, and D. Wolf. Force Schemes in Simulations of Granular Materials. *Journal de Physique*, 1996. DOI: https://doi.org/10.1051/jp1:1996129.

[108] S. Shayegan. *Enhanced Algorithms for Fluid-Structure Interaction Simulations*. Dissertation, Technische Universität München, München, 2023.

[109] S. A. Sicklinger. *Stabilized Co-Simulation of Coupled Problems Including Fields and Signals*. PhD thesis, Technical University of Munich, 2014. ISBN: 978-3-943683-28-8.

[110] J. C. Simo. Algorithms for static and dynamic multiplicative plasticity that preserve the classical return mapping schemes of the infinitesimal theory. *Computer Methods in Applied Mechanics and Engineering*, 99(1):61–112, 1992. ISSN: 0045-7825. DOI: https://doi.org/10.1016/0045-7825(92)90123-2. URL: https://www.sciencedirect.com/science/article/pii/0045782592901232.

[111] J. C. Simo. Numerical analysis and simulation of plasticity. In *Numerical Methods for Solids (Part 3) Numerical Methods for Fluids (Part 1)*. Volume 6, Handbook of Numerical Analysis, pages 183–499. Elsevier, 1998. DOI: https://doi.org/10.1016/S1570-8659(98)80009-4.

[112] J. C. Simo, P. Wriggers, and R. L. Taylor. A perturbed lagrangian formulation for the finite element solution of contact problems. *Computer Methods in Applied Mechanics and Engineering*, 50(2):163–180, 1985. ISSN: 0045-7825. DOI: https://doi.org/10.1016/0045-7825(85)90088-X. URL: https://www.sciencedirect.com/science/article/pii/004578258590088X.

[113] V. Singer, B. Chandra, R. Wüchner, and A. Larese. A Staggered Coupling Scheme of the Material Point Method and the Finite Element Method using Gauss Seidel Communication Pattern. *International Conference on Computational Methods for Coupled Problems in Science and Engineering*, 2021. DOI: https://doi.org/10.23967/coupled.2021.006.

[114] V. Singer, A. Larese, R. Wüchner, and K.-U. Bletzinger. Partitioned MPM-FEM Coupling Approach for Advanced Numerical Simulation of Mass-Movement Hazards Impacting Flexible Protective Structures. *International Conference on Computational Methods for Coupled Problems in Science and Engineering*, 2023. DOI: https://doi.org/10.23967/c.coupled.2023.026.

[115] V. Singer, K. B. Sautter, A. Larese, R. Wüchner, and K.-U. Bletzinger. A Partitioned Material Point Method and Discrete Element Method Coupling Scheme. *Advanced Modeling and Simulation in Engineering Sciences*, 2022. DOI: https://doi.org/10.1186/s40323-022-00229-5.

[116] V. Singer, K.B. Sautter, A. Larese, R. Wüchner, and K.-U. Bletzinger. Partitioned Coupling Approaches for the Simulation of Natural Hazards Impacting Protective Structures. *International Conference on Particle-Based Methods*, 2023. DOI: https://doi.org/10.23967/c.particles.2023.002.

[117] V. Singer, T. Teschemacher, A. Larese, R. Wüchner, and K.-U. Bletzinger. Lagrange multiplier imposition of non-conforming essential boundary conditions in implicit material point method. *Computational Mechanics*, 2023. DOI: https://doi.org/10.1007/s00466-023-02412-w.

[118] W. T. Sołowski, M. Berzins, W. M. Coombs, J. E. Guilkey, M. Möller, Q. A. Tran, T. Adibaskoro, S. Seyedan, R. Tielen, and K. Soga. Chapter two - material point method: overview and challenges ahead. In P.A. Bordas Stéphane and Daniel S. Balint, editors. Volume 54, Advances in Applied Mechanics, pages 113–204. Elsevier, 2021. DOI: https://doi.org/10.1016/bs.aams.2020.12.002. URL: https://www.sciencedirect.com/science/article/pii/S0065215620300120.

[119] A. Stomakhin, C. Schroeder, L. Chai, J. Teran, and A. Selle. A material point method for snow simulation. *ACM Trans. Graph.*, 32(4), July 2013. ISSN: 0730-0301. DOI: 10.1145/2461912.2461948.

[120] D. Sulsky, Z. Chen, and H. L. Schreyer. A Particle Method for History-Dependent Materials. *Computer Methods in Applied Mechanics and Engineering*, 118(1-2):179–196, 1994. DOI: https://doi.org/10.1016/0045-7825(94)90112-0.

[121] D. Sulsky, S.-J. Zhou, and H. L. Schreyer. Application of a particle-in-cell method to solid mechanics. *Computer Physics Communications*, 87(1):236–252, 1995. ISSN: 0010-4655. DOI: https://doi.org/10.1016/0010-4655(94)00170-7. URL: https://www.sciencedirect.com/science/article/pii/0010465594001707. Particle Simulation Methods.

[122] T. Teschemacher, A. M. Bauer, T. Oberbichler, M. Breitenberger, R. Rossi, R. Wüchner, and K.-U. Bletzinger. Realization of cad-integrated shell simulation based on isogeometric b-rep analysis. *Advanced Modeling and Simulation in Engineering Sciences*, 5(1):1–54, 2018. ISSN: 2213-7467. DOI: 10.1186/s40323-018-0109-4.

[123] C. Thornton, S. J. Cummins, and P. W. Cleary. An Investigation of the Comparative Behaviour of Alternative Contact Force Models During Inelastic Collisions. *Powder Technology*, 2013. DOI: https://doi.org/10.1016/j.powtec.2012.08.012.

[124] S. P. Timoshenko and J. N. Goodier. Theory of elasticity. *McGraw-Hill*, 1951.

[125] B. W. Uekermann. *Partitioned Fluid-Structure Interaction on Massively Parallel Systems*. Dissertation, Technische Universität München, München, 2016.

[126] L. Verlet. Computer "experiments" on classical fluids. i. thermodynamical properties of lennard-jones molecules. *Phys. Rev.*, 159:98–103, 1, 1967. DOI: https://doi.org/10.1103/PhysRev.159.98. URL: https://link.aps.org/doi/10.1103/PhysRev.159.98.

[127] A. Volkwein. *Numerische Simulation von flexiblen Steinschlagschutzsystemen. (German)*. PhD thesis, Swiss Federal Institute of Technology in Zurich, 2004. DOI: https://doi.org/10.3929/ethz-a-004879843.

[128] A. von Bötticher. *Flexible Hangmurenbarrieren: Eine numerische Modellierung des Tragwerks, der Hangmure und der Fluid-Struktur-Interaktion. (German)*. PhD thesis, Technical University of Munich, 2012. ISBN: 978-3-8440-1616-1.

[129] W. Wunderlich and W. D. Pilkey. *Mechanics of Structures : Variational and Computational Methods*. CRC Press, 2002. ISBN: 9780429115097. DOI: 10.1201/9781420041835. URL: https://www.taylorfrancis.com/books/mono/10.1201/9781420041835/mechanics-structures-%20walter-wunderlich-walter-pilkey.

[130] W. A. Wall. *Fluid-Struktur-Interaktion mit stabilisierten Finiten Elementen*. PhD thesis, 1999. DOI: 10.18419/opus-127.

[131] T. Wang. *Development of Co-Simulation Environment and Mapping Algorithms*. Dissertation, Technische Universität München, München, 2016.

[132] P. Wilson. A computational impact analysis approach leveraging non-conforming spatial, temporal and methodological discretisations, 2022. DOI: https://doi.org/10.14264/3e10f66.

[133] P. Wilson, T. Teschemacher, P. Bucher, and R. Wüchner. Non-conforming fem-fem coupling approaches and their application to dynamic structural analysis. *Engineering Structures*, 241:112342, 2021. ISSN: 0141-0296. DOI: https://doi.org/10.1016/j.engstruct.2021.112342. URL: https://www.sciencedirect.com/science/article/pii/S0141029621004922.

[134] P. Wilson, R. Wüchner, and D. Fernando. Distillation of the material point method cell crossing error leading to a novel quadrature-based c0 remedy. *International Journal for Numerical Methods in Engineering*, 122:1513–1537, 6, March 2021. ISSN: 10970207. DOI: 10.1002/nme.6588.

[135] A. Winterstein. *Modeling and Simulation of Wind-Structure Interaction of Slender Civil Engineering Structures Including Vibration Mitigation Systems*. PhD thesis, Technical University of Munich, 2020. ISBN: 978-3-943683-61-5.

[136] A. Winterstein, C. Lerch, K.-U. Bletzinger, and R. Wüchner. Partitioned Simulation Strategies for Fluid–Structure–Control Interaction Problems by Gauss–Seidel Formulations. *Advanced Modeling and Simulation in Engineering Sciences*, 2018. DOI: https://doi.org/10.1186/s40323-018-0123-6.

[137] P. Wriggers. *Nonlinear finite element methods*. Springer Science & Business Media, Berlin,Heidelberg, 2008.

[138] R. Wüchner. *Mechanik und Numerik der Formfindung und Fluid-Struktur-Interaktion von Membrantragwerken. (German)*. PhD thesis, Technical University of Munich, 2006. ISBN: 978-3-8322-6391-1.

[139] H. W. Zhang, K. P. Wang, and Z. Chen. Material point method for dynamic analysis of saturated porous media under external contact/impact of solid bodies. *Computer Methods in Applied Mechanics and Engineering*, 198(17-20):1456–1472, 2009. DOI: https://doi.org/10.1016/j.cma.2008.12.006.

[140] X. Zhang, Z. Chen, and Y. Liu. *The Material Point Method: A Continuum-Based Particle Method for Extreme Loading Cases*. Academic Press, 1st edition, 2016. ISBN: 978-0-124-07855-0.

[141] X. Zhang, K. Y. Sze, and S. Ma. An explicit material point finite element method for hyper-velocity impact. *International Journal for Numerical Methods in Engineering*, 66(4):689–706, 2006. DOI: 10.1002/nme.1579.

[142] O. C. Zienkiewicz and R. L. Taylor. *The finite element method*, volume 36. McGraw-hill London, 1977.

Bisherige Titel der Schriftenreihe

Band	Titel
1	Frank Koschnick, *Geometrische Lockingeffekte bei Finiten Elementen und ein allgemeines Konzept zu ihrer Vermeidung*, 2004.
2	Natalia Camprubi, *Design and Analysis in Shape Optimization of Shells*, 2004.
3	Bernhard Thomee, *Physikalisch nichtlineare Berechnung von Stahlfaserbetonkonstruktionen*, 2005.
4	Fernaß Daoud, *Formoptimierung von Freiformschalen - Mathematische Algorithmen und Filtertechniken*, 2005.
5	Manfred Bischoff, *Models and Finite Elements for Thin-walled Structures*, 2005.
6	Alexander Hörmann, *Ermittlung optimierter Stabwerkmodelle auf Basis des Kraftflusses als Anwendung plattformunabhängiger Prozesskopplung*, 2006.
7	Roland Wüchner, *Mechanik und Numerik der Formfindung und Fluid-Struktur-Interaktion von Membrantragwerken*, 2006.
8	Florian Jurecka, *Robust Design Optimization Based on Metamodeling Techniques*, 2007.
9	Johannes Linhard, *Numerisch-mechanische Betrachtung des Entwurfsprozesses von Membrantragwerken*, 2009.
10	Alexander Kupzok, *Modeling the Interaction of Wind and Membrane Structures by Numerical Simulation*, 2009.

Band	Titel
11	Bin Yang, *Modified Particle Swarm Optimizers and their Application to Robust Design and Structural Optimization*, 2009.
12	Michael Fleischer, *Absicherung der virtuellen Prozesskette für Folgeoperationen in der Umformtechnik*, 2009.
13	Amphon Jrusjrungkiat, *Nonlinear Analysis of Pneumatic Membranes - From Subgrid to Interface*, 2009.
14	Alexander Michalski, *Simulation leichter Flächentragwerke in einer numerisch generierten atmosphärischen Grenzschicht*, 2010.
15	Matthias Firl, *Optimal Shape Design of Shell Structures*, 2010.
16	Thomas Gallinger, *Effiziente Algorithmen zur partitionierten Lösung stark gekoppelter Probleme der Fluid-Struktur-Wechselwirkung*, 2011.
17	Josef Kiendl, *Isogeometric Analysis and Shape Optimal Design of Shell Structures*, 2011.
18	Joseph Jordan, *Effiziente Simulation großer Mauerwerksstrukturen mit diskreten Rissmodellen*, 2011.
19	Albrecht von Boetticher, *Flexible Hangmurenbarrieren: Eine numerische Modellierung des Tragwerks, der Hangmure und der Fluid-Struktur-Interaktion*, 2012.
20	Robert Schmidt, *Trimming, Mapping, and Optimization in Isogeometric Analysis of Shell Structures*, 2013.
21	Michael Fischer, *Finite Element Based Simulation, Design and Control of Piezoelectric and Lightweight Smart Structures*, 2013.
22	Falko Hartmut Dieringer, *Numerical Methods for the Design and Analysis for Tensile Structures*, 2014.
23	Rupert Fisch, *Code Verification of Partitioned FSI Environments for Lightweight Structures*, 2014.

Band **Titel**

24 Stefan Sicklinger, *Stabilized Co-Simulation of Coupled Problems Including Fields and Signals*, 2014.

25 Madjid Hojjat, *Node-based parametrization for shape optimal design*, 2015.

26 Ute Israel, *Optimierung in der Fluid-Struktur-Interaktion - Sensitivitätsanalyse für die Formoptimierung auf Grundlage des partitionierten Verfahrens*, 2015.

27 Electra Stavropoulou, *Sensitivity analysis and regularization for shape optimization of coupled problems*, 2015.

28 Daniel Markus, *Numerical and Experimental Modeling for Shape Optimization of Offshore Structures*, 2015.

29 Pablo Suárez, *Design Process for the Shape Optimization of Pressurized Bulkheads as Components of Aircraft Structures*, 2015.

30 Armin Widhammer, *Variation of Reference Strategy - Generation of Optimized Cutting Patterns for Textile Fabrics*, 2015.

31 Helmut Masching, *Parameter Free Optimization of Shape Adaptive Shell Structures*, 2016.

32 Hao Zhang, *A General Approach for Solving Inverse Problems in Geophysical Systems by Applying Finite Element Method and Metamodel Techniques*, 2016.

33 Tianyang Wang, *Development of Co-Simulation Environment and Mapping Algorithms*, 2016.

34 Michael Breitenberger, *CAD-integrated Design and Analysis of Shell Structures*, 2016.

35 Önay Can, *Functional Adaptation with Hyperkinematics using Natural Element Method: Application for Articular Cartilage*, 2016.

Band Titel

36 Benedikt Philipp, *Methodological Treatment of Non-linear Structural Behavior in the Design, Analysis and Verification of Lightweight Structures*, 2017.

37 Michael Andre, *Aeroelastic Modeling and Simulation for the Assessment of Wind Effects on a Parabolic Trough Solar Collector*, 2018.

38 Andreas Apostolatos, *Isogeometric Analysis of Thin-Walled Structures on Multipatch Surfaces in Fluid-Structure Interaction*, 2018.

39 Altuğ Emiroğlu, *Multiphysics Simulation and CAD-Integrated Shape Optimization in Fluid-Structure Interaction*, 2019.

40 Mehran Saeedi, *Multi-Fidelity Aeroelastic Analysis of Flexible Membrane Wind Turbine Blades*, 2017.

41 Reza Najian Asl, *Shape optimization and sensitivity analysis of fluids, structures, and their interaction using Vertex Morphing Parametrization*, 2019.

42 Ahmed Abodonya, *Verification Methodology for Computational Wind Engineering Prediction of Wind Loads on Structures*, 2020.

43 Anna Maria Bauer, *CAD-integrated Isogeometric Analysis and Design of Lightweight Structures*, 2020.

44 Andreas Winterstein, *Modeling and Simulation of Wind Structure Interaction of Slender Civil Engineering Structures Including Vibration Systems*, 2020.

45 Franz-Josef Ertl, *Vertex Morphing for Constrained Shape Optimization of Three-dimensional Solid Structures*, 2020.

46 Daniel Baumgärtner, *On the Grid-based Shape Optimization of Structures with Internal Flow and the Feedback of Shape Changes into a CAD Model*, 2020.

47 Mohamed Khalil, *Combining Physics-based models and machine learning for an Enhanced Structural Health Monitoring*,2021.

Band Titel

48 Long Chen, *Gradient Descent Akin Method*, 2021.

49 Aditya Ghantasala, *Coupling Procedures for Fluid-Fluid and Fluid-Structure Interaction Problems Based on Domain Decomposition Methods*, 2021.

50 Ann-Kathrin Goldbach, *The Cad-Integrated Design Cycle for Structural Membranes*, 2022.

51 Iñigo Pablo López Canalejo,, *A Finite-Element Transonic Potential Flow Solver with an Embedded Wake Approach for Aircraft Conceptual Design*, 2022.

52 Mayu Sakuma, *An Application of Multi-Fidelity Uncertainty Quantification for Computational Wind Engineering*, 2022.

53 Suneth Warnakulasuriya, *Development of methods for Finite Element-based sensitivity analysis and goal-directed mesh refinement using the adjoint approach for steady and transient flows*, 2022.

54 Klaus Bernd Sautter, *Modeling and Simulation of Flexible Protective Structures by Coupling Particle and Finite Element Methods*, 2022.

55 Efthymios Papoutsis, *On the incorporation of industrial constraints in node-based optimization for car body design*, 2023.

56 Thomas Josef Oberbichler, *A modular and efficient implementation of isogeometric analysis for the interactive CAD-integrated design of lightweight structures*, 2023.

57 Tobias Christoph Teschemacher, *CAD-integrated constitutive modelling, analysis, and design of masonry structures*, 2023.

58 Shahrokh Shayegan, *Enhanced Algorithms for Fluid-Structure Interaction Simulations – Accurate Temporal Discretization and Robust Convergence Acceleration*, 2023.

Band Titel

59 Ihar Antonau, *Enhanced computational design methods for large industrial node-based shape optimization problems*, 2023.

60 Rishith Ellath Meethal, *Hybrid modelling and simulation approaches for the solution of forward and inverse problems in engineering by combining finite element methods and neural networks*, 2023.

61 Máté Péntek, *Method Development for the Numerical Wind Tunnel in Applied Structural Engineering*, 2023.

62 Anoop Kodakkal, *High Fidelity Modeling and Simulations for Uncertainty Quantification and Risk-averse Optimization of Structures Under Natural Wind Conditions*, 2024.

63 Philipp Bucher, *CoSimulation and Mapping for large scale engineering applications*, 2024.

64 Martin Fußeder, *Methodological and Application-Oriented Advances in Sensitivity Analysis with a Focus on Structural Engineering*, 2024.

65 Wenjia Wang, *Adjoint Sensitivity Analysis for Non-parametric Shape Optimization with Geometric Nonlinearity and Elastoplasticity*, 2024.

66 Manuel Meßmer, *Efficient and robust quadrature for embedded solids: Application to isogeometric analysis and shape optimization*, 2024.